MODELLING THE NATURAL WIND :
WIND PROTECTION BY FENCES

A thesis presented for the degree of

Doctor of Phil hy

in

Mechanical Engineering

in the

University of Canterbury,

Christchurch,

New Zealand.

by

J.K. RAINE B.E.(Hons)

October, 19

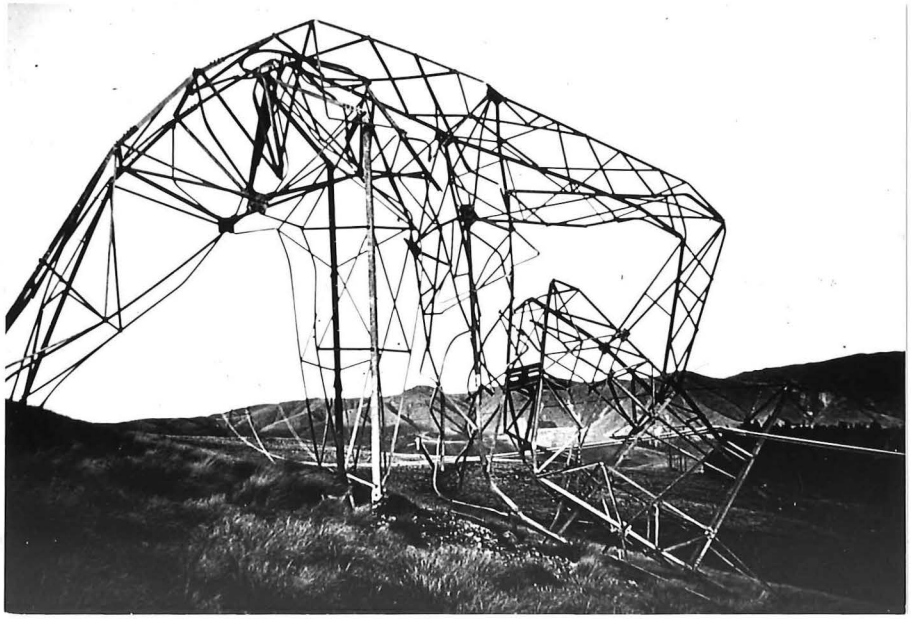

220 kV power pylon on the Benmore-Islington line, destroyed by high winds in 1964

VOLUME I

ACKNOWLEDGEMENTS

My sincere thanks are due to Professor D.C. Stevenson, who supervised this project throughout its duration. His guidance, encouragement and willingness to spend a great deal of time in discussion, have been much appreciated.

Many members of the academic, technical and secretarial staff of the Department of Mechanical Engineering have provided assistance in the execution of the project. In particular, my thanks go to colleagues Dr D. Lindley and Mr A.J. Bowen for their interest and helpful comments, to the Workshop staff directed by Mr E.D. Retallick, especially Messrs A.E. Taylor, M.E. Taylor and P.F. Towell for their diligence and enthusiasm in the construction of the wind tunnel, to Mrs V.J. Grey for her patience and care in tracing large numbers of drawings and diagrams, to Mrs P. Levicky for translation of papers from German to English, to Mrs J. Ritchie for her skill in handling all the photographic reproduction for the thesis, and to Mrs B. Stout for her willing co-operation and perseverance in typing the whole thesis.

The financial support of the University Grants Committee is gratefully acknowledged. Funds were provided in the form of a scholarship for the first year of study, and a grant for construction of the wind tunnel. Thanks are also due to Torro International (N.Z.) Limited, who donated 60,000 Torro blocks for use in wind tunnel modelling.

Finally, my thanks go to my wife for her continued encouragement, assistance with experimental work, and her patient acceptance of a long period of time where the wind tunnel assumed first priority.

ABSTRACT

This thesis describes the development of a simulated atmospheric boundary layer, and its application to the specific problem of windbreak aerodynamics.

A review is made of the state of the art in wind tunnel simulation of atmospheric boundary layers. An investigation of the use of grids to simulate atmospheric wind velocity profiles and turbulence in a short tunnel working section, is used to justify the construction of an atmospheric boundary layer wind tunnel in the Department of Mechanical Engineering. The design and construction of this wind tunnel is described. The main working section of the new facility is 4 ft x 4 ft in cross-section and 40 ft long.

The stepwise development of an accelerated growth, neutrally stable, simulated rural atmospheric boundary layer of approximately 1:300 linear scale is described. The boundary layer is grown in a distance nine times its its final depth by means of an initial coarse grid, followed by trip fences of successively decreasing height and a baseboard of uniform surface roughness. The linear scale of the model flow is larger than in most earlier simulations of the accelerated boundary layer growth type reviewed by the author.

An examination of the leeward flow behind model fence windbreaks was chosen as a first application for the simulated boundary layer. The object of this work was to give a clearer picture of the leeward flow field, and quantitatively relate mean velocity and turbulent intensity behind windbreaks. Measurements of mean and fluctuating velocities and energy spectra were carried out in the lee of model shelter fences of 0%, 20%, 34% and 50% geometric permeability. Results of the tests are compared with existing field and wind tunnel data, with due regard for the uncertainty of hot wire anemometer measurements in fence wakes. The mean velocity reduction data provide an extensive verification for Jensen's (1958) Model Law. The 20% permeable fence was found to give optimum mean wind reduction. The turbulence measurements have identified the regions dominated, respectively, by the bleed flow and by the displacement flow, and simple empirical equations are suggested to relate turbulent intensity and mean velocity in these two regions. Before a windbreak design manual can be compiled, further tests are required at a variety of 'fence height' to 'upstream surface roughness length' ratios. A basic format for a design manual is suggested.

VOLUME 1

CONTENTS

LIST OF FIGURES

LIST OF TABLES

LIST OF SYMBOLS

ABBREVIATIONS: App. Appendix
Ch. Chapter

A	Area of single opening in a permeable fence in Ch. 7, 8 and 9; cross-sectional area of section of wind tunnel App. 2.
A_w	Cross-sectional area of 4ft x 4ft working section in wind tunnel.
A_n, B_n, C_n	Fourier coefficients in App. 1.
B	Width of bar normal to flow in turbulence generating bar grid.
C	Turning vane chord length.
C_c	Contraction coefficient
$-C_b$	Shelter fence base pressure coefficient
C_f	Shelter fence front face pressure coefficient
C_D	$\frac{F_D}{\frac{1}{2}\rho \bar{U}_\infty^2 H}$, the fence drag coefficient referred to $\bar{U}_\infty$
C_{D_*}	$\frac{F_D}{\frac{1}{2}\rho u_*^2 H}$, the fence drag coefficient referred to u_*.
C_z	A constant used in empirical expressions for $\sqrt{\text{coherence}}$
D	Bar diameter in velocity profile or turbulence generating bar grid.
D	Equivalent pipe diameter in friction factor expression App. 2.
d	Zero plane displacement in logarithmic velocity profile.
d_m	Characteristic dimension of model
d_a	Characteristic dimension of prototype
d_m/d_a	Linear scaling of atmospheric boundary layer simulation
E	Anemometer output voltage; anemometer signal error term App. 6.
e	Fluctuating component of anemometer output voltage.
E_{Lin}	Linearised anemometer output voltage
F_D	Drag force
f, f_m	$\frac{nz}{\bar{U}}$, $\left(\frac{nz}{\bar{U}}\right)_p$ Dimensionless spectral frequencies
G	Subscript referring to the gradient height
$G_{u_i u_j}(n)$	Cross Spectral Density function
g	Gravitational constant in Ch. 2.3; elsewhere lateral correlation coefficient in isotropic turbulence.
H	Height of shelter fence; in Ch. 4 and App. 1, H is Wind Tunnel working section height.
H_*	Maximum height of the separation streamline behind a fence.

h Height of an object on the terrain.

$I_{u_i z}$ $\frac{u_i'}{\bar{U}_z}$, turbulent intensity of velocity component u_i, with $\bar{U}$ as a function of z.

K Pressure drop coefficient of component section of wind tunnel in App. 2, $= \Delta\bar{P}/\frac{1}{2}\rho\bar{U}^2$; in Ch. 4 and App. 1 K is local pressure drop coefficient of grid or screen based on mean velocity, $\bar{U}_1$, just upstream of grid, $= \Delta\bar{P}/\frac{1}{2}\rho\bar{U}_1^2$

K_w Pressure drop coefficient of section of wind tunnel, referred to mean velocity $\bar{U}_w$, in working section, not local mean velocity, $\bar{U}$.

K_o $\frac{\Delta\bar{P}}{\frac{1}{2}\rho\bar{U}_o^2}$, the overall pressure drop coefficient of grid or screen, based on the uniform spatial mean velocity, $\bar{U}_o$, far upstream.

K_M Eddy viscosity.

K_s Equivalent sand roughness.

k $n/\bar{U}$, spectrum wave number.

k_e Wave number characteristic of the energy containing eddies.

k_d Wave number characteristic of the viscous dissipation range of eddies.

k_p Spectral peak wave number, commonly assumed equal to k_e in the plot of form $\frac{nS(n)}{\overline{u^2}}$ vs k.

k_z $\left(\frac{u_*}{\bar{U}_z}\right)^2$, surface drag coefficient referred to height z metres.
e.g. $k_{10} = \left(\frac{u_*}{\bar{U}_{10}}\right)^2$

k_∞ $\left(\frac{u_*}{\bar{U}_\infty}\right)^2$ surface drag coefficient referred to boundary layer depth, δ.

L Scaling length in atmospheric model spectra, Eqns 2.46 & 2.47.

$L_{u_i x_j}$ Integral length scale of turbulence of velocity component u_i, with separation measured in direction x_j.

L_{u_x} Integral length scale of turbulence of streamwise velocity component in the streamwise direction.

L_{u_y} Integral length scale of turbulence of streamwise velocity component in the lateral direction.

L_{u_z} Integral length scale of turbulence of streamwise velocity component in the vertical direction.

L_{w_x} Integral length scale of turbulence of vertical velocity component in the streamwise direction.

L_o Reference length used to non-dimensionalise lengths in the Navier-Stokes equations.

ℓ Prandtl mixing length.

ℓ_e Length characteristic of the energy containing eddies.

M Mesh width in turbulence generating grid.

m Hot wire anemometer lineariser exponent.

N $\frac{1}{\alpha}$, reciprocal of the mean velocity profile power law exponent α.

n Normal to isobar in Ch. 2.2, - elsewhere frequency

N-- Prefix indicating lateral distance, to right of tunnel centre line when facing downstream, e.g. N25 = 25 cm to right of centre line.

o Subscript which in Ch. 3 indicates a reference quantity evaluated at a reference height which is a constant multiple of the roughness length, z_o, in both model and full scale flows.

P Static pressure. $\bar{P}$ = mean static pressure. p = fluctuating component.

$\bar{P}_b$ Base pressure.

p Subscript referring to a spectral peak value.

Q Air volume flow rate through wind tunnel.

q $\sqrt{\overline{u^2} + \overline{v^2} + \overline{w^2}}$; $\overline{q^2} = \overline{u_i^2}$, the kinetic energy of turbulence. In App. 2 only, q is the mean flow kinetic energy, $\frac{1}{2}\rho\bar{U}^2$.

R Gas constant for dry air

Re Reynolds number.

Re_{ℓ_e} Turbulent Reynolds number based on length characteristic of energy containing eddies, $Re_{\ell_e} = \frac{u'\ell_e}{\nu}$

Ri Gradient Richardson number.

RMS Root mean square

$R_{uu}(\tau)$ Auto-correlation function.

$R_{u_i u_j}(r;r';\tau)$ Cross-correlation function.

r,r' Position vectors (from arbitrary origin) where u_i and u_j, respectively, are measured.

S Spacing between adjacent bar centrelines in bar grid.

S-- Prefix indicating lateral distance, to left of tunnel centreline when facing downstream, e.g. S25 = 25 cm to left of centreline.

S(n) Energy spectrum function for a given turbulent velocity component as a function of frequency, n.

S(k,t) Energy spectrum for a given turbulent velocity component expressed as a function of wave number k, and time t.

$S_{u_i}(n)$, $S_{u_i}(k,t)$ Energy spectrum of a particular turbulent velocity component as a function of frequency, n, or wave number k, and time, t, respectively. e.g. $S_u(n)$, $S_w(k,t)$.

T	Absolute temperature in 2.3, elsewhere averaging period.
T_E	Eulerian time scale of turbulence.
t	Time
$\bar{U}$, $\bar{V}$, $\bar{W}$	Streamwise, lateral and vertical mean velocities, respectively.
u,v,w	(Alternatively given as u_1, u_2, u_3), fluctuating component of streamwise lateral and vertical velocity respectively.
U,V,W	Instantaneous velocity in streamwise, lateral and vertical directions, respectively.
u',v',w'	Streamwise, lateral and vertical RMS velocity fluctuations respectively.
$\bar{U}_b$	Bleed flow velocity through shelter fence
$\bar{U}_G$	Gradient wind velocity
$\bar{U}_H$	Shelter fence approach flow mean velocity at height $z = H$.
$\bar{U}_{Ref}$	Mean flow velocity at a reference height in the wind tunnel.
U_{prot}	A velocity accounting for both mean wind and turbulence, indicative of protection given by shelter fence.
$\bar{U}_z$	Mean velocity at height z above the surface.
$\bar{U}_o$	Reference velocity in similarity analysis of Ch. 3; spatial mean streamwise velocity far upstream of grid in Chs. 4 and 5, and App. 1; in Chs. 7, 8 and 9, $\bar{U}_o$ is the approach flow mean velocity at the same height as the leeward measurement height downstream of a shelter fence.
$\bar{U}/\bar{U}_o$	Relative mean velocity, ratio between local mean velocity, $\bar{U}$ at location (x/H, z/H) downstream of shelter fence, and the approach flow velocity, $\bar{U}_o$ defined above.
$\bar{U}_1$	Local mean velocity just upstream of grid in wind tunnel.
$\bar{U}_2$	Local mean velocity far downstream of grid in wind tunnel.
$\bar{U}_\infty$	Mean streamwise velocity at outside of boundary layer, i.e. at $z = \delta$.
u_*	$\sqrt{\frac{\tau_o}{\rho}}$, friction velocity; friction velocity in approach flow in Chs. 7. 8 and 9.
x, y, z	Streamwise, lateral and vertical direction, respectively.
X	Distance downstream from bar grid, or start of working section.
X_o	Virtual origin for grid turbulence
x	Distance downstream from fence in Chs. 7, 8 and 9.
x_1,x_2,x_3	Streamwise,lateral, and vertical direction in subscripted notation.
z_G	Gradient height.
z_o	Roughness length; roughness length of approach flow surface in Chs. 7, 8 and 9.
α	Angle between gradient wind direction and wind direction at height z in Ch.2.2; elsewhere the power law mean velocity profile expt.

Γ Adiabatic lapse rate in Ch. 2.3; gamma function in Ch. 2.5.8.

γ $-\frac{dT}{dz}$, the temperature lapse rate

$\gamma^2_{u_i u_j}(r;r';n)$ Coherence function

δ Boundary layer thickness, = z_G in atmosphere

δ_{ij} Kronecker delta

δ_S, δ_{min} Wind reduction extension factors (Kaiser 1959)

$\varepsilon(t)$ Turbulent energy dissipation rate in isotropic turbulence.

K von Karman constant $\simeq 0.4$

λ_f, λ_g Longitudinal and lateral microscale of turbulence, respectively in isotropic turbulence.

μ Absolute viscosity.

ν Kinematic viscosity.

ρ Mass density of air.

ρ_o Mass density of air at a reference height, used to non-dimensionalise density in Ch. 3.

$-\rho\overline{u_i u_j}$ Reynolds stress tensor

$\rho_{uu}(\tau)$ Auto-correlation coefficient.

$\rho_{u_i u_j}(r;r';\tau)$ Cross-correlation coefficient

θ Potential temperature in Ch. 2.3; elsewhere inclination of mean flow to the horizontal.

ϕ Latitude in Ch. 2.2; elsewhere geometric permeability of grid or fence, = (open area)/(total area) = $(\text{solidity})^{-1}$; in App. 6, ϕ = angle of inclination of wire in X probe.

ψ Stream function.

ψ' Perturbation stream function in region of grid

τ Time delay in correlation expressions; elsewhere shear stress

τ_o Surface shear stress

τ_{xz} Shear stress in the x - z plane, $=-\rho\overline{uw}$ in fully rough flow.

ω Angular velocity of the earth.

"The wind bloweth where it listeth, and thou hearest the sound thereof, but canst not tell whence it cometh, and whither it goeth".

Gospel according to St John, 3:8.

CHAPTER 1

INTRODUCTION

1.1 ATMOSPHERIC WIND RESEARCH

In recent years there has been growing interest in the effect of flows in the atmospheric boundary layer on the environment and on man-made structures. This has evolved into a field of engineering research allied to, but separate from traditional meteorology. Interest in the atmospheric boundary layer has been stimulated by man's developing technology, which has created modern buildings which are tall, and of light weight construction or unusual shape, electric power transmission line towers, tall chimneys, cooling towers, radio telescopes, VTOL aircraft and rockets. All of these are susceptible to wind induced oscillations or damage. Intensive and efficient farming of the land, to serve larger populations, requires protection of crops and animals from the wind, and densely populated cities, homing industry and thousands of motor vehicles, are sources of air pollution which must ultimately be dissipated by the wind. The proceedings of the international conferences on "Wind Effects on Buildings and Structures" (1963, 1967, 1971) describe, for example, many typical cases of interaction between the wind and man-made features on the earth's surface.

Field research into the structure of the atmospheric boundary layer and the behaviour of wind sensitive structures, has been accompanied by a parallel development of atmospheric wind model studies in wind tunnels. The practical appeal of being able to test a small scale model of a building or topographical region under controlled wind velocity conditions is self-evident, and if a rigorous approach is adopted in the modelling exercise, useful results may be obtained. A necessary prerequisite is, however, that the atmospheric boundary layer be simulated in the wind tunnel. This was not fully appreciated until the late 1950's and results of earlier wind tunnel model tests, in the uniform, low turbulence flow typical of aeronautical tunnels, generally gave an unrealistic idea of the full scale prototype performance. More recently, major efforts have been made to simulate the neutrally stable atmospheric boundary layer in relatively long working section tunnels, and now growing interest in air pollution is leading to the simulation of thermally stable and thermally unstable atmospheric flows.

The high winds experienced in many parts of New Zealand have caused

wind problems such as damage to electricity power transmission line pylons in the South Island high country (see Frontispiece), damage to forest plantations such as the Eyrewell Forest in the South Island and the Kaingaroa State Forest in the North Island, and damage to commercial and domestic buildings such as in Wellington during the "Wahine" storm of 1968. In 1970 a programme of research into atmospheric boundary layer phenomena was initiated in the Mechanical Engineering Department of the University of Canterbury. It was the purpose of the present project to develop a wind tunnel simulated, neutrally stable, atmospheric boundary layer, and test the model atmospheric flow with an investigation of a wind problem relevant to New Zealand. With the extensive need for wind protection for crops and animals in rural areas, and private homes and public recreation areas, in many parts of New Zealand, it was decided to investigate windbreak aerodynamics. Considerable field data for windbreak leeward mean velocity reduction were available at the outset, but very few experiments had been made, to show the value of model windbreak tests in a rigorously simulated boundary layer, and there was an almost complete dearth of windbreak leeward turbulence data. The scope and objectives of this thesis are described in detail in 1.2.

1.2 SCOPE AND OBJECTIVES OF THE PROJECT

The detailed objectives of the project were as follows :

(a) to review the current information on neutrally stable atmospheric boundary layers and set up a physical and mathematical description of atmospheric flow suitable as a reference model for a wind tunnel simulation;

(b) to set up modelling criteria for the simulation of the atmospheric boundary layer in a wind tunnel, and review the current state of the art in simulation techniques;

(c) to investigate whether the flow downstream of a coarse grid was suitable as a model of the atmospheric boundary layer;

(d) to simulate a neutrally stable rural atmospheric boundary layer of linear scale 1:500 or larger.

(e) to test model fence windbreaks of a range of permeabilities in the simulated boundary layer, with two major aims :

(i) by comparing results with existing field data, to provide a stronger justification for accepting the results of wind tunnel tests as indicative of full scale performance;

(ii) by measuring leeward mean velocity and turbulent velocity fluctuations, to obtain a clearer picture of leeward flow processes and a more quantitative relationship between mean velocity reduction and leeward turbulent intensity.

The impossibility of achieving objective (d) in the 4 ft x 3 ft Aeronautical Tunnel led to a secondary, but major objective, which was to design and construct a long working section wind tunnel suitable for atmospheric wind modelling.

The scope of the thesis is suggested by the above stated objectives. A rural boundary layer was chosen for the simulation as this was most suitable for the subsequent tests of model windbreaks. It was aimed to make the boundary layer simulation technique readily adaptable to an urban modelling project. The linear scale of 1:500 was considered the smallest that would be acceptable for model tests and in the new wind tunnel it was expected that a scale of 1:400 could be achieved. The range of model windbreaks tested included fences of 0%, 20%, 34% and 50% nominal geometric permeability. This range should be extended to higher permeabilities in future developments of this work.

The project has had a strong practical bias which stems from the intractability to solution of the equations of motion for turbulent flow. The researcher in this field is nevertheless able to make use of empirical descriptions of the flow phenomena, and statistical description of atmospheric turbulence enables a given flow to be clearly characterised. The hot wire anemometer is a valuable tool in wind tunnel turbulence measurements and has been essential to the performance of this project. Discussion of the operation of this instrument and its accuracy in flows of various turbulent intensities is therefore given in the appendices to the thesis.

Since it is intended that the atmospheric boundary layer modelling and windbreak aerodynamics studies in this project be continued, it was considered important to present a complete record of the research to date, as a starting point for future investigations. To aid the ease of reading, therefore, the thesis has been divided into three parts, as follows :

Part 1: The description of the neutrally stable atmospheric boundary layer; the derivation of wind modelling criteria and review of previous simulations; an investigation of atmospheric boundary layer modelling using bar grids. This part of the thesis justifies the construction of the new atmospheric boundary layer wind tunnel.

Part 2: A record of the design, construction and commissioning of the new dual facility wind tunnel which includes the 40 ft long atmospheric wind modelling working section; the simulation of the rural boundary layer. Developmental boundary layer generating apparatus arrangements, used during the simulation programme, have been included to show the stepwise process leading to the final model boundary layer. Some of the intermediate boundary layers may also be useful as smaller scale atmospheric models in the future.

Part 3: A review of research information on windbreak aerodynamics and shelter effect; tests of model shelter fences in the simulated boundary layer, analysis of the test results and comparison with existing data; a summary of conclusions to the project.

References are listed at the end of the thesis in alphabetical order. Where the work of a particular author was not able to be obtained this has been noted in the script.

PART 1

Description of the neutrally stable atmospheric boundary layer.

Derivation of wind modelling criteria and review of previous simulations.

Investigation of atmospheric boundary layer modelling using bar grids.

CHAPTER 2

2.0 THE ATMOSPHERIC BOUNDARY LAYER

In this chapter, a review is made of currently accepted descriptions of wind structure in a neutrally stable atmospheric boundary layer. Comprehensive treatments of this subject have been given by Sutton (1953), Davenport (1963, 1967), Harris (1970) and Teunissen (1970). The discussion in the following sections has been confined, where possible, to establishing simple mathematical models for atmospheric boundary layer phenomena. These enable a physical interpretation to be made of modelling criteria derived in Chapter 3, for wind tunnel simulation of the natural wind.

2.1 THE SOURCE OF THE WIND

The sun's radiation, which is more intense at the earth's equator than at the poles, causes differential heating of the earth's surface, so that pressure gradients are set up in the atmosphere, inducing wind flow. These pressure gradients are proportional to the spacing of isobars on a weather map, and mean wind velocity increases with increasing pressure gradient. Fig. 2.1 (after Davenport, 1963) shows a weather map over Great Britain during an intense depression. If the earth were flat and did not rotate, air would simply flow from a region of high pressure to a region of low pressure. Because the earth is rotating and the wind generally moving on a curved path, the air masses which begin to move under the influence of the pressure gradients are subject also to Coriolis and centripetal forces (see Hansen, 1967, p.40).

Far above the earth's surface, outside the influence of surface friction, the resultant of these forces produces a steady flow parallel to the isobars, called the gradient wind, $\bar{U}_G$. Sutton (1953) has shown that the gradient wind must flow along the isobars and, in the special case where the isobars are straight, or so slightly curved that centripetal acceleration is negligible, the gradient wind is called the geostrophic wind. The least height at which the gradient wind is obtained is known as the gradient height, z_G, and usually lies between about 300m and 600m above ground level. The gradient height is dependent on the nature of the surface, i.e. the rougher the ground, the greater the surface drag, planetary boundary layer thickness and thus gradient height.

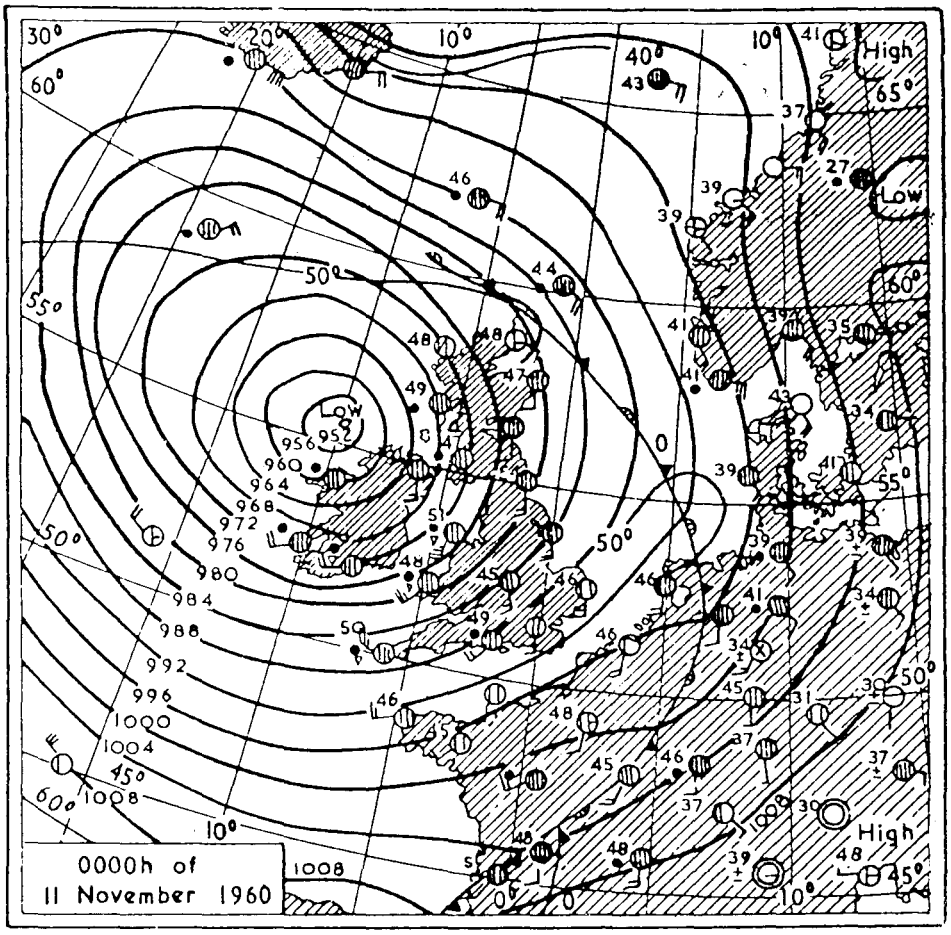

Fig.2.1 Weather map showing an intense depression with strong winds.

2.2 VARIATION OF MEAN WIND DIRECTION WITH HEIGHT:

If a case is considered where isobar curvature is very small, a mass of air moving down the pressure gradient is deflected by the Coriolis force to the right of its direction of motion in the Northern Hemisphere and to the left in the Southern Hemisphere. A state of balance is finally achieved with the Coriolis force equal in magnitude and opposite in direction to the pressure difference, a condition known as Geostrophic balance. This is illustrated in Fig. 2.2(a). The resultant wind direction is clockwise around a low pressure region in the Southern Hemisphere, so in Fig. 2.1 the wind flow will be anti-clockwise round the isobars.

The geostrophic wind is given approximately by :

$$\bar{U}_G = \frac{\frac{d\bar{P}}{dn}}{2\rho\omega\sin\phi} \qquad \ldots\ (2.1)$$

where $\bar{U}_G$ = the Geostrophic wind ≃ the gradient wind when isobar curvature small;

$\frac{d\bar{P}}{dn}$ = pressure gradient;

ρ = mass density of the air;

ω = angular velocity of the earth;

ϕ = latitude of the location considered.

The principle of Geostrophic Balance is generally considered invalid within a belt extending 10° north and south of the equator, since as the equator is approached $\sin\phi \to 0$, implying infinite wind speeds at the equator.

Nearer the ground, the action of surface friction and Reynolds stresses in the turbulent boundary layer introduces a force in the opposite direction to the wind velocity. The nett effect of the balance of forces is to turn the wind direction in towards a centre of low pressure, the angle made by the wind direction with the tangent to the isobar increasing as the ground is approached. (Fig. 2.2(b)).

Sutton (1953) gives two derivations for the variation of wind direction. In the first the mean component velocities $\bar{U}$ and $\bar{V}$ (see Fig. 2.3) are derived from the Navier-Stokes equations for turbulent flow using a Boussinesq expression for the Reynolds stress with the

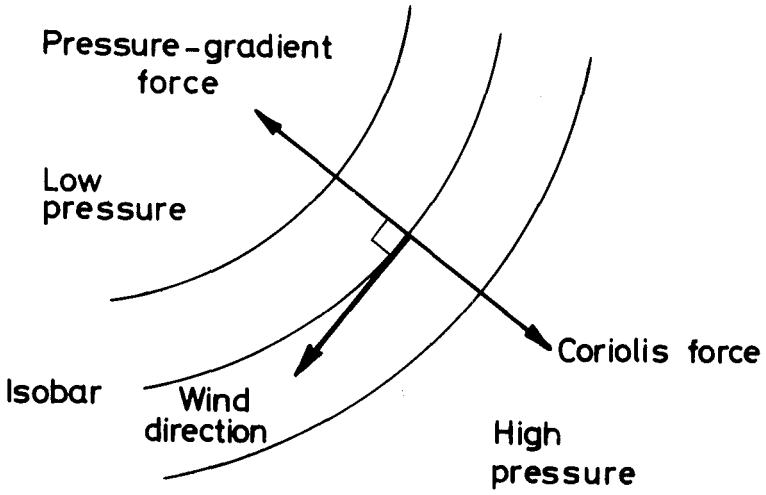

(a) At the gradient height.

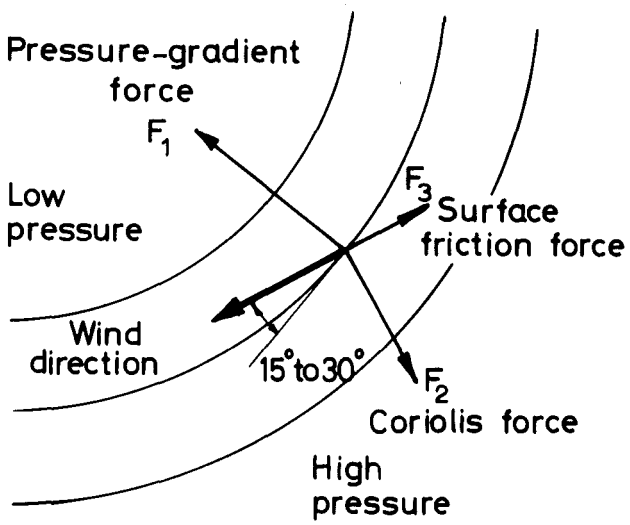

(b) Close to the ground.

Fig. 2.2 WIND DIRECTION IN SOUTHERN HEMISPHERE

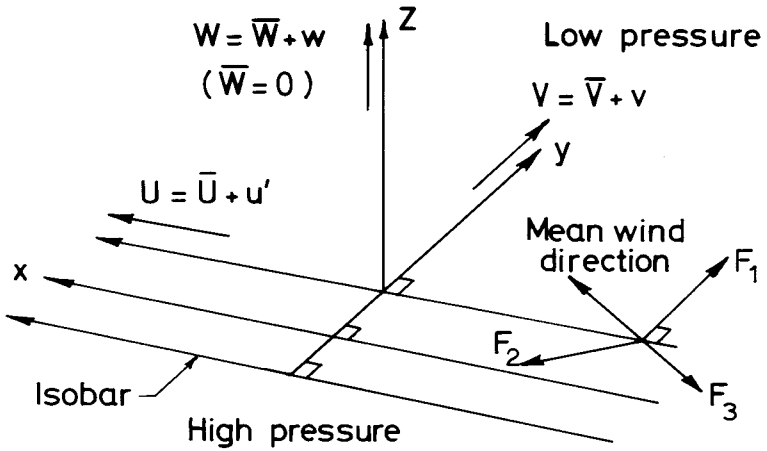

Reference axes used for velocity components $\overline{U}$ & $\overline{V}$ in Ekman Spiral. (Southern Hemisphere.) On the right, conditions close to the ground are represented as in Fig. 2·2 (b). In the surface layer the mean wind direction is chosen as the x axis.

Fig. 2·3

eddy viscosity, K , constant. The result is the so-called 'Ekman Spiral':

$$\bar{U} = \bar{U}_G(1 - e^{-\xi}\cos\xi)$$

$$\bar{V} = \bar{U}_G\, e^{-\xi}\sin\xi.$$

with the angle which the wind at any height makes with the Geostrophic direction given by:

$$\alpha = \tan^{-1}\frac{\bar{V}}{\bar{U}} = \tan^{-1}\left(\frac{\sin\xi}{e^{\xi} - \cos\xi}\right) \qquad \ldots.(2.2)$$

where $\xi = z\sqrt{\frac{\omega\sin\phi}{K_M}}$

Equation 2.2 predicts $\alpha = 45^{\circ}$ at the earth's surface. In reality the angle between the gradient wind and surface wind varies between 15° and 30°. The second derivation expreses K_M more realistically as a function of height, e.g. $K_M = K_{M1}z^m$, with K_{M1} the reference value, and m varying to suit local surface roughness and atmospheric stability. The end result is more complicated, but agrees more closely with observed values of α.

In analysing atmospheric wind effects on structures, it is usually considered valid to ignore the effects of the Ekman Spiral in the surface layer, i.e. the first ~ 100m above the earth's surface, and in wind tunnel simulation of atmospheric wind flow it is generally not possible to reproduce the Ekman Spiral at all. When wind effects on very tall structures, e.g. a 250m high tower, are considered, some allowance for variation of mean wind direction with height may be necessary.

2.3 THERMAL EFFECTS - ATMOSPHERIC STABILITY

Sutton (1953) gives an extensive traditional treatment of heat transfer and turbulent diffusion in the atmosphere. Atmospheric data to date have been most conveniently represented by the similarity theory of Monin and Obukhov as discussed by Calder (1966) and outlined by Cermak and Arya (1970). This theory is used to predict mean velocity and temperature profiles in thermally stratified atmospheric surface layers, which are the rule rather than the exception.

In this project the atmospheric boundary layer modelling work was restricted to neutrally stable flows and thermal stability is discussed

below only sufficiently to set up the conditions where neutrally stable flow can be expected.

At a given height above ground level, the pressure of the dry atmosphere is proportional to the mass of the column of air lying above that height, and consequently atmospheric pressure decreases with height above ground level.

$$P = P_o . e^{-\frac{g}{R}\int_o^z \frac{dz}{T}} \qquad \ldots.(2.3)$$

P_o = pressure at the surface

g = gravitational constant

R = gas constant for dry air

T = absolute temperature.

To obtain a numerical expression for the variation of pressure with height, z, T must be expressed as an explicit function of height, and is usually taken as varying linearly with z.

Consider now vertical movement of air in the atmosphere at rest. A volume of air forced to ascend will expand approximately adiabatically, if the process is rapid, and consequently undergo a drop in temperature. If the moving mass of air is considered to instantaneously take up the pressure of its surroundings, its density relative to its environment will be determined by its absolute temperature. For the atmosphere to be in neutral vertical equilibrium, or neutrally stable, an ascending or descending mass assumed to be moving adiabatically, must always have the same density as its environment. To satisfy this requirement, it may be shown that the atmosphere must have a characteristic temperature distribution of the form

$$T_z = T_o - \Gamma . z \qquad \ldots.(2.4)$$

where T_z is the absolute temperature at height z above the surface ($z = 0$) and Γ is the so-called 'dry adiabatic lapse rate'. In dry air,

$$\Gamma = \frac{g.A}{c_p} = 9.86 \times 10^{-5} \ ^oC/cm \simeq 1 \ ^oC/100m$$

A = reciprocal of the mechanical equivalent of heat

$$= \frac{R}{c_p - c_v}$$

c_p, c_v = specific heats of air at constant pressure and constant volume respectively.

If the temperature decreases more rapidly than the adiabatic lapse rate, i.e. if the lapse rate,

$$\gamma \equiv -\frac{dT}{dz} > \Gamma \qquad \text{(superadiabatic lapse rate)}$$

a vertically rising mass of air will remain hotter and therefore lighter than its surroundings and will continue to rise, leading to exchange of air masses between various heights due to convection currents. Under these conditions the atmosphere is said to be in a 'lapse period' and is classified 'hydrostatically unstable'. During so-called 'inversion periods' when $\gamma < \Gamma$, the mass of air displaced upwards will be at a lower temperature than its surroundings and will experience a restoring downward force, in which case the atmosphere is classified 'hydrostatically stable'. In a 'neutrally stable' atmosphere, $\gamma \simeq \Gamma$, or very slightly less.

Greater turbulence levels are obviously to be expected in an unstable atmosphere, since under these conditions heat convection is added to the 'mechanical' turbulence produced by surface friction. Consider again a vertically moving mass of air. The turbulent energy required to displace the air is extracted from the mean flow by Reynolds stresses. Whether the velocity fluctuations increase or decrease depends on whether the energy supply is greater or less than the rate at which work must be done in the gravitational field, in moving fluid volumes in the vertical direction. The parameter expressing this criterion is the gradient Richardson Number Ri, defined by

$$Ri \equiv \frac{g\left(\frac{\partial\theta}{\partial z}\right)}{\theta\left(\frac{\partial\bar{U}}{\partial z}\right)^2} = \frac{\text{mean rate of work against gravity/unit vol.}}{\text{work done by Reynolds stress/unit vol.}} \qquad \ldots.(2.5)$$

θ = Potential temperature related to T by

$$\frac{1}{\theta}\frac{\partial\theta}{\partial z} = \frac{1}{T}\left(\frac{\partial T}{\partial z} + \Gamma\right) \qquad \text{for an ideal gas} \qquad \ldots.(2.6)$$

There is a critical value of Ri between 0 and 1 above which turbulent motion will subside into laminar motion, and below which it will remain turbulent. This critical value is indefinite, but Teunissen (1970) suggests $Ri_{crit} \sim 0.25$

From equations 2.5 and 2.6,

$$Ri = \frac{g(\Gamma - \gamma)}{T\,(\partial\bar{U}/\partial z)^2}$$

$\therefore$ assuming ideal gas behaviour, Ri < 0 for unstable air and Ri > 0 for stable air.

Summarising, the atmosphere may be characterised by four Richardson number régimes :

Ri < 0 — unstable air, with considerable convective turbulence in addition to the mechanical turbulence;

Ri ≃ 0 — generally for $|Ri| < 0.03$, the air is termed 'neutral' or 'near-neutral' and the turbulence is purely mechanical. Neutrally stable conditions can be closely approached in cloudy weather with a moderate or high wind. In these circumstances convective turbulence can be ignored, surface friction causing sufficient mechanical 'stirring' of the atmosphere to destroy thermal gradients.

$0 < Ri < \sim 0.25$ — stable air with mechanical turbulence being damped out by the thermal stratification.

$Ri > \sim 0.25$ — very stable air in which no turbulence can exist at all, at least in the vertical direction.

In the atmosphere the Richardson number is more relevant than the molecular viscosity Reynolds number which is usually so large as to cease to be important.

2.4 THE NEUTRALLY STABLE ATMOSPHERIC WIND AS A TURBULENT BOUNDARY LAYER

2.4.1 General:

The wind at a point near the earth's surface is determined by :

(i) large scale movements of the pressure systems typically extending several hundred kilometres, giving rise to the gradient wind;

(ii) the influence of the ground surface generating fluctuations in the flow (thermally and/or mechanically).

The two processes give rise to fluctuations in wind velocity with completely different time scales. This is clearly shown in Van der Hoven's spectrum of horizontal wind speed near the ground for an extended

range of frequencies. See Fig. 2.4 (after Davenport, 1963). The important features of such spectra are :-

(i) A broad peak with a maximum at a period of approximately 1 minute. This part of the curve is characteristic of (gusts) turbulence generated almost entirely by surface friction.

(ii) A peak at a period of about 4 days corresponding to the movement of large scale weather systems.

(iii) An absence of energy (spectral gap) between periods of ~5 minutes and about 4-5 hours centred at a period of ~½ hour.

At a twelve hour period there is a minor peak corresponding to calmer conditions likely to occur at sunrise and sunset. Davenport has sketched in another peak (not included by the measurements) at a period of a year, corresponding to seasonal fluctuations in wind speed.

The atmospheric air movement can thus be usefully visualised as superimposed trains of wind waves, of different frequencies and amplitudes described by the energy spectrum.

The existence of the spectral gap in the wind's energy distribution is important in the study of wind loads on structures for the following reasons :-

(i) It enables micrometeorological fluctuations or gustiness to be clearly distinguished from macrometeorological (synoptic) fluctuations associated with movement of weather systems.

(ii) In analysis of the wind's turbulence, it enables an averaging period to be chosen which minimises non-stationarities in the random micrometeorological wind structure. Typically a 1 hour averaging period is used by meteorological stations, although means over as short a period as 5 minutes are taken in the U.S.A. Davenport (1967) suggests that 10 - 20 minutes is a suitable averaging time. With an averaging period of this order (10 min - 1 hour), synoptic fluctuations appear as a gradual change in the mean wind speed from one averaging period to the next.

In studies of wind effects on structures or wind flow over some

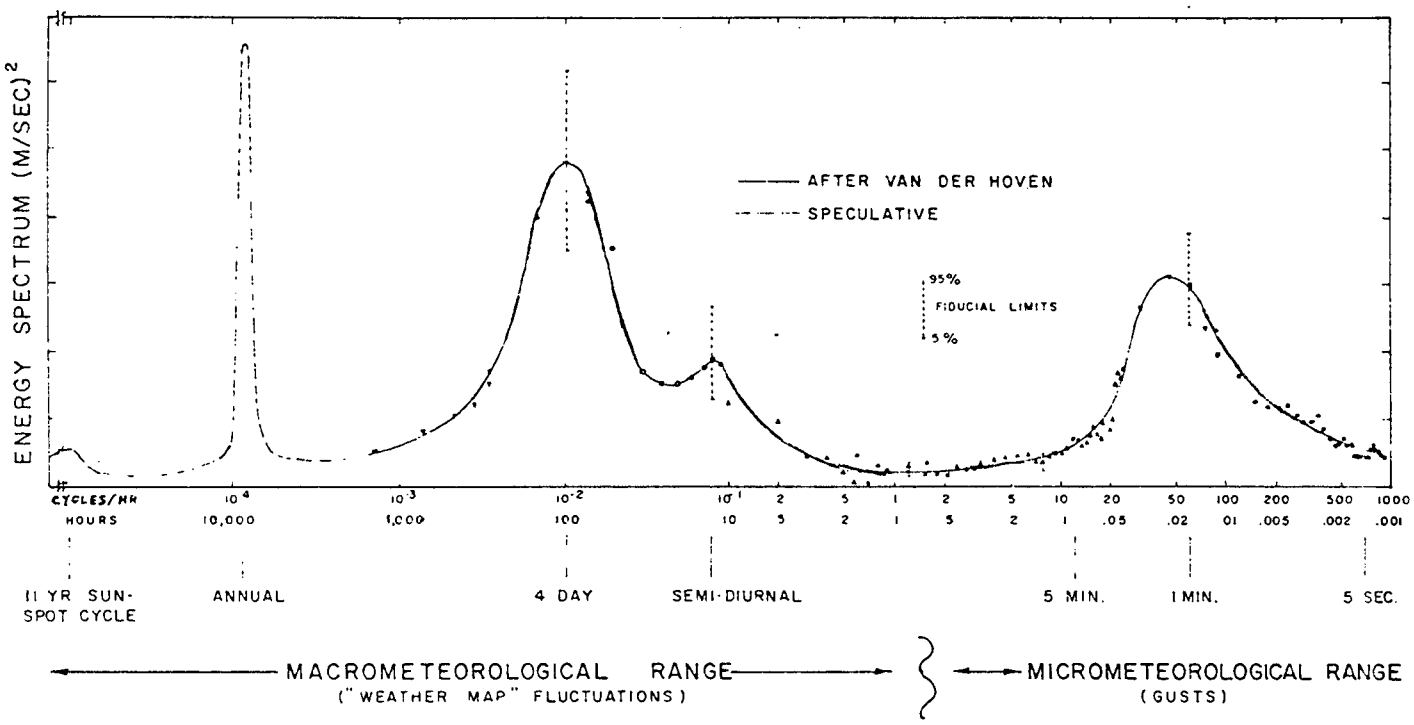

Fig.2.4 Spectrum of horizontal wind speed near the ground for an extensive frequency range (from measurements at 100 metre height by Van der Hoven at Brookhaven, N.Y., U.S.A.)

minute detail of the earth's surface, such as a farm, athletics venue or city centre, the important region of the spectrum is the part to the right of the spectral gap in Fig. 2.4. Periods of oscillation of structures range from ~10 seconds for, say, a long bridge, down to a fraction of a second for a light rigid structure, i.e. they fall at the high frequency end of the gust spectrum. Thus, the fluctuations in wind velocity that are important in exciting structural oscillations are those generated by surface friction. Mathematical expressions for the gust spectrum are considered in Section 2.5.6, and related to the local terrain where the wind is measured.

The atmosphere in motion close to the earth's surface may be divided into three regions :-

(i) The free atmosphere: where viscosity and surface friction can be neglected, where only inertial, Coriolis and pressure gradient forces act, and the resulting wind is the gradient wind;

(ii) The planetary boundary layer: the region between the earth's surface and the height at which the free atmosphere begins, i.e. z_G.

(iii) The surface boundary layer: a sublayer of the planetary layer, extending from the ground up to about 70 ± 30m. In this region Coriolis forces are assumed negligible and wind characteristics are determined only by surface conditions, thermal stability and height. In theoretical treatments the surface layer is characterised by constant shear stress, the depth of constant stress defining the depth of the layer. This is examined further in section 2.4.2.

It is known from Nikuradse's experiments on the flow of water through smooth and rough pipes, that the flow is independent of Reynolds number and dependent only on surface roughness in the third regime, i.e. fully aerodynamically rough flow. Schlichting (1960) gives the following criterion for the existence of fully aerodynamically rough flow :-

$$\frac{u_* K_s}{\nu} > 70 \qquad \ldots.(2.7)$$

where K_s = equivalent sand roughness,

$u_* = \sqrt{\frac{\tau_o}{\rho}}$ = friction velocity

ν = kinematic viscosity.

This criterion can also be applied to flat plate boundary layers.

In the lower atmosphere, under neutrally stable conditions, the wind is nearly always turbulent right down to the earth's surface and is regarded in analyses as a fully aerodynamic rough flat plate boundary layer, with the leading edge of the 'plate' an infinite distance upstream of the point of observation. The validity and consequences of this practice are discussed by Priestley and Sheppard (1952), Sutton (1949, 1953) and Ludwig and Sundaram et al (1969, 1970).

In practice, the criterion of equation 2.7 is expressed in terms of the surface 'roughness length', z_o, thus:

$$\frac{u_* z_o}{\nu} > \sim 2.5 \qquad \ldots.(2.8)$$

Very rarely in atmospheric flows is $\frac{u_* z_o}{\nu} < 2.5$. Table 2.1 (after Sutton 1949) shows values of u_*, z_o and $\frac{u_* z_o}{\nu}$ for various natural surfaces under moderate mean wind conditions.

TABLE 2.1

Values of u_* and z_o for various natural surfaces.
Mean wind speed $\bar{U}$ = 5m/sec at z = 2m above the ground.

Surface	z_o cm	u_* cm/sec	$\frac{u_* z_o}{\nu}$
Exceptionally smooth (ice, mud flats, calm sea)	9×10^{-4}	16	0.10
Lawn, grass up to 1cm high	0.10	26	17.7
Downland thin grass up to 10cm high	0.72	36	176.6
Thick grass up to 10cm high	2.3	45	708.9
Thin grass up to 50cm high	5.0	54	1839.2
Thick grass up to 50cm high	8.9	63	3819.5
Fully grown root crops	13.9	73	6912.1

From this table it can be seen that at a mean wind speed of 5m/sec. at z = 2m, only an exceptional surface such as smooth mud flats or ice can be called aerodynamically smooth (for which $\frac{u_* z_o}{\nu} < 0.13$). A closely cut lawn would exhibit a laminar sublayer at speeds < 1m/sec. at z = 2m, but for higher windspeeds would be fully rough.

Priestley and Sheppard (1952) also note that "all land surfaces are rough for any significant value of windspeed". In the present work,

where surfaces of $z_o \geq$ 1cm were of interest, with windspeeds > 5m/sec. at the 10m reference height, only fully aerodynamically rough flow required consideration.

2.4.2 The Constant Stress Surface Layer Model:

In 2.4.1 it was stated that in the surface layer the wind characteristics are determined only by surface conditions, thermal stability and height. Certain assumptions are implicit in this statement.

Ellison (1957) specifies the mathematical model for the surface layer as follows: an infinite uniform rough plane (z = 0) which supports a fluid of great depth, has applied to it a constant shear stress, ρu_*^2, and has a constant heat flux, the latter taken as zero in the present case. It is assumed that the flow near the plane reaches a steady state which is independent of conditions at a great height. A further necessary assumption, to enable the flow to be specified in terms of surface conditions alone, is that the flow is horizontally homogeneous (a condition rarely occurring in nature). Calder (1966) discusses this assumption in relation to the similarity theory of Monin and Obukhov, and the implications of horizontal homogeneity are discussed in relation to wind tunnel modelling of atmospheric boundary layers by Ludwig, Sundaram et al (1969, 1970) and in the present work in 3.3.2.

Consider now the Navier-Stokes equations for the conservation of momentum in the mean, turbulent surface layer flow:

Using subscripted notation,

$$\frac{\partial \bar{U}_i}{\partial t} + \rho \frac{\bar{U}_j \partial \bar{U}_i}{\partial x_j} = - \frac{\partial \bar{P}}{\partial x_i} + \frac{\mu \partial^2 \bar{U}_i}{\partial x_j^2} - \frac{\partial}{\partial x_j} \rho \overline{u_i u_j} \quad \ldots.(2.9)$$

The assumptions of steady flow and horizontal homogeneity are equivalent to the assumption that all statistical properties of the velocity and temperature fields are invariant with time and are homogeneous in the horizontal (x_1, x_2) plane, i.e.

$$\frac{\partial}{\partial t} \equiv 0, \quad \frac{\partial}{\partial x_1} \equiv 0 \equiv \frac{\partial}{\partial x_2}$$

Also, the steady mean motion is assumed to be unidirectional and horizontal at all heights in the direction of the x_1 axis, so that

$$\bar{U}_i = \bar{U}_1 \qquad \bar{U}_2 = \bar{U}_3 = 0.$$

For the present discussion, restricted to neutrally stable flows, heat flux is assumed to be zero.

With the above assumptions, the Stokes operator corresponding to the mean motion is identically zero,

i.e. $$\frac{\partial}{\partial t} + \bar{U}_j \frac{\partial}{\partial x_j} = 0.$$

$\therefore$ equation 2.9 yields three component equations :

$$-\frac{\partial \bar{P}}{\partial x_1} + \frac{\partial \tau_{31}}{\partial x_3} = 0 \qquad \ldots.(2.10a)$$

$$-\frac{\partial \bar{P}}{\partial x_2} + \frac{\partial \tau_{32}}{\partial x_3} = 0 \qquad \ldots.(2.10b)$$

$$-\frac{\partial \bar{P}}{\partial x_3} + \frac{\partial \tau_{33}}{\partial x_3} = 0 \qquad \ldots.(2.10c)$$

and conservation of mass : $\frac{\partial \bar{U}_1}{\partial x_1} = 0.$

These equations provide constraints on the possible forms of the turbulence structure. Symmetry conditions require also

$$\tau_{12} = \tau_{21} = -\rho \overline{u_1 u_2} = 0$$

$$\tau_{23} = \tau_{32} = -\rho \overline{u_2 u_3} = 0$$

Since $\tau_{32} = 0$, $\frac{\partial \bar{P}}{\partial x_2} = 0$. Also since $\frac{\partial \tau_{33}}{\partial x_3}$ is a function only of x_3 equation 2.10c gives

$$\frac{\partial^2 \bar{P}}{\partial x_1 \partial x_3} = \frac{\partial}{\partial x_3}\left(\frac{\partial \bar{P}}{\partial x_1}\right) = 0$$

$\therefore$ the horizontal pressure gradient $\frac{\partial \bar{P}}{\partial x_1}$ must be independent of x_3. Thus the integral of equation 2.10a is

$$\tau_{31}(x_3) \equiv \mu \frac{\partial \bar{U}}{\partial x_3} - \rho \overline{u_1 u_3} = x_3\left(\frac{\partial \bar{P}}{\partial x_1}\right) + \tau_{31}(0)$$

In the fully rough atmospheric flow the viscous shear stress is negligible compared with the Reynolds stress. Reverting to x, y, z cartesian notation,

$$\tau_{xz} = -\rho \overline{uw} = z \frac{\partial \bar{P}}{\partial x} + \tau_o \qquad \ldots.(2.11)$$

τ_o is the surface shear stress = $\tau_{xz}(0) = \rho u_*^2$.

Next, the far reaching assumption is usually made that in the surface layer, the streamwise pressure gradient $\frac{\partial \bar{P}}{\partial x}$ is approximately zero, so that

$$\tau_{xz} = \tau_o \qquad \ldots.(2.12)$$

Thus in the surface layer, a depth of constant stress will exist in the idealised model if the flow is steady, horizontally homogeneous, and free from pressure gradients.

Unfortunately there is a dearth of atmospheric shear stress measurements (other than at the surface) by which to judge this model. It is current practice in atmospheric wind simulation projects to try to create a depth of constant stress in the model boundary layer but this may not be justified. In laboratory flat plate boundary layers, Hinze (1959) considers the constant stress layer assumption is justified, but shows results for only a smooth wall boundary layer, which exhibited approximate constant stress for $z/\delta < 0.1$. The Reynolds stress necessarily decreases to zero right at the wall.

Plate (1971) discusses the existence of a constant stress layer in the atmosphere, and whether a more valid atmospheric model would be a constant thickness boundary layer as in fully developed pipe flow, therefore having a linear shear stress distribution. Plate concludes that in the atmosphere approximately constant stress, and, by implication, the Prandtl logarithmic mean velocity profile, exist over the lower 15% of the boundary layer, but comments that the assumption of a constant stress layer should not be considered critical in wind tunnel modelling. The limits on accuracy and general scarcity of field measurements at present justify this comment. There is clearly a need for comprehensive shear stress measurements over different surfaces, up to a height of ~ 100m above the ground.

2.4.3 Mean Velocity Profiles in the Atmospheric Boundary Layer:

In the lowest 15 - 20% of the neutrally stable atmospheric boundary layer, the Prandtl logarithmic law for a fully aerodynamically rough flow velocity profile has been well verified (Sutton, 1953). The derivation of this law is given by Schlichting (1960) and the final result is

$$\frac{\bar{U}}{u_*} = \frac{1}{K} \log_e \left(\frac{z}{z_o} \right) \qquad \ldots.(2.13)$$

where u_* = the friction velocity $= \sqrt{\frac{\tau_o}{\rho}}$

K = the von Karman constant $\simeq 0.4$

z_o = the roughness length = 1/30 the average size of roughness elements, K_s.

In addition to the z_o values listed in Table 2.1, a summary of z_o values for a wide range of surface roughnesses is given in Table 2.2. The friction velocity, u_* is probably most accurately evaluated by actual measurement of shear stress close to the surface.

Other forms of the logarithmic law applied to the surface layer are as follows :

(a) Rossby-Montgomery Form:

Proposed in 1935 by C.G. Rossby and R.B. Montgomery, this form assumes that the surface roughness modifies the mixing length near the surface, so that

$$\ell = K (z + z_o) \qquad (\text{cf } \ell = Kz \text{ in equ. } 2.13)$$

which implies that ℓ is small but finite at $z = 0$. This leads to

$$\frac{\bar{U}}{u_*} = \frac{1}{K} \log_e \left(\frac{z + z_o}{z_o} \right) \qquad \ldots.(2.14)$$

The effect of the surface roughness is confined to layers adjacent to the surface. $\bar{U} = 0$ at $z = 0$ now, and $\frac{d\bar{U}}{dz}$ remains finite right down to the surface. Both Sutton (1949) and Jensen and Franck (1963) favour this form. When $z >> z_o$, equation 2.14 → equation 2.13.

(b) The Zero Plane Displacement Form:

When very large roughness is present, e.g. trees, buildings, the velocity profile becomes uncertain within the surface roughness elements and an empirical form of the logarithmic law may be used, which is valid above the roughness elements :

$$\frac{\bar{U}}{u_*} = \frac{1}{K} \log_e \left(\frac{z - d}{z_o} \right) \qquad \ldots.(2.15)$$

TABLE 2.2 (ESDU, 1972)

Values of the Surface Roughness Parameter z_0

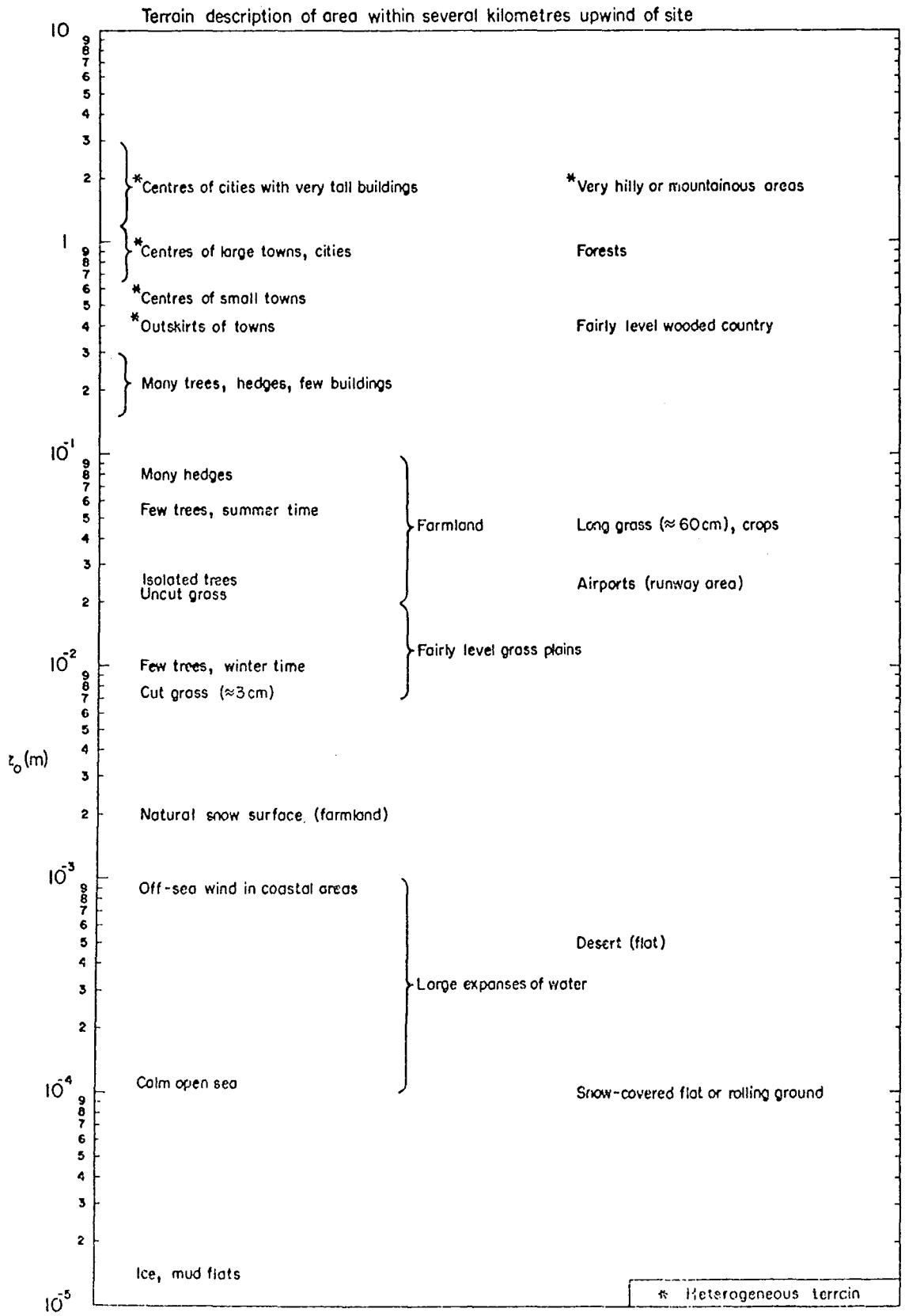

d = zero plane displacement, above which normal turbulent exchange occurs. Sutton (1953) suggests that equation 2.15 is valid for $z \geqslant d + z_o$. Length d is sometimes taken as the average roughness element height. Cermak and Arya (1970) state that equation 2.15 has been verified for flow over tall crops and forest canopies.

(c) Form for Non-neutral Stabilities:

Where thermal effects are important the logarithmic law can be modified such that

$$\frac{\bar{U}}{u_*} = \frac{1}{K}\left[\log_e \frac{z}{z_o} + \beta \frac{z}{L'}\right] \qquad \ldots.(2.16)$$

where L' is the Monin-Obukhov temperature dependent scaling length given by

$$L' = -u_*^3 \Big/ \left(K \frac{gH_o}{T_a \rho c_p}\right)$$

$H_o / \rho c_p$ = surface heat flux

T_a = ambient temperature.

For stable stratification $\beta \simeq 1.0$ and the range of applicability of the log/linear law is quite wide ($0 < z/L' < 0.5$). For unstable stratification $\beta \simeq 1.5$, and the law is valid over only a small range ($-z/L' < 0.05$).

Above the surface layer, when Coriolis forces start to become important, and the surface roughness effects decrease, empirical data begin to depart from the logarithmic law, equation 2.13. Modifications to the logarithmic law have been proposed, such as introducing power law variation of eddy viscosity with height, but these depend on empirically determined quantities, such as K_M. In practice, a power law mean velocity profile is found to fit the data for the whole planetary boundary layer well, under conditions of neutral stability. This has the form

$$\frac{\bar{U}_z}{\bar{U}_{ref}} = \left(\frac{z}{z_{ref}}\right)^{\alpha} \qquad \ldots.(2.17)$$

$\bar{U}_z$ = mean velocity at height z

$\bar{U}_{ref}$ = reference mean velocity at height z_{ref}

α = Power law exponent

A 10m reference height is commonly used in meteorological work, although Davenport (1963) favours the use of $\bar{U}_G$ and z_G as reference velocity and height respectively. Harris (1970) questions the use of z_G as reference, as z_G is difficult to determine.

Generally the power law form is favoured because of its simplicity in mathematical manipulation and adequacy under neutrally stable conditions over all types of relatively level terrain. Table 2.3 summarises power law exponents for several different locations, given by Davenport (1960). Davenport recommended three power law exponents for three different broad categories of terrain, together with the gradient height z_G, and surface drag coefficient k_{10}, as shown in Table 2.4 and illustrated in Fig. 2.5. Feasey (1973) indicates that a slight increase in α occurs with increasing mean wind velocity, e.g. 0.02 for 16 kph increase in surface wind speed. These small changes in power law exponent are generally disregarded.

The power law profile representation is somewhat idealised and atmospheric data rarely form a smooth profile. For instance, in Fig. 2.6 a mean wind velocity profile measured by Harris (1970) at Rugby Radio Station, England, is shown. The power law exponent for the best fit line here was $\alpha = 0.172$.

Like the logarithmic law, the power law can be of only limited usefulness in heavily built up areas, e.g. city centres. Below the level of the tops of obstructions the wind speed and turbulence structure is very much a function of the shapes and spacing of the obstructions (buildings, trees) themselves. In these areas it is uncertain whether it is more correct to use a power law with a larger exponent, as proposed by Davenport, or use a power law with a smaller exponent combined with an upwards displacement of the datum plane

$$\bar{U}_z \propto z^{\alpha_1}$$

$$\underline{\text{or}} \quad \bar{U}_z \propto (z - d)^{\alpha_2} \quad \text{where } \alpha_2 < \alpha_1$$

TABLE 2.3

Influence of surface roughness on values of exponent α in power law variation of mean wind velocity with height. Neutrally stable conditions.

No.	Source	Location	Upper Limit of Investigation in ft.	Description of Terrain in Site Locality	α
1	Goptarev	Caspian Sea	106	Coastal waters of inland sea	$\frac{1}{10.5}$
2	Juul	Masnedsund, Denmark	182	Flat shore on "Ocean of Small Islands"	$\frac{1}{8.3}$
3	Scrase	Salisbury Plain, U.K.	43	Open grassland, no hedgerows or trees	$\frac{1}{7.7}$
4	Wing	Ballybunion, Ireland.	492	Flat treeless grassland, Atlantic Ocean ½ mile dist.	$\frac{1}{7.4}$
5	Sherlock	Ann Arbor, Mich. U.S.A.	250	Open slightly rolling farmland	$\frac{1}{7}$
6	Taylor	Salisbury Plain, U.K.	-	Same as 3 above	$\frac{1}{7}$
7a	Giblett	Cardington, Beds., U.K.	150	Open level agric.land with few trees	$\frac{1}{7.8}$
7b	Frost	"	350	Same as above	$\frac{1}{5.9}$
7c	Frost	"	1000	Same as above	$\frac{1}{6.7}$
8	Deacon	Sale, Vic. Australia	503	Gently rolling grazing land with few trees	$\frac{1}{6.25}$
9	Heywood	Leafield, Oxfordsh. U.K.	313	Open fields divided by low stone walls & hedges	$\frac{1}{5.9}$
10	Kamei	Japan	-	Rough coast	$\frac{1}{5}$
11	Wax	Orkney Is.	118	Flat topped grass hill 1/3 mile inland from high cliff overlooking sea.	$\frac{1}{4.6}$
12	Hess & Portman	Akron, Ohio, U.S.A.	352	Gently rolling country with many bushes & small trees	$\frac{1}{4.55}$
13	Franckenberger & Rudloff	Quickborn, Germany	230	Rel. level meadow land, numerous hedges & trees around small fields	$\frac{1}{4.35}$
14a	Smith	Upton, Long Is. New York, USA	410	Level country uniformly covered with scrub oak & pine to a height of 30 ft.	$\frac{1}{4}$
14b	Panofsky	"	410		$\frac{1}{3.85}$
14c	U.S.Weather Bureau	"	410		$\frac{1}{3.3}$
14d	"	"	410		$\frac{1}{2.9}$
15	Kamei	Japan	-	3 Japanese towns	$\frac{1}{3}$
16	Dines	Farnborough U.K.	1650	Wooded, treed farmland	$\frac{1}{2.8}$
17	Jensen	Copenhagen Denmark	242	Centre of large city	$\frac{1}{2.3}$
18	Taylor	Paris (Eiffel Tower)	900	Centre of large city	$\frac{1}{2}$
19	Rathbun	New York (Empire State Blg)	1263	Centre of large city	$\frac{1}{1.6}$

TABLE 2.4

Influence of Surface Roughness on Parameters Relating to Wind Structure near the Ground

Type of Surface	Power Law exponent α	Gradient height z_G ft	Drag Coeff. k
(a) Open terrain with very few obstacles: e.g. open grass or farmland with few trees, hedge-rows & other barriers, etc. prairie; tundra; shores & low islands of inland lakes, deserts	0.16	900	0.005
(b) Terrain uniformly covered with obstacles 30-50ft in height: e.g. residential suburbs; small towns; woodland & scrub. Small fields with bushes, trees & hedges.	0.28	1300	0.015
(c) Terrain with large & irregular objects: e.g. centres of large cities; very broken country with many windbreaks of tall trees, etc.	0.40	1700	0.050

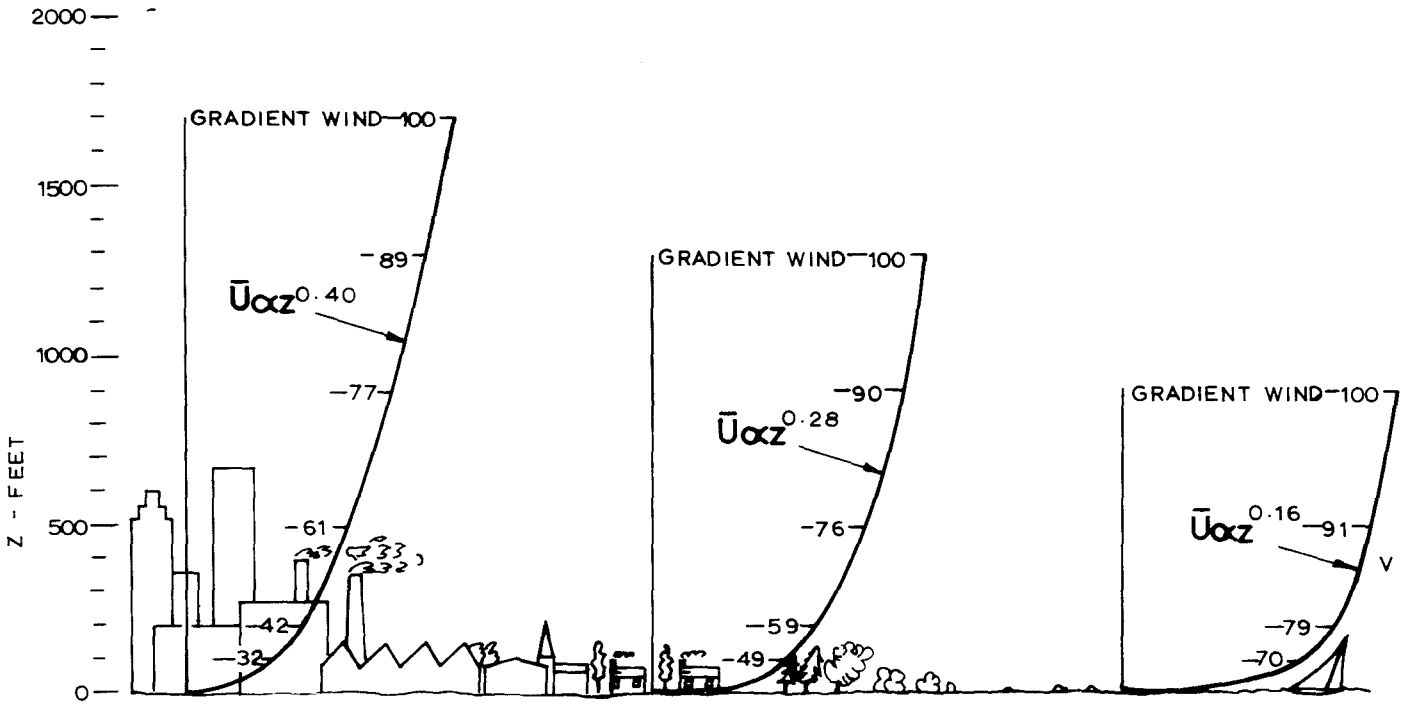

Fig. 2·5 PROFILES OF MEAN WIND VELOCITY OVER LEVEL TERRAINS OF DIFFERING ROUGHNESS. (AFTER DAVENPORT, 1963.)

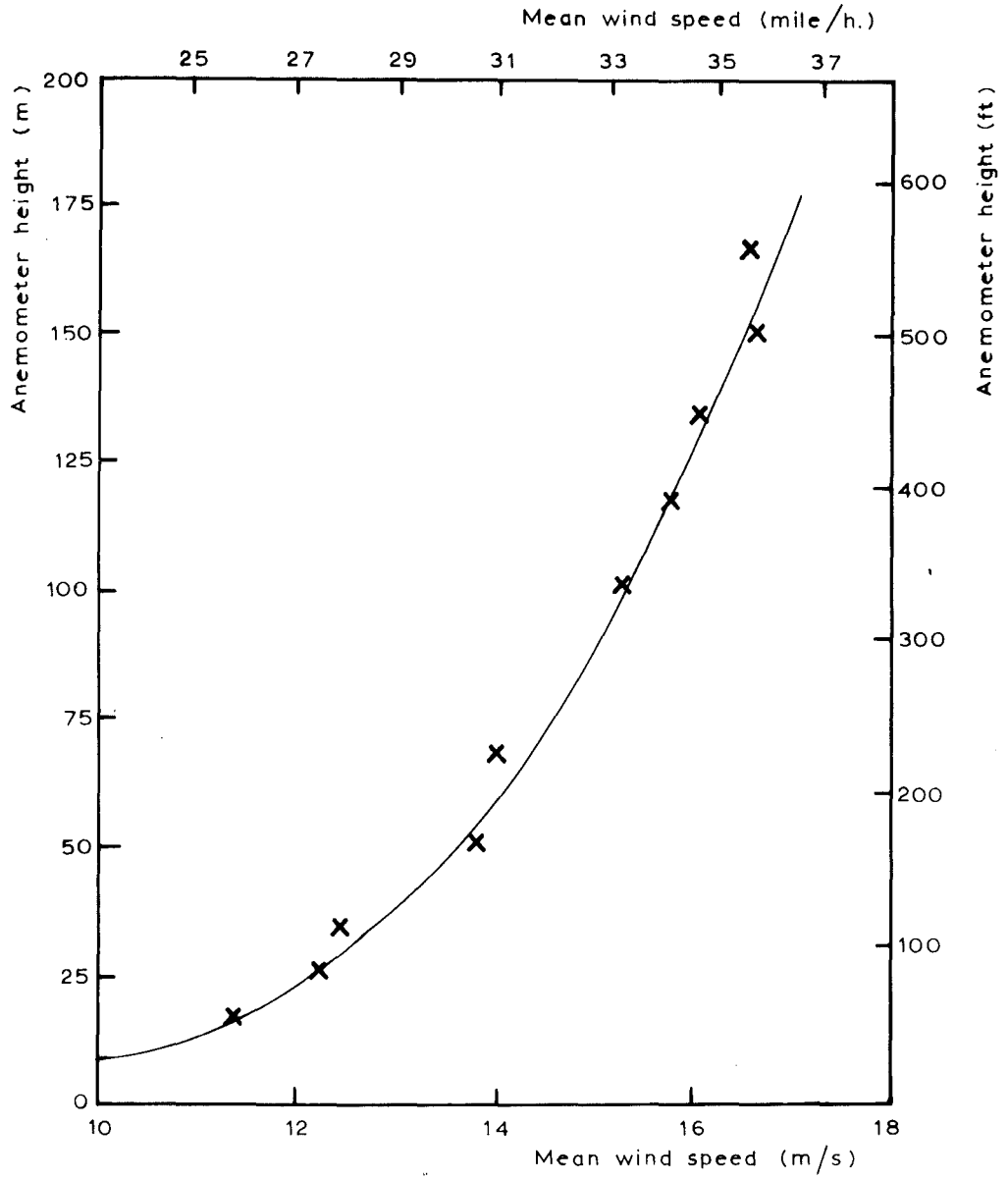

Fig. 2·6 MEAN WIND SPEED PROFILE MEASURED AT RUGBY. (AFTER HARRIS, 1970)

In general, the power law exponents of Table 2.4 give a satisfactory basis for a wind tunnel model flow. Closer approach to the exact exponent for a given terrain may be unrealistic, since the power law exponent in one location can readily be expected to vary by ± 10% depending on conditions of approach wind thermal stability, direction and velocity, e.g. see Jones, de Larrinaga and Wilson (1971). In Fig. 2.7 (after Davenport 1963) variations in power law exponent, gradient height and surface drag coefficient with roughness length z_o are summarised.

2.4.4 Surface Drag Coefficients:

For any given surface, the surface drag coefficient is defined as

$$k_z = \left(\frac{u_*}{\bar{U}_z} \right)^2$$

where $u_* = \sqrt{\frac{\tau_o}{\rho}}$

and $\bar{U}_z$ = mean velocity at a reference height.

The reference velocity is commonly taken to be that at z = 10m, and this will be assumed in the following chapters.

From the logarithmic surface layer mean velocity profile of equation 2.13,

$$k_{10} = \left(\frac{u_*}{\bar{U}_{10}} \right)^2 = \frac{K^2}{\log_e^2 \left(\frac{10}{z_o} \right)} \qquad \ldots(2.18)$$

e.g. for z_o = 5cm.

$$k_{10} = \frac{0.4}{\log_e^2 200} = 0.0057$$

Equation 2.18 predicts values of k_{10} close to those graphed by Davenport, Fig. 2.7, for $z_o < \sim 50$ cm.

Measurements of surface drag have been made in the atmosphere on many occasions (mostly over rural land) and measured surface drag

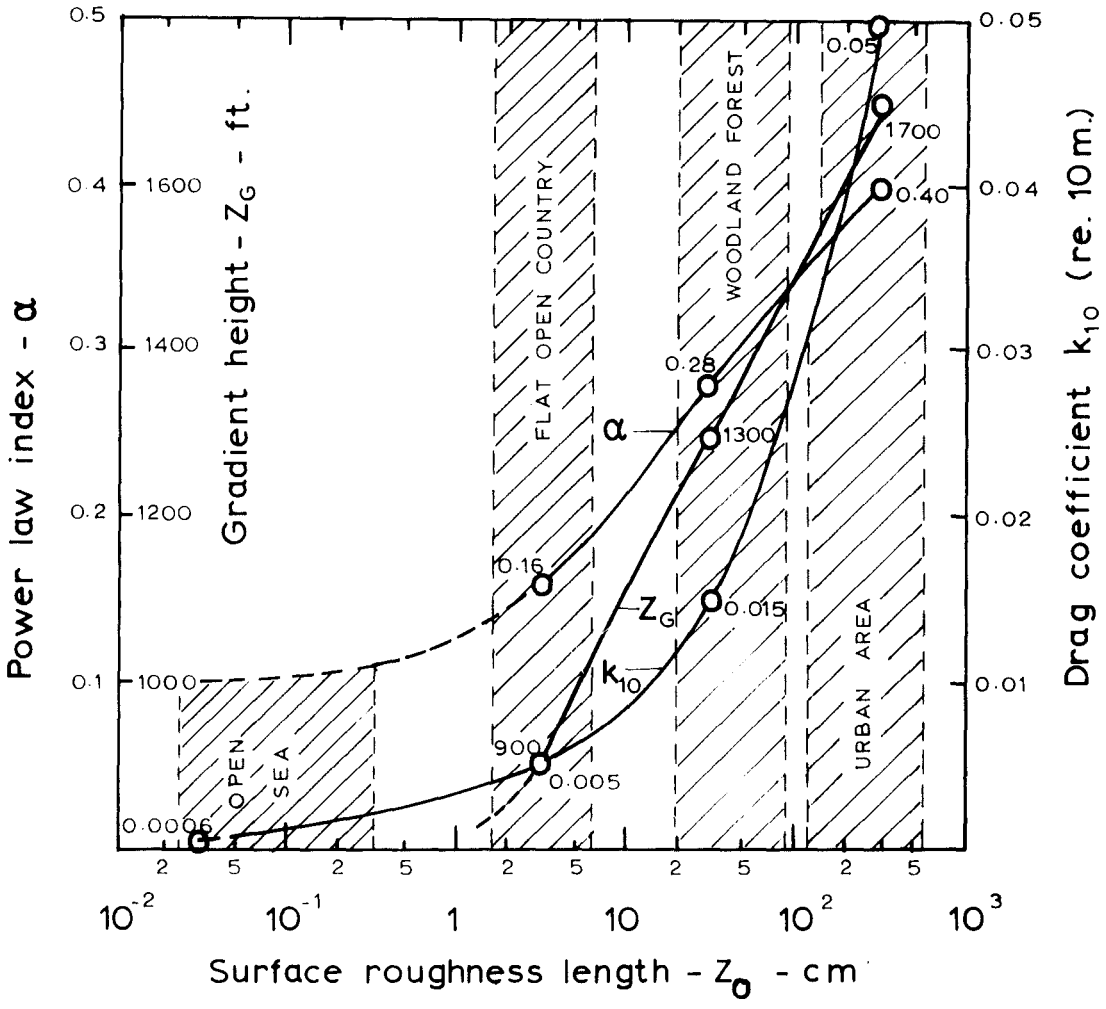

Fig. 2·7 PARAMETERS OF WIND PROFILE FOR DIFFERENT SURFACES. (AFTER DAVENPORT, 1963.)

coefficients have become important in defining the maximum stress in the constant stress surface layer.

Sutton (1953), for instance, gives values of k_2 (i.e. referred to a 2 m height) for several surfaces, as summarised in Table 2.5. Values of k_{10} have also been estimated, assuming a power law mean velocity profile whose exponent is determined using Table 2.1 and Fig. 2.7. Also, in Table 2.5, are broad classifications of k_{10} for different surfaces given by Harris (1970).

Priestley and Sheppard (1952) used equation 2.18 to calculate k_{10}, pointing out correctly that z = 10 m may not be a satisfactory reference height because at this height $\bar{U}$ tends to be a function of the local roughness and not characteristic of the surface as a whole. (This was also Davenport's defence for choosing z_G as reference height). Priestley and Sheppard suggest $k_{10} = 0.003 - 0.006$ for rolling, partly tree-covered terrain. Plate (1971) suggests $\left(\frac{u_*}{\bar{U}_\infty}\right)^2 = 0.0025$, which for a rural boundary layer with $\alpha = 0.16$ would correspond to $k_{10} = 0.007$.

In wind tunnel simulation of atmospheric boundary layers, the constant stress layer design shear stress is usually taken from tables of surface drag coefficients such as Table 2.5.

$$\text{i.e. } \tau_{const} = \tau_o = \rho u_*^2 = \rho k_{10} \bar{U}_{10}^2$$

This is at first sight reasonable, but the scarcity of atmospheric shear stress profiles of τ_{xz} vs. z makes this process uncertain. In laboratory boundary layers $-\rho\overline{uw}$ decreases close to the surface (e.g. see Hinze 1959, Fig. 7.14) and in the atmosphere near the ground the similar wall constraint on w should make τ_{xz} (= $-\rho\overline{uw}$ if viscous shear negligible) less than τ_{max} in the first few metres off the ground. It is suggested that τ_{max} will occur between $z/z_G = 0$ and $z/z_G = 0.1$ in the fully rough atmospheric surface layer, and may be greater than τ_o. Above $z/z_G = 0.1$ it is fairly well accepted that τ_{xz} steadily decreases.

Surface drag data at present available give insufficient information about shear stress above the ground, and standard Reynolds stress measurements should be incorporated in programmes for measurement of atmospheric turbulence. These measurements should be made at several stations between z = 0 and z = ~100m, using , say, fast response propeller anemometers measuring the u and w velocity components at each height. Recorded data could be digitised and then correlated in a computer. Such a system is being commissioned at the time of writing in the Department

TABLE 2.5

Values of Surface Drag Coefficient k for Natural and Man-made Surfaces

	Type of Surface	k_2	k_{10}
Sutton (1953)	Very smooth (mud flats, ice)	0.001	0.0007
	Lawn, grass up to 1cm high	0.0025	0.0018
	Downland, thin grass up to 10cm high	0.005	0.0035
	Thick grass up to 10cm high	0.008	0.0049
	Thin grass up to 50cm high	0.012	0.0067
	Thick grass up to 50cm high	0.016	0.0087
	Sea	0.001	0.0007
Harris (1970)	Rough, open water		0.001-0.002
	Open Grassland		0.003-0.005
	Woodland, forest, suburbs		0.015-0.03
	Urban Centres		0.03-0.05

of Mechanical Engineering, University of Canterbury, using a 7 track Kennedy Model 8107 Tape Recorder and the Departmental Hewlett-Packard 2100-A computer.

Listed values of surface drag coefficients and the postulation of a constant stress surface layer are based on the assumption of a fully developed steady state boundary layer. In reality, the atmospheric boundary layer is continually adjusting to changes in roughness of the earth's surface (except perhaps over the oceans) and shear stress values may be higher or lower than predicted for a given surface, particularly near the influence of a surface feature, such as a tall building, or narrow, dense windbreak.

2.4.5 Changes in Terrain Roughness:

As pointed out above, the assumption of uniformly rough terrain of unlimited extent is an idealisation which is rarely met by the earth's surface. The atmospheric boundary layer is rarely in equilibrium and is usually in a state of transition, to some degree, between one surface and another, so that profiles of mean wind velocity and temperature reflect effects of both the local surface roughness and a previous different surface roughness upstream.

At the change in roughness an internal boundary layer characteristic of the new roughness starts to grow, while above the internal boundary height, the flow properties remain unaltered and characteristic of the former surface. The interface between the two layers is assumed in analyses to begin at the surface discontinuity, and has a slope which depends to a degree on the ratio z_{o2}/z_{o1} (z_{o1} = roughness length upstream of discontinuity, z_{o2} = roughness length downstream of discontinuity).

Most theoretical studies of internal boundary layer growth following a step change in surface roughness have been made relatively recently. A comprehensive review of these analyses up to 1970 has been made by Plate (1971). Extensive laboratory experiments over step changes in surface roughness have been made by Antonia and Luxton (1969, 1972). In theoretical approaches, the Panofsky-Townsend theory (1964) (later modified by Townsend 1965), has been popular. Velocity profiles in

the atmosphere have been found to agree well with this theory going from smooth to rough, but less well going from rough to smooth, e.g. see Bradley (1968). Panofsky and Townsend (1964) modified an earlier theory by Elliot (1958). They assume a logarithmic law for the mean velocity profile upstream of the surface discontinuity and a log/linear law within the internal boundary layer consistent with an assumed linear distribution of shear stress in the internal layer. Mean velocity gradient and shear stress were also taken to be continuous across the internal boundary, where a discontinuity occurred in the earlier theory.

The original theory of Elliot predicted

$$\frac{\delta}{z_{o2}} = a \left(\frac{x}{z_{o2}} \right)^{0.8} \qquad \ldots.(2.19)$$

x = distance downstream of discontinuity

δ = internal layer thickness

where a is a slowly varying function of z_{o2}/z_{o1}, given approximately by

$$a = 0.75 - 0.03 \log_e \frac{z_{o2}}{z_{o1}}$$

Jones, de Larrinaga and Wilson (1971) found quite good agreement of equation 2.19 with their results for internal boundary layer development over an urban area. Plate (1971) indicates, however, that equation 2.19 yields results only roughly in agreement with observations.

For $\frac{x}{z_{o2}} \sim 10^4$ equation 2.19 predicts $\frac{\delta}{x}$, the slope of the internal boundary, approximately equal to 1:10, and for $\frac{x}{z_{o2}} \sim 10^6$, $\frac{\delta}{x}$ becomes approximately 1:20. Similar height to fetch ratios are predicted by the Panofsky-Townsend theory. Observed values of $\frac{\delta}{x}$ tend to be smaller than those predicted by equation 2.19 if adjustment of shear stress profiles is taken into account. Bradley (1968) concludes that for a new equilibrium to be established with complete adjustment of velocity and shear stress profiles, a height to fetch ratio of ~ 1:200 is more correct.

2.4.6 Three Dimensionality of the Flow, Mountainous Terrain

In the atmosphere, surface non-uniformities in a direction perpendicular to the mean wind flow are very common, e.g. flow along a

a sea shore or the edge of a forest, or flow across an athletics venue adjacent to a built-up area. Such non-uniformities invalidate the surface layer theory assumption of horizontal homogeneity, introducing secondary flows and non-equilibrium. For instance, a roughness patch in the form of an island will retard the flow near it, introducing higher shear stress and longitudinal vorticity into the flow. Changes in elevation or temperature may introduce three-dimensionality into the flow in the surface layer. The heat island effect of an urban area is important to meteorologists, particularly in the study of atmospheric air pollution. A research programme in this field is in progress at Colorado State University. (See Cermak and Arya,1970).

Wind tunnel modelling of atmospheric flows has generally been concentrated on two-dimensional flows. For these, theoretical treatment is simpler, and tunnel wall blockage effects are less important than in three-dimensional flow simulations, where large tunnel widths are needed.

The use of a flat plate boundary layer model for the atmosphere can only be accurate for fairly level terrain. The massive orographic effects on wind flow near mountain ranges mean that any wind problem in a hilly or alpine region requires a unique treatment, not handled by a generalised theory.

2.4.7 The Form of Large Eddies in the Atmospheric Boundary Layer:

Davenport (1963, 1967) briefly discusses the form of large eddies in the earth boundary layer. The more feasible model visualises the motion as two-dimensional jets which originate in the vicinity of the wall surface (ground) and interact with the main stream, so that in three-dimensions the flow within the jets and the enveloping flow resemble contra-rotating corkscrews with their axes lying parallel to the mean flow.

Davenport (1967) quotes directly from Faller who described the flow more succinctly: "Large eddies in a turbulent Ekman layer should take the form of stationary (or slowly moving) horizontal roll vortices orientated in the general direction of the wind, but at a small angle to the left of the geostrophic flow (Northern Hemisphere). Their horizontal wavelength should be 1 km or greater, dependent on geostrophic speed and latitude".

Little discussion is devoted to this topic in the literature, and Davenport's (1963) comment that more information is needed, is still true today.

2.5 STATISTICAL DESCRIPTION OF THE WIND'S TURBULENCE

On the micrometeorological scale, the atmospheric wind behaves approximately as a stationary random function, and a chart record of wind speed looks very similar to a record of random electrical noise. The statistical techniques of random function analysis (Bendat and Piersol, 1966) are therefore required to analyse this turbulence.

Statistical quantities used to describe atmospheric turbulence are set out below, with the aim of setting up a mathematical reference model for simulation of atmospheric wind in the wind tunnel. Probability distribution of the wind's velocity and cross-spectral density functions are only mentioned briefly as these were not measured in the present work. Extreme wind speeds have not been dealt with. This topic has been well discussed by Davenport (1961, 1963, 1967). Third and higher order correlations of turbulent velocity fluctuations have not been covered. Hinze (1959) treats these for the case of isotropic turbulence. Derivation of the statistical quantities used is covered by Bendat and Piersol (1966). Teunissen's (1970) review of the wind's turbulence structure probably represents the most concise but comprehensive available summary of recent research and analytical models.

2.5.1 Simplifying Assumptions:

(a) Stationarity:

Meteorological and aircraft wind records have shown that the wind velocity behaves as a stationary random function over averaging periods of 10-20 minutes and possibly up to 60 minutes. Thus use of random function analysis techniques is valid.

(b) Homogeneity:

The analytical assumption of horizontal homogeneity frequently breaks down in the surface layer, but should hold for a long fetch of uniform terrain. Vertical homogeneity does not exist, since the integral scale of turbulence and the ratio u':v':w' change with height.

(c) Isotropy:

Analysis of atmospheric turbulence spectra frequently involves the assumption of isotropic turbulence. This is reasonable in the free atmosphere and probably substantially correct in the outer part of the atmospheric boundary layer, but must fail close to the surface, where definite anisotropy exists in the sheared flow. Teunissen summarises evidence for the existence of isotropy in the atmosphere and discusses, in particular, the presence of local isotropy in the inertial subrange of the universal equilibrium range of the energy spectrum, in the sheared flow as well as in the free atmosphere. Characteristics of spectra in the inertial subrange are discussed in 2.5.6. Teunissen (1970) conludes that while true isotropy does not exist in the planetary boundary layer, a region of local isotropy should exist for wave numbers, $k > \sim \frac{3}{z}$. In practice, atmospheric spectra show deviation from isotropic models close to the ground, e.g. $z < 20m$, in particular a flattening of the peak.

(d) Taylor's Hypothesis:

Hinze presents this in the differential form:

$$\frac{\partial}{\partial t} = - \frac{\bar{U}\partial}{\partial x} \qquad \ldots.(2.20)$$

and points out that it can only be applied where $u/\bar{U} << 1$. This requirement is not satisfied in the highly sheared atmospheric flow near the ground, where $u'/\bar{U} \sim 0.2 - 0.5$ and Taylor's Hypothesis cannot be reliably applied to the whole velocity signal. Teunissen cites the work of Lin, who decided that the validity of Taylor's Hypothesis in shear flow could be related to eddy size or effectively wave number, k. Lin decided that the requirement $u' << \bar{U}$ should be satisfied for

$$k >> \frac{1}{\bar{U}} \frac{d\bar{U}}{dz}$$

or, for a logarithmic mean velocity profile of the form of equation 2.13

$$k >> \frac{1}{z \log_e \frac{z}{z_o}} \qquad \ldots.(2.21)$$

Field measurements suggest Taylor's Hypothesis is valid for $k >> 0.0016m^{-1}$ and Teunissen concludes that Taylor's Hypothesis becomes decreasingly accurate for $k < \sim 0.003m^{-1}$.

In a wind tunnel atmospheric boundary layer simulation, velocity fluctuation frequencies are scaled up by the reciprocal of the linear scaling factor d_m/d_a. If z_o is correctly scaled, then equation 2.21 suggests that the critical value of k is similarly scaled up, e.g. for a 1:500 scale simulation, Taylor's Hypothesis would be valid for

$k >> 0.8m^{-1}$ corresponding to $k >> 0.0016$ in the atmosphere.

The correctness of this procedure is uncertain.

Where Taylor's Hypothesis is applicable, it may be used in the form

$$\Delta x = \bar{U}.\Delta t.$$

in order to evaluate the integral length scale of turbulence L_{u_x}, knowing the Eulerian integral time scale, T_E.

2.5.2 The Mean Velocity:

The mean velocity profile in the streamwise (x) direction is given by

$$\bar{U} = \text{Lim}_{T\to\infty} \frac{1}{T} \int_0^T U(t)\, dt \qquad \ldots.(2.22)$$

It is assumed that $\bar{V} = \bar{W} = 0$.

(The co-ordinate system is as shown in the list of symbols).

Standard forms of the mean velocity profile for the atmosphere are as given in 2.4.3.

2.5.3 RMS Velocity Fluctuations:

Defining the fluctuating velocity components in the x, y, z directions as u, v, w respectively,

$$\bar{u} = \text{Lim}_{T\to\infty} \frac{1}{T} \int_0^T u(t)dt = 0, \text{ since } \text{Lim}_{T\to\infty} \frac{1}{T} \int_0^T U(t)dt = \bar{U}$$

and $U = \bar{U} + u$

Similarly $\bar{v} = \bar{w} = 0$.

The mean square velocity fluctuation, or mean square gust speed is defined as

$$\overline{q^2} = \frac{1}{T} \int_0^T (u(t)^2 + v(t)^2 + w(t)^2)\, dt$$

$$= \overline{u^2} + \overline{v^2} + \overline{w^2} \qquad \ldots.(2.23)$$

In practice, for studies of structural windloading, the RMS gust speed is commonly taken to be

$$q \simeq \sqrt{\overline{u^2}} = u' \qquad \ldots.(2.24)$$

The error involved in this process is considered at the end of this section.

For the component RMS velocity fluctuations, Davenport (1963) suggested on the basis of his invariant gust spectrum that the RMS gust speed, u', is given by

$$u' = 2.46\, k_{10}^{\frac{1}{2}}\, \bar{U}_{10} = 2.46\, u_* \qquad \ldots.(2.25)$$

k_{10} = surface drag coefficient.

Harris later modified this to give

$$u' = 2.58\, k_{10}^{\frac{1}{2}}\, \bar{U}_{10} = 2.58\, u_* \qquad \ldots.(2.26)$$

Using a power law mean velocity profile, equation 2.26 can be modified thus:

$$u' = 2.58\, k_{10}^{\frac{1}{2}} \left(\frac{10}{z_G} \right)^{\alpha} \bar{U}_G \qquad \ldots.(2.27)$$

Then with Davenport's suggested values for z_G and α, the following are obtained:

Open country	:	$u' = 0.106\, \bar{U}_G$
Woodland, suburbs	:	$u' = 0.11\, \bar{U}_G$
City Centre	:	$u' = 0.115\, \bar{U}_G$

Hence equations 2.26 and 2.27 indicate that the RMS gust speed is approximately independent of height and terrain and equal to $\sim 0.11\bar{U}_G$.

In the atmosphere, u' in fact decreases slowly with height, as shown for instance by results of Harris (1970), reproduced in Fig. 2.8. However, equations 2.25 and 2.26, which indicate $u' \simeq 2.5u_*$ (as given by Teunissen 1970) adequately describe u' close to the ground.

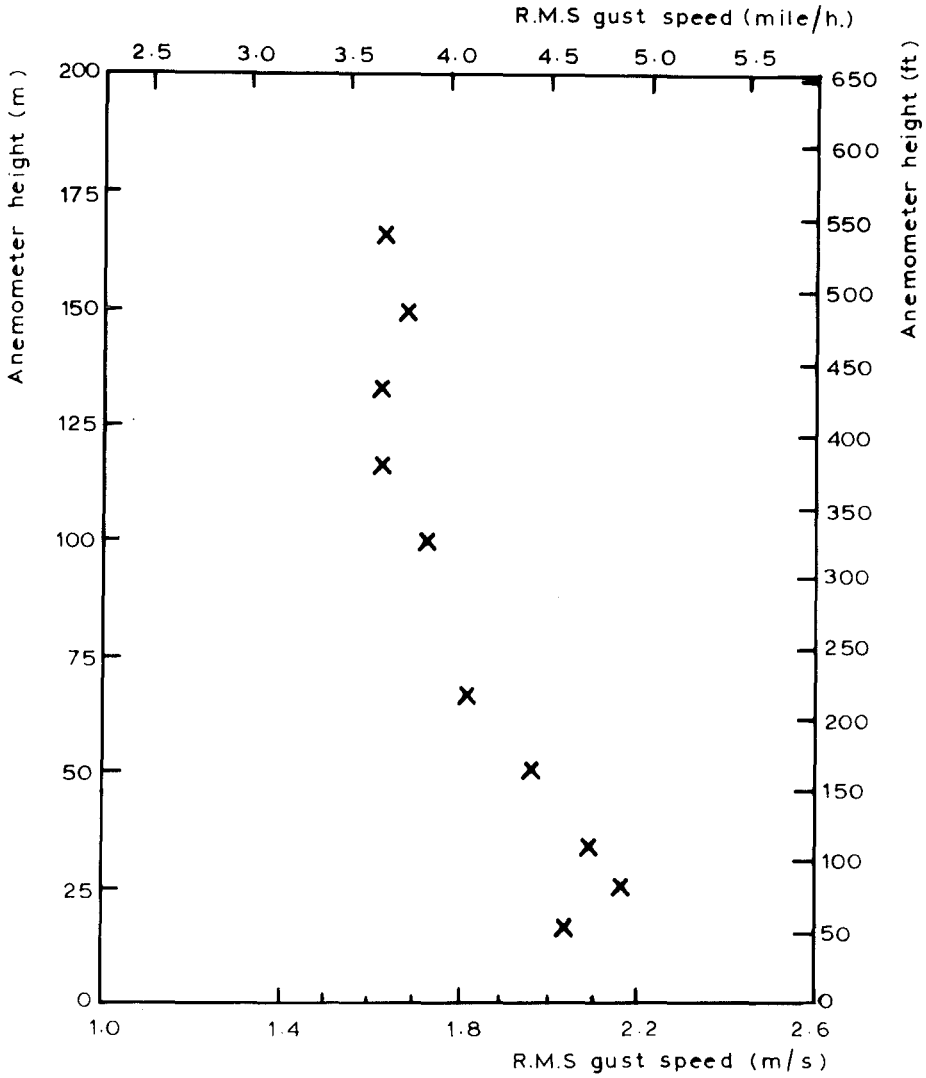

Fig. 2·8 R.M.S. GUST SPEED MEASURED AT RUGBY.
(AFTER HARRIS, 1970)

Fichtl and McVehil, (1969), from wind measurements at the NASA 150 m meteorological tower at Cape Kennedy, Florida, obtained in neutral stability

$$u' = 2.23\ \beta_u^{\frac{1}{2}}\ u_* \qquad \ldots.(2.28)$$

$$\text{where } \beta_u = \left(\frac{z}{18}\right)^{-0.63} \quad (z \text{ in metres})$$

e.g. evaluated at z = 10m this gives $u' = 2.68u_*$

Equation 2.28 shows $u' \propto z^{-0.315}$, i.e. decreasing with height. Hence typically $u' \simeq 2.5u_*$. Consider now data for the ratio u':v':w'.

Values of v':u' and w':u' vary with atmospheric stability. Singer (1964) found w':u' = 0.4, and v':u' = 0.9. These ratios tended to increase slightly with instability, but were essentially constant with height (upper height limit 300 ft). The ratio u':v':w' remained fairly constant with increasing wind speed. Using $u' = 2.5u_*$ the Singer data would give

$$u':v':w':u_* = 2.5:2.25:1:1.$$

Analysing spectra measured over several different sites, Busch and Panofsky (1968) found $w' = 1.29u_*$ independent of atmospheric stability. Fichtl and McVehil (1969) found for neutrally stable conditions

$$v' = 1.68\ \beta_v^{\frac{1}{2}}\ u_* \qquad \ldots.(2.29)$$

$$\text{where } \beta_v = \left(\frac{z}{18}\right)^{-0.35}$$

i.e. $v' \propto z^{-0.175}$ and decreases with height, e.g. at z = 10m, $v' = 1.86u_*$. Panofsky (1969) concludes on the basis of the Monin-Obukhov similarity theory that over the range $-0.5 < Ri < 0.2$, the ratio $w':u_*$ is essentially constant and equal to 1.3. It is also stated that $u':u_*$ and $v':u_*$ show systematic variation from place to place, indicating that terrain features of larger scale than z_o influence their behaviour.

Panofsky et al (1970) report turbulence measurements over heterogeneous terrain from three field studies. The first involved aircraft measurements made over plains, low and high mountains, and sea. The second two studies were made in the vicinity of wooded country. Over all the tests there was good agreement that $w' = 1.3u_*$, and the following ratio was typical of the data:

$$u':v':w':u_* = 2.6:2.2:1.3:1.$$

Some decrease in u':w' and v':w' with height was observed in the last test, made over fairly mountainous country.

Bowne and Ball (1970) found, under conditions averaging neutral to slightly stable over rural terrain,

$$u':v':w':u_* = 2.45:2.11:1.37:1$$

(or $u':v':w' = 1.79:1.54:1$).

and over urban terrain, where the heat island effect produced thermally unstable conditions,

$$u':v':w':u_* = 3.32:2.33:1.82:1$$

(or $u':v':w' = 1.82:1.28:1$).

Rural values of $u_i':u_*$ were approximately constant with height, but showed a marked decrease with height over the urban area.

Laboratory measurements of u', v' and w' in a rough wall boundary layer given by Hinze (1959) and shown in Fig. 2.9, show that at $z/\delta \simeq 0.1$

$$u':v':w' = 2.1:1.3:1$$

but as $z/\delta \to 1$, u', v' and w' tend to show more isotropy with

$$u':v':w' = 1.4:1:1.$$

Teunissen (1970) concluded his review of atmospheric data for u', v' and w' by stating that under conditions of neutral stability, a satisfactory model for the surface layer is

$$u':v':w':u_* = 2.5:2.0:1.3:1 \qquad \ldots.(2.30)$$

(Or $u':v':w' = 1.92:1.54:1$).

Harris (1970) suggested that for conditions of neutral stability $u' = 3v' > w'$, but later (1972) favours the ratio given by equation 2.30.

Data above are in fairly good agreement with equation 2.30, which appears to represent a satisfactory model for the neutrally stable atmospheric surface layer. Field data indicate that u', v' and w' will decrease with height. With increasing isotropy further away from the ground u', v' and w' can be expected to approach a common value at $z = z_G$.

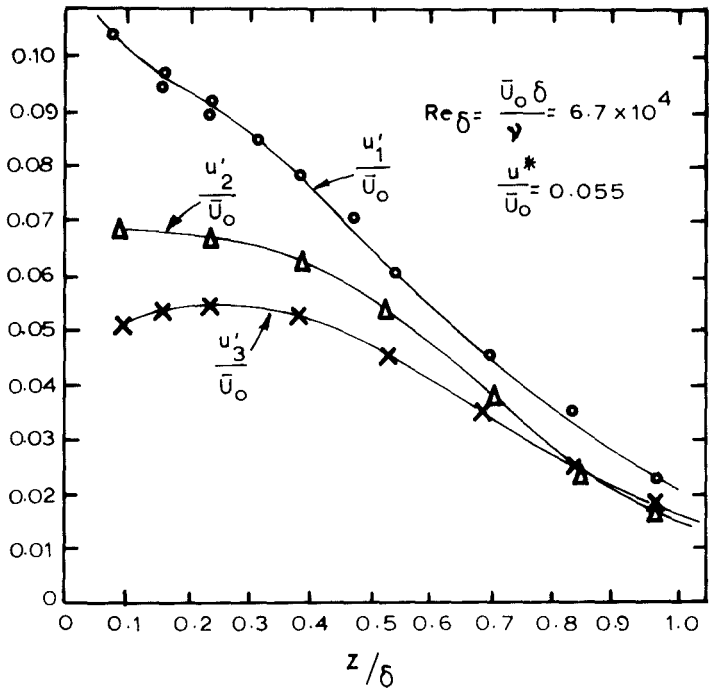

Fig.2.9 RELATIVE TURBULENCE INTENSITIES IN A BOUNDARY LAYER ALONG A ROUGH WALL WITH ZERO PRESSURE GRADIENT. (AFTER HINZE, 1959)

Using equation 2.30, the error involved in assuming $\overline{q^2} = \overline{u^2}$ in the surface layer is calculated as about 48% of the true value of $\overline{q^2}$, or an error of about 28% on q. This may be significant in some studies of wind effects on structures.

Turbulent Intensity: This is defined:

$$I_{u_z} = \frac{u'}{\bar{U}_z}, \quad I_{v_z} = \frac{v'}{\bar{U}_z}, \quad I_{w_z} = \frac{w'}{\bar{U}_z} \qquad \ldots.(2.31)$$

The intensity is sometimes presented in the form $\frac{u'}{\bar{U}_\infty}$ or $\frac{u'}{\bar{U}_G}$, etc.

If the RMS velocity fluctuations are assumed constant with height, equation 2.31 predicts decreasing turbulent intensity with height, as $\bar{U}$ increases. If a logarithmic mean velocity profile such as equation 2.13 is assumed for the surface layer, then

$$u_* = \frac{K\bar{U}}{\log_e \frac{z}{z_o}} \quad \text{and} \quad K = 0.4$$

and using equation 2.30,

$$\frac{u'}{\bar{U}_z} = \frac{1}{\log_e \frac{z}{z_o}}, \quad \frac{v'}{\bar{U}_z} = \frac{0.80}{\log_e \frac{z}{z_o}}, \quad \frac{w'}{\bar{U}_z} = \frac{0.52}{\log_e \frac{z}{z_o}} \qquad \ldots.(2.32)$$

Outside the surface layer, where u', v' and w' definitely decrease, the turbulent intensity will decrease more rapidly than predicted by equation 2.32. A plot of equation 2.32 falls close to design curves for $\frac{u'}{\bar{U}_z}$ given by ESDU (1972), e.g. as shown for z_o = 5cm in Fig. 2.10. It is seen in Chapter 6 that atmospheric data conform quite well with the $\frac{u'}{\bar{U}_z}$ curves of ESDU (1972).

The u component intensity varies from a maximum in an urban area, where $\frac{u'}{\bar{U}}$ may be 0.6 or higher among the buildings, to a minimum at heights of ~ 300m over smooth terrain where $\frac{u'}{\bar{U}} < 0.05$. Davenport and Harris use the power law velocity profile equivalent of equation 2.32 with

$$\frac{u'}{\bar{U}_z} \simeq 2.5\, k_{10}^{\frac{1}{2}} \left(\frac{\bar{U}_{10}}{\bar{U}_z}\right) \qquad \ldots.(2.33)$$

This is also shown in Fig. 2.10 for z_o = 5cm, α = 0.18.

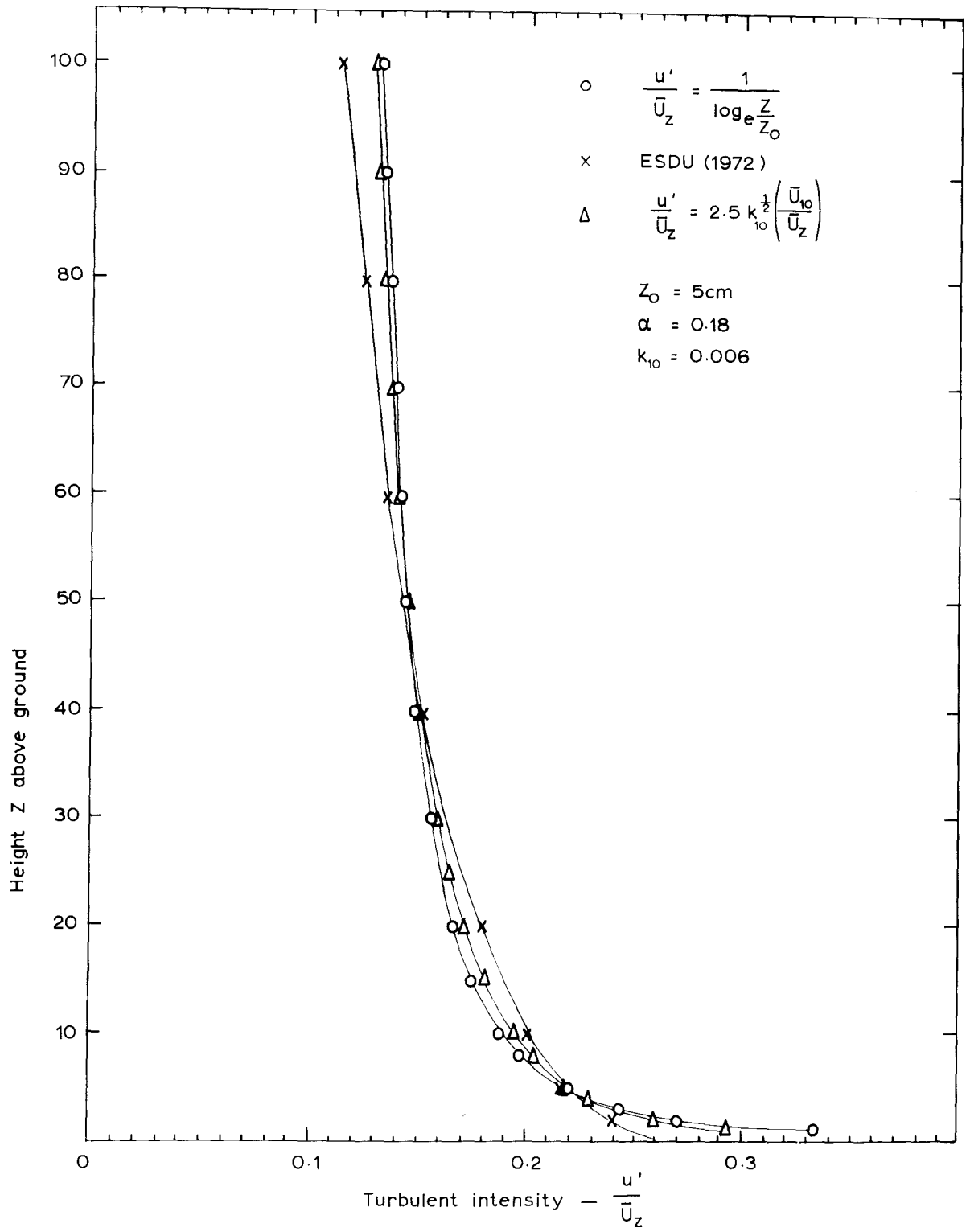

Fig. 2·10 MATHEMATICAL MODELS FOR VARIATION OF TURBULENT INTENSITY IN THE ATMOSPHERE.

Harris (1970) gives values of $\frac{u'}{\bar{U}_{10}}$ for the three broad categories of site using

$$\frac{u'}{\bar{U}_z} = 2.58\, k_{10}^{\frac{1}{2}}\, \frac{\bar{U}_{10}}{\bar{U}_z}$$

Open country $\frac{u'}{\bar{U}_{10}} = 0.18$

Woodland, suburbs $\frac{u'}{\bar{U}_{10}} = 0.32$

City centre $\frac{u'}{\bar{U}_{10}} = 0.58$

The last value is probably not very meaningful as z = 10m is below the height of roughness elements in a city centre. High values of $\frac{u'}{\bar{U}}$ make hot wire anemometer measurements uncertain, and hot wire signals require cautious interpretation in an urban boundary layer simulation.

2.5.4 Other Reynolds Stresses:

In 2.5.3 the diagonal components of the Reynolds stress tensor $-\rho\overline{u_i u_j}$ were considered. There is little atmospheric data available for the non-diagonal terms $\overline{uv}$, $\overline{vw}$, $\overline{uw}$, although Teunissen (1970) states that $\overline{uw} > \overline{uv} >> \overline{vw}$.

In the surface layer very close to the ground

$$u_* \simeq \sqrt{-\overline{uw}}$$

From this Teunissen (1970) deduced, using equation 2.30 that

$$\frac{-\overline{uw}}{u'w'} = -0.31 \qquad \ldots.(2.34)$$

This may be true at the surface, but as commented in 2.4.4, $-\overline{uw}$ may increase above the surface before decreasing in the expected manner outside the surface layer.

2.5.5 Probability Distribution of Wind Velocities:

There is strong evidence that wind velocity behaves as a Gaussian random variable to a reasonable degree of accuracy. The appropriate probability density function is, for a one-dimensional case:

$$p(U)\,dU = \frac{1}{\sqrt{2\Pi\overline{u^2}}} \cdot e^{\frac{-u^2}{2\overline{u^2}}}\,dU \qquad \ldots.(2.35)$$

and the corresponding probability distribution function is

$$F(U_1) = \frac{1}{\sqrt{2\Pi}} \int_0^{U_1} \frac{1}{\sqrt{\overline{u^2}}}\, e^{\frac{-u^2}{2\overline{u^2}}}\,dU \qquad \ldots.(2.36)$$

Davenport (1967) considers the usual case where velocity fluctuations occur in more than one direction. The postulation of a normal distribution of wind velocities enables the statistical distribution to be plotted, knowing only the mean velocity $\bar{U}$ and the RMS gust speed u'.

2.5.6 One Dimensional Spectral Density Functions:

Here the high frequency part of the spectrum (or 'gust spectrum') of Fig. 2.4 is considered. The spectrum function for the u component, say, of the fluctuating velocity is given by

$$S_u(n) = \lim_{\Delta n \to 0} \frac{\overline{u^2}\Big|_n^{n+\Delta n}}{\Delta n} \qquad \ldots.(2.37)$$

n = frequency.

From equation 2.37, $\overline{u^2} = \int_0^\infty Su(n)\,dn$

$S_u(n)$ is always a real valued non-negative function. For the streamwise component, the RMS velocity is given by

$$\overline{U^2} = \bar{U}^2 + \int_0^\infty S_u(n)\,dn$$

The component spectra are often expressed as functions of wave number k $(k = \frac{n}{\bar{U}})$, and it may be shown that $n\,S_{u_i}(n) = kS_{u_i}(k)$.

Turbulence energy is extracted from the mean flow in regions of high velocity gradient, i.e. near the ground in the atmosphere, and eddies characteristic of turbulence generation are therefore anisotropic. The turbulence energy is transferred to higher wave numbers, and smaller

and smaller eddies, by inertial interaction, and is finally dissipated into molecular kinetic energy (or, loosely, 'heat') in the smallest eddies at very high wave numbers. In general, a one-dimensional energy spectrum $Su_i(n)$ consists of three broad regions:

(i) a low frequency region where energy is transferred to turbulent motion from the mean flow. In this region the turbulence has a more permanent character and shows definite anisotropy.

(ii) the range of energy containing eddies; smaller eddies than the large scale low frequency motion, characterised by $\frac{\varepsilon t^2}{\nu}$ = constant (or ε = constant if steady state, constant viscosity conditions).

(iii) A high frequency region, Kolmogoroff's (1941) universal equilibrium range, where viscous dissipation becomes increasingly important as frequency increases.

Length and velocity scales characteristic of the above frequency ranges have been considered in detail by Hinze (1959) and are discussed, in part, in 3.3.3.

If a spectrum is plotted in the form $nS_u(n)$ vs. $n/\bar{U}$, then the wave number at the spectral peak $\left(\frac{n}{\bar{U}}\right)_p$ or k_p, is taken as the characteristic wave number of the range of energy containing eddies. At wave numbers smaller than k_p dissipation is very small, and Hinze (1959) states that if energy dissipation is neglected for wave numbers $k < k_p$, the total energy supply in the equilibrium range in isotropic turbulence, is practically equal to:

$$\varepsilon(t) = -\frac{3}{2}\frac{du'^2}{dt} = 2\nu\int_0^\infty k^2 S(k,t)\,dk \qquad \ldots.(2.38)$$

$$= -\tfrac{1}{2}\frac{d\overline{q}^2}{dt}$$

In a steady state situation this must also be equal to the dissipation. Now, at very high turbulent Reynolds numbers, Kolmogoroff's second hypothesis postulates the existence of an 'inertial subrange' at the low frequency end of the universal equilibrium range (upper end of the range of energy containing eddies). In the inertial subrange no production or dissipation of turbulence energy occurs, only inertial transfer of energy from larger anisotropic eddies to smaller, high frequency eddies.

In this region local isotropy is considered to exist, and the ratios $S_u(n):S_v(n)$ and $S_u(n):S_w(n)$ should have their isotropic turbulence value, 3:4. In the inertial subrange, the spectral density is proportional to the -5/3 power of frequency, or

$$S_{u_i}(k) \propto \varepsilon^{\frac{2}{3}} k^{\frac{-5}{3}} \qquad \ldots.(2.39)$$

If the spectral distribution of energy is constant so that ε = constant, then a log/log plot of $S_{u_i}(n)$ vs.n (or $S_{u_i}(k)$ vs. k) will exhibit a -5/3 slope in the inertial subrange. Presence of a -5/3 slope region in the spectrum is commonly taken as an indication of the extent to which wave numbers characterising the energy containing eddies and dissipation eddies are separated, on the wave number axis. This is mentioned further in 3.4.

Batchelor (1953) gives the criterion for the existence of the inertial subrange as

$$Re_{\ell_e}^{\frac{3}{8}} >>> 1 \qquad \ldots.(2.40) \qquad \left(Re_{\ell_e} = \frac{u'\ell_e}{\nu}\right)$$

where $\ell_e = 1/k_p$. Equation 2.40 is applied in 3.4.

In general, the frequency dependence of $S_{u_i}(k)$ is roughly as k^0 in the low frequency region, $k^{-5/3}$ in the inertial subrange, and k^{-7} in the high frequency viscous dissipation range (the last only true if Heisenberg's hypothesis holds - see Hinze, 1959).

The postulation of local isotropy in the atmosphere is reasonable for the smaller eddies which are statistically decoupled from the largest eddies generated by shear and thermal processes in the boundary layer. Atmospheric spectra close to the ground do tend to exhibit a region where $S(k) \propto k^{-5/3}$, although this cannot be taken as proof of local isotropy. From measurements at 75,150 and 300 ft heights over wooded country, Singer (1964) concluded that local isotropy existed for $k > 0.01m^{-1}$ and that horizontal isotropy existed for $k > 0.002m^{-1}$. Measurements at heights up to 60m by Bowne and Ball (1970) over rural and urban sites in flat country, however, showed no evidence of local isotropy, or a 4:3 ratio between $S_w(n)$ and $S_u(n)$. Generally evidence for the existence of a 4:3 ratio between $S_v(n)$ & $S_u(n)$, & $S_w(n)$ & $S_u(n)$, has been inconclusive such as that of Busch & Panofsky (1969). For wind tunnel modelling purposes it was decided to use Teunissen's criterion of assuming local isotropy for $k > \frac{3}{z}$.

In the past 15 years several mathematical expressions have been proposed to fit atmospheric spectral data. Notable presentations of atmospheric spectra include those of Davenport (1961), Singer (1964), Busch and Panofsky (1968), Harris (1968), Fichtl and McVehil (1969), Panofsky et al (1970) and Bowne and Ball (1970). The reader is referred to Teunissen (1970) for a concise review of atmospheric data, including the effects of thermal stratification, up to 1970. Below, accepted expressions for the different component spectra are set out, for conditions of neutral stability.

(a) Vertical Component Spectrum:

Busch and Panofsky (1968) suggested the following form for the vertical component spectrum:

$$\frac{n\,S_w(n)}{u_*^2} = \frac{1.075\,f_m}{1 + 1.5\left(\frac{f}{f_m}\right)^{\frac{5}{3}}} \qquad \ldots.(2.41)$$

or $$\frac{n\,S_w(n)}{\overline{w^2}} = \frac{0.636\,f_m}{1 + 1.5\left(\frac{f}{f_m}\right)^{\frac{5}{3}}} \quad \text{assuming } w' = 1.3\,u_*$$

$$f = \frac{nz}{\bar{U}}\,,\quad f_m = k_p z.$$

This expression was found to fit atmospheric data well for heights up to 50m and it can be seen that it predicts a -5/3 slope for the spectrum curve at frequencies somewhat higher than those characterised by wavenumber k_p. Singer's (1964) field data showed a -5/3 slope for $k > 0.01 m^{-1}$, and the data of Bowne and Ball (1970) showed a similar result. Panofsky et al (1970) found that vertical component spectra had a shape given closely by equation 2.44, which is a modification of equation 2.41 (C_{u_i} and r_{u_i} were set to unity).

Above the surface layer, von Karman's expression for $S_w(n)$ developed for isotropic turbulence, is found to adequately describe atmospheric data:

$$S_w(k) = 2\,\overline{w^2}\,L_{u_x}\left(\frac{1 + 188.4(L_{u_x}k)^2}{\left[1 + 70.7(L_{u_x}k)^2\right]^{\frac{11}{6}}}\right) \qquad \ldots.(2.42)$$

$$\text{or} \quad \frac{k\,S(k)}{\overline{w^2}} = \frac{n\,S(n)}{\overline{w^2}} = 2L_{u_x} k \left[\frac{1 + 188.4(L_{u_x} k)^2}{\left[1 + 70.7\,(L_{u_x} k^2)\right]} \right] \frac{11}{6}$$

where L_{u_x} is the integral length scale of turbulence of the u velocity component in the streamwise direction

$= 2L_{w_x}$ in isotropic turbulence.

Both the von Karman and Busch-Panofsky spectrum models tend to underestimate the spectrum energy at low frequencies. The flatter peak of the Busch-Panofsky model suits atmospheric spectral measurements near the ground better, and it was decided to use both equations 2.41 and 2.42 to compare with spectra in the simulated wind tunnel boundary layer, within and above the surface layer respectively.

(b) Lateral Component Spectrum:

The von Karman isotropic model spectrum is also found to provide a good fit to atmospheric data for the lateral velocity component spectrum above the surface layer:

$$\text{i.e.} \quad \frac{n\,S_v(n)}{\overline{v^2}} = 2L_{u_x} k \left[\frac{1 + 188.4\,(L_{u_x} k)^2}{\left[1 + 70.7\,(L_{u_x} k)^2\right]^{\frac{11}{6}}} \right] \qquad \ldots(2.43)$$

Fichtl and McVehil (1969) used a modification of the Busch-Panofsky vertical spectrum model equation 2.41 to represent their lateral spectra (and longitudinal spectra) as shown in Fig. 2.11. This spectrum has the form:

$$\frac{nS_{u_i}(n)}{\beta_{u_i} u_*^2} = \frac{c_{u_i} (f/f_{m_{u_i}})}{\left[1 + 1.5\left(f/f_{m_{u_i}}\right)^{r_{u_i}}\right]^{\frac{5}{3} r_{u_i}}} \qquad \ldots(2.44)$$

β_{u_i} as defined for equations 2.28 and 2.29.

c_{u_i} and r_{u_i} are constants dependent on the velocity component and stability.

Teunissen (1970) recommends the von Karman model, equation 2.43, with suitable choice of length scale L_{u_x}, as a reasonable general model for the whole planetary boundary layer.

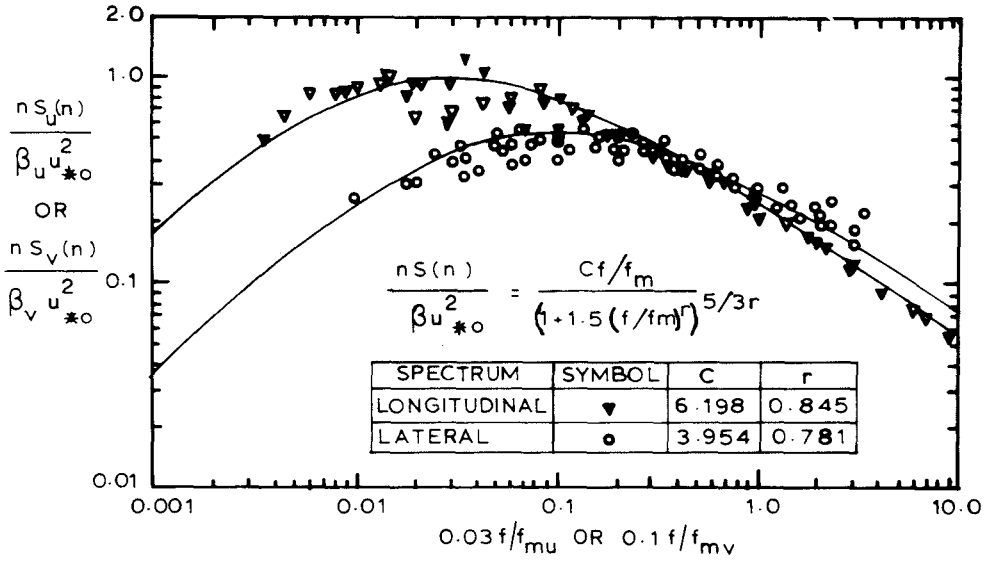

Fig. 2·11 ATMOSPHERIC SPECTRA MEASURED BY FICHTL & McVEHIL (1969).

(c) Longitudinal Component or Gust Spectrum:

Probably most important in the analysis of wind loading on structures, and other atmospheric wind problems, is the longitudinal component spectrum $S_u(n)$. The most notable contribution in the fitting of a mathematical model to atmospheric data here, was that of Davenport (1961), who analysed ~ 90 strong wind spectra obtained at different heights and locations, and suggested the following expression for the spectrum of horizontal gustiness in high winds and neutral stability:

$$\frac{n\,S_u(n)}{u_z^2} = \frac{\frac{2}{3}x_1^2}{\left[1 + x_1^2\right]^{\frac{4}{3}}} \qquad \text{....(2.45)}$$

(Davenport 1967)

where $x_1 = \frac{nL_z}{\bar{U}_z}$ and L_z is a scale length varying with height.

The peak of this spectrum is at $x_1 = \sqrt{3}$, so that $L_z = \sqrt{3}\,k_p$.

Davenport first applied the spectrum in a form invariant with height by referring it to the 10m height, thus

$$\frac{n\,S_u(n)}{k_{10}\bar{U}_{10}^2} = \frac{n\,S_u(n)}{u_*^2} = \frac{4x_1^2}{\left[1 + x_1^2\right]^{\frac{4}{3}}} \qquad \text{....(2.46)}$$

with $x_1 = \frac{nL}{\bar{U}_{10}}$ and $L \simeq 4000$ ft $\simeq 1200$m.

Equation 2.46 is shown plotted against atmospheric data in Fig. 2.12 (after Davenport 1963). Note in this figure and in equation 2.46:

(i) The non-dimensional spectral peak at a wavelength of approximately 2300 ft (700m)

(ii) The $-\frac{5}{3}$ slope predicted for $S_u(n)$ at large values of $\frac{n}{\bar{U}}$.

(iii) The proportionality of $nS_u(n)$ to u_*^2.

Davenport's spectrum yields a zero value for $S_u(n)$ at $n = 0$. Harris (1968) put forward a similar form to that of Davenport (and one that Davenport (1967) says is possibly better), the modified form yielding a finite value for $S_u(n)$ at $n = 0$. Harris' model is as follows :-

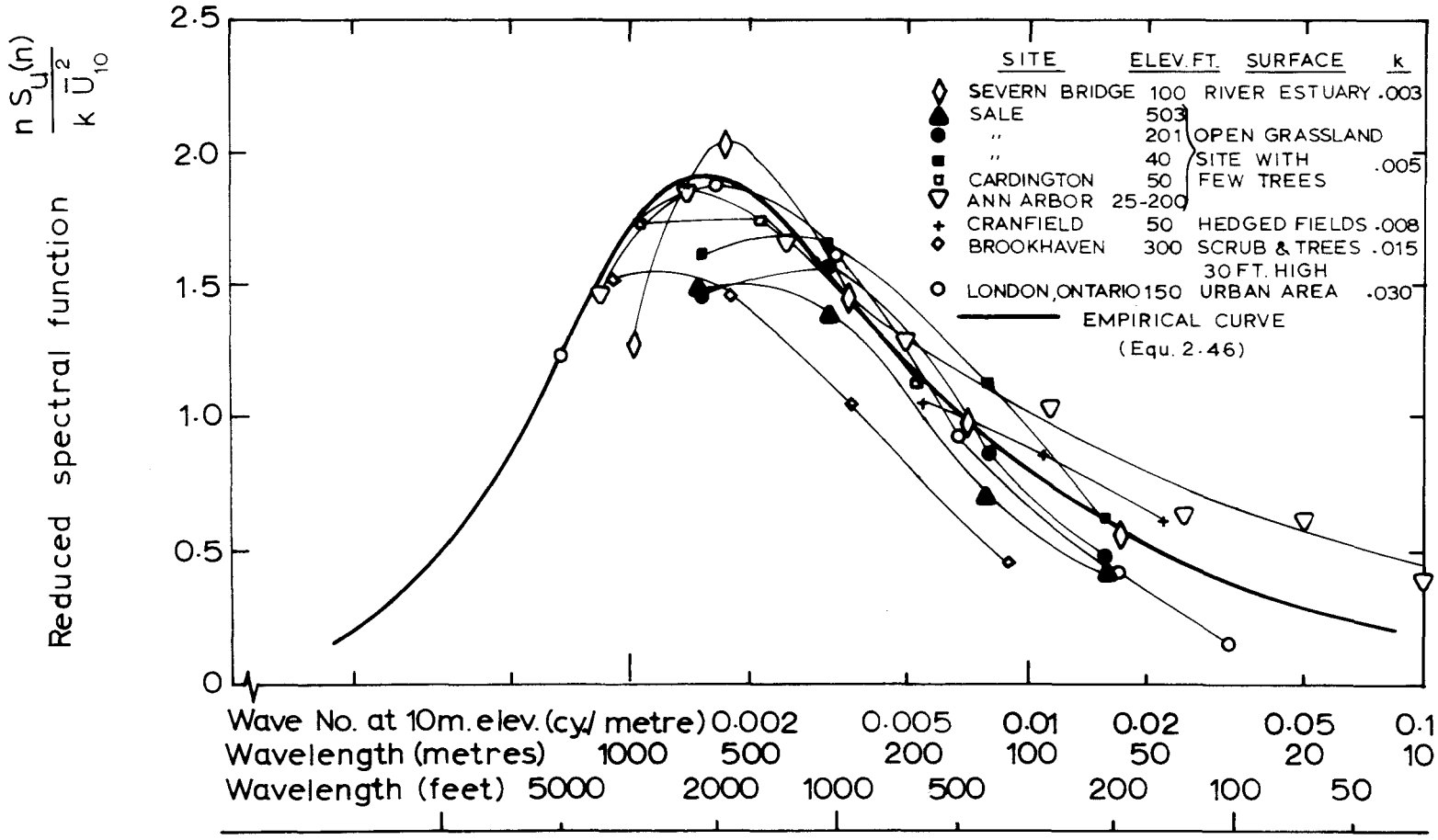

Fig. 2.12 SPECTRUM OF HORIZONTAL GUSTINESS IN HIGH WINDS.
(AFTER DAVENPORT, 1963)

$$\frac{n\,S_u(n)}{\overline{u^2}} = \frac{\frac{2}{3}\,x_1}{\left[2 + x_1^{\,2}\right]^{\frac{5}{6}}} \qquad \ldots.(2.47)$$

where $x_1 = \frac{nL}{U_{10}}$, with the scale length L = 1800m.

Note that equation 2.47 is again referred to the 10m height.

When determining the linear scaling of a wind tunnel atmospheric boundary layer simulation, one estimate may be obtained by matching the Davenport or Harris spectrum to the wind tunnel data. This process is detailed in Appendix 7.

The Harris spectrum is in fact very similar to the von Karman spectrum for isotropic turbulence :

$$\frac{n\,S_u(n)}{\overline{u^2}} = \frac{4L_{u_x}\,k}{\left[1 + 70.7(L_{u_x}\,k)^2\right]^{\frac{5}{6}}} \qquad \ldots.(2.48)$$

The von Karman form gives a good fit to atmospheric data under conditions of varying stability, and with the Harris spectrum predicts a $-\frac{5}{3}$ slope for $S_u(n)$ at high wave numbers.

The Fichtl-McVehil form of equation 2.44 may be most suitable near the ground with its flatter peak, but the Harris or von Karman form is a satisfactory general model for the atmospheric boundary layer, and it was decided to use equation 2.47 to compare with the longitudinal component spectra in the wind tunnel simulation.

Teunissen (1970) discusses the effects of atmospheric stability. Generally an increase in stability will damp out low frequency large scale turbulence, while unstable conditions enhance the generation of low frequency turbulence, as observed by Bowne and Ball (1970).

Note that the atmospheric spectrum models of equations 2.41 - 2.48 do not show $S_{u_i}(n) \propto k^{-y}$, where y ~ 7 at very high wavenumbers. This does not generally matter in the atmosphere as the viscous dissipation wave number range is beyond the range of wave numbers of interest.

2.5.7 Auto and Cross Correlations:

(a) Auto-correlation Function: The auto-correlation function is defined as :-

$$R_{uu}(\tau) = \lim_{T\to\infty} \frac{1}{T} \int_0^T u(t).u(t+\tau)dt \qquad \ldots.(2.49)$$

The function $R_{uu}(\tau)$ describes the general dependence of u at time t on the value of u at time $t + \tau$, where τ is a variable time delay. $R_{uu}(\tau)$ is always a real-valued function with a maximum at $\tau = 0$, and may be positive or negative valued.

The non-dimensional auto-correlation coefficient $\rho_{uu}(\tau)$ as

$$\rho_{uu}(\tau) = \frac{\rho_{uu}(\tau)}{\rho_{uu}(o)} = \frac{\rho_{uu}(\tau)}{\overline{u^2}} \qquad \ldots.(2.50)$$

and $\rho_{uu}(\tau) \leqslant 1$.

A plot of $\rho_{uu}(\tau)$ against τ gives an indication of the extent in time of a gust. Integration of the area under an auto-correlation curve, such as in Fig.6.46 gives the so-called Eulerian Time-scale of the turbulence T_E, which indicates the gust size in time.

$$\text{i.e. } T_E = \int_0^\infty \rho_{uu}(\tau)\, d\tau \qquad \ldots.(2.51)$$

Taylor's Hypothesis may then be applied (if valid) to obtain an integral length scale, see 2.5.9.

An important property of the power spectral density function and auto-correlation function is that they form a Fourier cosine transform pair

$$\text{i.e. } S_u(n) = 4 \int_0^\infty R_{uu}(\tau) \cos 2\Pi n\tau d\tau$$

$$R_{uu}(\tau) = \int_0^\infty S_u(n) \cos 2\Pi n\tau dn$$

When wind records are processed on a digital computer, the auto-correlation function may be calculated and thence the energy spectrum by taking Fourier transforms.

(b) Cross-correlation Function:

In studying wind loading on structures, it is helpful to know the extent in time of a gust, but also very important to know the spatial extent of a gust in the streamwise lateral and vertical directions. This gives an idea of the size of a gust incident on a structure. The cross-correlation function is used to determine the spatial extent of a gust, and is defined as :

$$R_{u_i u_j}(r;r';\tau) = \lim_{T\to\infty} \frac{1}{T}\int_0^T u_i(r;t)u_j(r';t+\tau)dt \quad ....(2.52)$$

This is a second order cartesian tensor with r,r' position vectors from an arbitrary origin. The cross-correlation coefficient is defined:

$$\rho_{u_i u_j}(r;r';\tau) = \frac{R_{u_i u_j}(r;r';\tau)}{\sqrt{R_{u_i u_i}(r;r;o)R_{u_j u_j}(r';r';o)}}$$

$$= \frac{R_{u_i u_j}(r;r';\tau)}{u'_i u'_j} \quad ....(2.53)$$

$R_{u_i u_j}(r;r';\tau)$ is always a real valued function which may be positive or negative. Its maximum is not necessarily at $\tau = 0$. A typical cross-correlation curve is shown in Fig.6.47 where wind tunnel and atmospheric data are compared. Note that $\rho_{u_i u_j}(r,r',\tau) \leq 1$.

In practical wind loading problems, e.g. fluctuating pressures on the face of a structure, the streamwise velocity component is often of main interest. Here important correlations would be those showing the longitudinal, lateral and vertical extent of a gust in terms of the u velocity component.

The correlation function of interest would be:

$$R_{uu}(r;r';\tau) = \lim_{T\to\infty} \frac{1}{T}\int_0^T u(r;t).u(r';t+\tau)dt$$

And, referring to Fig. 2.13, three correlation coefficients would be measured, usually with τ set to zero.

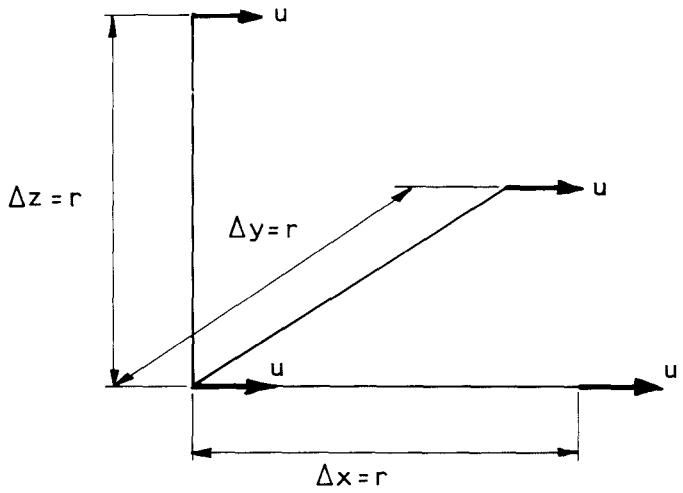

Fig. 2·13 LONGITUDINAL , LATERAL AND VERTICAL SEPARATIONS FOR CORRELATIONS OF THE u VELOCITY COMPONENT.

$$\rho_{uu}(\Delta x;0) = \frac{R_{uu}(\Delta x,0)}{\overline{u^2}}$$

Similarly $\rho_{uu}(\Delta y;0)$, $\rho_{uu}(\Delta z;0)$

Harris (1970) outlines the simplification that is made to the lateral and longitudinal cross-correlations when homogeneous isotropic conditions prevail. This is covered in detail by Hinze (1959)

2.5.8 The Cross-Spectral Density Function:

The cross-spectral density function is the Fourier transform of the cross-correlation function, and is effectively a narrow band cross-correlation, i.e. it gives a measure of the correlation of components of similar frequency in the cross-correlation of two signals. The cross-correlation function may be an asymmetrical function of time lag, τ, and thus, the cross-spectral density function is generally a complex function and is obtained by taking the Fourier transforms of the symmetrical and anti-symmetrical parts of the cross-correlation function respectively. The cross-spectral density function, consisting of a real part, $C_{u_iu_j}$ (co-spectrum), and an imaginary part $Q_{u_iu_j}$ (quad-spectrum) has no simple physical interpretation. However, the coherence function, defined below, gives a numerical value to the cross-spectral density function:

$$\text{Coherence function } \gamma^2_{u_iu_j} = \frac{C_{u_iu_j}^2 + Q_{u_iu_j}^2}{S_{u_i}(n)S_{u_j}(n)} \qquad \ldots.(2.54)$$

A detailed discussion of the cross-spectral density function is given by Davenport (1967) and Harris (1970), and these authors present atmospheric coherence data.

2.5.9 Integral Length Scales of Turbulence:

The integral length scale of turbulence is a measure of the longest correlation distance between the velocities at two points of the flow field. Three length scales can be defined for each gust component by integration of the cross-correlation coefficient for zero time lag, τ, with respect to separation in either the x, y or z direction. These are

$$L_{u_{ix_j}} = \int_0^\infty \rho_{u_iu_i}(\Delta x_j;0)dx_j \qquad \ldots.(2.55)$$

e.g. for the streamwise velocity component

$$L_{u_x} = \int_0^\infty \rho_{uu}(\Delta x;0)\, dx$$

$$L_{u_y} = \int_0^\infty \rho_{uu}(\Delta y;0)\, dy$$

$$L_{u_z} = \int_0^\infty \rho_{uu}(\Delta z;0)\, dz$$

In the special case where the turbulence is homogeneous and isotropic

$$L_{u_y} = L_{u_z} = \tfrac{1}{2}L_{u_x}$$

and $L_{v_x} = L_{w_x} = \tfrac{1}{2}L_{u_x}$, etc.

Integral length scale estimates may thus be obtained by integrating the area under a cross-correlation curve. This method is subject to errors, because at large separations low frequency fluctuations are important, and the use of a finite averaging time leads to oscillation of the correlation coefficient about the zero axis as Δx_j becomes large and $\rho_{u_i u_i}(\Delta x_j;0) \to 0$.

A second method of estimating integral length scales is to make use of the Eulerian time scale T_E. Assuming Taylor's Hypothesis may be applied

$$\Delta x = \bar{U}\Delta t$$

$$\text{then } L_{u_x} = \bar{U}\, T_E \qquad \ldots.(2.56)$$

This expression supplies an estimate of L_{u_x} only. Here also, use of finite averaging times results in oscillation of $\rho_{uu}(\tau)$ about its zero axis at large values of τ, where low frequencies are important. This is sometimes handled by calling T_E that value of τ at which $\rho_{uu}(\tau)$ has dropped to a value of 1/e, but this relies on $\rho_{uu}(\tau)$ decreasing exponentially. In reality $\rho_{uu}(\tau)$ decreases only approximately exponentially.

A third method for estimating integral length scales, and one that is very common in the interpretation of atmospheric turbulence data, is based on the location of the spectral peak on the k axis (i.e. location of k_p) in a plot of $nS_{u_i}(n)$ vs. k. Consider first the von Karman model

of equation 2.48:

$$\text{Let} \quad (L_{u_x} k) = x_1$$

$$\text{then} \quad \frac{d\, n\, S(n)}{dx_1} = 0 \quad \text{at } n\, S(n)_p.$$

This leads to $x_{1_p} = 0.146$

$$\therefore \quad L_{u_x} = \frac{0.146}{k_{p_u}} \qquad \ldots.(2.57)$$

For the vertical component model, equation 2.42

$$x_{1_p} = 0.212$$

$$L_{u_x} = \frac{0.212}{k_{p_w}} = \frac{0.212}{k_{p_v}} = 2L_{v_x} = 2L_{w_x} \qquad \ldots.(2.58)$$

Integral length scales of turbulence may be derived in a similar manner from the peak of the Davenport and Harris spectrum models. In the Davenport and Harris expressions, equations 2.45 and 2.47

$$x_{1_p} = \sqrt{3}$$

$$\therefore \quad L = \frac{\sqrt{3}}{k_{p_u}} \rightarrow k_{p_u} = \frac{\sqrt{3}}{L}$$

If the von Karman expression, equation 2.57, is applied,

$$L_{u_{x_{10\ \text{Davenport}}}} = \frac{0.146 \times 1200}{\sqrt{3}} \simeq 101.0\text{m}$$

$$L_{u_{x_{10\ \text{Harris}}}} = \frac{0.146 \times 1800}{\sqrt{3}} \simeq 151.0\text{m}$$

or, at an arbitrary height

$$L_{u_x} = 0.084L \frac{\bar{U}_z}{\bar{U}_{10}} \qquad \ldots.(2.59)$$

Using Davenport's value of L = 1200m,

$$L_{u_x} = 101\left(\frac{\bar{U}_z}{\bar{U}_{10}}\right) \text{m} = 101 \left(\frac{z}{10}\right)^{\alpha} \text{m} \qquad \ldots.(2.60)$$

or, using Harris' value of L = 1800m,

$$L_{u_x} = 151\left(\frac{\bar{U}_z}{\bar{U}_{10}}\right)^m = 151\left(\frac{z}{10}\right)^\alpha \text{ m} \qquad \ldots.(2.61)$$

Equations 2.59 and 2.60 assume a power law mean velocity profile.

Note:

(a) Equations 2.57, 2.58, 2.60 and 2.61 give the integral length scale of turbulence from the location of the spectral peak wave number k_p. The accuracy of the method is limited for two reasons:

(i) the spectral peak is often ill-defined, particularly near the ground, where it tends to be flat, making location of k_p uncertain.

(ii) The spectral peak is usually located near the low frequency limit of the spectral analysis equipment, where restricted averaging times again make data less reliable and the location of k_p uncertain.

(b) The assumption of homogeneous, isotropic turbulence is implicit in equations 2.57 and 2.58. In particular, equation 2.58 assumes that $L_{v_x} = L_{w_x} = \frac{1}{2}L_{u_x}$. Isotropic turbulence models have been found to fit non-isotropic atmospheric data quite well, but the above relation between the integral scales cannot be expected to hold near the ground, where equation 2.58 becomes invalid. Teunissen (1970) concludes, however, that

$$L_{u_x} = \frac{0.146}{k_{p_u}}, \quad L_{v_x} = \frac{0.106}{k_{p_v}}, \quad L_{w_x} = \frac{0.106}{k_{p_w}}$$

can still be considered reasonably accurate near the ground.

In regard to the effect of surface roughness and thermal stability on integral length scales, Teunissen (1970) states, "increasing surface non-uniformity tends in general to increase integral scales, but more at small heights than at large; decreasing thermal stability tends to increase scale, but more so at large heights than at small. Also, roughness length has little effect on scales, while increasing large scale non-uniformities on the surface tends to increase them".

It is generally accepted that integral length scales increase with height above the ground. Teunissen (1970) plotted data from several

field investigations which show that for the planetary boundary layer as a whole

$$L_{w_x} = 0.4\ z \qquad \ldots.(2.62)$$

It is interesting to note that this is the same expression as that for the mixing length ℓ, in the derivation of Prandtl's logarithmic mean velocity profile.

For L_{u_x}, equations 2.60 and 2.61 predict a power law variation with height in the same manner as the mean velocity. Note that if Harris' scaling length, L = 1800m, is used, the predicted value of L_{u_x} is 50% greater than if Davenport's L = 1200m is used. Teunissen (1970) reviewed considerable field data and concluded that for the planetary boundary layer as a whole, a suitable expression for the variation of L_{u_x} with height is

$$L_{u_x} = 20\sqrt{z}\ \text{ft} = 11.04\sqrt{z}\ \text{m} \qquad \ldots.(2.63)$$

or, if only the region above the surface layer is considered, a more suitable form is

$$L_{u_z} = 3.05\ z^{0.73}\text{m} \qquad \ldots.(2.64)$$

Teunissen (1970) plotted data showing that equation 2.63 fits atmospheric data well in the surface layer, and the much larger integral scales predicted for the surface layer by equations 2.60 and 2.61 are probably unrealistic. At greater heights, equations 2.60 and 2.63 predict similar integral scales, while equation 2.61 appears to overestimate L_{u_x}.

Atmospheric data for L_{v_x} indicate that it increases with height in roughly the same manner as L_{w_x} above the surface layer, but data are scarce and fairly inconclusive. Data for other integral length scales, e.g. L_{u_y}, L_{v_y} are scarce. Teunissen's (1970) summary indicates that L_{u_x} tends to be considerably greater than the other scales in stable air, but in an unstable atmosphere L_{u_x}, L_{u_y}, L_{v_x}, L_{v_y} all tend to be larger than in a stable atmosphere and are approximately equal. Measurements made by Harris (1970), 10m above a smooth surface, indicated that $L_{u_y} : L_{u_x} = \frac{1}{4}$. For L_{u_z} asymmetry caused by the proximity of the earth's surface gave two values of L_{u_z} at each height, the smaller value for downwards separation. At large heights (182m), L_{u_z} was approximately the same for both upwards and downwards separations and approximately equal to $0.29L_{u_x}$ (compared

with $L_{u_z} = 0.5L_{u_x}$ in isotropic turbulence.) Similar asymmetry in L_{u_z} was found in the present work, as shown by Fig. 6.48.

In the present work, integral length scales were later calculated using auto-correlation and cross-correlation data, and the spectral peak location method. The term 'integral length scale' is sometimes referred to as 'length scale', but always refers to the integral scale, not the micro-scale, which was not measured or considered important in the experiments.

Integral scales measured in the wind tunnel simulation were compared with those in the atmosphere by calculating the model atmospheric scales as follows:

(i) L_{u_x} : $L_{u_x} = 11.04\sqrt{z}$ m ....(2.63)

$$L_{u_x} = 101 \frac{\bar{U}_z}{\bar{U}_{10}} \text{ m} \quad \text{....(2.60)}$$

In the second case a suitable mean velocity profile was chosen. Equation 2.60, corresponding L = 1200m was used, as this form was closer to equation 2.63. A sample comparison of wind tunnel values of L_{u_x} with the atmospheric models is shown in Fig. 6.51.

(ii) L_{w_x} : $L_{w_x} = 0.4\ z$ ....(2.62)

A comparison of integral length scales of turbulence between wind tunnel and atmosphere represents an important method of determining the linear scaling of a simulated atmospheric boundary layer, as detailed in Appendix 7. It is therefore regrettable that all the methods described above for determining these length scales are subject to uncertainty, as discussed above and in 6.4. For instance, estimation of L_{u_x} to greater accuracy than ± 10% is not really possible. This is probably an unimportant fault, since available atmospheric data over similar terrains exhibit greater variability in L_{u_x} than ± 10%.

2.6 CONCLUSION

In the foregoing, a description of the neutrally stable atmospheric boundary layer has been presented, and mathematical models set up where

required, to form the basis for a wind tunnel simulation of an atmospheric boundary layer. It is noticeable that a certain amount of variability exists between different mathematical models proposed to describe the same atmospheric phenomenon, e.g. variation in turbulent length scale with height. This is to be expected, since these empirical expressions are usually derived from atmospheric data, which differ from one country to the next with the inhomogeneity of the earth's surface, and local weather conditions.

In wind tunnel modelling of the atmosphere, the most appropriate mathematical models must be chosen to suit the terrain and weather conditions characteristic of the problem. In Chapter 3, flow processes in the atmosphere are examined more closely in order to determine rigorous modelling criteria for scaling down the atmospheric flow in the wind tunnel. These criteria are then interpreted in terms of readily measurable statistical quantities which can be compared with the atmospheric models set up in 2.5.

CHAPTER 3

3.0 WIND TUNNEL SIMULATION OF THE ATMOSPHERIC BOUNDARY LAYER: MODELLING CRITERIA AND REVIEW

In this chapter the problem of simulating a neutrally stable atmospheric boundary layer in a wind tunnel is examined. Criteria are established for simulating at least the atmospheric surface layer accurately in the wind tunnel, and interpreted in terms of parameters readily measurable in the laboratory. Previous atmospheric boundary layer simulations are reviewed, together with the modelling criteria used.

3.1 WHY MODEL ATMOSPHERIC WIND FLOW IN WIND TUNNEL STUDIES?

The need for field studies of the atmospheric boundary layer, carried out in conjunction with wind tunnel model studies of atmospheric phenomena, was established in Chapter 1. Assuming now that it is desired to test, say, a model structure in a wind tunnel, one might first question the necessity for producing a scaled down atmospheric wind flow for the model test. Early model tests of the earth's surface features were frequently studies of wind pressures on building faces (Irminger and Nokkentved, 1936) or studies of wind reduction by wind breaks (Woodruff and Zingg, 1952), carried out in the uniform, low turbulence flow of an aeronautical wind tunnel. Frequently tests of this type failed to correctly predict full scale performance, or, disagreement was found between similar experiments carried out in different wind tunnels. More recent analyses of such tests attribute their lack of realism to the absence of a turbulent, fully aerodynamically rough boundary layer flow in the wind tunnel used.

The need for flow modelling criteria in studies of atmospheric boundary layer problems in the wind tunnel, was not thoroughly acknowledged until the early 1950's, when it was accepted that in fully rough turbulent flow, Reynolds number modelling had little significance. In his simple but graphic paper of 1958, Jensen demonstrated by means of full scale tests and model tests in various flows, that similarity between wind tunnel flow and atmospheric flow must be satisfied if meaningful results are to be obtained. Jensen's (1958) model law (q.v., 3.3.3) also evolves in more recent derivations of modelling criteria based on similarity theory.

3.2 DIFFERENT TYPES OF ATMOSPHERIC FLOW PROBLEMS. SCOPE OF THIS WORK

Currently in wind tunnel research of atmospheric wind problems a number of different areas are being investigated, and the type of approach wind structure required in the model flow varies according to the problem. Several broad problem areas are listed below. Some of them place common requirements on the simulated flow:

(a) Dynamic wind loading on buildings, tall or unusual shaped structures, electric power transmission line towers, radio telescopes, chimneys, cooling towers, etc.

Problems of this type have received much attention in the past decade. See, for instance, "Wind Effects on Buildings and Structures" (1963, 1967) or Cermak (1970). In the last twenty years advances in technology, architecture and structural materials have led to taller, more slender buildings and structures, with decreased structural damping. These factors increase the likelihood of dynamic excitation or damage by the wind. In these studies the simulated wind is typically required to show partial or complete similarity of the energy spectrum of at least the streamwise velocity component, and possibly also the mean velocity profile.

(b) Flow over a surface object or region of topography.

Here the problem may be a local one such as the flow pattern around a building, among a group of buildings or over a windbreak, or may be the study of the large scale flow over an area of land 20 square miles in extent. This type of study generally requires the maximum possible verisimilitude between wind tunnel and atmospheric flows. Thermal stability of the flow must be accounted for, and if the full scale flow is other than neutrally stable, Richardson Number similarity will be important.

(c) Particular Boundary Layer Phenomena.

This group would include model studies of flow over water surfaces, crops and forest canopies, such as the work of Plate and Quraishi (1965). Flow similarity would need to be rigorous, and care and experimentation necessary in the choice of the material for the boundary surface. Caborn (1957) for

instance, used beds of nails as forest models, but flow among the 'trees' and dynamic effects on the trees were not important. Papesch (1972) found that wire handled tapered nylon bottle brushes were unsatisfactory as dynamic models of pine trees, in forest wind damage studies.

(d) Diffusion and Pollutant-Dispersal Problems.

In recent years there has been increasing interest in pollution of the air and water in our environment. Problems of dispersal of smoke and gases from industrial plant, road transport vehicles and domestic appliances are widespread, and are fortunately now receiving considerable overdue attention. Smoke plume dispersion studies have been made for a number of years (e.g. Strom and Kaplin, 1960), but general pollutant dispersal studies have become common only recently. Cermak (1973) describes some problems that have been examined in the United States. In this country, pollution studies have been initiated, and related topics such as agricultural spray drift and diffusion in aerial spraying operations (Garden, 1973, unpublished) are being investigated. In these problems, the wind simulation facility must be capable of low speeds, ~ 1m/sec, and provision for creating a range of thermally stable and unstable flows must be made. An environmental wind tunnel of this type is in use at Colorado State University (Cermak and Arya, 1970).

In modelling certain structures, for instance, a tall chimney, it may be sufficient to model only part of the wind's spectrum and neglect the mean velocity profile. Gust frequencies of the order of the natural frequency of the structure would be of interest. On the other hand, a problem may demand rigorous simulation of the lower atmospheric boundary layer in regard to mean velocity, turbulence, and thermal stability, e.g. a group of tall buildings troubled by oscillation in high winds, and where the leeward flow from the upstream buildings creates two problems :

(i) In light winds and stable conditions boiler fumes from the upstream buildings are induced into the fresh air intakes of the downstream buildings. (thermal stability important).

(ii) In high winds, turbulence shed by the upstream buildings creates dangerous gusting around ground-level entrances of the downstream buildings. (high wind flow patterns important).

The primary restriction on the scope of the present work was that it was aimed to model only neutrally stable flows, and the first phase of the modelling work, described in this thesis, covers only the generation of a rural boundary layer, which was used in studies of mean wind reduction and turbulence in the lee of windbreaks.

Similarity parameters for scaling of the thermally stratified atmospheric boundary layer have been presented by McVehil, Ludwig, and Sundaram (1967), Blackadar et al (1969) and Cermak (1973). Only parameters for the scaling of neutrally stable flows are covered in 3.3. The most comprehensive discussion and similarity analysis of the atmospheric surface layer in relation to wind tunnel simulation is probably that of Ludwig, Sundaram et al (1967, 1969, 1970), and guidance has been drawn from this work in the initial treatment of the Navier-Stokes equations.

3.3 WIND MODELLING CRITERIA

3.3.1 Extent of Similarity Possible Between Atmospheric Flow and Wind Tunnel Flow:

Before deriving similarity, or modelling parameters, for simulating atmospheric flow in the wind tunnel, certain important differences between the atmospheric and laboratory wind tunnel boundary layers must be made clear. First of all, there is the obvious difference in scale with typical linear scaling of simulations ranging from 1:100 down to about 1:5000. Ellison (1957) has pointed out that the most accessible region of the atmospheric flow, i.e. the surface layer, is the least accessible in the wind tunnel flow. A second major difference, which has usually been neglected in engineering model studies, is that the wind tunnel free stream velocity, $\bar{U}_\infty$, does not correspond strictly to the gradient wind in the atmospheric flow. In the atmosphere the wind arises through the thermally induced, large scale pressure gradients and it is assumed that the horizontal mean wind velocity $\bar{U}_z$, increases with height toward the gradient wind, $\bar{U}_G$, so as to maintain equilibrium between the surface friction force (transmitted by Reynolds stresses) and the Coriolis force. Flow in the wind tunnel is also controlled by pressure gradients in the flow direction, but the horizontal mean

velocity approaches the free stream velocity in such a manner as to maintain an equilibrium between horizontal convection and vertical eddy diffusion. (The wind tunnel streamwise pressure gradient may be set to zero in the working section by varying duct cross-section area). Now, one of the prerequisites for similarity between two flows is that they must be described by the same mass, momentum and energy conservation equations and boundary conditions (Sedov, 1959). This condition is not satisfied by the atmospheric and wind tunnel boundary layers, the most simple and obvious discrepancy being the existence of the Coriolis body force in the momentum conservation equation for the atmospheric flow. Thus, strictly speaking, the entire planetary boundary layer, including the variation in wind direction with height (Ekman Spiral) cannot be simulated in the wind tunnel. In order to model Coriolis force in the laboratory, a device such as a rotating tank would be required, and scaling and operational problems would be immense. Some approximation to a Coriolis effect might be obtainable in the wind tunnel by introducing a small amount of swirl into the mean flow.

Adopting the above rigorous approach, Ludwig and Sundaram (1969) suggest that the only portion of a laboratory boundary layer that can be used as a model of the atmospheric boundary layer, is that part which can be described in terms of certain 'external parameters' e.g. u_*, z_o, specified at the surface alone, and which does not depend explicitly on the free stream velocity $\bar{U}_\infty$, i.e. the surface layer discussed in Chapter 2. Surface layer theories, such as that due to Monin and Obukhov (see Calder, 1966) do in fact neglect Coriolis force and the change in wind direction with height, and describe the surface layer in terms only of quantities specified close to the ground, e.g. the Monin-Obukhov scaling length, L', of equation 2.16.

Ludwig and Sundaram (1969) show that below a height of about 100m the effects of Coriolis force can be neglected, and that below z = 100m the variation in shear stress, τ_{xz} $(-\rho\overline{uw})$ with height is given by

$$\tau_{xz} = \tau_o \left(1 - \frac{\Pi z \omega \sin\phi}{K u_*}\right) \qquad \ldots.(3.1)$$

which, in steady, horizontal homogeneous flow, corresponds to

$$\tau_{xz} = \tau_o + \frac{\partial \bar{P}}{\partial x} z \qquad \ldots.(2.11)$$

From equation 3.1 it is found that the variation in shear stress over the first 100m above the ground should be about 20%. Ludwig and Sundaram conclude that this region, where shear stress is constant to within 20% of τ_o, adequately defines the surface layer, and therefore that only that portion of the wind tunnel boundary layer corresponding to the first ~100 m above the ground in the atmosphere, is accurate as a model of the atmospheric flow.

Now, in wind tunnel simulations of wind problems in engineering, e.g. structural oscillations in a tall building, the fact that strictly only the surface layer of the wind tunnel boundary layer is an accurate model of the atmosphere, has usually been disregarded. From the engineering viewpoint this is probably excusable, as the major error in the flow, i.e. the failure of the wind direction to change with height, would, over a building height say 200m, in most cases have only a minor effect. For the present work, modelling of the surface layer was satisfactory for the proposed tests of model windbreaks (less than 20m high), but it was aimed to produce a boundary layer whose depth corresponded to z_G, so that approximate modelling of certain engineering problems could be tackled. In reality most problems require only the surface layer to be modelled, as they occur below a height of 100m, for instance the following proposed studies in this department:

(i) Wind flow over and within forest plantations; wind damage to trees.

(ii) Wind forces on electricity transmission pylons and suspended cables.

(iii) Design of public recreation areas to afford maximum freedom from human discomfort due to wind.

(iv) Study of oscillations in buildings up to ~ 60m tall.

(v) Study of flow over low cliffs and escarpments.

Other differences that exist between the wind tunnel and atmospheric flows include:

(i) Roof and Wall Effects: These restrict the three-dimensionality of the flow, cause unwanted wall boundary layer growth and can cause flow blockage effects if a model in the simulated boundary layer occupies more than about 5% of the cross-sectional area of the working section. The linear scale must be chosen small enough for these factors to be unimportant.

(ii) Fan Effects: Pressure fluctuations or swirl may be present and produce anomalous effects. These should be avoidable with careful design of the modelling facility.

Thus, summarising, it can be asserted that fundamental differences between the wind tunnel and atmospheric boundary layers prevent exact simulation of the atmospheric boundary layer in the laboratory, but that with due regard for restrictions on scale imposed by the modelling facility, accurate simulation of the surface layer should be possible. In model tests, increasing loss of accuracy is likely as the model height increases above the surface layer depth, towards z_G, but approximate results in engineering applications should be obtainable where wind forces on, and dynamic excitation of structures are involved.

3.3.2 General Requirements of the Simulated Atmospheric Boundary Layer:

In Chapter 2 it was established that atmospheric wind flow has the characteristics of a fully aerodynamically rough flat plate boundary layer. Additionally, the surface layer theory assumptions of horizontal homogeneity and steady flow lead, in the absence of a streamwise pressure gradient, to the concept of a constant stress layer close to the surface. Before considering the implications of fully aerodynamically rough flow and horizontal homogeneity in the simulated flow, it is relevant to consider briefly the flow processes occurring in the full-scale wind.

If we postulate an equilibrium atmospheric boundary layer over uniformly rough terrain, a turbulent energy balance should exist as given by equation 3.2 (after Hinze, 1959):

$$\underset{\text{I}}{\frac{d}{dt}\frac{\overline{q^2}}{2}} = \underset{\text{II}}{-\frac{\partial}{\partial x_i}\overline{u_i\left(\frac{p}{\rho}+\frac{q^2}{2}\right)}} \underset{\text{III}}{-\overline{u_i u_j}\frac{\partial \bar{U}_j}{\partial x_i}} \underset{\text{IV}}{+\nu\frac{\partial}{\partial x_i}\overline{u_j\left(\frac{\partial u_i}{\partial x_j}+\frac{\partial u_j}{\partial x_i}\right)}} \underset{\text{V}}{-\nu\overline{\left(\frac{\partial u_i}{\partial x_j}+\frac{\partial u_j}{\partial x_i}\right)\frac{\partial u_j}{\partial x_i}}} \quad \ldots.(3.2)$$

This equation states:

The change (I) in kinetic energy of turbulence per unit mass of the fluid is equal to (II) the convective diffusion by turbulence of the total turbulence energy, plus (III) the energy extracted from the mean motion by the action of the Reynolds stresses on the mean velocity gradient, or the production of turbulence energy, plus (IV) the work done per unit of mass and of time by the viscous shear stresses of the turbulent motion, plus (V) the dissipation per unit mass by the turbulent motion. Many of

the terms of equ. 3.2 disappear if horizontal homogeneity prevails. In particular, if also $\bar{V} = \bar{W} = 0$, term I becomes zero, so that the kinetic energy of turbulence per unit mass is constant and the energy production term (III) can be set equal to the other terms (II),(IV),(V), which involve turbulent energy transfer or dissipation.

Hinze (1959) discusses the form of terms in equ.3.2 for the special case of wall turbulence. Boundary layer measurements by Townsend (1956) in an approximately horizontally homogeneous, zero pressure gradient wall boundary layer have shown that the major terms in the turbulent energy balance are the production and dissipation terms, if the region near the outer edge of the boundary layer is excluded. Production and dissipation are nearly in balance with each other especially as the wall is approached. Near the outer edge the dissipation is greater than the production. Term IV is small and the balance is practically made up by the diffusion term II, which supplies turbulent energy to the outer part of the boundary layer. Further inward this turbulent diffusion changes sign representing an energy loss. This loss reaches a maximum just outside the true constant stress layer (i.e. at $z/\delta \simeq 0.2$), but within the constant stress layer appears to change sign, producing a gain in turbulence energy in this region.

In the atmospheric boundary layer, therefore, turbulent energy is produced by the action of the Reynolds stresses on the velocity gradient in the mean flow, and in a horizontally homogeneous flow with $\bar{V} = \bar{W} = 0$, the energy production term will be :

$$\varepsilon = -\overline{uw}\,\frac{d\bar{U}}{dz} = \frac{\tau}{\rho}\,\frac{d\bar{U}}{dz} \quad \text{(per unit of mass and of time)} \quad \ldots.(3.3)$$

This extraction of energy from the mean flow and generation of turbulence tends to be at low wave numbers, and energy is transferred by inertial interaction to higher and higher wave numbers, viscous dissipation only becoming important in the small, high wave number eddies. From equ. 3.3, in agreement with the earlier comments, it can be seen that most of the turbulent energy production takes place close to the ground, where mean velocity gradient and shear stress are high. This energy is partly dissipated and partly diffused out into the region away from the ground. Because the production and dissipation are approximately equal, the energy diffused to the outer part of the boundary layer is the small difference of two large terms, and thus this diffusion of energy is a

relatively slow process. In the atmosphere, long upstream fetches of terrain are available for the generation and diffusion of turbulence and substantial quantities of turbulent energy reach the outer part of the boundary layer (assumed neutrally stable). In a wind tunnel there is a limited distance over which the boundary layer may be grown, and if natural rough wall boundary layer growth is used, the outer part of the boundary layer will tend to lack turbulent energy by comparison with the atmosphere. In practice this is manifested as low values of turbulent intensity and length scale. Techniques for alleviating this problem are discussed in 3.5. Assuming for the meantime that a long tunnel working section is available, the establishment of an equilibrium rough wall boundary layer requires continuous production of turbulent energy, and from equ.3.3 it is therefore important that the Reynolds stresses and mean velocity profile are simulated. In this conclusion there is an implied condition that the surface roughness length be scaled according to some rule. In 3.3.3 actual similarity parameters are derived to substantiate the above requirements of the model flow.

Ludwig and Sundaram (1969) set down basic conditions for the simulated atmospheric boundary layer as follows : "... regardless of the manner of its generation, any flow that is fully aerodynamically rough, horizontally homogeneous, and relatively free from any pressure gradients, constitutes a suitable model for the atmospheric surface layer". In the atmosphere, fully aerodynamically rough flow exists in almost all cases, and pressure gradients are generally very small, but the condition of horizontal homogeneity is more of an idealisation. Let us consider the implications of fully rough flow and horizontal homogeneity in the model flow:

(a) Fully Aerodynamically Rough Flow: The condition for fully aerodynamically rough flow to exist was given in Chapter 2 as

$$\frac{u_* z_o}{\nu} > \sim 2.5 \qquad \ldots.(2.8)$$

Now in the wind tunnel boundary layer it evolves that the roughness length, z_o, must be scaled down in proportion to the linear scale of the simulation, and on small scale simulations this may lead to $\frac{u_* z_o}{\nu} < 2.5$, i.e. a laminar sublayer would appear in the surface layer.

Thus if it is vital that equ.2.8 be satisfied, the following steps might be taken:

(i) increase $\bar{U}_\infty$ to increase u_*.

(ii) make z_o disproportionately large. This may lead to loss of similarity, e.g. in mean velocity or turbulent intensity profiles.

(iii) use a larger wind tunnel modelling facility in order to increase linear scale of the simulation.

(b) Horizontal Homogeneity: Implications of the assumption of horizontal homogeneity have been discussed by Calder (1966) and, in some detail, by Ludwig and Sundaram (1969). This assumption is necessary in surface layer theories, as otherwise conditions near the surface cannot be described in terms of surface conditions, e.g. u_*, z_o, alone. As shown in 2.4.2, the assumption of horizontal homogeneity was necessary, along with those of steady flow and negligible Coriolis effects, to postulate (in the absence of pressure gradients) a constant stress surface layer in the neutrally stable atmosphere. The constant stress assumption is in turn necessary to the derivation of Prandtl's logarithmic mean velocity profile which is found to apply in the atmospheric surface layer. The validity of the logarithmic velocity profile in the atmospheric surface layer is a justification for the surface layer theory assumption of horizontal homogeneity, but not proof of horizontal homogeneity. It must be remembered that in the rough plane model of, say, Ellison (1957), the plane is moved tangentially to the fluid to generate a constant stress (and horizontal homogeneity can only exist at large times when the flow has become steady), whereas in the atmosphere shear stress arises fundamentally by virtue of geostrophic pressure gradients. i.e. different flow processes are involved, and only close to the surface are the two flow situations similar.

Now, in a laboratory duct boundary layer, horizontally homogeneous conditions may be achieved, and the momentum equation analysis follows that of 2.4.2, which was applied to the atmosphere. For both the atmosphere and the laboratory duct therefore, close to the surface,

$$\frac{\partial \tau_{xz}}{\partial z} = -\frac{\partial \bar{P}}{\partial x}$$

if horizontally homogeneous, steady flow conditions exist. $\frac{\partial \bar{P}}{\partial x}$ is much higher in the laboratory boundary layer than in the atmospheric boundary layer and this will increase $\frac{\partial \tau_{xz}}{\partial z}$. The duct area may be increased in the streamwise direction so that $\frac{\partial \bar{P}}{\partial x}$ becomes zero, but the convective acceleration terms $\bar{U}\frac{\partial \bar{U}}{\partial x} + \bar{W}\frac{\partial \bar{U}}{\partial z}$ are reintroduced into equ.2.9, so that

$$\bar{U}\frac{\partial \bar{U}}{\partial x} + \bar{W}\frac{\partial \bar{U}}{\partial z} = \frac{\partial \tau_{xz}}{\partial z} \qquad \ldots.(3.4)$$

Ludwig and Sundaram (1969) state that close to the surface, the left hand side of equ.3.4 will be small, so that approximately constant stress exists in the surface layer. However, only approximate horizontal homogeneity can now exist because $\frac{\partial}{\partial x}$ is now finite for the statistical properties of the velocity.

In conclusion, an approximately horizontally homogeneous flow, with approximately constant shear stress in the surface layer, out to $z/\delta \simeq 0.2$, may be generated in the wind tunnel over a rough floor with $\frac{\partial \bar{P}}{\partial x} \simeq 0$. This flow should be an adequate model of the atmospheric surface layer.

The emphasis given above to the generation of a horizontally homogeneous, constant stress surface layer in the model flow, has not generally been made in engineering modelling applications, where exactness of the surface layer flow simulation has been considered secondary to obtaining good approximate similarity of energy spectra, and profiles of mean velocity and turbulent intensity. The careful simulation of the surface layer flow is probably important, however, when undertaking topographical modelling, keeping in mind that horizontal homogeneity is an ideal only approximately, if ever, achieved in the atmosphere.

3.3.3 Similarity Parameters:

A fundamental problem with turbulent flows is the intractability

of the Navier-Stokes equations describing the fluid motion to solution by available mathematical techniques. However, an attempt to relate the equations describing atmospheric flow to those describing the wind tunnel model flow, may be made by using the techniques of similarity theory, such as described by Sedov (1959). Flow similarity parameters are derived by non-dimensionalising the equations of motion for the flow using characteristic dimensions which are fundamental to the problem. Provided that these non-dimensional similarity parameters, together with the appropriate initial and boundary conditions applicable to the differential equations, are the same in both the model and atmospheric flows, the flows should be similar in all respects. McVehil, Ludwig & Sundaram (1967) carried out a detailed similarity analysis of the Navier-Stokes equations for the general case of a thermally stratified atmospheric surface layer. In this work the treatment is restricted to neutrally stable flows, but the similarity analysis is extended to include the energy equation for the turbulent motion.

(a) Mean Flow Similarity.

In 3.3.1 it was commented that because the atmospheric and wind tunnel flows are not satisfied by the same differential equations and boundary conditions, strict similarity is not possible between these flows. Thus the similarity analysis which follows is restricted to the surface layer, where Coriolis force can be neglected, and close similarity is possible.
Using subscripted Cartesian notation, the equations of motion for the mean incompressible turbulent flow, with zero body force, are :

Continuity: $$\frac{\partial \bar{U}_i}{\partial x_i} = 0 \qquad \ldots.(3.5)$$

Conservation of Momentum:

$$\frac{\partial \bar{U}_i}{\partial t} + \bar{U}_j \frac{\partial \bar{U}_i}{\partial x_j} = - \frac{1}{\rho} \frac{\partial \bar{P}}{\partial x_i} + \frac{\partial}{\partial x_j}\left(\nu \frac{\partial \bar{U}_i}{\partial x_j} - \overline{u_i u_j} \right) \qquad \ldots.(3.6)$$

Let ρ_o, $\bar{U}_o$ and L_o be characteristic values of density, velocity and length for the problem. The subscript o here implies a reference quantity evaluated at a reference height which is the same multiple of roughness length, z_o, in both model and full scale flows. Since only differences of pressure are involved here $\rho_o \bar{U}_o^2$ may be used to non-dimensionalise the pressure. The Boussinesq expression

for the Reynolds stress is now used with K_M assumed constant:

$$\therefore \quad -\rho\overline{u_i u_j} = \rho K_M \left(\frac{\partial \bar{U}_i}{\partial x_j} + \frac{\partial \bar{U}_j}{\partial x_i} \right)$$

This is not valid for i = j (see Hinze, 1959, pp 20-21), so $\rho\overline{u_i^2}$ is extracted, and assuming also steady flow, equation 3.6 becomes:

$$\bar{U}_j \frac{\partial \bar{U}_i}{\partial x_j} = - \frac{\partial}{\partial x_i} \left(\frac{\bar{P}}{\rho} + \overline{q^2} \right) + \left[\nu + K_M (1-\delta_{ij}) \right] \cdot \frac{\partial^2 \bar{U}_i}{\partial x_j^2} \qquad \ldots.(3.7)$$

where $\overline{q^2} = \overline{u_i^2}$.

Non-dimensionalising using ρ_o, $\bar{U}_o$, L_o and $\rho_o \bar{U}_o^2$, equation 3.7 becomes:

$$\bar{U}_j' \frac{\partial \bar{U}_i'}{\partial x_j'} = - \frac{\partial}{\partial x_i'} \left(\frac{\bar{P}'}{\rho'} + \overline{q^{2'}} \right) + \left(\frac{\nu}{\bar{U}_o L_o} \right) \cdot \frac{\partial^2 \bar{U}_i'}{\partial x_j^{2'}}$$

$$+ \left(\frac{K_M}{\bar{U}_o L_o} \right) \frac{\partial^2 \bar{U}_i'}{\partial x_j^{2'}} \quad (1 - \delta_{ij}) \qquad \ldots.(3.8)$$

Primes denote dimensionless quantities.

The appropriate non-dimensional groupings, or similarity parameters, characteristic to the problem are $\nu/\bar{U}_o L_o$ and $K_M/\bar{U}_o L_o$. These must be the same for both model and full scale flows for similarity to occur, given that the same boundary conditions occur.

Note: (i) McVehil, Ludwig & Sundaram (1967) neglected the failure of the Boussinesq shear stress expression when i = j, but this makes no difference to the end result of the analysis;

(ii) $\overline{q^2}$, the turbulent kinetic energy would be more correctly non-dimensionalised with a reference mean square velocity fluctuation, e.g. $\overline{u_o^2}$. This would lead to another similarity parameter $\bar{U}_o^2 / \overline{u_o^2}$. The omission of this here is of no concern, as this parameter evolves in the similarity analysis of the turbulent velocity fluctuations.

(iii) A constant value of K_M is satisfactory for making order of magnitude estimates. The only mathematically acceptable representation of K_M is as a 4th order tensor (Hinze, 1959), but this makes the analysis extremely complicated.

Representation of K_M as a scalar varying in space, however, introduces no new similarity parameters, but K_M is now non-dimensionalised with a reference value, K_{Mo}, corresponding to the reference height. Equation 3.8 becomes:

$$\bar{U}_i' \frac{\partial \bar{U}_i'}{\partial x_j'} = \frac{\partial}{\partial x_i'}\left(\frac{\bar{P}'}{\rho'} + \overline{q^2}' \right) + \left(\frac{\nu}{\bar{U}_o L_o} \right) \frac{\partial^2 \bar{U}_i'}{\partial x_j'^2}$$

$$+ \left(\frac{K_{Mo}}{\bar{U}_o L_o} \right) \frac{\partial}{\partial x_j'} \cdot \left(K_M' \left(\frac{\partial \bar{U}_i'}{\partial x_j'} + \frac{\partial \bar{U}_j'}{\partial x_i'} \right) \cdot (1 - \delta_{ij}) \right) \quad ....(3.9)$$

If the problem is confined to horizontally homogeneous flows, with $\bar{U}_2 = \bar{U}_3 = 0$ ($\bar{V} = \bar{W} = 0$), then

$$\frac{\bar{U}}{\bar{U}_o} = f\left(\frac{z}{L_o}, \frac{\bar{U}_o L_o}{\nu}, \frac{\bar{U}_o L_o}{K_{Mo}} \right) \quad ....(3.10)$$

If the flow is fully aerodynamically rough the molecular viscosity Reynolds number should not appear in equation 3.10. Therefore unless the atmospheric flow is at very low speed over exceptionally smooth terrain such as mud flats, equation 3.10 reduces to :

$$\frac{\bar{U}}{\bar{U}_o} = f\left(\frac{z}{L_o}, \frac{\bar{U}_o L_o}{K_{Mo}} \right) \quad ....(3.11)$$

Note that with the shear stress equal to Reynolds stress, the existence of a constant stress layer requires K_M, the eddy viscosity, to vary inversely as $\frac{d\bar{U}}{dz}$.

Let the fully aerodynamically rough, horizontally homogeneous flow be characterised by roughness length z_o. This length may be used to non-dimensionalise the surface layer flow equations. Equation 3.11 then becomes :

$$\frac{\bar{U}}{\bar{U}_o} = f\left(\frac{z}{z_o}, \frac{\bar{U}_o z_o}{K_{Mo}} \right) \quad ....(3.12)$$

and this is the equation for the mean flow similarity.

For the reference height, Ludwig and Sundaram (1969) quote the value $z_{ref} = e^6 z_o \simeq 400 z_o$, suggested by Ellison, but point out that the value chosen for the reference height does not affect the similitude of equation 3.12.

Now, in the atmosphere a convenient reference velocity does not really exist, and $\bar{U}_o$ must be chosen to suit the region of interest in the atmosphere. Ludwig and Sundaram show that if $\bar{U}_o$ is set equal to K_{Mo}/z_o and τ_{xz} is assumed constant, then $\frac{\bar{U}}{u_*}$ is a function of z/z_o alone, leading to the Prandtl logarithmic mean velocity profile of equation 2.13.

The first of the two similarity parameters in equation 3.12 is simply a linear, or geometric, scaling parameter which indicates that in the two flows the relationship between the height, h, of some object or measurement and the roughness length, must be

$$\left(\frac{h}{z_o}\right)_m = \left(\frac{h}{z_o}\right)_a \qquad \ldots.(3.13)$$

a = atmosphere

m = model flow

Equation 3.13 is in fact the model law proposed by Jensen (1958).

The second similarity parameter in equation 3.12 is a turbulent Reynolds number for the mean flow. The physical interpretation of K_{Mo} is discussed in 3.4.

(b) Similarity of the Turbulent Fluctuations.

Here it is assumed that the Navier-Stokes equations provide an adequate description of the turbulent phenomena considered. The basic continuity and momentum equations are then:

Continuity: $$\frac{\partial U_i}{\partial x_i} = 0 \qquad \ldots.(3.14)$$

Momentum: $$\frac{\partial U_i}{\partial t} + U_j \frac{\partial U_i}{\partial x_j} = -\frac{1}{\rho}\frac{\partial P}{\partial x_i} + \nu \frac{\partial^2 U_i}{\partial x_j^2} \qquad \ldots.(3.15)$$

where $U_i = \bar{U}_i + u_i$

$P = \bar{P} + p.$

Equations for the fluctuating quantities can now be obtained by subtracting equations 3.5 and 3.6 from equations 3.14 and 3.15 respectively, to obtain :

$$\frac{\partial u_i}{\partial x_i} = 0 \qquad \ldots.(3.16)$$

$$\frac{\partial u_i}{\partial t} + u_j \frac{\partial \bar{U}_i}{\partial x_j} + u_j \frac{\partial u_i}{\partial x_j} + \bar{U}_j \frac{\partial u_i}{\partial x_j} = -\frac{1}{\rho}\frac{\partial p}{\partial x_i} + \nu \frac{\partial^2 u_i}{\partial x_j^2} + \frac{\partial}{\partial x_j}\overline{u_i u_j} \ldots.(3.17)$$

Because of the random nature of turbulence and the unknown initial and boundary conditions for these equations, it is not possible to solve for the dependent variables as functions of space and time. Considerable information may, however, be obtained about the nature of turbulence, and the importance of various eddy transport mechanisms, without solving these equations. This is done by forming non-dimensional similarity parameters from equations 3.16 and 3.17 in the same manner as for the mean flow equations.

As with the mean flow similarity, the eddy viscosity, K_M, is introduced in the expression for Reynolds stress. Mean and fluctuating quantities must be non-dimensionalised with different characteristic scales, appropriate to the particular term non-dimensionalised.

(i) Mean Flow: The mean flow velocity may be normalised in each place it appears, with the longitudinal velocity $\bar{U}_o$, at some reference height, e.g. $\bar{U}_{10}$ or $\bar{U}_G$ (and their scaled equivalents in the wind tunnel flow). $\bar{U}_G$ is probably impractical in most cases and a reference velocity closer to the ground is probably more suitable. The friction velocity, u_* could be used, but u_* is probably less characteristic of the boundary layer as a whole than, say, $\bar{U}_{10}$ or $\bar{U}_G$. For a length scale z_o can again be used. Density is again non-dimensionalised with the reference height air density ρ_o.

(ii) Turbulent Fluctuations: Here the situation is more complicated as several possible scales can be used to form non-dimensional terms, depending on the wave number range of the energy spectrum that is of interest. Hinze (1959) discusses in detail the length and velocity scales that characterise the various wave number ranges of the energy spectrum, for isotropic turbulence, and which are taken to approximately apply to the higher wave number fluctuations in non-isotropic turbulence. These scales are considered in the similarity analysis of the energy equation for the turbulent fluctuations.

For the present purpose, a suitable velocity scale is the RMS streamwise reference velocity fluctuation

$$\sqrt{\overline{u_o^2}}$$

In wind modelling exercises intended for the simulated flow, such as flow over windbreaks or wind forces on structures, the range of energy containing eddies characterised by length $\ell_e = \frac{1}{k_p}$ is of interest. In isotropic turbulence, at least, ℓ_e bears a constant relationship with the integral length scale L_{u_x}. Thus a suitable scaling length for the turbulent fluctuations is $L_{u_{xo}}$. Pressure fluctuations in the turbulence may be non-dimensionalised with the product $\rho\overline{u_o^2}$ while a characteristic time may be taken as the ratio of characteristic length to characterise velocity:

$$L_{u_{xo}} \Big/ \sqrt{\overline{u_o^2}} \ .$$

Hence equations 3.16 and 3.17 are non-dimensionalised to give:

$$\text{Continuity:} \quad \frac{\partial u_i'}{\partial x_i'} = 0 \qquad \ldots.(3.18)$$

Momentum:

$$\frac{\partial u_i'}{\partial t'} + \left(\frac{\bar{U}_o}{\sqrt{u_o^2}} \right) \cdot \bar{U}_j' \frac{\partial u_i'}{\partial x_j'} + \left(\left(\frac{\bar{U}_o}{\sqrt{u_o^2}} \right) \left(\frac{L_{u_{xo}}}{z_o} \right) \right) \cdot u_j' \frac{\partial \bar{U}_i'}{\partial x_j'}$$

$$+ u_j' \frac{\partial u_i'}{\partial x_j'} = \frac{-\partial}{\partial x_i'} \left(\frac{p'}{\rho'} + \overline{q^2}' \right) + \left(\frac{\nu}{\sqrt{u_o^2} \cdot L_{u_{xo}}} \right) \cdot \frac{\partial^2 u_i'}{\partial x_j^{2\prime}}$$

$$- \left(\left(\frac{K_{Mo}}{\sqrt{u_o^2}\, z_o} \right) \left(\frac{L_{u_{xo}}}{z_o} \right) \right) \cdot \frac{\partial}{\partial x_j'} \left(K_M' \left(\frac{\partial \bar{U}_i'}{\partial x_j'} + \frac{\partial \bar{U}_j'}{\partial x_i'} \right) (1 - \delta_{ij}) \right)$$

....(3.19)

Note that K_M has again been allowed to vary as a scalar in space. Primes again denote dimensionless quantities.

Equations 3.18 and 3.19 show that if two neutrally stable turbulent flows are such that the parameters

$$\frac{\bar{U}_o}{\sqrt{u_o^2}}, \quad \frac{L_{u_{xo}}}{z_o}, \quad \frac{\nu}{\sqrt{u_o^2}\, L_{u_{xo}}} \quad \text{and} \quad \frac{K_{Mo}}{\sqrt{u_o^2}\, z_o}$$

are the same for the two flows, then the relative importance of the terms governing the fluctuating quantities is the same for both flows. Constancy of these parameters is a necessary but not sufficient condition for similarity between the two flows, because exact similarity requires the same initial and boundary conditions to apply to equations 3.18 and 3.19 in both wind tunnel and atmospheric flows. However, constancy of the above similarity parameters does provide an approximate flow similarity, particularly in the surface layer. The third parameter

$$\frac{\nu}{\sqrt{u_o^2}\, L_{u_{xo}}}$$

is a turbulent Reynolds number based on the molecular

viscosity, and outside the dissipation range of spectral frequencies can be neglected. If the dissipation range were important, a more correct length scale for this parameter would be, say, λ_{go}, the microscale of turbulence at the reference height. Use of λ_{go} as a length scale for this parameter would introduce another parameter

$$\frac{\lambda_{go}}{L_{u_{xo}}}$$

which is discussed in 3.4.

Neglecting the viscous dissipation range of eddies, three parameters remain, normally written

$$\frac{\sqrt{u_o^2}}{\bar{U}_o}, \quad \frac{L_{u_{xo}}}{z_o}, \quad \frac{\sqrt{u_o^2}\, z_o}{K_{M_o}}$$

The first of these is a non-dimensional turbulent intensity, and implies similarity of

$$\frac{\sqrt{v_o^2}}{\bar{U}_o} \quad \text{and} \quad \frac{\sqrt{w_o^2}}{\bar{U}_o}$$

also. The parameter

$$\frac{\sqrt{u_o^2}}{\bar{U}_o}$$

indicates that the turbulent intensity at each scaled down height in the simulated flow must be the same as at the equivalent height in the atmosphere. The second similarity parameter indicates that the integral length scale of turbulence must at each height be scaled down from the atmospheric value, in the ratio of the roughness lengths.

i.e. $$\frac{L_{u_{x_{zm}}}}{L_{u_{x_{za}}}} = \frac{z_{om}}{z_{oa}} = \frac{d_m}{d_a} \qquad \ldots.(3.20)$$

This is an important result. The third similarity parameter is a turbulent Reynolds number based on K_{Mo}. Since products and quotients of similarity parameters are themselves similarity parameters, this parameter is equivalent to:

$$\sqrt{\frac{\overline{u_o^2}}{K_{Mo}}}\, z_o \times \frac{\bar{U}_o}{\sqrt{\overline{u_o^2}}} \quad \text{or} \quad \frac{\bar{U}_o z_o}{K_{Mo}} ,$$

which was obtained in the mean flow similarity analysis.

Hence the similarity analysis of the equations of conservation of mass and momentum for the mean flow and turbulent fluctuations, has shown that with correct linear scaling, required by parameter z/z_o, a basic requirement for similarity between atmospheric and wind tunnel flows is that the parameters

$$\frac{\sqrt{\overline{u_o^2}}}{\bar{U}_o} , \quad \frac{L_{u_{xo}}}{z_o} , \quad \frac{\bar{U}_o z_o}{K_{Mo}}$$

be the same in both flows. Interpretation of these parameters in terms of quantities measurable in the wind tunnel is made in 3.4.

(c) Similarity of the Turbulence-Energy Equation:

Taking the turbulence energy equation, Equation 3.2, term I may be broken down to give:

$$\underbrace{\frac{\partial}{\partial t}\frac{\overline{q^2}}{2} + \frac{\partial}{\partial x_i}\frac{\bar{U}_i\overline{q^2}}{2}}_{I} = \underbrace{-\frac{\partial}{\partial x_i}\overline{u_i\left(\frac{p}{\rho}+\frac{q^2}{2}\right)}}_{II} \underbrace{-\overline{u_iu_j}\frac{\partial \bar{U}_j}{\partial x_i}}_{III}$$

$$+ \underbrace{\nu\frac{\partial}{\partial x_i}\overline{u_j\left(\frac{\partial u_i}{\partial x_j}+\frac{\partial u_j}{\partial x_i}\right)}}_{IV} \underbrace{-\nu\overline{\left(\frac{\partial u_i}{\partial x_j}+\frac{\partial u_j}{\partial x_i}\right)\frac{\partial u_j}{\partial x_i}}}_{V} \qquad \ldots.(3.2a)$$

where terms I to V are as described in 3.3.2.

Equation 3.2a is non-dimensionalised in a similar manner to that for mean flow and turbulent fluctuations. Where mean flow quantities or their gradients are involved, the characteristic scales $\bar{U}_o$, z_o, and ρ_o will be used. However, where the turbulent fluctuations are involved, the choice of characteristic dimensions depends, as pointed out earlier, on the wave number range of interest in the turbulent energy spectrum.

It is assumed first that Reynolds number is high enough for an inertial subrange to exist in the energy spectrum, and that atmospheric turbulence is approximately isotropic at high wave

numbers. Hinze (1959) states that the range of energy containing eddies is characterised by ε, ν and t, or by ε and t alone if Equation 2.40 is satisfied. If further an equilibrium boundary layer is postulated, t should not appear, and this region will be characterised solely by ε. The universal equilibrium range is characterised by ε and ν, and if equation 2.40 is satisfied, solely by ε in the inertial subrange. Below the range of energy containing eddies Hinze defines the "medium range", characterised by ε and K_M. This range is associated with generation of turbulence.

Length and velocity scales may now be formulated, characteristic of the ranges of the spectrum important in the terms of Equation 3.2a. Length and velocity scales L and V are postulated, so that

$$L_{K_M} = \left(\frac{K_{Mo}^3}{\varepsilon}\right)^{\frac{1}{4}} \qquad \ldots.(3.21)$$

$$V_{K_M} = (K_{Mo}\varepsilon)^{\frac{1}{4}} \qquad \ldots.(3.22)$$

$$L_\nu = \left(\frac{\nu^3}{\varepsilon}\right)^{\frac{1}{4}} \qquad \ldots.(3.23)$$

$$V_\nu = (\nu\varepsilon)^{\frac{1}{4}} \qquad \ldots.(3.24)$$

Using L_ν and V_ν in terms IV and V of equation 3.2a where viscous effects dominate, and elsewhere L_{K_M} and V_{K_M}, Equation 3.2a is non-dimensionalised to give :

$$\frac{\partial}{\partial t}\frac{q^{2'}}{2} + \frac{\partial}{\partial x_i'}\frac{\bar{U}_i'\overline{q^{2'}}}{2}\left(\frac{V_{K_M} z_o}{L_{K_M} \bar{U}_o}\right)$$

I

$$= -\frac{\partial}{\partial x_i'}\overline{u_i'\left(\frac{p'}{\rho'} + \frac{q^{2'}}{2}\right)} - \overline{q^{2'}}\frac{\partial \bar{U}_i'}{\partial x_i'}\left(\frac{V_{K_M}}{L_{K_M}}\frac{z_o}{\bar{U}_o}\right)$$

II III a.

$$+ \quad K_M' \left(\frac{\partial \bar{U}_i'}{\partial x_j'} + \frac{\partial \bar{U}_j'}{\partial x_i'} \right) \cdot \frac{\partial \bar{U}_j'}{\partial x_i'} \cdot (1 - \delta_{ij}) \cdot \left(\frac{V_{K_M}^{\ 3} \ z_o^{\ 2}}{L_{K_M} \bar{U}_o^{\ 2} \ K_{Mo}} \right)$$

III b.

$$+ \left[\frac{\partial}{\partial x_i'} \overline{u_j' \left(\frac{\partial u_i'}{\partial x_j'} + \frac{\partial u_j'}{\partial x_i'} \right)} - \overline{\frac{\partial u_j'}{\partial x_i'} \left(\frac{\partial u_i'}{\partial x_j'} + \frac{\partial u_j'}{\partial x_i'} \right)} \right] \cdot \left(\frac{V_{K_M}^{\ 3} \ L_\nu^{\ 2}}{L_{K_M} \ V_\nu^{\ 2} \nu} \right)$$

IV V ....(3.25)

In the production term III of Equation 3.25, the term

$$\overline{u_i^{\ 2}}, \frac{\partial \bar{U}_i'}{\partial x_i'},$$

IIIa, has been taken separately since the Boussinesq expression fails for i = j. In isotropic turbulence, term IIIa becomes zero. In the general case shown, separation of term III into IIIa and IIIb introduces no further similarity parameters.

From Equation 3.25 it can be seen that three similarity parameters apparently evolve, which must be kept the same in both atmospheric and model flows: i.e.

$$\frac{V_{K_M} z_o}{L_{K_M} \bar{U}_o} \rightarrow \frac{\varepsilon^{\frac{1}{2}} z_o}{\bar{U}_o K_{Mo}^{\frac{1}{2}}}$$

$$\frac{V_{K_M}^{\ 3} \ z_o^{\ 2}}{L_{K_M} \bar{U}_o^{\ 2} K_{Mo}} \rightarrow \left(\frac{\varepsilon^{\frac{1}{2}} z_o}{\bar{U}_o K_{Mo}^{\frac{1}{2}}} \right)^2$$

$$\frac{V_{K_M}^{\ 3} \ L_\nu^{\ 2}}{L_{K_M} V^2 \nu} \rightarrow \left(\frac{K_M}{L_{K_M} V_{K_M}} \right) \left(\frac{L_\nu V_\nu}{\nu} \right) \rightarrow 1.$$

(from Equations 3.21 - 3.24).

Interpreted in terms of equations 3.21 - 3.24, the first two parameters turn out to be the same (since products and quotients of similarity parameters are also similarity parameters), and the last parameter collapses to 1.

These parameters are now considered separately :-

(i) $\dfrac{\varepsilon^{\frac{1}{2}} z_o}{\bar{U}_o K_{Mo}^{\frac{1}{2}}}$ or $\dfrac{\varepsilon z_o^2}{\bar{U}_o^2 K_{Mo}}$:

This parameter is able to be represented in several forms. Making use of the previously derived similarity parameters:

$$\frac{\sqrt{\overline{u_o^2}}}{\bar{U}_o}, \quad \frac{L_{u_{x_o}}}{z_o} \text{ and } \frac{\bar{U}_o z_o}{K_{Mo}},$$

the parameter $\dfrac{\varepsilon z_o^2}{\bar{U}_o^2 K_{Mo}}$ could equally well be represented as:

$$\frac{\varepsilon L_{u_{x_o}}^2}{\sqrt{\overline{u_o^2}}\, K_{Mo}} \quad \text{or} \quad \frac{\varepsilon L_{u_{x_o}}}{\left(\sqrt{\overline{u_o^2}}\right)^3}, \text{ etc.}$$

The second of these latter two forms relates directly to an energy supply (and dissipation) expression for the universal equilibrium range, given by Hinze (1959) for isotropic turbulence. Hinze stated that Equation 2.38 was equal to

$$\varepsilon(t) = -\frac{3}{2}\frac{du'^2}{dt} = C.\frac{u'^3}{\ell_e} \qquad \ldots.(3.26)$$

(C is a constant O(1)).

From Equation 3.26 it can be seen that

$$\frac{\varepsilon \ell_e}{u'^3} = \text{constant} \qquad \ldots.(3.27)$$

Remembering that $\ell_e \propto L_{u_x}$ (Hinze, 1959), the condition given by Equation 3.27 is contained in the similarity parameter

$$\frac{\varepsilon L_{u_{x_o}}}{\left(\sqrt{\overline{u_o^2}}\right)^3},$$

which must be kept the same in both model and full scale flows.

Nemoto (1961) made a similarity analysis which led to the similitude :

$$\frac{d_m}{d_a} = \frac{\varepsilon_a \bar{U}_{om}^3}{\varepsilon_m \bar{U}_{oa}^3} \qquad \ldots.(3.28)$$

This is simply another form of the similarity condition given by the parameter

$$\frac{\varepsilon z_o^2}{\bar{U}_o K_{Mo}} ,$$

taken together with the parameter $\frac{\bar{U}_o z_o}{K_{Mo}}$.

Armitt and Counihan (1968) also used a similitude involving ε. They assumed a logarithmic mean velocity profile so that the turbulent energy production was

$$\varepsilon = \frac{\tau}{\rho}\frac{d\bar{U}}{dz} \quad \text{(horizontally homogeneous flow).}$$

$$= \frac{u_*^3}{Kz} .$$

In the equilibrium flow this must, in isotropic turbulence, be equal to the dissipation, so that

$$\varepsilon = 15\nu \frac{u'^2}{\lambda_g^2} \quad \text{(Hinze, 1959)} \qquad \ldots.(3.29)/$$

Taking

$$\frac{u_*^3}{Kz} = 15\nu \frac{u'^2}{\lambda_g^2} \text{ in the shear flow, and}$$

assuming constancy of

$$\frac{z}{z_o} \text{ and } \frac{\sqrt{\overline{u_o^2}}}{\bar{U}_o} , \text{ Armitt and Counihan obtained:}$$

$$\frac{Re_m \lambda_m^2}{d_m^2} = \frac{Re_a \lambda_a^2}{d_a^2} \qquad \ldots.(3.30)$$

$$\text{Where } Re = \frac{\bar{U}_o z_o}{\nu} , \text{ say.}$$

This similitude implies the same condition as one proposed by Cermak and Arya (1970), for scaling the small scale, high wave number eddies. Cermak and Ayra suggest that the small scale motion in model and full scale should be related by :

$$\frac{\varepsilon L_{d_o}^{\,2}}{\overline{u_o^2}\,\nu} = \text{Constant.} \quad \text{(Referred to the reference height).} \qquad \ldots.(3.31)$$

L_d is simply termed a "length scale", but is such that

$$\frac{L_{d_m}}{L_{d_a}} = \frac{d_m}{d_a}, \text{ i.e. } \frac{L_{d_m}}{L_{d_a}} \text{ is equivalent to}$$

the linear scaling, whence from equation 3.20:

$$\frac{L_{d_m}}{L_{d_a}} = \frac{z_{o_m}}{z_{o_a}} \qquad \ldots.(3.32)$$

Further, it will be recalled that in the similarity analysis for the turbulent fluctuations, the similarity parameter

$$\frac{\sqrt{\overline{u_o^2}}}{\bar{U}_o} \quad \text{evolved.}$$

$$\therefore \quad \frac{\overline{u_{o\,m}^2}}{\bar{U}_{o\,m}^2} = \frac{\overline{u_{o\,a}^2}}{\bar{U}_{o\,a}^2} \qquad \ldots.(3.33)$$

Substituting from Equations 3.32 and 3.33 into 3.31:

$$\frac{\varepsilon z_o^{\,2}}{\bar{U}_o^2\,\nu} = \text{constant} \qquad \ldots.(3.31a)$$

This is identical to the parameter $\dfrac{\varepsilon z_o^{\,2}}{\bar{U}_o^2 K_{Mo}}$,

except that the molecular viscosity appears in place of the eddy viscosity. In the present analysis

$$\frac{\varepsilon z_o^{\,2}}{\bar{U}_o^2\,\nu}$$

would have evolved only if the characteristic viscous length and velocity scales L_ν and V_ν, had been used throughout. It seems, however, that

$$\frac{\varepsilon z_o^{\,2}}{\bar{U}_o^2 K_{Mo}}$$

is more realistic when scaling the energy containing

eddies, inertial subrange, and eddies of wave number similar to the turbulence generation wave numbers.

(ii) $\left(\frac{K_M}{L_{K_M} V_{K_M}}\right) \left(\frac{L_\nu V_\nu}{\nu}\right)$:-

This parameter is simply the product of two turbulent Reynolds numbers, characteristic of the lower wave number energy containing eddies and the higher wave number viscous dissipation eddies respectively. By definition of L_{K_M}, V_{K_M}, L_ν and V_ν, both these are equal to unity and the scaling parameter degenerates to unity and therefore vanishes from the similarity conditions.

If the characteristic lengths and velocities for the similitude had been selected differently, the similarity parameter relating to the viscous effects would still appear, e.g. For the energy containing eddies, let the characteristic length & velocity be $L_{u_{x_o}}$ and $\sqrt{\overline{u_o^2}}$. For the viscous dissipation range of eddies, let the characteristic length and velocity be λ_{go} and $\sqrt{\overline{u_o^2}}$. Then, the similarity parameters obtained turn out to be products or quotients of

$$\frac{\sqrt{\overline{u_o^2}}}{\bar{U}_o}, \quad \frac{L_{u_{x_o}}}{z_o} \quad \text{and} \quad \frac{\bar{U}_o z_o}{K_{Mo}},$$

except for the one relating to the viscous effects, which becomes

$$\frac{\lambda_{go}\sqrt{\overline{u_o^2}}}{\nu} \cdot \frac{\lambda_{go}}{L_{u_{x_o}}}$$

This last similarity parameter is the product of a turbulent Reynolds number based on the molecular viscosity, and the ratio of microscale to integral scale of turbulence at the reference height. It will be noticed that the parameters

$$\frac{\lambda_{go}\sqrt{\overline{u_o^2}}}{\nu} \quad \text{and} \quad \frac{\lambda_{go}}{L_{u_{x_o}}}$$

are the same as those that occur in the similarity analysis of the momentum equation for the turbulent fluctuations if the viscous dissipation range of wave numbers is considered important.

Thus the similarity analysis of the turbulence-energy equation produces the additional similarity parameters

$$\frac{\varepsilon z_o^2}{\bar{U}_o^2 K_{Mo}}, \quad \text{or} \quad \frac{\lambda_{go}\sqrt{\overline{u_o^2}}}{\nu} \quad \text{and} \quad \frac{\lambda_{go}}{L_{u_{x_o}}}$$

depending on the choice of characteristic scaling dimensions.

(d) Summary of Similarity Parameters:

Similarity analysis of the equations of conservation of mass and momentum for the mean flow, and equations of conservation of momentum and energy for the turbulent fluctuations, produces the following similarity parameters for the neutrally stable, fully aerodynamically rough, atmospheric surface layer:

For mean flow similarity:

$$\frac{z}{L_o}, \quad \frac{\bar{U}_o L_o}{K_{Mo}} \qquad \text{with } L_o = z_o \text{ for the neutrally stable flow.}$$

For similarity of the turbulent fluctuations:

$$\frac{\sqrt{\overline{u_o^2}}}{\bar{U}_o^2}, \quad \frac{L_{u_{x_o}}}{z_o}, \quad \frac{\varepsilon z_o^2}{\bar{U}_o^2 K_{Mo}}$$

$\left\{ \frac{\varepsilon z_o^2}{\bar{U}_o^2 K_{Mo}} \right.$ can be equally well and possibly better, represented as: $\frac{\varepsilon L_{u_{x_o}}}{\left(\sqrt{\overline{u_o^2}}\right)^3}$ or $\frac{\varepsilon z_o^2}{\overline{u_o^2} K_{Mo}}$ or $\left. \frac{\varepsilon L_{u_{x_o}}^2}{\overline{u_o^2} K_{Mo}} \right\}$.

The latter group should include

$$\frac{\lambda_{go}\sqrt{\overline{u_o^2}}}{\nu} \quad \text{and} \quad \frac{\lambda_{go}}{L_{u_{x_o}}}$$

when the dissipation range of wave numbers is important.

Note: For simulation of Coriolis effects in the mean flow, Cermak (1973) gives the similarity parameter

$$\frac{L_o \omega_o}{\bar{U}_o}$$

This cannot be held the same between wind tunnel and atmosphere. (ω_o is a reference angular velocity).

It must be re-emphasised that the above similarity parameters, held the same in both model and full scale atmospheric flows, are necessary but not sufficient conditions for exact flow similarity, which cannot be achieved between wind tunnel and atmosphere because of the different boundary conditions for the two flows.

3.4 PRACTICAL INTERPRETATION AND SUMMARY OF WIND MODELLING CRITERIA

The similarity parameters derived from the generalised flow equations in 3.3.3 are themselves generalised. For instance, similarity of $\frac{\sqrt{u_o^2}}{\bar{U}_o}$ implies similarity of $\frac{\sqrt{u_o^2}}{\bar{U}_o}$, $\frac{\sqrt{v_o^2}}{\bar{U}_o}$ and $\frac{\sqrt{w_o^2}}{\bar{U}_o}$.

Similarity of $\frac{L_{u_{x_o}}}{z_o}$ implies similarity of each of $\frac{L_{u_{i x_j o}}}{z_o}$ and so on.

Below, these similarity parameters are interpreted in terms of quantities measurable in the wind tunnel:

(a) z/z_o: As explained in 3.3.3, this parameter simply calls for linear scaling of all features of the atmospheric flow in the same ratio as the model:prototype scale, d_m/d_a, used in model tests.

So, $\frac{z_{om}}{z_{oa}} = \frac{d_m}{d_a} = \frac{z_{ref_m}}{z_{ref_a}}$, etc.

(b) $\frac{\bar{U}_o z_o}{K_{Mo}}$: This is a turbulent mean flow Reynolds number, and relates to the production of turbulence by the action of Reynolds stress on the mean velocity gradient. From the discussion of 3.3.2, it is seen that this parameter requires correct scaling of :

(i) mean velocity profile, hence $\frac{d\bar{U}}{dz}$.

(ii) Reynolds stress profile $-\rho\overline{uw}_z$.

The eddy viscosity cannot be simply measured since it is a mathematical device, used in analogy with the molecular viscosity, ν. A better idea of its meaning is perhaps obtained if eddy viscosity is expressed in terms of the Prandtl mixing length, ℓ, and the mean velocity gradient:

e.g. $$K_M = \ell^2 \left|\frac{d\bar{U}}{dz}\right| .$$

The mixing length appears to be quite closely related to the integral length scale of turbulence. For instance in the atmosphere,

$$L_{w_x} \simeq 0.4z \qquad \ldots.(2.62)$$

and in the Prandtl derivation of the logarithmic mean velocity profile:

$$\ell = 0.4z.$$

Hence in the parameter

$$\frac{\bar{U}_o z_o}{K_{Mo}}$$

K_{Mo} suggests correct scaling of the mean velocity gradient (as deduced earlier) and length scales of turbulence. The importance of the similarity parameter

$$\frac{\bar{U}_o z_o}{K_{Mo}}$$

is probably greatest in the lowest ~ 30% of the boundary layer, where most of the turbulent energy production occurs. (See Hinze, 1959, Fig.7.21).

(c) $\frac{\sqrt{\overline{u_o^2}}}{\bar{U}_o}$: This parameter is simply a turbulent intensity scaling parameter whose function was given in 3.3.3(b).

(d) $\frac{L_{u_{x_o}}}{z_o}$: This parameter indicates that integral length scales of turbulence must be scaled down according to the linear scaling ratio.

i.e. $$\frac{L_{u_{x_{om}}}}{L_{u_{x_{oa}}}} = \frac{z_{om}}{z_{oa}} = \frac{d_m}{d_a} \qquad \ldots.(3.20)$$

This applies to each of the nine integral scales $L_{u_{ix_j}}$.

Equation 3.20 is of great importance in scaling down the energy containing eddies in the wind's turbulence. It may also be interpreted as a requirement that the distribution of turbulent energy across the spectrum wave number range (i.e. spectrum shape) be the same in both model and full scale flows. It was noted in 2.5.6 and 2.5.9 that in practice length scale estimates are often obtained from the peak of the energy spectrum. Hence correct scaling of spectrum shape and integral length scales are mutually dependent requirements.

(e) $\frac{\varepsilon z_o^2}{\bar{U}_o^2 K_{M_o}}$: This similarity relates to production of turbulent energy and its transfer through the spectrum frequency range. It requires that the ratio of energy supplies to the universal equilibrium range in the two flows be equal to

$$\frac{\bar{U}_{om}^2 K_{Mom}}{\varepsilon z_{o\,m}^2} \Big/ \frac{\bar{U}_{oa}^2 K_{Moa}}{\varepsilon z_{o\,a}^2}$$

or alternatively

$$\frac{\left(\sqrt{\overline{u_o^2}}\right)_m^3}{\varepsilon L_{u_{x_{om}}}} \Big/ \frac{\left(\sqrt{\overline{u_o^2}}\right)_a^3}{\varepsilon L_{u_{x_{oa}}}} \quad , \text{ etc.}$$

In practical terms it again imposes the requirement of correct energy spectrum shape, and correct profiles of mean velocity, turbulent intensity and Reynolds stress.

(f) $\frac{\lambda_{go} \sqrt{\overline{u_o^2}}}{\nu}$: This parameter, kept the same between model and full scale flows, implies that for flows of the same turbulent intensity (a requirement already established), the microscale must be the same at the same height (correctly scaled) in both flows.

In homogeneous isotropic turbulence:

$$\frac{1}{\lambda_g^2} = -\frac{1}{2}\left(\frac{\partial^2 g}{\partial y^2}\right)_{y=o}$$

where g is the lateral correlation coefficient.

Evaluation of

$$\left(\frac{\partial^2 g}{\partial y^2}\right)_{y=o}$$

requires extremely accurate measurement of g at small separations, and in the wind tunnel a simpler approximate estimate of λ_g could be obtained by considering similarity of k_d^{-1}, where k_d could be taken as that wave number where the slope of the spectrum curve $nS(n)$ vs. k (plotted log/log) has increased significantly above -2/3, e.g. that k where the curve slope equals -2.

(g) $\frac{\lambda_{go}}{L_{u_{x_o}}}$: This parameter simply requires the same ratio between integral and microscale of turbulence in the model and full scale flows. This is one parameter that cannot be maintained constant between wind tunnel and atmosphere. λ_g is much the same in the two flows, but L_{u_x} is very much smaller (2 to 3 orders of magnitude) in the wind tunnel than in the atmosphere. This is manifested as a much smaller inertial subrange in the wind tunnel model flow energy spectrum, than in the atmospheric spectrum. In practice, checks may be applied to see whether this scale effect, introduced by linearly scaling down the energy containing eddies, has an undesirable effect on the wind tunnel flow. In the wind tunnel flow it is important that the range of energy containing eddies, characterised by k_p, is well separated from the dissipation range, characterised by k_d, so that unwanted viscous effects do not occur in the range of energy containing eddies. It is therefore required that $k_p << k_d$. To ensure that $k_p << k_d$ in the tunnel, the turbulent Reynolds number must be sufficiently high for a definite inertial subrange, as shown by a -5/3 spectrum curve slope, to exist within the equilibrium range. An extended region of -5/3 slope indicates wide separation between k_p and k_d. Batchelor's (1953) criterion for the existence of an inertial subrange, given in 2.5.6, is :

$$Re_{\ell_e}^{\frac{3}{8}} = \left(\frac{u'\ell_e}{\nu}\right)^{\frac{3}{8}} = \left(\frac{u'}{\nu k_p}\right)^{\frac{3}{8}} >>> 1 \qquad \ldots.(2.40)$$

For instance, in the atmosphere, 10m off the ground in a rural boundary layer with $\bar{U} = 15$m/sec,

typically $u' = 2.5$m/sec

$k_p = 0.0016\text{m}^{-1}$

$\nu = 1.47 \times 10^{-5}\ \text{m}^2/\text{sec}$

$\therefore \quad Re_{\ell_e} \simeq 10^8$

$\therefore \quad Re_{\ell_e}^{\frac{3}{8}} \simeq 10^3 >>> 1.$

In the wind tunnel k_p is scaled down by the linear scaling ratio. So, if a 1:400 scale simulation is considered with $\bar{U}$, u' and ν as in the atmosphere, then

$Re_{\ell_e} \simeq 250{,}000$

$\therefore \quad Re_{\ell_e}^{\frac{3}{8}} \simeq 106 >> 1.$

Hence in the wind tunnel a substantial inertial subrange should still exist, and viscous effects cause no problems.

Templin (1969) used a slightly different but closely related criterion for the existence of the inertial subrange:

$$\frac{k_d}{k_p} = 0.015 \left(\frac{u'}{\nu k_p}\right)^{\frac{3}{4}} = 0.015\ Re_{\ell_e}^{\frac{3}{4}} \qquad \ldots.(3.34)$$

The larger k_d/k_p, the larger the extent of the inertial subrange should be. e.g. using the data from the above example, in the atmospheric flow $k_d/k_p \simeq 15670$, while in the wind tunnel $k_d/k_p \simeq 175$. Thus the inertial subrange, which typically extends about 4 orders of magnitude along the k abscissa, in the atmosphere, tends to extend only about 2 orders of magnitude along the k abscissa in the wind tunnel. In very small scale simulations, e.g. 1:5000 scale, the inertial subrange may be as short as one order of magnitude on k, and unwanted viscous effects may occur.

Summary of Wind Modelling Criteria (for neutrally stable flow)

1. General Requirements of the Wind Tunnel Flow:

(i) Fully aerodynamically rough flow $\frac{u_* z_o}{\nu} > 2.5$

(ii) Horizontally homogeneous flow (approximate)

(iii) Freedom from streamwise pressure gradient.

2. Similarity Parameters:

The following parameters should be the same in the wind tunnel and in the atmosphere :

$$\frac{z}{z_o}, \frac{\bar{U}_o z_o}{K_{Mo}}, \frac{\sqrt{u_o^2}}{\bar{U}_o}, \frac{L_{u_{x_o}}}{z_o}, \frac{\varepsilon z_o^2}{\bar{U}_o^2 K_{Mo}}, \frac{\lambda_{go}\sqrt{u_o^2}}{\nu}, \frac{\lambda_{go}}{L_{u_{x_o}}}.$$

These parameters are not all independent, and the first four may be taken as the major similarity parameters.

In practice, the above similarity parameters may be interpreted as requirements of similarity of the following, as functions of altitude, between wind tunnel and atmosphere:

(i) mean velocity $\frac{\bar{U}}{u_*} = f\left(\frac{z}{z_o}\right)$

(ii) turbulent intensity of each velocity component.

(iii) integral scales of turbulence.

(iv) microscales of turbulence (less important).

(v) correlations between turbulent velocity components particularly Reynolds stress $-\rho\overline{uw}$.

(vi) Energy spectra of turbulence for each velocity component.

In the flow modelling process it is attempted to set the above quantities equal to the mathematical models set up in Chapter 2, suited to the terrain of interest. The criteria (i) to (vi) above, are not independent of each other and it is difficult to say whether any particular criteria are of overriding importance. It has been suggested, for instance, (Vickery, 1965) that in certain applications, correctness of the turbulent energy spectra is most important, while mean velocity profile similarity is relatively unimportant, e.g. dynamic excitation of a tall flexible tower. In an equilibrium rough wall boundary layer, correctness of the mean velocity profile and shear stress profile is indicative that

the turbulence generation, dissipation and diffusion processes are similar to those in the full scale case, and these would be important criteria in topographical modelling work.

It would be expected that for certain wind tunnel modelling problems, generation of a flow with substantially correct turbulence structure, but poor mean velocity profile, would be acceptable. The relative importance of various modelling criteria can really only be determined by a series of experiments where, as far as possible, one similarity parameter in the flow is varied at a time, while the others are held constant.

3.5 REVIEW OF PREVIOUS ATMOSPHERIC BOUNDARY LAYER SIMULATIONS:

In this section a selection of previous atmospheric boundary layer simulation work is briefly reviewed. Where the simulation was attempted predominantly with wire screens or coarse bar grids, it is reviewed in Chapter 4, which deals purely with use of grids and screens to generate atmospheric boundary layer mean velocity profiles and turbulence. Where possible, the following details have been included in each case reviewed below :

(i) Flow speed and dimensions of the tunnel working section.
(ii) Particular modelling purpose, if any, for the simulated boundary layer.
(iii) Flow modelling criteria, and flow measurements made.
(iv) Linear scale of the simulation, and any particular good or bad features of the flow.

Cases are considered chronologically, except where similar work by the same author appears in different years.

Jensen (1958), Jensen & Franck (1963):

In this work tests were carried out in an open circuit tunnel with a 5.5m long working section, of 0.6m x 0.6m cross section. In the early experiments, which were used to verify Jensen's model law, the wind shelter effect of fences and groups of houses was examined, together with wind pressures on the walls and roof of a house. The later publication also includes smoke dispersion tests and more detailed wind pressure measurements from different building configurations and different levels of wind tunnel turbulence.

The modelling criteria observed were the requirement of fully aerodynamically rough flow, a logarithmic mean velocity profile of the Rossby-Montgomery form (Eqn. 2.14), and obedience to the model law proposed by Jensen (Eqn. 3.13). The relative unimportance of a molecular viscosity Reynolds number in atmospheric flow phenomena is pointed out, and the model tests verify the model law quite clearly. Pure boundary layer growth over various surface roughnesses was used to generate the model atmospheric boundary layer. Linear scaling of models was ~ 1:100, and with this large scale, exact surface layer similarity was probably not achieved.

Measurements were generally restricted to mean velocity and pressure. Sample results from these model tests are included in Chapter 9.

Strom & Kaplin (1960):

Here tests were carried out in a 40 ft long working section, of 7 ft wide x 3 ft 6 in high cross section. The first 25 ft of the working section was occupied by an electric heating grid, a variably spaced grid of flat plates with attached roughness elements, and finally floor roughness. Thermal stratification of the atmosphere had to be modelled as the purpose of the experiments was a study of smoke plume dispersion. The linear scale of the chimney model used was 1:96 and Froude number similarity was assumed for scaling velocities, the maximum tunnel velocity being about 5 m/sec. Temperature gradients were scaled according to

$$\left(\frac{dT}{dz}\right)_a = \frac{1}{96}\left(\left(\frac{dT}{dz}\right)_m + \Gamma\right) - \Gamma$$

A mean velocity profile of power law form was used with α ranging from 0.14 to 0.31 depending on flow stability. Agreement between the model and full scale smoke plume movement was only fair, and the authors conclude that closer attention needed to be paid to the turbulence generated by the roughness elements on the flat plate grid.

Nemoto (1961):

The first part of this work involves a similarity analysis of the Navier-Stokes momentum equations describing the fully rough atmospheric surface layer flow. The similarity parameters that evolve place the same requirements on the model flow as those summarised in 3.4. Nemoto

places a great deal of emphasis on the scaling law given in Eqn. 3.28 and states that under certain conditions this law will become

$$\frac{\bar{U}_{om}}{\bar{U}_{oa}} = \left(\frac{d_m}{d_a}\right)^{\frac{1}{3}} \qquad \ldots.(3.35)$$

The second part of the work compares wind tunnel and atmospheric measurements to verify the mean velocity profile similarity law

$$\frac{\bar{U}}{u_*} = f\left(\frac{z}{z_o}\right)$$

The model tests were made in a 1.5m throat diameter, Gottingen-type wind tunnel with a speed range of 0.5 - 60 m/sec. The simulated velocity profiles were generated over a flat plate roughened with wood wool of ~ 35mm thickness.

The third part of Nemoto's paper discusses three model tests used to verify the law given in Eqn. 3.35. The third of these was a distorted scale 1:3333 vertical scale, 1:10000 horizontal scale test and is not discussed below. The first test was a 1:600 linear scale test of a model of Enoshima Island which receives a prevailing wind off open sea. Various wood wool floor roughness configurations were used to achieve mean velocity profile and turbulence intensity similarity between model and full scale flows; however, energy spectra and integral scale measurements showed that the scale of the turbulence structure tended to be too small, particularly near the ground.

The second test was simply a comparison of velocity profiles downstream of model fences (ϕ = 0) of different height, and profiles were found to become similar when Eqn 3.35 was satisfied. The result was dependent, however, on the arrangement of turbulence generating trip fences placed upstream of the main fence.

In general, Nemoto's tests provide verification that the similarity parameters of 3.4 must be satisfied for flow similarity to occur, but the verification of Eqn 3.35 was somewhat doubtful. In each case (as Nemoto himself pointed out) a prerequisite for satisfaction of Eqn 3.35 was similarity of mean velocity profiles, turbulent intensity profiles, energy spectra and integral scales of turbulence. If $\varepsilon_m = \varepsilon_a$, Eqn 3.35 should then be satisfied automatically, and is more a consequence of similarity than a major prerequisite. Nemoto's results do in fact indicate that flow similarity exists at other values of $\bar{U}_o$ than that satisfying Eqn 3.35.

Plate & Quraishi (1965):

In this work, mean velocity distributions inside and above a model crop were investigated. Experiments were carried out in the Colorado State University Wind tunnel, which has a total working section length of 96 ft and a cross-section of approximately 6 ft x 6 ft. Maximum flow speed in this tunnel ranges up to 130 ft/sec. The model crops consisted of strips of flexible plastic 0.25 in wide, 0.0075 in thick and 4 in high fastened to wooden strips on the floor of the wind tunnel. The model velocity profile for the flow above the crops was taken to be the displacement height form of the logarithmic profile (Eqn 2.15), or a power law form as follows :

$$\frac{\bar{U}_z}{\bar{U}_\infty} = \left(\frac{z - h}{\delta - h}\right)^{\alpha} \qquad h = \text{crop height}$$

The tests were made at speeds $\bar{U}_\infty$ = 20 and 40 ft/sec.

The tests showed that at some distance X_o downstream from the start of the crop roughness the velocity profiles were fully developed, and became similar both inside and above the roughness. Experiments with other surface roughness forms, e.g. wooden pegs, showed that X_o depended on the roughness form. Experimental data for the plastic strip model crop compared favourably with field measurements inside crop canopies, but for a crop height h, velocities $\bar{U}/\bar{U}_h$ at a given height z/h tended higher in the wind tunnel tests, indicating that density of the crops must be carefully modelled. No mention is made in this work of simulating the atmospheric flow upstream of the area where the crops were modelled.

Armitt (1966), Armitt & Counihan (1968):

This work was concerned with the generation of a neutrally stable model atmospheric boundary layer of 1/7 power law mean velocity profile in the wind tunnel, using a combination of 'step change' and boundary layer growth techniques. The earlier work by Armitt was a pilot study in a 1 ft square cross-section tunnel and the flow was approximately 1:6000 linear scale. The boundary layer generating equipment used in this work was more or less directly scaled up to give a linear scaling for the later work of 1:250. In the preamble to the experimental report a discussion of flow processes in the atmosphere is given, and criteria for flow similarity used, were similarity of profiles of mean velocity, turbulent intensities, Reynolds stresses, integral and micro scales of turbulence, and similarity of energy spectra. The condition of Eqn. 3.30

was also used for scaling the small scale motion. In the later work the CERL. Low Speed Wind Tunnel (England) was used. This tunnel has a 15 ft x 5 ft cross section, 36 ft long, working section, with flow speed 35 ft/sec. The boundary layer generating apparatus consisted of an initial 6 in high fence immediately followed by four triangular vortex generators 4 ft high and 4 ft apart, spaced about the longitudinal centre line of the tunnel with an alternating incidence $+10^{o}$, -10^{o}, etc. and the hypotenuse as the leading edge. Surface roughness downstream of the vortex generators was simulated using LEGO baseboard and blocks, the blocks measuring 1¼ in x 5/8 in x 3/8 in. In later work a 2 in diameter tube was positioned 25 in above the vortex generators to attempt to cure a deficit in turbulence intensity in the outer part of the boundary layer. Measurements were made of longitudinal, lateral and vertical turbulent intensities and spectra, $-\rho\overline{uw}$ Reynolds stress and mean velocity profiles, 6 ft and 12½ ft downstream of the vortex generator trailing edges. Profiles of mean velocity and turbulent intensity were fair, but lateral uniformity was poor and Reynolds stress values tended high, e.g.

$$-\frac{\overline{uw}}{\bar{U}_{\infty}^{2}} = 0.005$$

at the more downstream position. Energy spectra showed reasonable agreement with the Davenport and Harris models. It was suggested that improved performance of the simulation might be obtained by setting the vortex generators to a lower incidence and fitting a second, lower set of vortex generators downstream of the first.

Counihan (1969 a and b):

The work described in these papers is an extension of the earlier work by Armitt and Counihan (1968), in which vortex generators in the form of an elliptic wedge were used in place of the earlier triangular vortex generators. The intention of the elliptic wedge vortex generators was to give a more evenly graded mean flow momentum deficit in the boundary layer and to remove the asymmetry left in the flow by the triangular vortex generators. The aim of both types of vortex generator was to produce a flow with turbulent intensity decreasing with height above the ground, in the manner of the atmospheric boundary layer, but it does not seem to have been recognised that the system used tends to produce decreasing integral scale of turbulence with height, contrary to the requirements of the atmospheric boundary layer set out in 2.5.9. Counihan's later experiments were carried out in the CERL boundary layer wind tunnel which has a working

section 24 in wide x 7.3 in high x 5 ft long, and the test free stream velocity was about 30 ft/sec. It was aimed to produce a 6 in deep boundary layer in a distance of three to four times the boundary layer depth. The final boundary layer generating arrangement was as follows: (See Fig. 3.1) - an initial 3/4 in high trip fence with a castellated top was fitted 5 in upstream of the leading edge of the vortex generators. The side view of the elliptic wedge was a quarter ellipse with major axis twice the minor axis, and the 6 in half major axis as trailing edge. In plan view the section was wedge shaped, with the apex as the leading edge and an included angle of 12° for the wedge. The elliptic wedge vortex generators were spaced at 3 in between centre lines and at zero incidence to the flow, to avoid introducing asymmetry in the flow. LEGO baseboard surface roughness was fitted downstream of the vortex generators.

Measured profiles of mean velocity, u', v' and w' turbulent intensities and $-\rho\overline{uw}$ Reynolds stress were to a linear scale of about 1:2000 with good profile shape and lateral uniformity. Turbulent intensity levels $\frac{u'}{\bar{U}_{\infty}}$ may have been a little low at the outside of the boundary layer, where they were less than 1%. Gust spectra showed good shape similarity with the Davenport and Harris atmospheric models, but estimates of integral scale from the spectra and auto-correlation measurements showed that the scale of the turbulence structure in the flow was too small, corresponding to a linear scaling for the simulation of about 1:4000. This must be expected, with the small physical size of the boundary layer generating apparatus and the short downstream flow development distance (furthest downstream measurement station was 27 in from the vortex generator trailing edges). Variation of integral length scale with height was not particularly good, with the correct sort of increase in scale up to $z/\delta \simeq 0.4$, but thereafter a decrease with height.

In general this simulation is quite a good small scale rural atmospheric boundary layer simulation (1/7 power law velocity profile). This simulation would require scaling up by a factor of at least 10 to make it useful for model studies, and in scaling up there is the possibility that unwanted scale effects may arise, such as excessive levels of Reynolds stress. (See 6.4.) Counihan's (1969) u' turbulent intensity profile is compared with results of the present work in Fig. 6.42b (p.289)

Davenport & Isyumov (1967):

This work describes the generation of simulated atmospheric rural and urban boundary layers in the University of Western Ontario Boundary

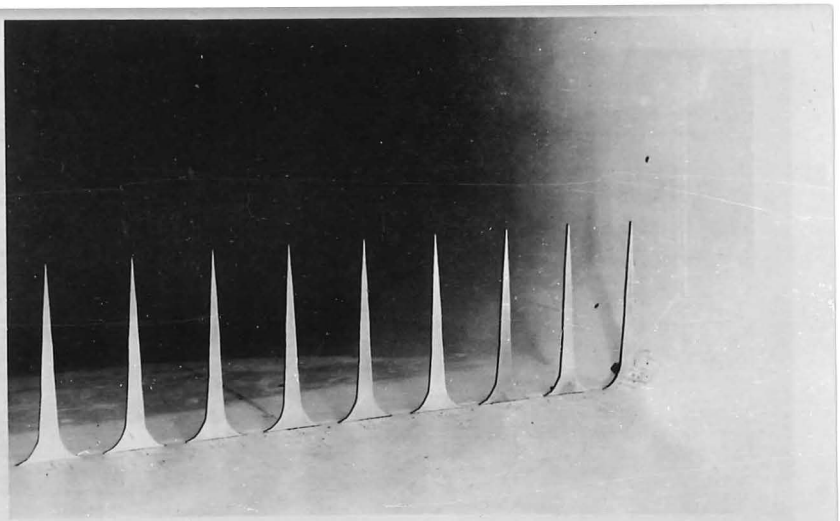

Fig 3.1 MODIFIED HALF-WIDTH SPIRES (After Campbell & Standen, 1969)

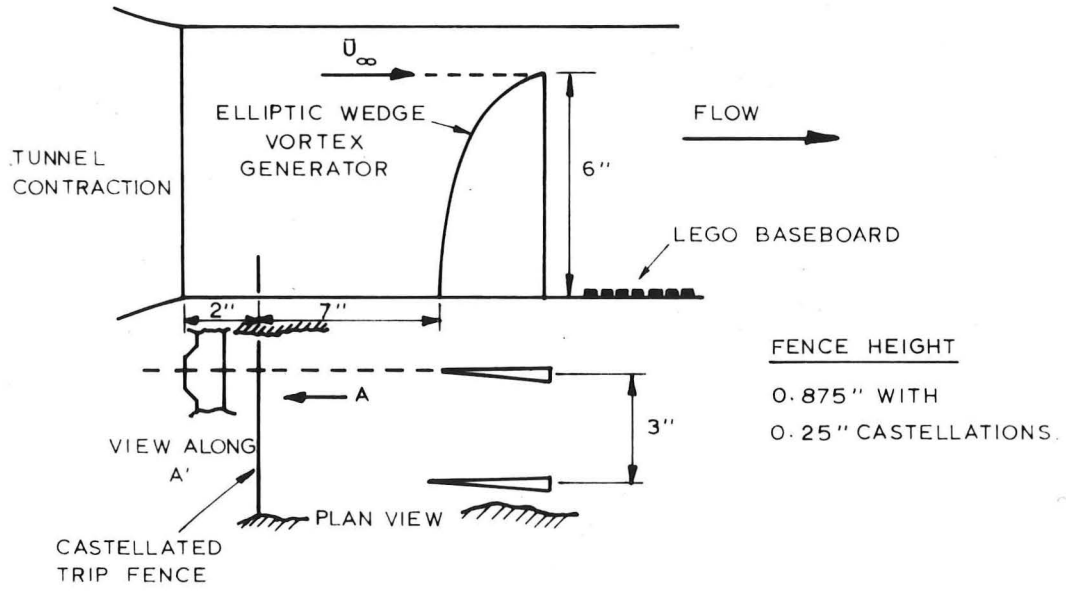

Fig. 3.1 BOUNDARY LAYER GENERATING LAYOUT.
– COUNIHAN (1969)

layer wind tunnel. This tunnel has a working section approximately 80 ft long, 8 ft wide and height variable from 5½ ft at the inlet to 7½ ft at the outlet with speed continuously variable to a maximum of about 50 ft/sec. For the rural boundary layer growth carpet was used for the surface roughness, while for the urban case, rectangular blocks of height varying between 1 in and 4 in were used. Design velocity profiles were 0.16 and 0.36 power law (of the form of equation 2.17) for the rural and urban cases respectively. With pure boundary layer growth, boundary layer thicknesses 68 ft downstream of the inlet were 1¼ ft and 3 ft for the two surfaces, whereas for the desired 1:400 linear scaling for the simulation, boundary layer thicknesses of about 2 ft (rural) and 4 ft (urban) were wanted. A 1 ft high tripping fence introduced at the entrance to the working section to thicken up the boundary layer, excessively increased the turbulence levels in the boundary layer and free stream and was replaced by a 1 ft high grid of horizontal graded round bars. This produced the required boundary layer thickening without excessively increasing turbulence levels. Satisfactory profiles of mean velocity and $\frac{u'}{\bar{U}_z}$ turbulent intensity were obtained to a linear scale of about 1:400, but accompanying gust spectra (u component), while showing good shape similarity to Davenport's atmospheric model spectrum, were linearly scaled about 1:680 and 1:500 respectively for the rural and urban cases. Here again it is seen that the turbulence scale tends to be characteristic of a smaller linear scale than the mean velocity and turbulent intensity profiles. In general Davenport & Isyumov indicate that the simulated boundary layer requires similarity of mean velocity profile, turbulent intensities, probability distributions, spectra and the higher order correlations of the u,v,w, velocity components. The technique used in this work, of almost pure boundary layer growth, must be the most favoured way of generating the model flow, as an approximately equilibrium, horizontally homogeneous flow is more likely to be obtained. The disadvantage is, however, the long working section required. For instance, here the boundary layer was generated in a distance ~ 34 times its height (rural boundary layer, after addition of initial bar grid), whereas that of Counihan (1969), while probably less accurate as an atmospheric model, took only about 4 times the boundary layer height to grow. Some of the turbulent intensity data of Davenport & Isyumov are plotted in Fig.6.42b.

Melbourne & Styles (1967):

In this work, wind tunnel tests were made of model Antarctic station buildings to devise a way of preventing snow drift accumulation and

consequent burying of the buildings. Only a short fetch of the local topography appears to have been modelled upstream of these model buildings and no simulation of the atmospheric boundary layer made. However, in this particular case, where the drifting problem was caused by flow separation around the buildings, the results obtained, which indicated that the buildings should be raised off the ground and their windward faces streamlined, probably showed the correct solution to the problem.

McVehil, Ludwig & Sundaram (1967), Ludwig & Sundaram (1969):

The modelling criteria used in this work are as covered in section 3.4, except that the similarity parameters

$$\frac{\varepsilon z_o^2}{\bar{U}_o^2 K_{Mo}}, \quad \frac{\lambda_{go}\sqrt{\overline{u^2}_o}}{\nu}, \quad \frac{\lambda}{L_{u_{x_o}}}$$

were not explicitly used. In the boundary layer generation experiments carried out, no distinct type of terrain was used as a model, but a fairly rough floor surface was used. The test section of the tunnel used was 22.5 in high (with rough ground installed) x 17 in wide x about 130 in long, and the free stream flow speed for the experiments was about 40 ft/sec. The primary aim of the work was to generate a thick constant stress model atmospheric surface layer over a short distance. The most satisfactory boundary layer generating arrangement was found to be a 2 in high trip fence, followed by a continuous array of four-sided regular pyramids 0.75 in high and 0.75 in along each side of the square base, these pyramids constituting the floor roughness. By matching the fence height and ground roughness, it was hoped to produce an approximately horizontally homogeneous flow over a short distance. In the earlier work, measurements of only mean velocity, u component turbulent intensity and u component energy spectrum were made. The later work included, in addition, measurements of w component intensity and spectrum, and $-\rho\overline{uw}$ Reynolds stress. Measurement stations were located 73.4 and 109.4 in from the trip fence.

Mean velocity profiles approximately followed the logarithmic profile form of Eqn. 2.16, with a displacement of the zero plane of 0.25 in and z_o = 0.02 in. Complete homogeneity of the flow in the streamwise direction was not achieved as z_o increased with downstream distance by about 30% in a distance approximately 9 times the depth of the constant stress layer. The boundary layer depth 109.4 in from the trip fence was about 12 in, with a constant stress depth of about 0.4δ.

The maximum value of the non-dimensional stress $\frac{-\overline{uw}}{\bar{U}_{\infty\,max}^2}$ was about 0.0045, occurring at $z/\delta = 0.25$. This is a little high for a rural boundary layer where $\frac{-\overline{uw}}{\bar{U}_{\infty\,max}^2} = 0.0025 - 0.003$, but would be suitable for a suburban or urban shear stress. Values of u'/u_* and w'/u_* were about 2.2 and 1.0 respectively, which is in satisfactory agreement with the suggested values in 2.5.3. These values of u'/u_* and w'/u_* remained substantially constant over the lowest 20% of the boundary layer depth. Energy spectra measured for the streamwise and vertical velocity components at heights $z = 0.945$ in and 3.95 in showed reasonable agreement with atmospheric models, and from these spectra the author has estimated the linear scale of the simulation at about 1:1000. Overall, this simulation was fairly successful as a small scale model of the atmospheric surface layer, but measurements of spectra and integral scale are needed over the whole boundary layer depth to give a more complete picture of the turbulence structure. Shear stress data from the above work are plotted in Fig. 6.44.

Torrance (1968):

Torrance tested a building model in three different boundary layer velocity profiles, generated first by roughness on the wind tunnel floor and secondly by use of screens of varying mesh density. Two different wind tunnels were used for the tests, both of working section cross-section about 2 ft square and open circuit flow. Subsequent field tests were run with an 18 in x 18 in x 6 ft high building model. In all tests only mean velocity flow measurements were made, together with readings from pressure tappings on the building faces. No rigorous attempt was made to simulate atmospheric turbulence in the wind tunnel. The wind tunnel mean velocity profiles are shown in Fig. 4.6. The atmospheric profile power law exponent lay between 0.13 and 0.17. The atmospheric results were closest to wind tunnel results obtained with the floor roughness profiles, which is to be expected as some sort of turbulence simulation had been achieved with the floor roughness. (This was designed roughly on Jensen's (1958) model law). The value of the wind tunnel results was somewhat lessened by the disparities in results from the first and second wind tunnels.

Cockrell & Lee (1969):

In this work, boundary layer mean velocity profiles were generated in a small wind tunnel using natural growth, grids of rods (tensioned

stainless steel piano wire) and flow mixing devices which could act as ramps or ploughs. The tunnel working section was 14m long x 0.3m wide x 0.1m high, with a maximum speed of 60 m/sec. Recognised modelling criteria were the need to obtain an equilibrium boundary layer satisfying Eqn. 2.11, and the requirement of similarity of mean velocity profile, turbulent intensity and integral length scale. Results included only mean velocity profiles and shear stress profiles. It was found that a grid of Cowdrey design (see Chapter 4) was most satisfactory for velocity profile production, but that flow equilibrium was more rapidly achieved with the flow mixing devices, which also gave a better turbulence structure than the other schemes.

de Bray (1969/70):

Here tests were carried out in an open jet wind tunnel at atmospheric pressure. The test channel consisted of a 12 ft long ground board with vertical side plates giving a 28 in wide section. Maximum jet speed was 90 ft/sec. The object of these tests was to investigate the effects of wind on container stacks and protection of these stacks by fences of various permeabilities. Three boundary layer profiles were used: the natural grown boundary layer on the smooth ground board, a 1/7 power law profile generated with a curved metal mesh screen, and a 1/4 power law profile again generated by the screen and maintained with floor roughness consisting of small wooden blocks. The linear scale used for the simulation was 1:96. Measurements were made of only mean velocities and static pressures. Results obtained concerning the toppling forces on container stacks were probably realistic, but measurements of wind reduction behind the protective fences were probably optimistic, because the turbulence scale in the simulation was almost certainly too small. This feature is mentioned again in Chapter 9. Generally, a linear scaling of 1:96 requires integral scales of turbulence in the simulation of about 30 in and the boundary layer generation scheme used would not have achieved this.

Campbell & Standen (1969):

Following on from work initiated by Templin (1969) (see Chapter 4), these authors investigated a variety of 'step change + boundary layer growth' atmospheric wind simulation schemes in the N.A.E. (Canada) 3 ft wind tunnel. In this pilot study it was aimed to grow a 6 in deep boundary layer, correctly simulating the atmospheric mean velocity profile

(¼ power law), turbulent intensity $\frac{u'}{U}$, and u component spectrum. It was recognised that this was an imcomplete description of the atmospheric boundary layer and that the techniques would produce a non-equilibrium boundary layer. The basis of the boundary layer generation process was to use graded blockage to generate the mean velocity profile and turbulence. Floor roughness was used to maintain velocity profile stability, and in some cases an additional coarse grid was fitted upstream of the graded blockage to improve the downstream turbulence structure. The most successful graded blockage scheme was the 'modified half-width spires' (see Fig. 3.1) which gave good mean velocities and turbulent intensities. Energy spectra from this scheme gave too much energy at high frequencies, i.e. the integral scale of turbulence was too small. The best energy spectra were obtained with 'short spires' downstream of the uniform coarse mesh grid. The coarse grid did, however, make the turbulent intensity remain high in the upper part of the boundary layer. Use of this grid also improved two-dimensionality of the flow, but its high drag might prevent its use in a tunnel where the fan was operating close to the stall.

A basic defect with the spire form of graded blockage was that, like Counihan's (1969) elliptic wedge vortex generators, the spires tended to generate turbulence whose intensity decreased with height in approximately correct fashion, but whose integral length scale also decreased with height, contrary to the requirement of increasing length scale with height. This defect is also seen to be present with horizontal bar grid turbulence in Chapter 4. The u component spectra measured at heights of $z/\delta \simeq 0.08$, 0.33, 0.67 (generally), showed negligible decrease in k_p with increasing height, thus indicating decreasing integral length scale with height. The linear scale of the Campbell & Standen simulation was about 1:2000 based on profiles of mean velocity and turbulence intensity, but based on the most favourable integral scales derived from the spectral peaks the linear scale was not better than about 1:3000 and decreased with height. Examination of this work and that of Counihan (1969) shows that some means is required of generating large scale but low intensity turbulence in the upper part of the boundary layer. This cannot be achieved using graded blockage alone.

Cermak & Arya (1970):

This review paper discusses modelling criteria for the simulation of neutrally stable and thermally stratified atmospheric flows. Mention

is made of atmospheric boundary layer simulation in the Colorado State University meteorological wind tunnel (dimensions given previously), where naturally grown boundary layers of thickness between 70 and 120cm have been obtained over a generation distance of about 25m, with various surface roughnesses and a flow speed of about 6 m/sec.

Littlebury (1970):

This work involved simulating an atmospheric boundary layer in order to test a model of a steerable paraboloid dish aerial. The following parameters were considered important in the simulation: profiles of mean velocity and turbulent intensity, vertical, lateral and streamwise spectra and integral scales of turbulence, and vertical and lateral co-coherence functions. The simulation was carried out in a 26 ft x 14 ft cross-section tunnel with the boundary layer structure measured 45 ft from the trailing edge of delta or plough shaped vortex generators. These generators, shown in the layout of Fig. 3.2 were similar in effect to those of Cockrell & Lee (1969). A trip fence 1 ft high was necessary at the trailing edge of the vortex generators to break up the large stable vortex filaments which rolled off the leading edge of the generators. Strips of 1½ in x 1½ in "Dexion" angle were used as floor roughness. The mean velocity profile generated had a power law index of approximately 0.2, corresponding to rough open country, and spectra of the longitudinal and vertical velocity fluctuations followed the Harris and Panofsky forms (see Chapter 2) quite well. No measurements of shear stress or integral scale variation with height were presented. The linear scale of the simulation was given as 1:300, although the boundary layer depth appeared to be only about 2 ft.

Threadgill & Bryant (1971):

In this work an open circuit wind tunnel was used, and a combination of electric heating grid and wire mesh velocity profile grid introduced to generate a 1/7 power law mean velocity profile. The test section, excluding boundary layer generating equipment, was 36 ft long x 4 ft wide x 7 ft high, with speed variation in 9 steps from 0 to 32 ft/sec. Measurements of mean velocity and turbulent intensity were presented showing that the design velocity profile was achieved, but that turbulent intensities were considerably lower than atmospheric values (predictable with a fine mesh grid - see Chapter 4). It was found that an unstable

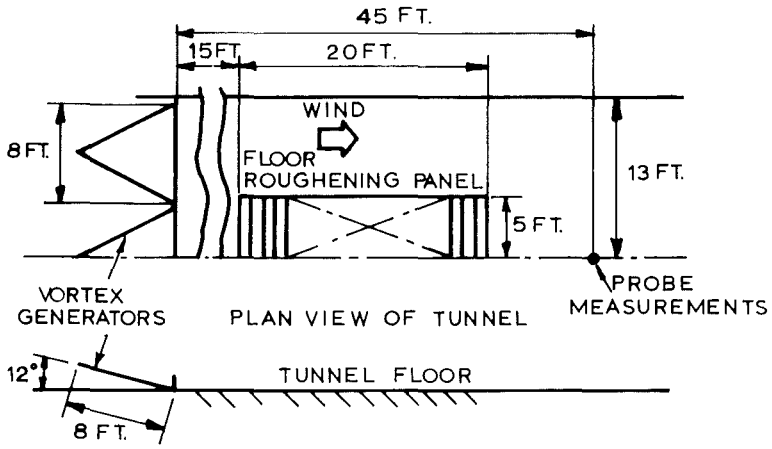

BOUNDARY LAYER GENERATING LAYOUT.
- LITTLEBURY (1970)

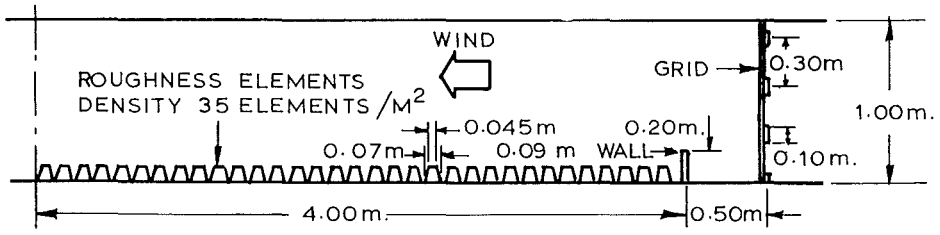

BOUNDARY LAYER GENERATING LAYOUT - COOK (1973)

Fig. 3.2

temperature gradient could be used to increase turbulent intensities. The aim of this work was to study the influence of atmospheric wind on the motion and deposition of agricultural pesticide particles, and low speed simulation of thermal gradients may, in this case, be more important than simulation of roughness-characterised turbulence intensity. Boundary layer depth was about 7 ft in these tests, but lack of similarity to atmospheric turbulence structure prevents realistic estimation of the linear scale of the simulation.

Schon & Mery (1971):

In this work the simulated atmospheric flow was generated by tripping the flow at the entrance to the working section using a 'fluid mechanical' fence in the form of vertical air injection through a plate on the tunnel floor. The test section was 10m long x 1m wide x 1.2m high, with a movable roof section (to control pressure gradient) and a smooth floor panel which could be heated. The mean velocity profiles with and without air injection were similar with power law index slightly less than 1/7, but at 9.2m from the air injection point the boundary layer thickness had increased from 17cm to 34cm. The u component turbulent intensity profile showed improved similarity to atmospheric models after introducing air injection, but were still too low by about 40% , 9.2m from the air injection point. This is to be expected with a smooth tunnel floor. The v and w component turbulent intensities showed very little change from the case with no air injection, at the 9.2m point. Energy spectra for the u and w components showed good shape similarity to atmospheric measurements, but changed negligibly when air injection was added. A linear scale for the simulation of ~ 1:350 was suggested but an examination of the data indicates that a linear scale of nearer 1:700 would be more realistic. Future work was intended, to study the effect of adding floor roughness and introducing temperature gradients into the flow.

Teunissen (1972):

As in the previous work of Schon & Mery, air injection was used here, but in a different manner. Teunissen used a vertical bank of air jets, injecting different amounts of air and injecting parallel to the main wind tunnel flow. The tunnel working section downstream of the air jets was 76 in long x 8 in wide x 8 in high. In the work described the tunnel was actually driven by the array of 64 air jets using the ejector principle. One of the aims of the work was to simulate atmospheric

boundary layers characteristic of several different types of terrain, and it was felt that the bank of individually controllable jets would enable the correct mean velocity profile and turbulence structure to be more readily obtained than use of the more conventional techniques described earlier. It was aimed to correctly model mean velocity profiles, u,v, and w component turbulent intensities, $-\rho\overline{uw}$ Reynolds stress, integral length scales of turbulence and energy spectra for each velocity component.

The investigation showed that the jets alone produced excellent mean velocity profiles but the turbulent intensity in the flow was too low even after the addition of surface roughness (e.g. LEGO baseboard). Turbulent intensity profiles were corrected by the addition of a 1 in high solid trip fence about 9 in downstream of the jet outlets. Most of the turbulence measurements were done with a power law mean velocity profile exponent of 0.16. Energy spectra showed reasonable shape similarity to the von Karman models of Equns. 2.42, 2.43, and 2.48 for the w, v and u component spectra respectively. The shear stress profile followed Eqn. 2.34 quite closely. The integral scale L_{u_x} showed an increase with height but was lacking in the middle region of the boundary layer when compared with Eqn. 2.63. (See Fig.6.51). L_{w_x} showed constancy over the middle region of the boundary layer, but decreased at higher altitude. The linear scale of the simulation was about 1:1700 and the final boundary layer structure was achieved in a distance about 6-8 times the height of the working section.

Counihan (1973):

In this work Counihan extended his previous boundary layer simulation scheme (Counihan 1969) to model a neutrally stable urban boundary layer. The layout of the boundary layer generating apparatus was more or less identical to that of the rural boundary layer simulation, except that a 1½ in high trip fence was used and the floor roughness downstream of the elliptic wedge vortex generators consisted of LEGO bricks as used by Armitt & Counihan (1968), spaced two brick widths between brick centres in a spanwise direction and three brick widths in a streamwise direction.

Counihan suggests that the 0.28 power law mean velocity profile obtained is typical of urban boundary layers, although this disagrees with Davenport's earlier conclusion (1960). At the measurement station 4½ boundary layer heights (27 in) downstream of the vortex generator trailing edges, the turbulent intensity and Reynolds stress profiles have

acceptable shape, but magnitudes were low for an urban boundary layer simulation. For instance, $\frac{u'}{\bar{U}_{\infty max}} = 0.15$ and $\frac{-\overline{uw}}{\bar{U}_{\infty\,max}^2} = 0.0025$.

Reynolds stress was fairly constant up to a height of about $z/\delta = 0.6$. Integral length scales were found to increase up to a height of about $z/\delta = 0.4$, as in the rural case, and then decreased with further height. Energy spectra plotted in the form $nS(n)/\overline{u^2}$ vs.n gave similar curves to the rural data so that for the u component spectrum the Harris atmospheric model was closely followed. The linear scale of the simulation was about 1:4000 based on the 6 in boundary layer depth.

Cook (1973):

This was again an urban atmospheric boundary layer simulation, but this time scaled about 1:250 and with only the lower third of the full scale boundary layer modelled. The wind tunnel working section used was 6.5m long x 2m wide x 1m high. The boundary layer was generated with the layout shown in Fig. 3.2. The coarse grid was followed by a 20cm high trip fence and then floor roughness elements consisting of inverted plastic cups. Mean velocity profiles showing a certain amount of spanwise scatter were obtained, with exponents of 0.28 (solid 20cm trip fence) and 0.33 (porous 23cm trip fence). Measurements of turbulence 4m from the trip fence showed that turbulent intensities and Reynolds stress were more or less constant over the height of the simulation (50cm of the boundary layer depth, only, was shown in the results). Based on the suggested linear scaling of 1:250, the maximum approximately constant stress, over the equivalent 125m depth of the boundary layer, was such that the surface drag coefficient $k_{10} = 0.025$, which is acceptable for an urban boundary layer. The turbulent intensities were in the ratio

$u' : v' : w' : u_* = 2.7 : 2.2 : 1.75 : 1$ (20cm wall)

$u' : v' : w' : u_* = 2.6 : 2.1 : 1.65 : 1$ (perforated wall)

Based on a power law profile exponent of about 0.3 the intensity $u'/\bar{U}_{ref_{max}} = 0.25$ (equiv. to $u'/\bar{U}_{10_{max}} = 0.53$) is acceptable for a model urban boundary layer. Good agreement of spectra of the u, v, and w velocity components with atmospheric models was obtained, although the required shift of the peak wave number to lower values at greater height does not appear to be present. The author indicates that the linear scale of 1:250 is verified by the spectra. Streamwise, lateral and vertical correlations ρ_{uu_x},

ρ_{uu_y}, ρ_{uu_z} respectively were measured. L_{u_x} showed an increase with height up to z ~40cm, but thereafter began to decrease. L_{u_x} was about 45cm at z = 38cm. If this value is compared with integral ^{x} scales in the atmosphere using Eqn. 2.63, the suggested linear scale of 1:250 seems fairly accurate.

This simulation seems to have achieved quite good similarity to the atmospheric surface layer over urban terrain and the linear scale of 1:250 is useful for model studies. This work was of interest in regard to the present work, where a system of coarse grid, trip fence and surface roughness were used for a rural boundary layer simulation. Cook's paper was obtained towards the completion of the experimental work in the present project.

3.6 WORKING SECTION SIZE REQUIREMENTS OF A WIND TUNNEL USED FOR ATMOSPHERIC BOUNDARY LAYER SIMULATION

From the review of 3.5 it can be seen that atmospheric boundary layer generation techniques can be separated into two broad categories:

(i) where the boundary layer is grown naturally over a long fetch of correctly scaled surface roughness, e.g. as used by Jensen (1958), Cermak & Arya (1970) and (more or less) Davenport & Isyumov (1967).

(ii) where thick turbulent boundary layers are developed artificially over a short distance by using bar grids, screens, vortex generators, or trip fences, or a combination of these, with or without downstream surface roughness.

Air injection schemes would fall into the second category.

In the case of the naturally grown boundary layer, surface roughness, scaled approximately by Eqn. 3.20, is modelled upstream of the test area for a distance of 20 to 30 times the final boundary layer depth. Closer to the test area additional features may be modelled, e.g. buildings, trees, etc. and these may be continued for a short stretch downstream of the model being tested. Growing a boundary layer in this way is similar to boundary layer growth in the atmosphere, and there is a reasonable chance of obtaining a horizontally homogeneous boundary layer with the flow similarity criteria of 3.4 generally satisfied. The one drawback

is the great length of working section required, e.g. 25m development distance to grow a 1m deep rural/suburban boundary layer. For this reason much of the recent atmospheric boundary layer simulation work has been concentrated on the step change, or step change + boundary layer growth schemes falling into category (ii).

Boundary layers generated by inducing an initial large scale disturbance in the flow, e.g. by trip fence, grid or vortex generators, tend to be less accurate as models of the atmospheric boundary layer. It is very difficult to obtain an equilibrium boundary layer over a short distance, and the equilibrium that is set up in the atmosphere between turbulence production, dissipation, and diffusion towards the outer part of the boundary layer, cannot be achieved in a short wind tunnel working section. It is therefore normal in the second type of simulated atmospheric boundary layer for the flow not to be fully developed in the test area, but for there to be gradual changes in profiles of mean velocity and turbulent intensity occurring, together with a streamwise increase in the integral scale of turbulence. In the schemes reviewed, it appears that achievement of the correct profiles of mean velocity and turbulent intensities, together with correct shape for the various component spectra, is readily possible. However, a fault with most schemes is a decrease in integral length scale of turbulence above the surface layer, instead of the required increase, e.g. according to Eqn. 2.63. This typically arises where a graded blockage has been used to generate a profile of mean velocity increasing with height, and turbulent intensity decreasing with height. The decrease in blockage with height required to provide the correct turbulent intensity profile also produces an integral scale which decreases with height. To provide large scale, low intensity turbulence in the outer part of the boundary layer a device such as a coarse grid is required far upstream of the test area, and upstream of other devices used to generate mean velocity and turbulent intensity profiles.

Assuming that a combined step change and boundary layer growth scheme is used, with matching of step change and rough ground to try to approach an equilibrium flow, the review shows that a development distance of 8 - 10 boundary layer heights should be adequate.

Now, in the present work it was hoped to achieve a linear scaling of the simulation of about 1:500, and as large as 1:400 if possible. Assuming for the meantime that the linear scale is 1:400, a rural boundary

layer 300m deep would be 0.75m deep in the wind tunnel. It was decided to base the design working section size of a new atmospheric wind simulation tunnel on a final boundary layer depth of 1m. This meant that a boundary layer development distance of about 10m had to be allowed. With a further length of 2 - 3m for the test area, this meant that the total length of the working section should be about 12m, or 40 ft. Assuming now that the boundary layer height is about 75% of the working section height, and that a minimum width:height ratio is about 1, a tunnel cross-section of about 1.3m x 1.3m would be acceptable. Cook (1973) has shown that in a working section of about this size, an integral scale of turbulence of about 40cm, or about ¼ to 1/3 of the working section width, should be obtainable.

* * * * * *

In this chapter, the derivation of modelling criteria, and a review of previous simulations of the atmospheric boundary layer, have given a broad idea of the size of wind tunnel required to produce a simulation of 1:500 scale, or better. In Chapter 4, application of a single coarse grid in the simulation of atmospheric boundary layers in short working section wind tunnels is evaluated. In the present project preliminary work with coarse grids in the 4 ft x 3 ft aeronautical tunnel was carried out to show the need for a long working section atmospheric boundary layer modelling wind tunnel.

CHAPTER 4

4.0 USE OF GRIDS AND SCREENS IN THE SIMULATION OF ATMOSPHERIC BOUNDARY LAYER MEAN VELOCITY PROFILES AND TURBULENCE.

Fine woven wire screens have traditionally been used in aeronautical wind tunnels for the damping of turbulence. For many years bar grids and wire screens have also been used to produce turbulence of a certain scale and intensity, particularly where an approximation to isotropic turbulence was required. During the past twenty years, frequent use has been made of non-uniform horizontal bar grids and of curved wire woven screens to produce thick boundary layer mean velocity profiles over a short generation distance. More recent is the use of coarse square mesh and horizontal bar grids in attempts to simulate atmospheric turbulence.

In this chapter velocity profile generation and simulation of atmospheric turbulence using bar grids and wire screens are discussed, and the literature reviewed. Different velocity profile grid design techniques are evaluated and a computer grid design method presented. Finally, limitations on the use of coarse grids in atmospheric turbulence modelling are evaluated, and the need for a long working section atmospheric boundary layer wind tunnel shown.

4.1 THE USE OF GRIDS AND SCREENS FOR VELOCITY PROFILE GENERATION.

4.1.1 Review of Applications of Grids and Screens in the Modification of Wind Tunnel Velocity Distributions:

Screens have for a long time been used to reduce variations in mean wind speed in an airstream, and laws to predict velocity modifications by screens appeared about 40 years ago. Schubauer, Spangenberg & Klebanoff (1950), for example, cite the work of Prandtl (1933) and Collar (1939) who produced different expressions for the reduction of differences in mean velocity of a stream flowing through a screen.

Simmons & Cowdrey (1945) reported normal and tangential force coefficients for wire gauzes set obliquely to a stream to turn the air through an angle. They also showed the important result that above a Reynolds number, $\frac{\bar{U}_o D}{\nu}$, based on 'bar' diameter, D, of about 4×10^3, the pressure drop coefficient, K_o, of the screen or grid may be expressed by:

$$K_o \simeq \frac{1 - \phi}{\phi^2} \qquad \ldots.(4.1)$$

where ϕ is the permeability of the grid or screen.

Schubauer, Spangenberg & Klebanoff (1950) presented normal and tangential force coefficients for wire screens tested in normal and oblique flow, and also investigated the effects of screens on the scale and intensity of turbulence in the flow. An expression for the change in the tangential velocity component, $\bar{U}_T$, on passing two-dimensional flow through a screen was given:

i.e. referring to Fig. 4.1, as the angle of incidence, θ, of the flow to the screen approaches zero, the fractional change in the velocity component tangential the screen is given by

$$\alpha_T = \frac{1.1}{\sqrt{1 + K_o}}$$

This was stated to be true for woven wire screens, but appears to hold also for grids of parallel bars.

Dryden & Schubauer (1947) derived an expression for the reduction in intensity of turbulence by one or more fine wire screens normal to the flow. For a single screen:

$$\frac{u'_{\text{downstream}}}{u'_{\text{upstream}}} = \frac{1}{\sqrt{1 + K_o}}$$

This expression was compared with alternative forms by Schubauer, Spangenberg & Klebanoff (1950), and found to give best agreement with experiments.

Baines & Peterson (1951) reported an extensive wind tunnel investigation into flow through screens. Useful grid and screen design data were presented in three areas :

(i) Pressure drop coefficients of grids and screens as a function of permeability and permeability configuration, e.g. biplane bar grid or punched metal sheet.

(ii) Modification of mean velocity distribution by grids and screens.

(iii) Characteristics of turbulence produced by grids and screens.

Baines & Peterson derive a velocity modification equation in the form:

$$\left(\frac{\bar{U}_2}{\bar{U}_o}\right)^2 = \frac{K_o + (\bar{U}_1/\bar{U}_o)^2}{K_o + 1} \qquad \ldots.(4.4)$$

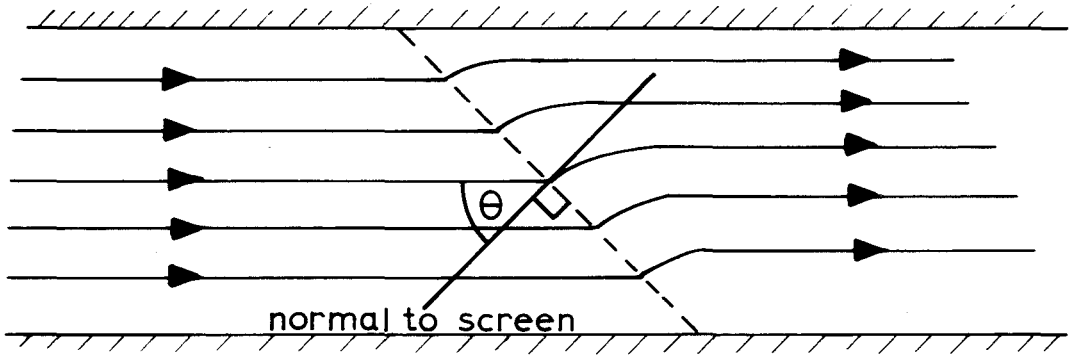

Flow passing through screen is refracted towards the normal to the screen.

Fig. 4·1

where $\bar{U}_o$ is the spatial mean velocity far upstream of the grid.
$\bar{U}_1$ is the local mean velocity a short distance upstream of the grid.
$\bar{U}_2$ is the local mean velocity downstream of the grid.

This equation predicts that velocities in a non-uniform stream approaching the uniform grid are corrected towards the spatial mean, $\bar{U}_o$, on passing through the grid. Expanding Eqn. 4.4 in a Taylor series about the point $\frac{\bar{U}_2}{\bar{U}_o} = 1$, and taking the first term,

$$\frac{\bar{U}_2}{\bar{U}_o} - 1 = \frac{1}{K_o+1}\left(\frac{\bar{U}_1}{\bar{U}_o} - 1\right) \qquad \ldots.(4.5)$$

This is the form proposed by Prandtl in 1932, and was compared with experimental data by Baines & Peterson. Good agreement was found between Eqn. 4.5 and experiments where ϕ, the grid permeability, was greater than 0.5. When permeability was less than 0.5 the flow downstream of the grid became unstable and the mean velocity distribution unpredictable (See Fig. 4.2).

Owen & Zienkiewicz (1957) present a grid design theory, for the generation of uniform shear in the wind tunnel flow. The method is strictly applicable only to weakly sheared flows and involves the matching of two potential flow solutions at a point of discontinuity, located at the grid. A vertical non-uniform grid of horizontal bars placed in initially uniform flow and designed for a shear parameter $\bar{U}_{2_{max}}/\bar{U}_o = 1.225$, gave results in close agreement with the theory, and lateral uniformity of the downstream flow was good to within 2% at any height. (See Fig. 4.3). In 4.1.2, the Owen & Zienkiewicz grid design method is adapted for a downstream power law mean velocity profile.

Elder (1959) made a more complicated potential flow perturbation analysis to predict the downstream mean velocity profile for flow through arbitrarily shaped gauzes of non-uniform permeability. Results close to theoretical prediction were obtained for uniform approach flow through an inclined uniform gauze and through a parabolic gauze, but the method was not very satisfactory with a gauze designed to produce uniform shear downstream. Later use of Elder's method by Cockrell & Lee (1966) to predict 1/7 and 1/4 power law profile grid designs, resulted in downstream velocity profiles which deviated from design values close to the floor of the tunnel. Fundamental to the accuracy of the method (and that of Owen & Zienkiewicz) is that deviation of streamlines from the horizontal in the region of the screen be small. Elder's analysis assumes that :

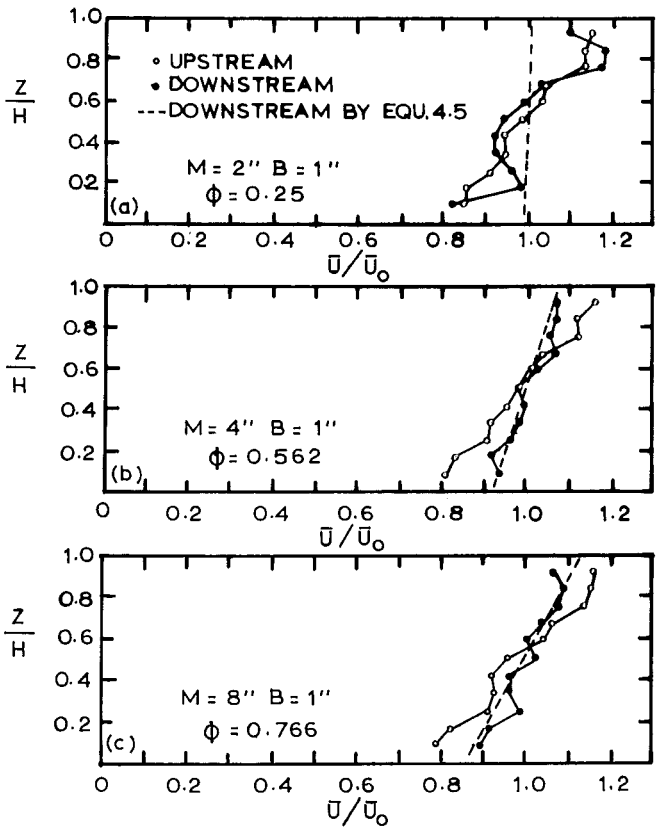

EFFECTS OF SCREENS WITH DIFFERENT SOLIDITY RATIOS ON ONE DIRECTIONAL VELOCITY VARIATION.

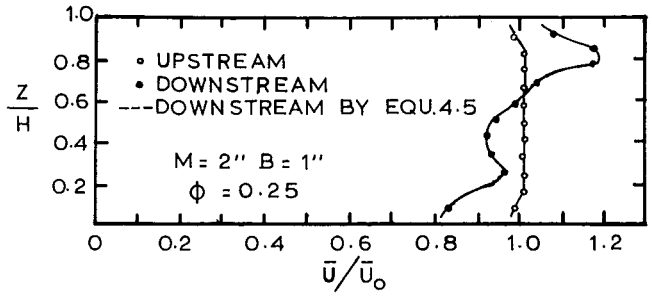

EFFECT OF SCREEN WITH HIGH SOLIDITY RATIO ON A UNIFORM VELOCITY DISTRIBUTION.

Fig.4.2 AFTER BAINES & PETERSON (1951).

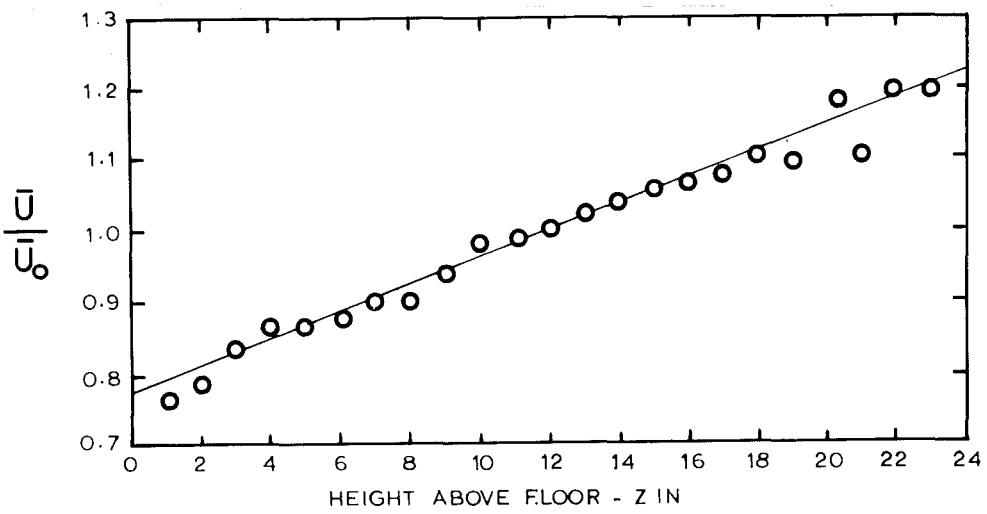

GRID VELOCITY PROFILE - LLOYD (1966)

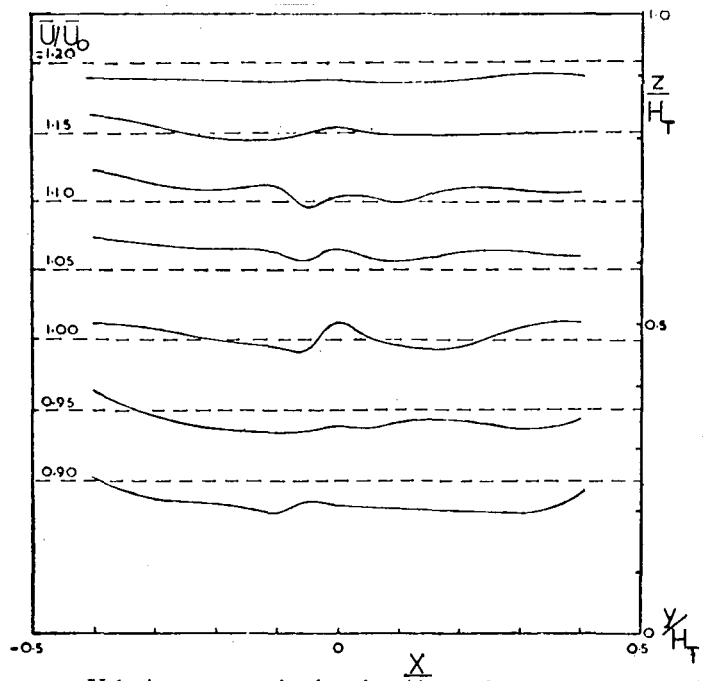

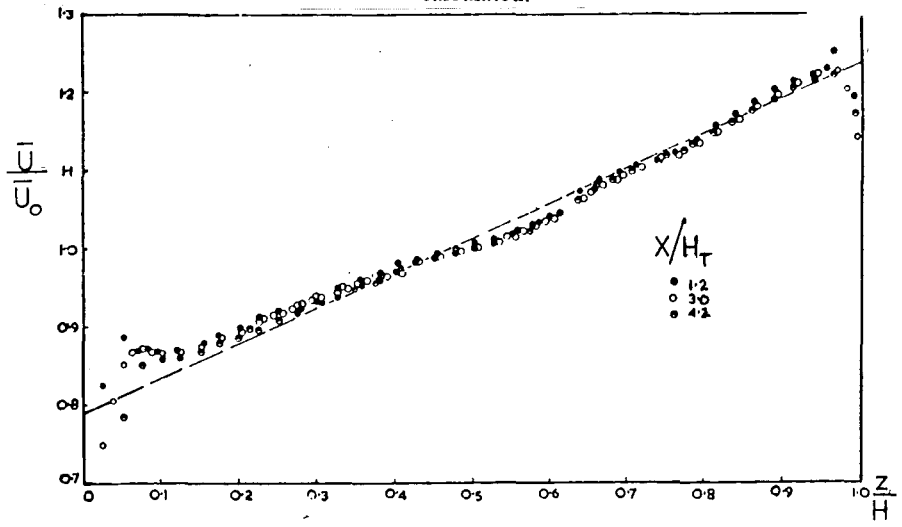

GRID VELOCITY PROFILES - OWEN & ZIENKIEWICZ (1957)

Fig. 4.3

$$K \simeq \left(\frac{1-\phi}{\phi}\right)^2 \qquad \ldots.(4.6)$$

Examination of results of Baines & Peterson (1951) shows that the expression given by Simmons & Cowdrey (1945), Equ. 4.1, falls closer to experimental data for both round rod and sharp-edged permeability than does Equ. 4.6, particularly for $\phi > 0.5$, where grid design methods can be reliably used. (See Baines & Peterson, 1951, Fig.3).

Lau & Baines (1968) present a rigorous, but complicated, screen design method which again involves matching stream functions upstream and downstream of the screen, at the screen. The method will predict the screen design for an arbitrary downstream mean velocity profile in neutrally stable or stratified flow. The method requires that only small streamline deflections and small density variations occur in the flow. Curved screens with large slope can, however, be used satisfactorily. This was not possible with Elder's theory.

Cowdrey (1967) made an important contribution from the engineering viewpoint in the form of a simple method for designing velocity profile grids. Experiments with ½ in bars in a tunnel 24 in high x 12 in wide verified the prediction method for linear shear, and 1/3 and 1/5 power law velocity profiles downstream. The method is less restrictive than those of Elder, and Owen & Zienkiewicz as there is no requirement that only minor perturbations to the stream function occur, or that the shear,

$$d\left(\frac{\bar{U}_1}{\bar{U}_o}\right) \Big/ d\left(\frac{z}{H}\right)$$

be limited to less than 0.5. The Cowdrey method is examined in more detail in 4.1.2 and in Appendix 1.

Several authors report the use of bar grids and curved wire screens to simulate atmospheric boundary layer mean velocity profiles in the wind tunnel. These schemes have generally been designed by trial and error or by using Cowdrey's (1967) method. Results of some of these efforts appear in 4.1.3 and 4.2.2.

Generation of Velocity Profiles using Flat Plate Grids:

Strom & Kaplin (1960) used a non-uniform grid of flat plates together with turbulence generators, heating grid and floor roughness to generate a thermally stratified model atmospheric boundary layer. This has been described in Chapter 3.

Lloyd (1966) reported a flat plate velocity profile grid design method based on calculation of boundary layer growth in the space between adjacent plates. Satisfactory performance was obtained with a grid designed to give a linear shear mean velocity profile, in which the maximum variation was ± 22.5% of the centre line velocity. (Same amount of shear as Owen & Zienkiewicz grid - see Fig. 4.3). The method could not be used when turbulence generators were added to the flat plates for simulation of atmospheric turbulence, and a trial and error scheme was used instead, approximate 1/7, 1/4 and 1/2 power law mean velocity profiles being achieved.

4.1.2 Adaption of Velocity Profile Grid Design Methods to the Computer:

In the present work, it was intended to use velocity profile grids or screens designed, in attempts to generate a neutrally stable simulated atmospheric boundary layer in a short wind tunnel working section. Thus a fundamental requirement of the grid or screen was that its elements generate turbulence of as large a scale as possible, without losing the ability to produce a smoothly varying mean velocity profile. Curved wire or expanded metal screens ($D < 1/8$ in), while satisfactory for velocity profile generation, produce turbulence of too small a scale and intensity, particularly high above the floor where mean flow shear is minimal.

It was therefore decided to concentrate on the design of bar grids, using single plane, non-uniform grids of parallel, horizontal, round bars which were to be set normal to the flow, as shown in Fig. A1.1. The Owen and Zienkiewicz (1957) Grid Design method was adapted to produce a power law mean velocity profile downstream of the grid. This method and Cowdrey's grid design method were then used in a computer program to predict the grid bar spacing required to produce a power law mean velocity profile. The problem involves a simple iterative procedure to set up the desired bar spacing, starting at the wind tunnel floor and working upwards. This was ideally suited to the computer, and a flexible program evolved, generalised to cope with any power law exponent, bar diameter, D, tunnel height, H, or overall pressure drop coefficient, K_o.

Some reservations were held in adapting the Owen & Zienkiewicz method to a velocity profile where there existed a region of high shear near the floor, since the theory requires the amount of shear introduced by the grid to be small.

The Grid Design Process:

This is detailed in Appendix I, where steps in the computer design process are summarised and sample computer output presented. In both methods an expression for the local pressure drop coefficient, K, at any point on the grid is derived, and then an iterative procedure used to set up successive bar spacings, so that at each height the value of K suits the design downstream velocity profile. The expressions for K in the two methods are as follows :

(i) Adapted Owen & Zienkiewicz Method:

$$K = \frac{H^{\frac{2}{N}}\left(1+K_o\right)\left(1.1+\sqrt{1+K}\right)^2 - \left(\frac{N+1}{N}\right)^2\left(1.1+\sqrt{1+K}\right)^{\frac{2N}{N+1}} . Z_1^{\frac{2}{N}}\left(\sqrt{1+K} + 1.1\left(\frac{H}{Z_1}\right)^{\frac{1}{N}}\right)^{\frac{2}{1+N}}}{\left(Z_1^{\frac{1}{N}}\left(\frac{N+1}{N}\right)\sqrt{1+K} \quad + 1.1H^{\frac{1}{N}}\right)^2}$$

where in this and the Cowdrey method,

Z_1 is a streamline height at the grid;

H is the tunnel height;

$N = \frac{1}{\alpha}$, where α is the power law exponent.

(ii) Cowdrey Method:

$$K = \frac{H^{\frac{2}{N}} . (1 + K_o) - \left(\frac{N+1}{N}\right)^2 Z_1^{\frac{2}{N}}}{\left(\frac{N+1}{N}\right)^2 . Z_1^{\frac{2}{N}}}$$

It can be seen that the Cowdrey expression for K is much simpler. The adapted Owen & Zienkiewicz expression for K is not explicit and in this method iteration is used in the computer solution to make K exact. As $Z_1 \rightarrow H$, and if N is large, the two expressions for K become similar.

The description of the design process in Appendix 1 is accompanied by a flow diagram and a sample listing of the program with grid design output data for three different power law velocity profiles. The program was run on the University of Canterbury IBM 360/44 computer. Typical run time is about 3 minutes for 15 different grid designs involving various values of N, H, D and K_o.

In practice the overall pressure drop coefficient of the grid, K_o, must be kept reasonably low

(a) to avoid excessive losses in the wind tunnel flow; and

(b) to avoid large regions near the floor where K is high and ϕ less than 0.5. If ϕ is less than 0.5 the downstream design velocity profile will tend to be lost.

In wind tunnel tests in the present work, K_o was set at 1.0 to enhance generation of turbulence. With $K_o = 1.0$ the grid permeability, ϕ, was less than 0.5 for $z/H < 0.1$.

The computer generation of velocity profile grid designs is a rapid and convenient process, and much simpler for the user than former manual calculation techniques.

4.1.3 Comparison of Experimental Grid and Screen-Generated Velocity Profile Data:

In this section, grid and screen-generated velocity profiles from experiments in this project are examined, and compared with velocity profile data from the literature.

Early in the course of the present project a 1/7 power law mean velocity profile was generated in the 4ft x 3ft working section of the aeronautical wind tunnel using an expanded aluminium, diamond mesh curved screen. The trial and error method was tedious and not really satisfactory in that small changes in screen shape had a large effect on the profile. A sample 1/7 power law profile obtained, accurate only in the lower part of the boundary layer, is shown in Fig. 4.4. Preliminary trial and error bar grid tests were also run using a grid of 1/2 in diameter bars, and a 1/7 power law profile was again obtained as shown in Fig. 4.5. The trial and error process was again slow, but simpler than with the curved screen. As noted in other reports, a very small change in bar spacing near the floor, e.g. 0.03 in. (0.08cm) change, where K was high, could change the downstream velocity at the same height by more than 5%. This made fine adjustment of the downstream profile difficult.

Other trial and error velocity profile generation schemes have been used by Torrance (1968) who used a basic open mesh screen overlaid with screen portions of various permeabilities, and de Bray (1969, 1970), who used a curved coarse metal mesh screen. Sample results from Torrance's work are shown in Fig. 4.6. Cockrell and Lee (1966), using Elder's (1959) grid design method produced 1/7 and 1/4 power law velocity profiles as shown in Fig. 4.7. These profiles, and a 1/5 power law profile by the same authors, reproduced by Cowdrey (1967), tend to deviate from the design curve near the floor.

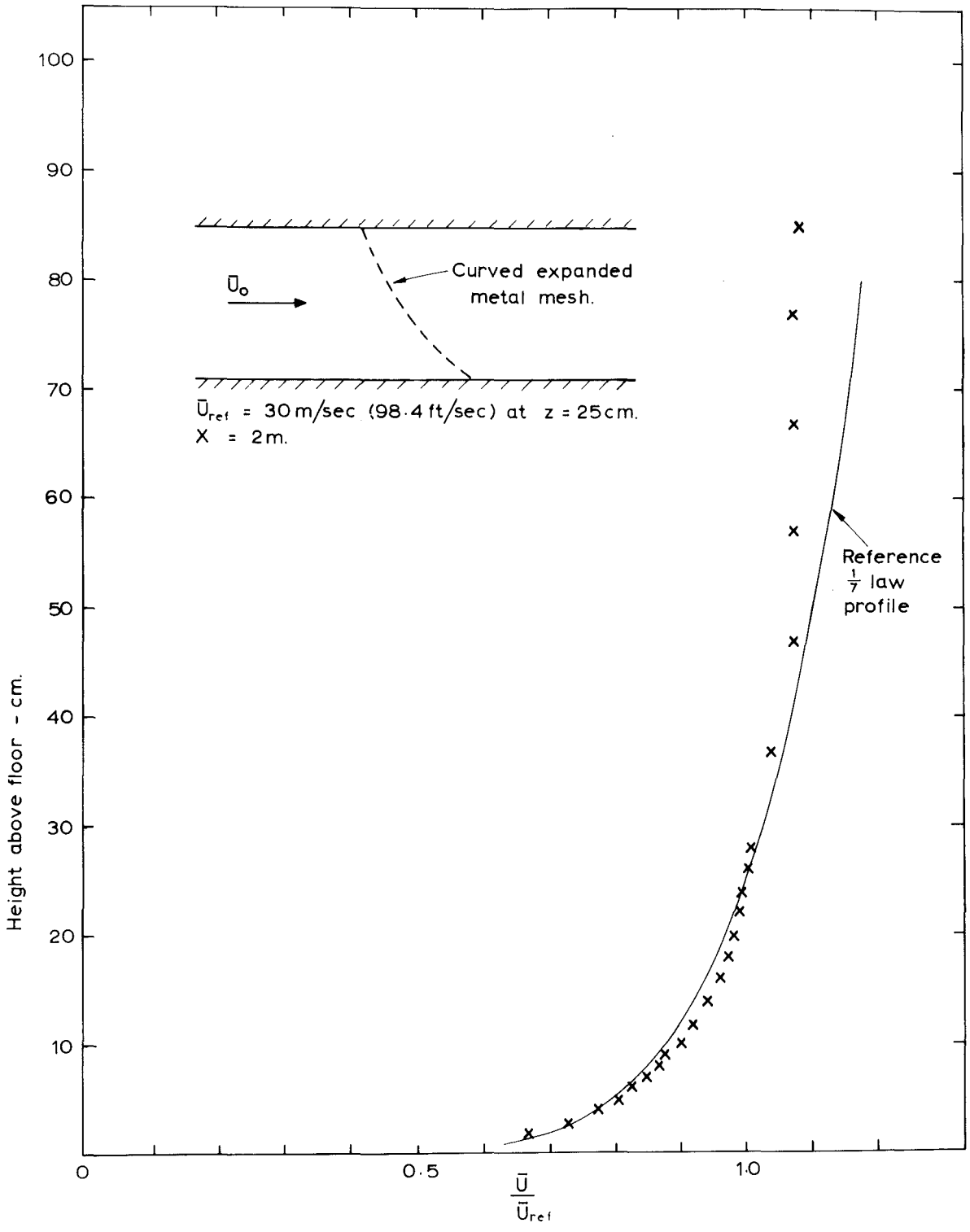

Fig. 4.4 $\frac{1}{7}$ POWER LAW VELOCITY PROFILE FROM COARSE SCREEN.

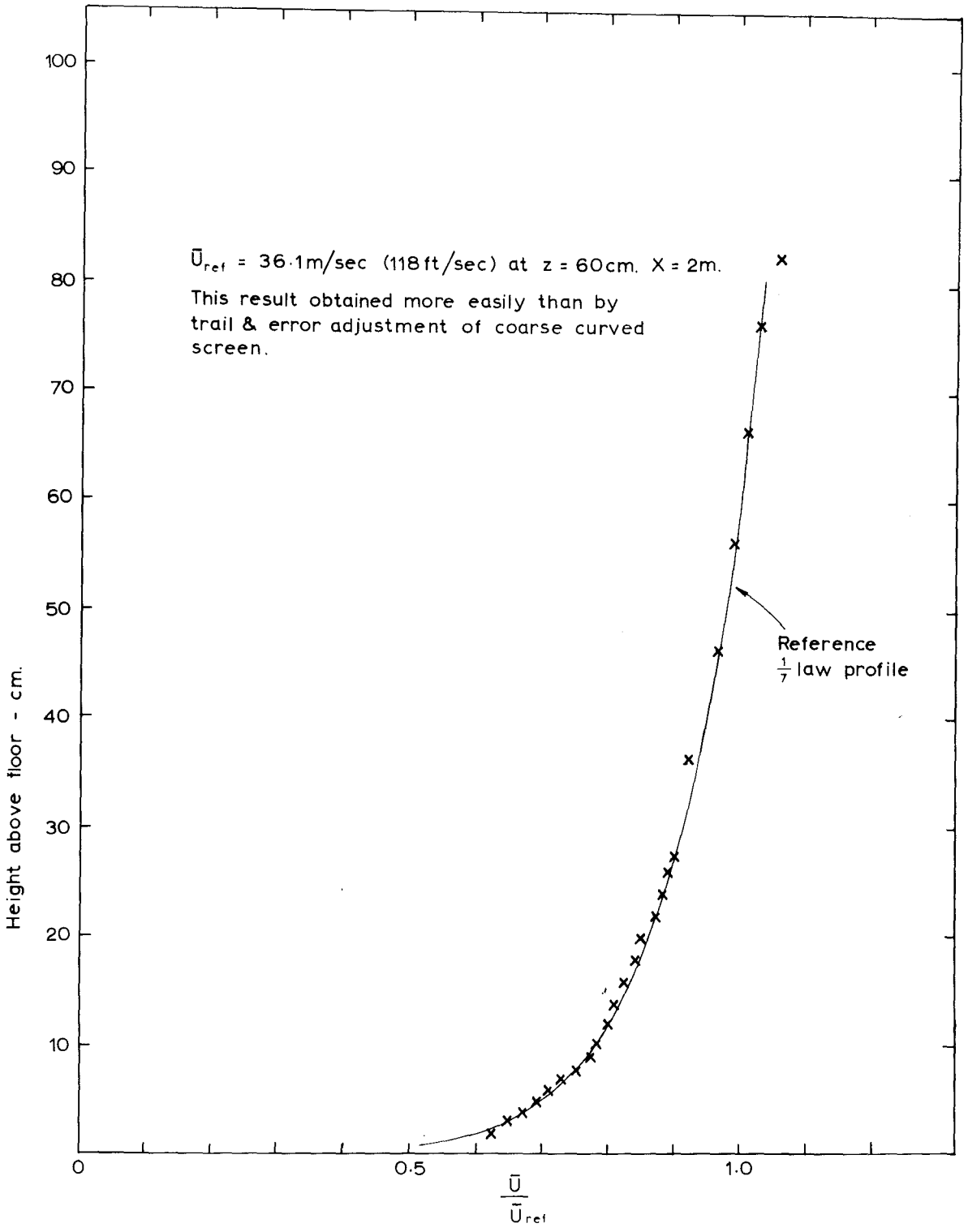

Fig. 4·5 $\frac{1}{7}$ POWER LAW VELOCITY PROFILE ACHIEVED BY TRIAL AND ERROR DOWNSTREAM OF $\frac{1}{2}$ IN. BAR GRID.

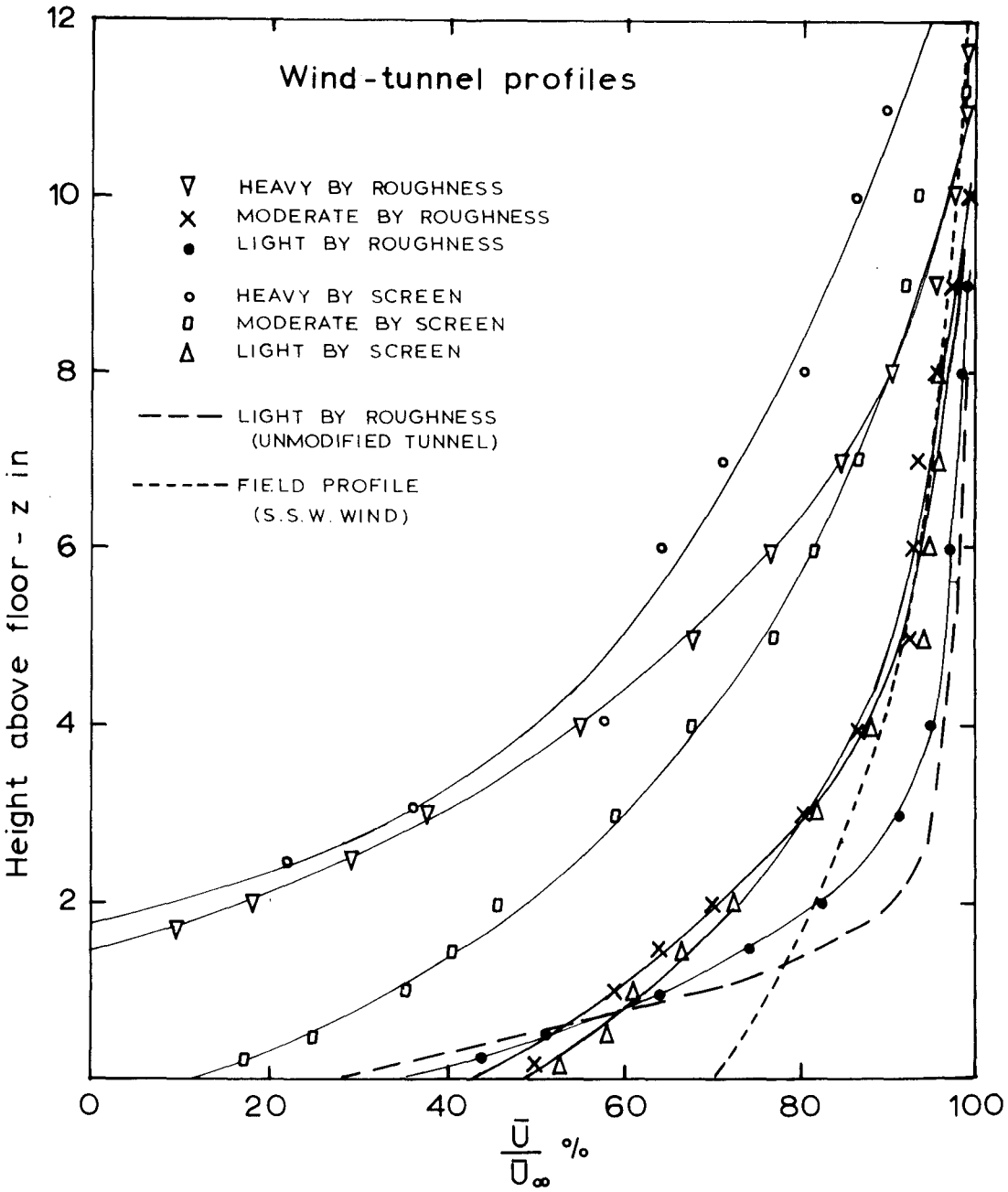

Fig. 4.6 VELOCITY PROFILES FROM TORRANCE (1968)

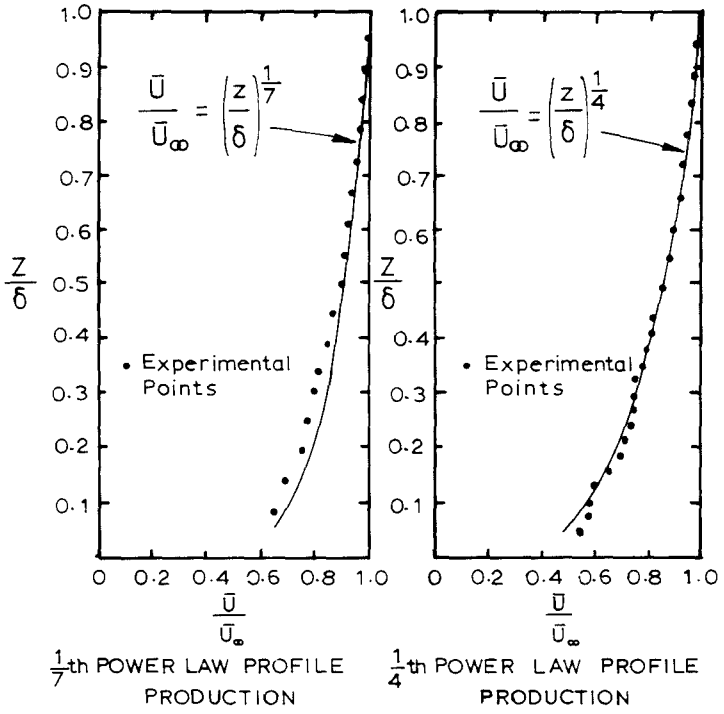

Fig.4.7 SCREEN VELOCITY PROFILES - COCKRELL & LEE (1966).

Preliminary tests of the Cowdrey (1967) grid design method by undergraduate students working under the author's supervision, yielded reasonably accurate 1/7 and 1/5 power law velocity profiles, shown in Fig. 4.8. Note that the design profile is followed more closely when N is larger (i.e. α smaller). The grid bar diameter was increased to 1 in for these and subsequent tests, to avoid vibration of the bars and enhance turbulence generation. Turbulence measurements in these preliminary tests showed that a Cowdrey-type grid is unsatisfactory as a generator of atmospheric turbulence, and later experimental comparison of the Cowdrey, and Owen and Zienkiewicz design methods was restricted to 1/7 power law velocity profiles.

In Fig. 4.9 velocity profiles obtained by the two design methods are compared. These profiles were measured 2.20m from the grid, on the centre line of the 4 ft wide x 3 ft high x 8 ft (2.44m) long working section of the aeronautical tunnel.

The Cowdrey method 1/7 and 1/5 power law velocity profiles of Fig. 4.8 are adequate for an atmospheric boundary layer simulation. Self-preservation of the 1/5 power law profile is poorer than with the 1/7 power law, streamwise acceleration near the floor being evident in the former. de Bray (1969, 1970) overcame this problem by using a roughened floor to maintain a screen-generated 1/4 power law profile. There is a tendency in the Cowdrey grid-generated 1/7 power law profile for velocities to be low by up to 5% in the region near the floor. This was noticeable in both Figs. 4.8 and 4.9, and is apparent in some of Cowdrey's own results for a 1/3 power law profile grid, as can be seen for $z/\delta < 0.1$ in Fig. 4.10. The magnitude of this type of error is dependent on the positioning of the reference power law curve.

In Fig. 4.9, the profile generated by the grid designed by the adapted Owen and Zienkiewicz method shows a closer fit to the design 1/7 power law curve than the Cowdrey grid velocity profile does. However, the O and Z method profile is no closer to the design curve than the Cowdrey method profile of the earlier work, Fig. 4.8. Comparing the O and Z method 1/7 power law profile with results of Cockrell and Lee (1966), Fig. 4.7, it appears that the design method presented in Appendix I is at least as accurate as that of Cockrell and Lee. Both methods assume inviscid flow and match stream functions at the grid, but the initial value assumed for K in the O and Z method is different from that used by Cockrell and Lee.

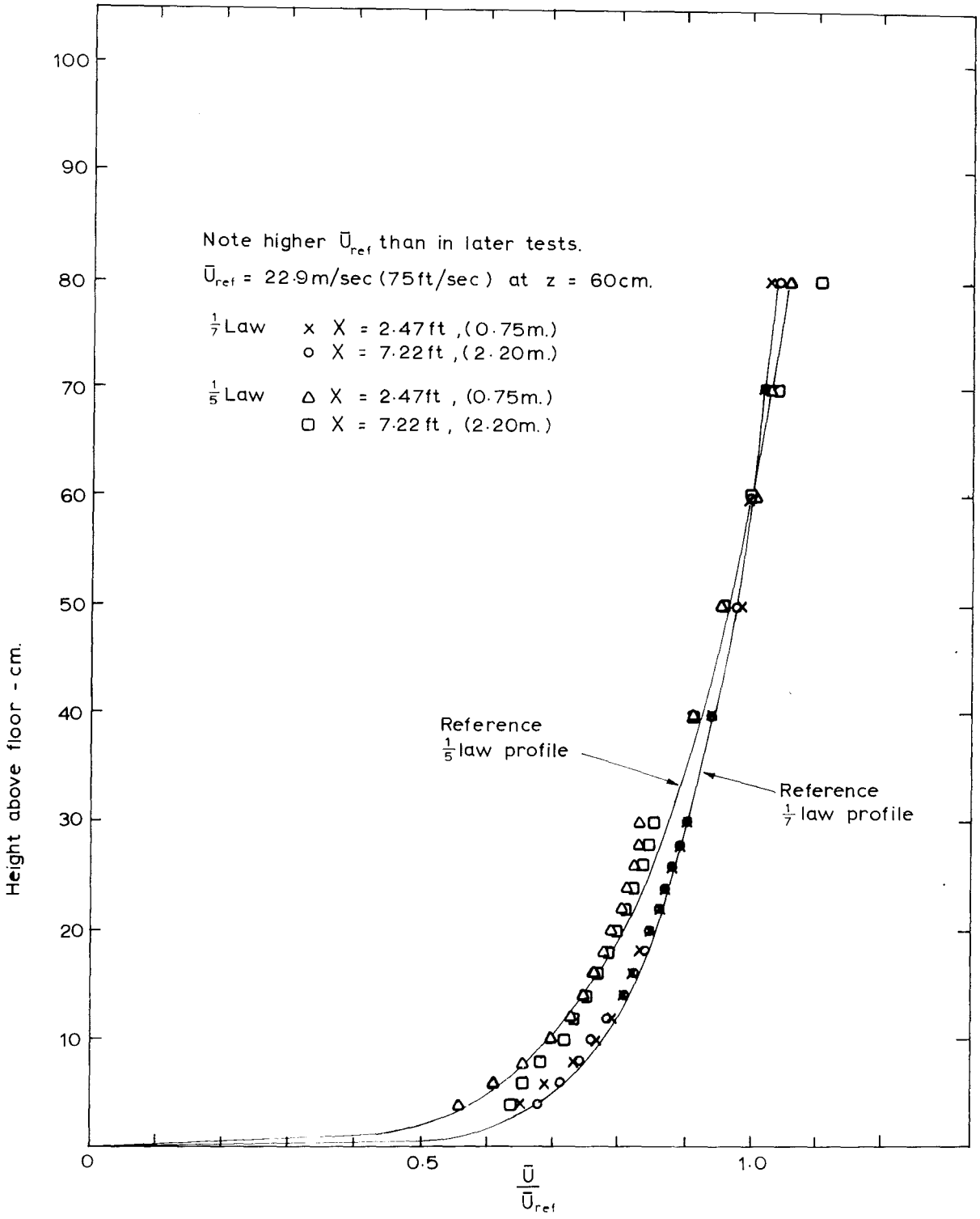

Fig. 4·8 $\frac{1}{5}$ & $\frac{1}{7}$ POWER LAW PROFILES FROM PRELIMINARY TEST OF COWDREY GRID DESIGN METHOD.

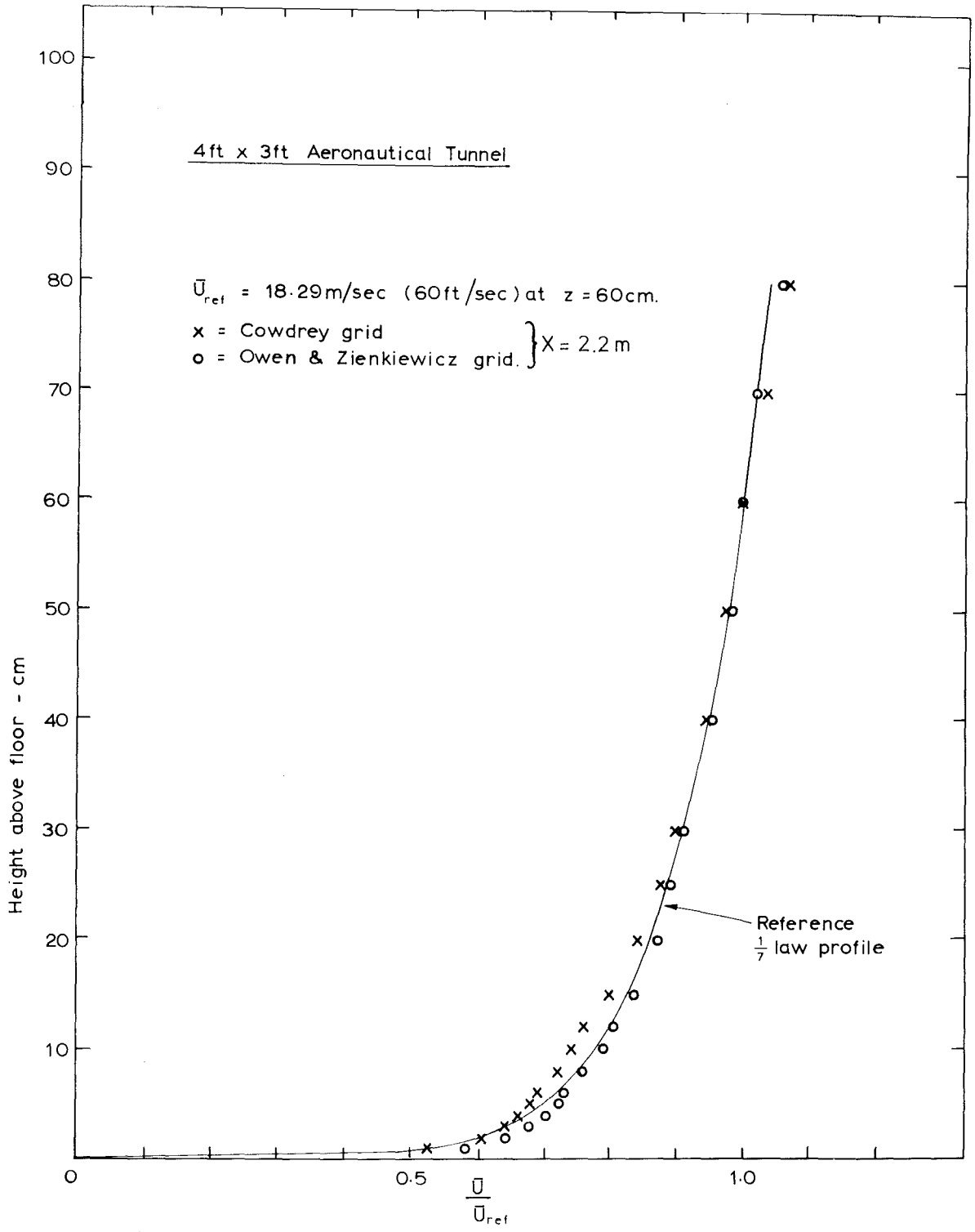

Fig. 4·9 $\frac{1}{7}$ POWER LAW MEAN VELOCITY PROFILES BY COWDREY, AND OWEN AND ZIENKIEWICZ METHODS.

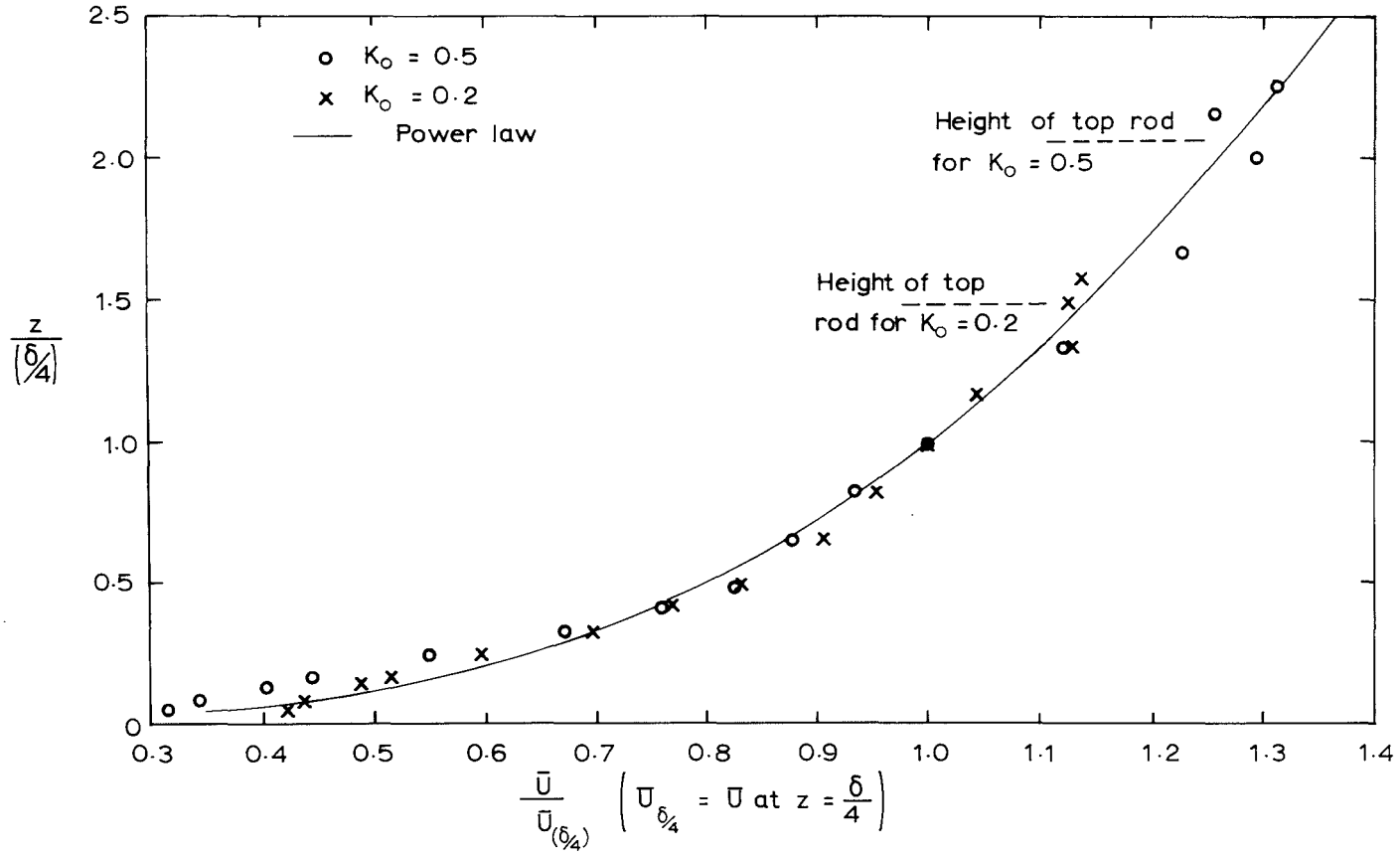

Fig. 4·10 EXPERIMENTAL RESULTS FOR $\frac{1}{3}$ POWER LAW GRID – COWDREY (1967)

The final accuracy of a velocity profile generated, depends on the accuracy to which the design spacing between adjacent bars of a grid can be set up, and a proper comparison of different grid design methods would require testing of all methods under the same conditions, with bar spacings in, say, a 1 in bar grid set up to within 0.01 in of the design values.

From the results obtained it can be concluded :

(i) The adapted Owen and Zienkiewicz method results in velocities that are higher near the floor than those from the Cowdrey method. (This is expected as the former method predicts wider bar spacings near the floor).

(ii) Either method is probably sufficiently accurate for atmospheric boundary layer velocity profile simulation, but the Cowdrey method has the advantage of simplicity.

Note: The tendency for velocities to be too high near the duct walls in profiles generated by grids designed on the assumption of inviscid flow (Owen and Zienkiewicz (1957), Elder (1959)) was explained by Lau and Baines (1968). It would be expected that the fluid in the floor boundary layer, for instance, having a lower velocity than assumed, would experience a smaller loss in total head on passing through the grid than predicted by theory, so that the total head and hence velocities would tend high downstream of the grid. This is in fact true only when $K \gtrsim 1$.

Consider a region close to the floor such that

$$\bar{U}_{upstream} = \bar{U}_{floor} < \bar{U}_o .$$

The energy balance along a streamline close to the floor is

$$\frac{1}{2}\rho K \bar{U}_1^2 = (\bar{P}_o - \bar{P}_2) + \frac{1}{2}\rho\,(\bar{U}^2_{floor} - \bar{U}_2^2)$$

(refer to Fig.A1.1 in Appendix 1).

Lau and Baines assume displacement of this streamline is small such that

$$\bar{U}^2_{floor} \simeq \bar{U}_1^2$$

$$\therefore \quad \frac{1}{2}\rho \bar{U}_2^2 = (\bar{P}_o - \bar{P}_2) - \frac{1}{2}(K - 1)\rho \bar{U}^2_{floor}$$

In this equation it can be seen that $\frac{1}{2}\rho\bar{U}_2^2$, hence $\bar{U}_2$ will tend higher than that predicted by theory, since $\bar{U}_{floor} < \bar{U}_o$, except when $K < 1$, in which case the downstream dynamic head will be less than that predicted by theory. Allowance for this could be made by adjustment of $\bar{U}_o$ close to the floor.

The effectiveness of 1 in bar grids in simulating atmospheric turbulence is discussed in 4.2.

4.2 THE USE OF BAR GRIDS IN SIMULATION OF ATMOSPHERIC TURBULENCE

In the 'step change' method of simulating atmospheric boundary layers in short wind tunnel working sections, described in Chapter 3, coarse single plane parallel or biplane square mesh bar grids are frequently used to generate the scaled down turbulence. The validity of this practice is evaluated in this section, by examining the structure and decay of grid turbulence, and results of grid simulation of atmospheric turbulence in the light of modelling criteria set down earlier. Important features of grid turbulence were obtained mainly from the texts of Batchelor (1953) and Hinze (1959), and the more recent paper of Naudascher and Farell (1970).

4.2.1 Grid Turbulence v. Atmospheric Turbulence.

(a) General. It will be recalled that a suitable basis for a simulated atmospheric boundary layer is any wall boundary layer which is:

(i) Fully aerodynamically rough;

(ii) Horizontally homogeneous;

(iii) Free from pressure gradients.

Also, in the idealised equilibrium atmospheric flow, the mean velocity profile, Reynolds stresses, and energy spectra, intensity and length scales of each turbulent velocity component would remain constant with distance downstream. Vertical homogeneity does not exist in the atmosphere, although for engineering applications it could be assumed approximately over small increments of height, e.g. 30m, except very close to the ground. It must be remembered also, that horizontal homogeneity is not often achieved in the atmosphere because of the heterogeneity of the earth's surface.

Consider now, in contrast, the flow of a uniform stream through a biplane square mesh lattice grid of rectangular, square or round bars, with B and M chosen so that K_o is less than about 2 (ensuring stable flow downstream). The many openings in the grid act as a bank of orifices, the flow emerging as an array of discrete jets which rapidly mix downstream of the grid, so that in a closed duct, the flow will attain

the same uniform mean velocity far downstream of grid as it had far upstream. The magnitude of the pressure drop across the grid will be proportional to the quantity of mean flow energy converted to turbulence.

With a uniform grid, the turbulence generated is homogeneous in the vw plane, normal to the streamwise direction, but decays as it moves downstream. The grid turbulence therefore differs from atmospheric turbulence in two basic respects :-

(i) Horizontal homogeneity does not exist, since the turbulence decays in the streamwise, x, direction;

(ii) Homogeneity in the vertical direction, i.e. normal to the mean flow, does exist.

A further difference between atmospheric and grid turbulence exists in the ratio u':v':w'. In Chapter 2 it was established that in the lower atmosphere the ratio u':v':w' could be assumed approximately equal to 1.92:1.54:1. Further out in the atmospheric boundary layer the difference between u', v' and w' decreases so that the turbulence becomes more isotropic. For grid turbulence, however, Batchelor (1953) states that at about 10^M downstream of the grid, homogeneity in the plane normal to the grid is established and approximate isotropy exists:

$$\text{i.e.} \quad u':v':w' = 1:1:1 \qquad \ldots.(4.7)$$

Batchelor suggests that this isotropy remains "until the permanent anisotropy of the biggest eddies becomes important in the final period of decay". Hinze (1959) also treats the decay of grid turbulence as the decay of isotropic turbulence. Naudascher and Farell (1970) state that more recent experimental evidence indicates that

$$\overline{u^2} = k\,\overline{v^2} = k\,\overline{w^2} \qquad \ldots.(4.8)$$

where k is a constant = 1.35 - 1.45, and does not vary as the turbulence decays. Batchelor himself expresses doubts about the assumption of isotropy in grid turbulence, for which he suggests that at X/M = 60 - 100, the turbulence reaches a statistical state in which about 75 - 80% of the total energy, distributed over the high wave number eddies, is approximately independent of the initial conditions, while the decay of the remaining 20 - 25% of the energy at low wave numbers indicates anisotropy in the larger eddies, especially for a single plane bar grid turbulence. Rose (1970) demonstrated the dependence of the low wave number spectral energy on the grid configuration. A flow with uniform mean shear was passed through parallel bar and square mesh grids of equal permeability, $\phi = 0.66$, but different mesh sizes, so that the initial length scale of turbulence

in each case differed. It was found that the length scale of the initial disturbance tended to fix the energy level of the resulting turbulence field.

Results of Naudascher and Farell (1970) and Baines and Peterson (1951) show that the turbulence field in the flow downstream of a grid has its virtual origin, X_o, between about 3M and 15M downstream of the grid. X_o/M decreases as the grid Reynolds number $Re_B = \frac{\bar{U}_o B}{\nu}$ increases. Beyond X_o the turbulence can be regarded as a decaying, approximately isotropic turbulence, laterally and vertically homogeneous. The degree of anisotropy can be assumed to be higher with a single plane parallel bar grid than with a square lattice grid, but still much less than the anisotropy in the atmospheric surface layer.

(b) The Decay of Grid Turbulence. In the present work high mesh Reynolds numbers are of interest. For instance, with the square mesh turbulence - generating grid later used in the 4 ft x 4 ft (1.22m x 1.22m) atmospheric boundary layer wind tunnel:

$$\bar{U}_o = 60 \text{ ft/sec} \quad (18.29 \text{ m/sec})$$
$$M = 6 \text{ in} \quad (15.24\text{cm})$$
$$B = 1.5 \text{ in} \quad (3.81\text{cm})$$
$$\nu = 1.58 \times 10^{-4} \text{ ft}^2/\text{sec} \quad (1.47 \times 10^{-5} \text{ m}^2/\text{sec}).$$

$$Re_M = \frac{\bar{U}_o M}{\nu} \simeq 1.9 \times 10^5, \quad Re_B = \frac{\bar{U}_o B}{\nu} = 0.475 \times 10^5.$$

The turbulence is generated at relatively low wave numbers, of the order of the Strouhal vortex shedding wave number, and as turbulent decay proceeds, there is inertial transfer of the turbulent energy across the wave number range and viscous dissipation of the turbulent energy at high wave numbers.

Traditional treatments of the decay of turbulence subdivide the flow field into an 'initial' and 'final' period of decay where u', λ_f, L_{u_x}, etc. are given by different expressions. Naudascher and Farell (1970) present a unified treatment of grid turbulence decay, pointing out that with the more traditional treatments the extent of each period of decay is poorly defined. In the present work, with coarse, turbulence-generating grids, the so-called initial period is of concern, where the range X/M = 60 - 100 will give a downstream fetch of 30 - 50 ft (~12m) from the grid.

Batchelor (1953) gives, for the initial period decay,

$$\frac{\bar{U}^2}{\overline{u^2}} = \frac{C}{K_o}\left(\frac{X}{M} - \frac{X_o}{M}\right) \qquad \ldots.(4.9)$$

where C = constant dependent on grid geometry.

K_o = grid pressure drop coefficient, or drag per unit area of grid, and

$$\lambda_f^2 = \frac{10\nu}{\bar{U}}(X - X_o) \qquad \ldots.(4.10)$$

Naudascher and Farell (1970) eliminate the subdivision of the flow into different zones of decay, and replace existing laws with functions that are generally applicable over the whole range of decay. Near the virtual origin, X_o, these functions reduce to

$$\frac{u'}{\bar{U}} \cdot \frac{Re_B}{C_1} \simeq \sqrt{2.5}\left(\frac{X - X_o}{B\ Re_B}\right)^{-\frac{1}{2}} \qquad \ldots.(4.11)$$

$$\frac{\lambda_f}{B} \simeq \sqrt{10}\left(\frac{X - X_o}{B\ Re_B}\right)^{\frac{1}{2}} \qquad \ldots.(4.12)$$

$$\frac{L_{u_x}}{B} = \left(\frac{L_{u_{x\infty}} - L_{u_{xo}}}{\lambda_{f_\infty}}\right)\frac{\lambda_f}{B} + \frac{L_{u_{xo}}}{B} \qquad \ldots.(4.13)$$

where C_1 = f (Re_B, grid geometry) and has the significance of an initial turbulence Reynolds number.

subscript o refers to conditions at X_o.

" ∞ " " final conditions at X = ∞

Equations 4.11 and 4.12 correspond to the traditional equations 4.9 and 4.10 respectively, and these equations enable calculation of $\frac{u'}{\bar{U}}$ and λ_f, hence L_{u_x} in equation 4.13, provided the required constants, initial and final conditions are known.

Earlier, Baines and Peterson (1951) suggested a decay law for $\frac{\bar{u}'}{\bar{U}}$, based on experiments, in the form

$$\frac{u'}{\bar{U}} = 1.12\left(\frac{X}{B}\right)^{-\frac{5}{7}} \qquad \ldots.(4.14)$$

The non-inclusion of a virtual origin, X_o, partly explains the higher exponent of -5/7 compared with equation 4.11. For the length scale of turbulence, the Baines and Peterson data fits the equation

$$\frac{L_{u_y}}{B} \simeq C_2\left(\frac{X}{B}\right)^{\frac{5}{7}} \qquad \ldots.(4.15)$$

where, for constant B, the constant C_2 increases as M increases.

Equations 4.9 to 4.13 give for the early decay, in general,

$$L_{u_x} \propto \lambda_f \propto \left(\frac{u'}{\bar{U}}\right)^{-1}$$

and $$\frac{u'}{\bar{U}} \propto \frac{1}{Re_B} \left(\frac{X - X_o}{B\ Re_B}\right)^{-\frac{1}{2}}$$

Thus, by suitable choice of grid bar and mesh size, the tunnel speed $\bar{U}_o$, a flow of turbulent intensity similar to that of a particular atmospheric flow, may be obtained at one downstream location in the flow. The length scale of turbulence at that point will determine the linear scaling between the wind tunnel and atmospheric flows.

(c) A Possible Scale Effect: In 3.4 the effect of scaling down atmospheric turbulence on the ratio λ_f/L_{u_x} was examined, and it was seen that the scaling down process shortens the inertial subrange of wave numbers in the energy spectrum, so that in a small scale simulation, unwanted viscous effects may become important in the range of energy containing eddies. To avoid unwanted viscous effects and ensure an adequately long inertial subrange, the integral length scale of turbulence in the wind tunnel flow must be as large as possible. In grid-generated turbulence, the length scale grows with distance downstream from the grid, so that it is desirable that the test position in the flow is as far as possible downstream from the grid, compatible with there being high enough turbulent intensity.

Consider the application of Batchelor's criterion, Equation 2.40, for the existence of the inertial subrange in the spectrum:

> Grid turbulence results show that at a distance of about 30 ft (~9m) from a grid with B = 1.5 in., M = 6 in., and $\bar{U}_o$ = 60 ft/sec, a length scale of turbulence, L_{u_x}, of ~6 in could be expected.
>
> Applying equation 2.57 :
>
> $$k_p = \frac{0.146}{L_{u_x}} = \frac{0.146}{0.5}$$
>
> $$= 0.292\ ft^{-1}$$
>
> Also, at X = 30 ft a turbulent intensity of 0.02 can be expected.
>
> Now, the requirement of Equation 2.40 is :
>
> $$\left(\frac{u'}{\nu k_p}\right)^{\frac{3}{8}} >>> 1.$$

$$u' \simeq 0.02 \times 60 = 1.2 \text{ ft/sec.}$$

$$\therefore \left(\frac{u'}{\nu k_p}\right)^{\frac{3}{8}} = \left(\frac{1.2}{1.58 \times 10^{-4} \times 0.292}\right)^{\frac{3}{8}} \simeq 45.$$

In the atmosphere $\left(\frac{u'}{\nu k_p}\right)^{\frac{3}{8}}$ is typically ~1000. Thus in the grid turbulence an inertial subrange should still appear but it will be much shorter than in the atmosphere.

Summarising, it appears that a grid of sufficiently large bar and mesh size will give turbulence with a range of energy containing eddies, adequately separated from the viscous dissipation range for unwanted viscous effects to be avoided. However, the mean wind speed in the tunnel should not be too low, otherwise Equation 2.40 may not be satisfied.

(d) The Spectrum of Grid Turbulence: Where a grid is coarse enough to ensure a high turbulent Reynolds number, e.g. $Re_B \sim 10^5$, and thus ensure an inertial subrange in the spectrum, the von Karman interpolation formula is found to describe the grid turbulence quite closely:

$$S(k) = \frac{2}{\sqrt{\pi}} \cdot \frac{\Gamma\left(\frac{5}{6}\right)}{\Gamma\left(\frac{1}{3}\right)} \cdot \frac{\overline{u^2}}{k_p} \cdot \left[1 + \left(\frac{k}{k_p}\right)^2\right]^{-\frac{5}{6}} \quad \ldots.(4.16)$$

(Hinze, 1959)

This is encouraging in the use of grid turbulence as a model for atmospheric turbulence, since Teunissen (1970) has concluded that Equation 4.16, written in the form of Eqn. 2.48 adequately describes the spectrum of atmospheric turbulence for the u velocity component.

(e) Scale and Intensity of Grid Turbulence: Grid turbulence data of Baines and Peterson (1951), and Naudascher and Farell (1970), were examined to obtain an estimate of the likely intensity and length scale of turbulence downstream of a coarse grid, which it was intended to fit at the entrance to the working section of a new atmospheric boundary layer modelling wind tunnel.

Square mesh grids were considered, with rectangular bars, and

B = 1½ in (3.81cm) or 3 in (7.62cm)

corresponding M = 6 in (15.24cm) or 12 in (30.48cm)

$\bar{U}_o$ = 60 ft/sec (18.29 m/sec).

For these grids $x_o/M \simeq 3$ (Naudascher and Farell, 1970).

Values of turbulence length scale and intensity at positions downstream of the grid are shown in Table 4.1. Of the figures in Table 4.1, the Baines and Peterson data are probably more realistic, as the coarseness of the grid used in this example puts it almost out of the range of applicability of the Naudascher and Farell grid performance graphs. It can be seen that the turbulent intensity rapidly falls to less than 5% downstream, while length scale is still small. e.g.

At X = 30 ft $\frac{u'}{\bar{U}}$ = 3½% and $L_{u_x} \simeq 6$ in when B = 3 in.

Generally the Naudascher and Farell (1970) data show an increase in L_{u_x} at lower tunnel speed but no significant change in $\frac{u'}{\bar{U}}$.

Results reviewed in 4.2.2 suggest that the figures for L_{u_x} in Table 4.1 are a little conservative, but the problem nevertheless remains, that it is difficult to achieve a large enough length scale of turbulence before the intensity has decayed below the desired atmospheric value. A grid of ~6 in (15cm) bar size would be required, to give a length scale of ~12 in (30cm) at the point where $\frac{u'}{\bar{U}}$ had decayed to ~10%.

Summarising, it appears that a coarse grid, with Re_B may generate turbulence that, during an early stage in its decay, represents atmospheric turbulence of similar intensity. The small length scale of the turbulence during initial decay would dictate a small linear scaling of probably less than 1:1000 in the first 10 ft (3m) from the grid. The decay of grid turbulence with distance, and the lack of variation of $\frac{u'}{\bar{U}}$ and L_{u_x} with height above the floor, z, render the grid turbulence unacceptable as an accurate model of atmospheric turbulence.

4.2.2 Experimental Evaluation of Grids used for Atmospheric Boundary Layer Simulation.

In this section the turbulence downstream of grids designed by the Cowdrey (1957) and modified Owen and Zienkiewicz (1957) methods is evaluated as a model for atmospheric turbulence. Earlier it was shown that these grids generate sufficiently accurate model atmospheric boundary layer mean velocity profiles, e.g. 1/7 power law, typical of flat open country. Do these grids adequately simulate atmospheric turbulence?

In 4.2.1 it was established (Naudascher and Farell, 1970) that grid turbulence shows some anisotropy, even early in its decay, with :

TABLE 4.1 GRID TURBULENCE DATA

Distance from Grid, ft	B = 1½ in		B = 3 in		Source
	$\frac{u'}{\bar{U}}$ %	L_{u_x} ft	$\frac{u'}{\bar{U}}$ %	L_{u_x} ft	
10	5	0.22*	8	0.25*	Baines & Peterson (1951)
	3.6	-	-	-	Naudascher & Farell (1970)
20	3	0.3*	5	0.35*	Baines & Peterson (1951)
	2.4	0.38	-	-	Naudascher & Farell (1970)
30	2.2	0.38*	3.5	0.48*	Baines & Peterson (1951)
	2.0	0.44	-	-	Naudascher & Farell (1970)

* Assuming isotropic turbulence

TABLE 4.2

Height above floor cm	Turbulent Length Scale assuming $L_{u_x} = \frac{0.146}{k_p}$	Linear Scaling d_m/d_a based on				
		Equation 2.63 $L_{u_x} = \frac{\text{atmos}}{11\sqrt{zm}}$	Spectrum Matching		Turbulent Intensity Profiles	Velocity Profile, Boundary Layer Depth
			Eqn 2.60 $L_{u_x} = 101\frac{\bar{U}_z}{\bar{U}_{10}}$	Eqn 2.61 $L_{u_x} = 151\frac{\bar{U}_z}{\bar{U}_{10}}$		
5	18.3cm	1:180	1:650	1:1050	1:1000	1:325
15	14.6cm	1:850	1:1000	1:1650	1:1000	1:325
60	4.3cm	1:39000	1:5400	1:8500	-	1:325

Linear Scaling between Wind Tunnel and atmospheric flows, 2.20 m downstream of Cowdrey, and O and Z 1/7 power law velocity profile grids

$$\overline{u^2} : \overline{v^2} : \overline{w^2} = 1.4:1:1 \qquad \ldots.(4.8)$$

This is less anisotropy than is shown by the atmospheric surface layer, but could probably be accepted.

Consider now the profiles of turbulent intensity produced by the 1/7 power law velocity profile grids in the 4 ft x 3 ft tunnel. The hot wire anemometer apparatus used for turbulence measurements is described in Chapter 6 and Appendix 6. In Fig. 4.11, $\frac{u'}{\bar{U}}$ turbulent intensity profiles are shown. Only data for the Cowdrey grid are shown for the positions X = 1.12m and X = 0.46m, nearer the grid. In Fig. 4.11 note:

(i) Higher initial rate of decay of the turbulent intensity with with distance as predicted by Eqn. 4.11.

(ii) The intensity decreases with height to an approximately constant value at ~z = 20cm. This trend is clearest at the station X = 0.46m. Turbulent diffusion causes an improvement in the intensity profiles further downstream. The height z = 20cm, where the constant value $\frac{u'}{\bar{U}}$ = 0.14 is reached, corresponds to a local pressure drop coefficient K = 1.22 on the grid. The drag coefficient for an isolated round bar is approximately 1.2, so that for z > 20cm the drag exerted by the grid is due to the separate influence of each bar. For z < 20cm, K increases rapidly as the wakes of adjacent bars interact to create a larger scale effective blockage.

(iii) The $\frac{u'}{\bar{U}}$ values between z = 20cm and z = 70cm show close agreement with data for 1 in bar grids given by Baines and Peterson (1951).

(iv) Turbulent intensity data of Harris (1970) are plotted for comparison to a scale of 1:1000. The grid intensity profiles can be seen to match the Harris data best between X = 1m and X = 2m, but the agreement is only fair. Far above z = 20cm the grid turbulent intensity remains too high for a 1:1000 scale simulation. For instance, at z = 50cm, equivalent to roughly twice the gradient height in a 1/7 power law atmospheric velocity profile, the turbulent intensity in a neutrally stable boundary layer should be < 1%.

(v) Significant difference between the results of the Cowdrey and adapted Owen and Zienkiewicz grids occurs only below z = 15cm, where the lower permeability of the Cowdrey grid causes local turbulent intensities about 10% higher.

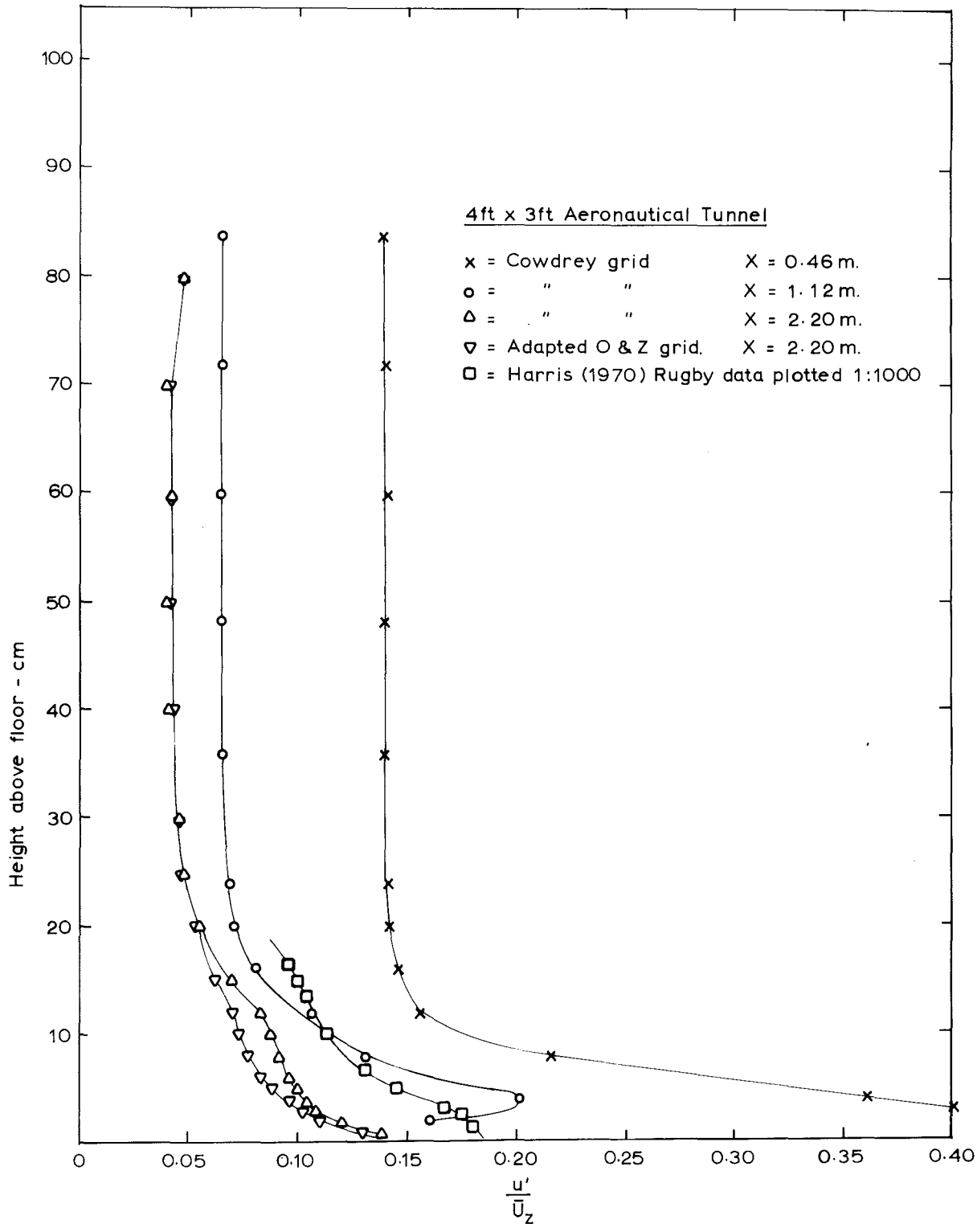

Fig. 4.11 u COMPT. TURBULENT INTENSITY $\frac{u'}{U_z}$ DOWNSTREAM OF $\frac{1}{7}$ POWER LAW VELOCITY PROFILE GRID.

In Fig. 4.12, vertical velocity fluctuations are plotted in the form $\frac{w'}{\bar{U}_\infty}$. Again, the Cowdrey grid shows slightly higher turbulent intensity values near the floor, and a decrease to an approximately constant intensity has occurred at the height z = 20cm. $\frac{w'}{\bar{U}_\infty}$ tends to be too low over the whole boundary layer depth, and would fall closer to the desired profile nearer the grid in a region of higher turbulent intensity. Note that the desired profile has been plotted as a constant value of $\frac{w'}{\bar{U}_G}$ following Eqn. 2.32. In the atmosphere $\frac{w'}{\bar{U}_G}$ will actually decrease with height. Comparing u' and w' values in the two intensity profiles at X = 2.20m (with the assistance of Fig. 4.9), it is found that the ratio u':w' is approximately 1.35. This is lower than the value of 1.92 suggested in the atmospheric model of Eqn. 2.30, but higher than the value of ~1.18 suggested for uniform grid turbulence by Naudascher and Farell (1970) in Eqn. 4.8.

The approximate 80cm depth of the bar grid-generated boundary layer corresponds to a linear scale for the mean velocity profile of ~1:350 between the wind tunnel flow and a 1/7 power law atmospheric velocity profile. There is therefore a discrepancy between this linear scale and that for the turbulent intensity profile for the u velocity component, which is nearer 1:1000.

The $\frac{-\overline{uw}}{\bar{U}_\infty^2}$ dimensionless Reynolds stress profile is plotted in Fig. 4.13 for both grids at X = 2.20m. The trends are similar to those for the turbulent intensity profiles, with $\frac{-\overline{uw}}{\bar{U}_\infty^2}$ tending too low near the floor but too high in the outer part of the boundary layer.

In Fig. 4.14, energy spectra are shown for the u velocity component at sample locations. Harris' atmospheric model spectrum, Eqn. 2.47, is plotted for comparison. At X = 0.46m and z = 4cm, the spectrum shape is reasonably close to the von Karman (or Harris) form, but k_p corresponds to a linear scaling of the simulated flow of ~1:3000. (See Appendix 7). At X = 0.46m and z = 36cm, the spectrum shape lacks similarity to the Harris spectrum, and k_p is still dominated by the vortex shedding frequency of the grid bars so that the linear scaling of the simulation based on k_p is ~1:15000. This linear scaling has no practical meaning other than that the length scale of turbulence, high off the floor, is far too small.

At X = 2.20m, the decaying turbulence shows the expected shift of the spectral peak to lower wave number, accompanying the increasing length

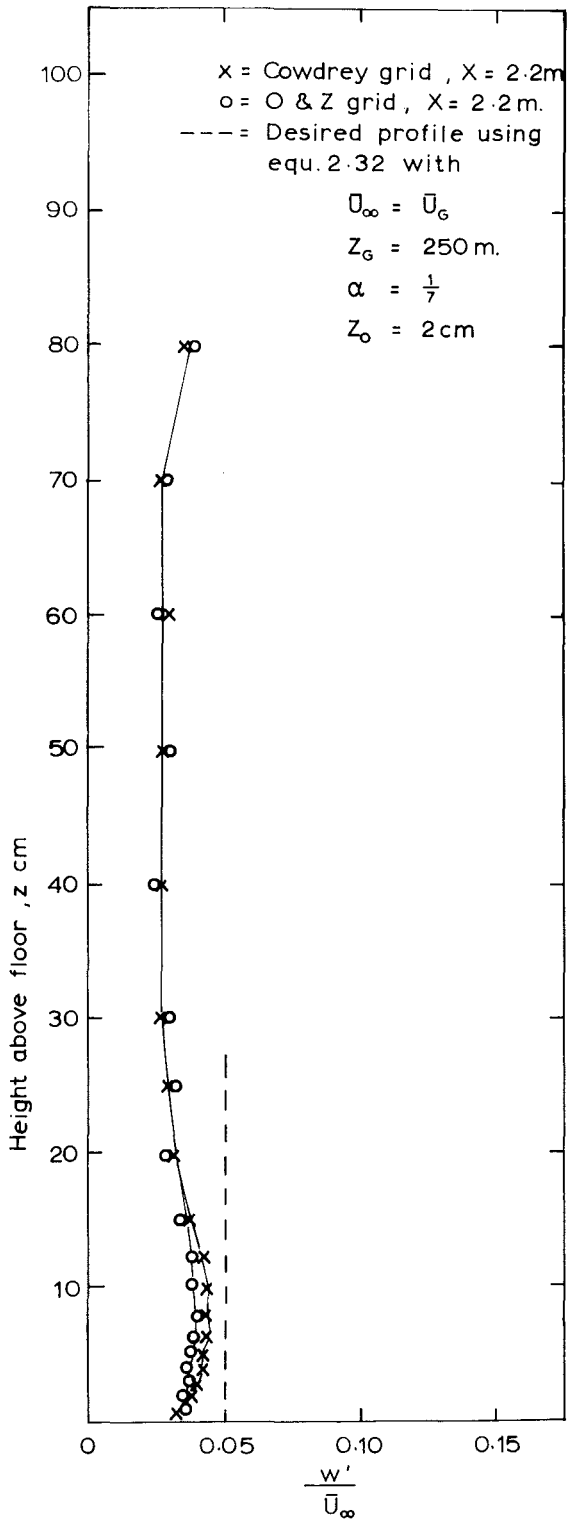

Fig. 4·12 w COMPONENT TURBULENT INTENSITY DOWNSTREAM OF $\frac{1}{7}$ POWER LAW GRID.

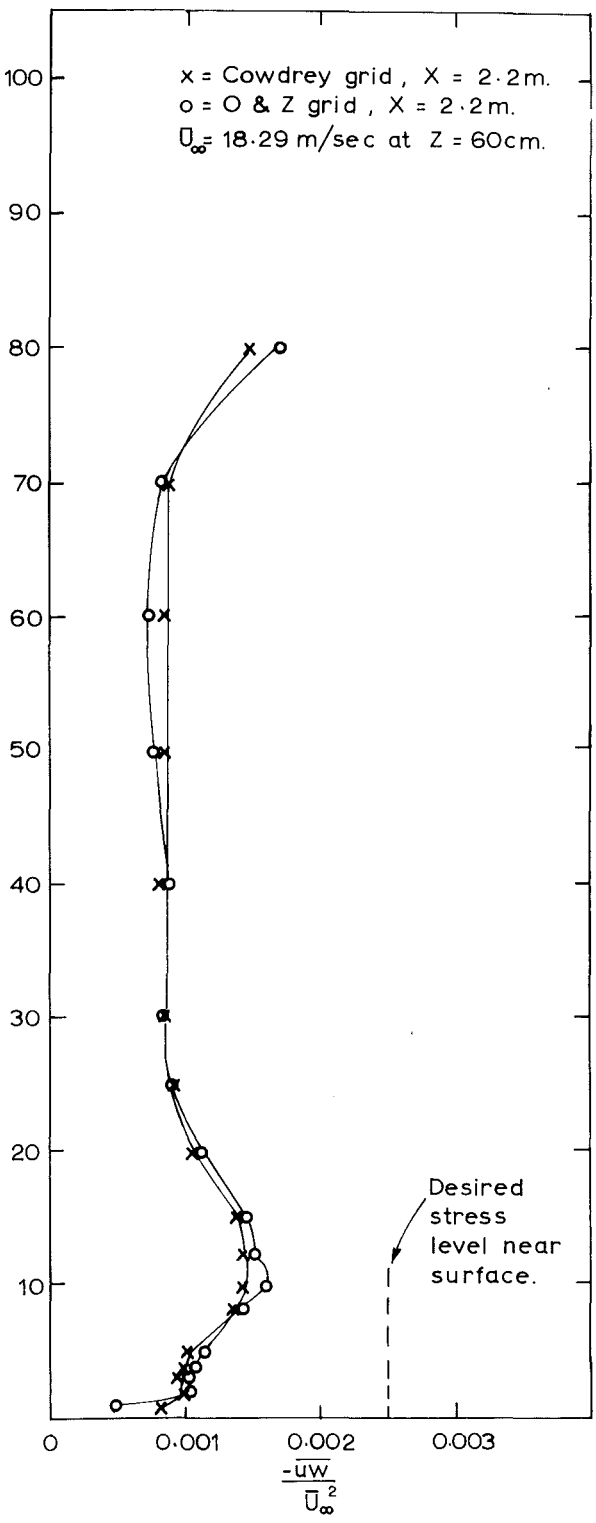

Fig. 4·13 REYNOLDS STRESS PROFILE DOWNSTREAM OF $\frac{1}{7}$ POWER LAW GRID.

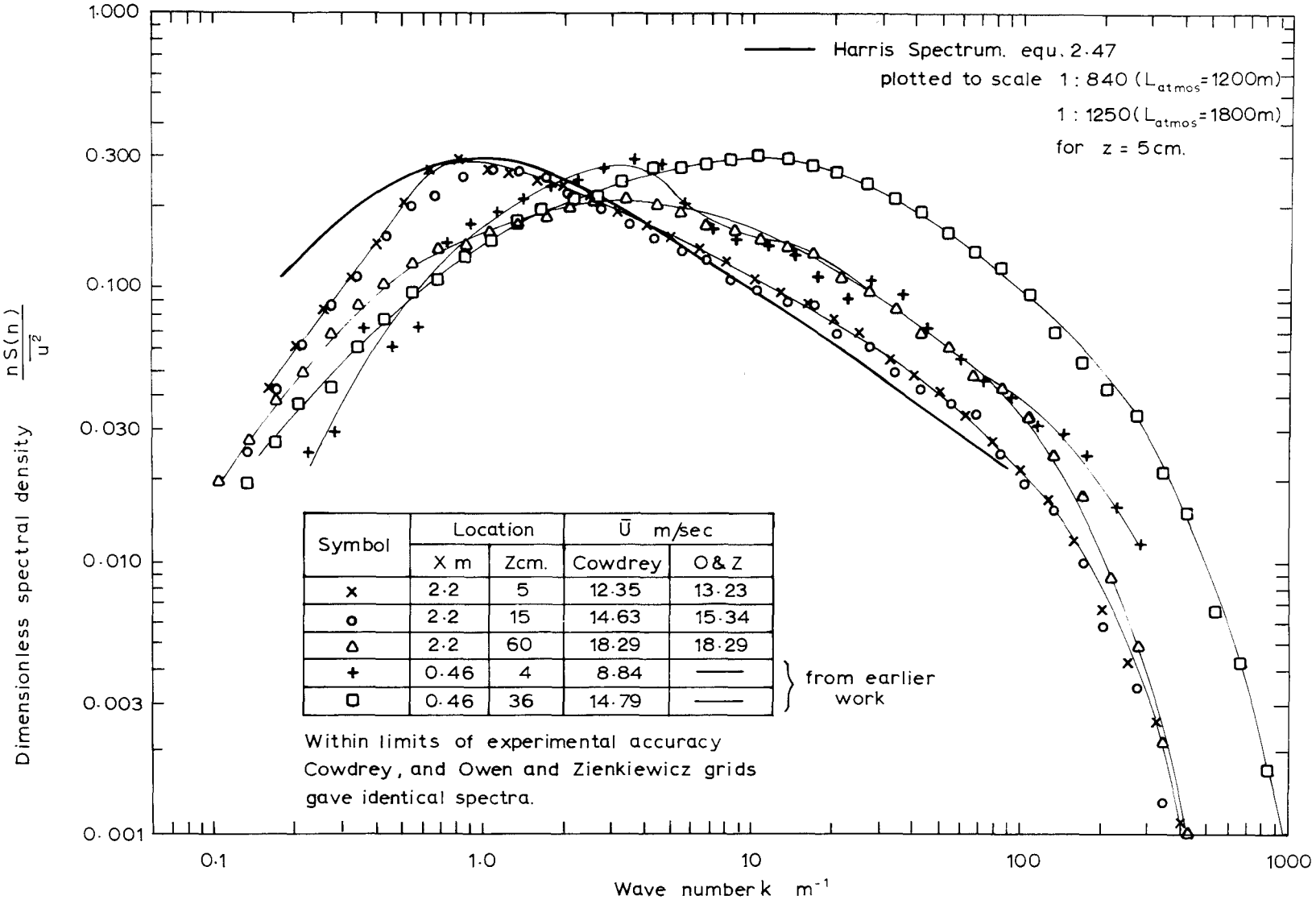

Symbol	Location		$\bar{U}$ m/sec	
	X m	Zcm.	Cowdrey	O & Z
×	2·2	5	12·35	13·23
o	2·2	15	14·63	15·34
Δ	2·2	60	18·29	18·29
+	0·46	4	8·84	——
□	0·46	36	14·79	——

Fig. 4·14 ENERGY SPECTRA FOR u VELOCITY COMPONENT, DOWNSTREAM OF $\frac{1}{7}$ POWER LAW GRIDS.

scale. Reasonable agreement with the Harris spectrum model is evident at z = 5cm and z = 15cm, but not at z = 60cm, where k_p is considerably higher (where by Equations 2.57 and 2.63 it should be lower) and there is no clearly defined region of -2/3 slope in the spectrum $\frac{nS(n)}{\overline{u}^2}$ vs k, to indicate the existence of an inertial subrange. In Table 4.2, the linear scaling of the model atmospheric flow at X = 2.20m is listed. Estimates were made using the methods set down in Appendix 7.

The results in Table 4.2 show that the low permeability of the grid leads to quite large scale turbulence near the floor, but as permeability increases with increasing height the turbulent length scale decreases. At z = 60cm L_{u_x} has become so small that the estimates of linear scaling based on comparisons of length scale are meaningless. Decreasing length scale of turbulence with height is a fault characteristic of graded blockage schemes as pointed out in 3.5 and 3.6. Pure graded blockage schemes are therefore unsatisfactory in simulating, simultaneously, profiles of mean velocity, turbulent intensity and length scale.

Summing up, it can be seen that the 1/7 power law velocity profile grids, using 1 in bars, produce:

(i) satisfactory mean velocity profiles.

(ii) turbulent intensity profiles, which below z = 20cm, are acceptably close to atmospheric data plotted on a 1:1000 scale, near the downstream end of the working section.

(iii) u component spectra, which, again below z = 20cm, show acceptable similarity to Harris' atmospheric model, Eqn. 2.47, with a linear scaling of ~1:1000. Near the floor equations 2.63 and 2.60 indicate a somewhat larger linear scaling than 1:1000 (See Table 4.2).

Outside the region of higher shear below z = 20cm, the small length scale of turbulence renders the flow unsuitable as a model of the atmospheric boundary layer.

If small linear scaling of ~1:1000 were acceptable (based on turbulence structure rather than the mean velocity profile), together with an intensity of turbulence less than 0.1 in the surface layer, the lowest 20cm of the grid-generated boundary layer tested could be used as an approximate rural atmospheric boundary layer model, at X ≃ 2.20m from the grid. This would not be a very useful simulation in the 4 ft x 3 ft aeronautical tunnel, where the working section is only 8 ft (2.44m) long.

Greater bar width, B, or diameter D could be used in a longer working section to obtain higher turbulent intensity at a given value of X/B and greater turbulent length scale. Surface roughness would almost certainly be required in addition to the bar grid to maintain the turbulent intensity at a high enough value, e.g. 0.15, close to the floor. The results of Fig. 4.11 indicate the the Cowdrey-type grid would probably be preferred because of the higher turbulent intensity it gives near the floor.

4.2.3 Review of Coarse Grid Simulations of Atmospheric Turbulence.

Very coarse, uniform square mesh grids appear to give a more satisfactory simulation of atmospheric turbulence than the grids considered in 4.2.2, but of course do not reproduce the required mean velocity profile.

Vickery (1965) gives a detailed account of measurements downstream of a coarse square mesh grid, tested in the NPL (England) 7 ft x 7 ft (2.13m x 2.13m) tunnel. The grid mesh, M, was 1/4 the tunnel width, with B/M ≃ 1/5, so that B = 4.33 in (10.67cm). To obtain a sufficiently high turbulent intensity most turbulence measurements were made at X = 8M, i.e. 14 ft (4.27m) from the grid, where mean velocity variation across the tunnel was not greater than 3%. The turbulent intensity was 0.1, and the most reliable estimate of L_{u_x}, from the peak of the spectrum nS(n) vs k, was $L_{u_x} \simeq 6$ in (15cm). Vickery's grid turbulence spectrum, shown in Fig. 4.15, exhibits a small deficit in energy at the spectral peak compared with the atmospheric models of Harris (Eqn. 2.47) and Davenport (Eqn. 2.45), but the shape is generally good. If the turbulence is assumed to be approximately isotropic, Vickery's turbulent length scale of 6 in (15cm) shows good agreement with results of Baines and Peterson (1951) for a location 40B downstream of the grid. (See Baines and Peterson, Fig. 13, 1951).

Vickery suggested a linear scaling of 1:500 for this atmospheric turbulence model, which is reasonable if the model is used to simulate the lowest 30m of the atmospheric boundary layer, but a linear scaling of nearer 1:1000 would be more suitable for simulation of the region outside the surface layer. Vickery pointed out that this model was unsuitable for conditions close to the ground where the flow is highly sheared and the turbulence very much a function of local roughness. The flow would be suitable, for instance, where the building tested is tall compared with the roughness of the local terrain and the incident mean velocity profile less important.

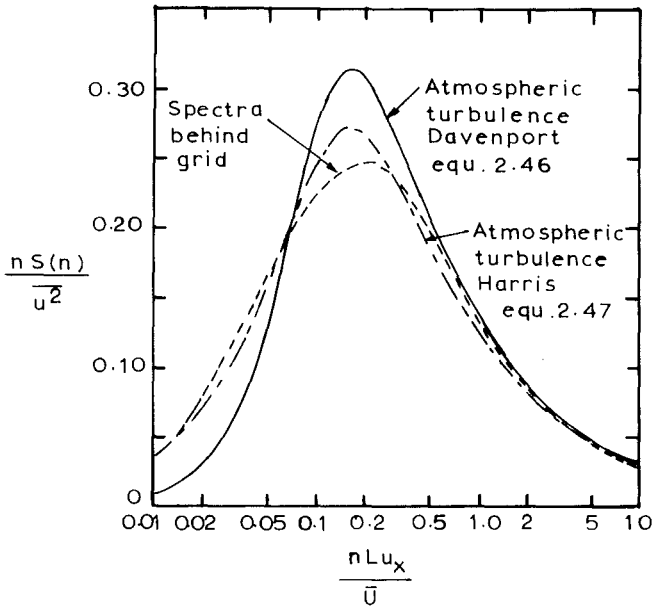

Fig. 4.15 ENERGY SPECTRUM FOR u VELOCITY COMPONENT DOWNSTREAM OF COARSE GRID. — VICKERY (1965)

Surry (1967) used a grid similar to that of Vickery in a 4 ft octagonal cross-section wind tunnel working section 4 ft (1.22m) long, again with the aim of producing homogeneous approximately isotropic turbulence of 10% intensity and large length scale. Several bar and mesh sizes were tried, with intensities ranging from 0.09 to 0.15 at 10M downstream from the grid, and length scales ranging from 0.3in (0.76cm) to 6 in (15.24cm). Anisotropy was found to be greatest with grids of high solidity and large bar width, e.g. with B = 2.9 in, M/B = 4.9 and $\phi = 0.63$,

$$u':v':w' = 1.28:1:1$$

More anisotropy than this was found in the present work using single plane parallel bar grids. Surry's turbulence spectra showed good similarity to the Dryden isotropic turbulence model (see Teunissen, 1970). Surry also tested a non-uniform coarse grid to introduce a velocity profile as well as turbulence, but the velocity profile and lateral uniformity of the mean flow were unsatisfactory.

Whitbread (1968) used two grids:

(i) that used by Vickery (1965) with models 10M from the grid;
(ii) a shear grid of 1 in (2.54cm) diameter bars placed 10.5 ft (3.2m) upstream of building models.

Whitbread's assumed linear scaling of 1:400 is probably reasonable, close to the floor, in view of results in the present work with 1 in bar grids, but would be optimistic above the surface layer. Whitbread found considerable spectral mismatch between wind tunnel and atmospheric spectra, in particular the low turbulent intensity and high spectral peak wave numbers. Whitbread presents a method for matching wind tunnel and atmospheric spectra over a portion of the wave number range, and also a square mesh coarse grid design graph based on the data of Baines and Peterson (1951).

Templin (1969) used a grid of 1/2 in (1.27cm) bars, 20 in (50.8cm) high, designed by Cowdrey's (1967) method, in conjunction with surface roughness. The addition of the bar grid thickened the profile obtained over roughness alone from about 10 in (25.4cm) to about 24 in (61cm) at a measurement point 13.58 ft (4.14m) downstream of the grid, but deviation of as much as 20% below the design 1/4 power law profile velocities occurred in the lower 40% of the boundary layer depth. The maximum turbulent intensity $\frac{u'}{\bar{U}_\infty}$ was only 0.05 and occurred at $z/\delta = 0.1$. Further out in the boundary layer $\frac{u'}{\bar{U}_\infty}$ decreased too rapidly. The spectrum of the u velocity component close to the floor plotted quite close to the von Karman model, Eqn. 2.48, but with $\frac{u'}{\bar{U}_{\infty max}}$ only 0.05, and a linear scaling of the

simulation at X = 13.58 ft of 1:1000, the flow was not a very satisfactory atmospheric boundary layer model.

Campbell and Standen (1969) tested the following grid arrangements in their small scale pilot simulation (see 3.5):

(i) a horizontal bar grid of 1/8 in (0.32cm) bars, 4.5 in (11.43cm) high designed by Cowdrey's method. A reasonable 1/4 power law mean velocity profile was obtained, but turbulent intensity profiles were poor. The u component spectrum 18 in (0.46m) downstream showed good similarity to the von Karman form at $z/\delta = 1/12$, but linear scaling was only ~1:3000.

(ii) Horizontal bar grid as above with a uniform square mesh grid 18 in (0.46m) upstream. For the square mesh grid, M = 6 in (15.24cm) and B = 0.8 in (2.03cm). The resulting mean velocity profile was fair, but lacking in lateral uniformity. Addition of the second grid upstream made turbulent intensity values too high in the outer part of the boundary layer, but good near the floor, e.g. $\frac{u'}{\bar{U}}$ = 0.12 at $z/\delta = 0.2$ and X = 18 in. Linear scaling of the simulation was about 1:1600 at $z/\delta = 1/24$, but decreased with height, as in the bar grid simulation in the present work.

(iii) Horizontal bar grid of (i) with an upstream two-size mesh grid. A finer mesh was used in the upper part of the first grid to avoid the high turbulent intensity values of (ii) at high altitude. The results were, however, generally poorer than those of (ii).

Generally, Campbell and Standen (1969) found that a coarse uniform mesh grid gave a good spectrum shape and large length scale of turbulence, but their results again show the inability of a bar grid to produce large length scale of turbulence at the same time as low turbulent intensity at high altitude.

4.3 CONCLUSIONS

(a) The Cowdrey (1967) and adapted Owen and Zienkiewicz (1957) grid design methods used in a grid design computer program predict grid designs which adequately simulate atmospheric boundary layer mean velocity profiles. The turbulence structure downstream of these grids is unsatisfactory as a rigorous model of atmospheric turbulence. The main problem is that the turbulent length scale L_{u_x} decreases as M increases

with height. L_{u_x} can only increase with height when B is constant if the permeability of the grid decreases with height, a requirement incompatible with correct mean velocity profile production. Further, as K decreases with height, $\frac{u'}{\bar{U}}$ tends to be more or less constant for $K < 1.2$ so that the turbulent intensity profile is unsatisfactory at higher altitudes.

The Cowdrey-type 1 in bar grid turbulence may be marginally acceptable as an atmospheric turbulence model if local turbulent intensities as low as 0.1 can be accepted near the floor, together with a linear scaling of the simulation of ~1:1000 (8-10 ft, or ~3m, downstream of the grid). Larger linear scaling could be obtained if the bar diameter D or width B were increased to the maximum value compatible with production of a smoothly varying mean velocity profile.

(b) Where the variation of turbulent intensity and length scale with height is unimportant, grid turbulence theory and experimental results show that turbulence from a very coarse uniform square mesh grid, e.g. B ≯ 4 in (10cm) and B/M = 1/5 is a satisfactory model of atmospheric turbulence, during the early decay of the grid turbulence. For instance, at X = 8 - 10M, where $\frac{u'}{\bar{U}} \simeq 0.1$ and $L_{u_x} \simeq 6$ in (15 cm) could be obtained, the linear scaling of the simulation would be 1:500 - 1:1000. Generally grid bar size should be as large as possible compatible with obtaining homogeneous turbulence in the plane normal to the streamwise direction. A coarse grid simulation does not meet the atmospheric surface layer requirements of

(i) anisotropy;
(ii) horizontal homogeneity;
(iii) mean velocity profile;

and is therefore unsuitable for work where flow patterns over surface features, e.g. windbreaks or embankments, are important.

(c) In general, grid simulations of the atmospheric boundary layer are used in short working section tunnels. Results in this chapter show that even if the unsatisfactory aspects of grid turbulence are accepted, a linear scaling of larger than 1:500 - 1:1000 cannot be achieved for the simulated atmospheric flow in a distance less than about 10 ft, or 3m, from the grid, so that modelling to a 1:400 linear scale in the 8 ft (2.44m) long working section of the aeronautical tunnel is not possible. Further, grid turbulence is not a satisfactory model for atmospheric turbulence in studies of flow over topographical features, such as intended

in this project. It was therefore decided to construct a new atmospheric boundary layer modelling wind tunnel and generate the simulated atmospheric flow using a combination of step-change and boundary layer growth techniques. To provide a base level of turbulence in the new tunnel working section, it was decided to fit a coarse biplane grid of 1.5 in or 3 in rectangular bars at the entry to the working section. Data of Baines and Peterson (1951) in Table 4.1 show that with a uniform approach flow of $\bar{U}_o$ = 60 ft/sec (18.29m/sec) turbulent intensity of ~0.035 and length scale of ~6 in (15cm) could be expected with the larger bar size, 30 ft (9.15m) downstream of the grid, before addition of surface roughness.

PART 2

Design, construction and commissioning of the dual facility wind tunnel.

Generation of a simulated neutrally stable rural atmospheric boundary layer.

CHAPTER 5

THE DESIGN, CONSTRUCTION AND COMMISSIONING OF AN ATMOSPHERIC BOUNDARY LAYER WIND TUNNEL

The atmospheric wind modelling criteria of Chapter 3 and the preliminary simulation experiments of Chapter 4 have shown that there was a need for a new atmospheric boundary layer wind tunnel. The design of the new facility, begun late in 1971, was dictated by three major factors:

(i) the presence, in the confined space of the aeronautical laboratory, of a recently constructed Low Noise Level Blower Wind Tunnel (Tang, 1971), of which it was desirable that part or all be included in the new construction;

(ii) the need to make the new tunnel operational as soon as possible;

(iii) available finance.

The existing tunnel had an 8 ft (2.44m) long working section, 30 in x 30 in (0.76m x 0.76m) in cross-section, with a maximum speed of 27.4 m/sec. The tunnel was driven by a single Woods 48J½ variable pitch impeller aerofoil fan, delivering 37500 CFM at about 3 in W.G.

The initial plan was to extend the existing working section length to 20 ft (the maximum possible in the 70 ft laboratory length), but this working section size was still too restrictive for a large scale simulation. Working drawings were begun on the basis of a second scheme in which a 32 ft (9.76m) long x 4 ft (1.22m) square cross-section working section was to replace components of the Low Noise tunnel downstream of the splitter silencer. Preliminary performance calculations showed that a maximum speed of 50 ft/sec (15.24 m/sec) would be obtainable in this working section, this speed being considered just adequate for the wind modelling work.

Shortage of storage space in the laboratory would have necessitated the construction of a storage platform for the redundant Low Noise tunnel components, and with construction of the new tunnel well under way, an objective assessment showed that the waste of space and equipment involved in stowing the Low Noise tunnel components should be avoided if possible. Therefore, with the assistance of a $6,000 research grant, a second stage fan was purchased and plans modified to re-erect the low noise tunnel on a mezzanine floor above the new tunnel, with a vertical corner section to connect the two tunnels. With more space at floor level, the wind modelling working section was extended to 40 ft (12.2m) in length. The final

layout gave a more versatile, dual purpose facility, with higher performance in the Low Noise working section than previously obtained. The final tunnel assembly, shown in Fig. 5.1 and DRG W36, involved design compromises which are discussed in 5.1 and was a more substantial construction than the initially planned experimental rig, but has evolved into a useful permanent facility.

A three month period was spent commissioning the tunnel for normal use. Modifications were made to some components, and measures were taken to improve the flow at the entrance to the working section. Pressure drop coefficients for most of the new tunnel sections were measured for comparison with calculated values. Tunnel performance is close to the design value, but reduced slightly by the inability of the second stage fan to deliver full power to the flow. This problem is being examined at the time of writing.

5.1 TUNNEL DESIGN CONSTRAINTS

This discussion is restricted to the construction of the wind modelling working section tunnel and corner section. Performance changes in the Low Noise tunnel are mentioned. Imperial units are used throughout this chapter as the tunnel was designed before metrication.

5.1.1 Working Section Size:

In Chapter 3 it was concluded that a 1:400 linear scale rural atmospheric boundary layer simulation should be possible in a wind tunnel working section 40 ft (12.2m) long, and 4 ft x 4 ft (1.22m x 1.22m) in cross-section. Ideally, a larger working section cross-section and length would have been desirable, to enable as large as possible a linear scaling of the simulated atmospheric boundary layer, and provide greater boundary layer growth distance. The length of the laboratory dictated the possible working section length, and the 40 ft length finally selected was obtained only at the expense of working close to the fans, where flow uniformity is normally poor. The 4 ft x 4 ft cross-section was selected as a compromise between large size (hence large linear scaling) and small size for higher speed. The maximum design velocity in the 4 ft x 4 ft section was approximately 70 ft/sec with the flow exhausting from the diffuser on the mezzanine floor. The working section size chosen is somewhat smaller than those shown in Table 5.1, but reference to CAARC C.C.663 Tech.26(1970) shows that in Commonwealth countries, working sections of this size are still relatively rare.

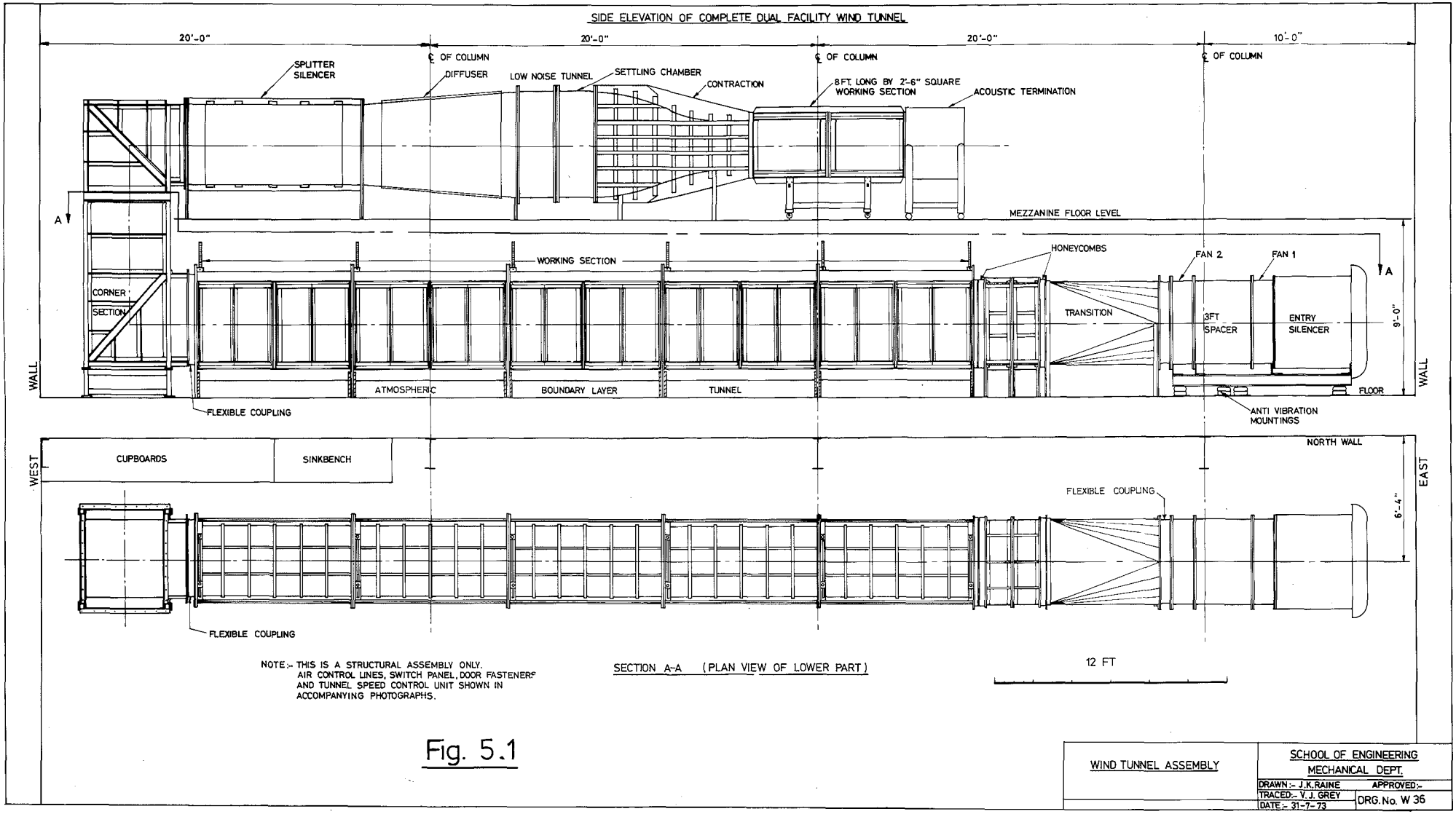

Fig. 5.1

WIND TUNNEL ASSEMBLY	SCHOOL OF ENGINEERING MECHANICAL DEPT.	
	DRAWN:- J.K.RAINE	APPROVED:-
	TRACED:- V.J. GREY	DRG. No. W 36
	DATE:- 31-7-73	

TABLE 5.1

Author	Location	Wind Tunnel Cross - section		Length ft.	Max. speed ft/sec.
		Wide ft	High ft		
Armitt & Counihan (1968)	CERL	15	5	36	35
Davenport & Isyumov (1967)	UWO	8	5½-7½	80	50
Cermak & Arya (1970)	CSU	5.9	5.9	96	130
		13.12	6.56-9.54	56	-
Vickery (1965)	NPL	7	7	24	130
	UNIV.OF AUCKLAND	6	2 - 5	32	60

On the basis of the conclusions to Chapter 3, the first 30 ft of the working section were set aside for simulation of the atmospheric flow, and the remaining 10 ft length was designated as the test section.

To increase working section versatility, the design allowed for adjustment of the roof panel height between 3 ft and 4 ft 6 in. This enabled a suitable duct divergence to be set up to give a desired streamwise pressure gradient down the working section.

5.1.2 Different Configurations of the Wind Tunnel:

The tunnel performance calculations of Appendix 2 show that the addition of the Low Noise tunnel on the mezzanine floor reduces the performance of the wind modelling working section below. The ability to extract maximum performance from the wind modelling working section was felt important, and to make the vertical corner section removable would have unnecessarily complicated the design. Pressure drop calculations showed that the air volume throughput would be reduced by only 1½% if the tunnel exhausted at the outlet from the diffuser on the mezzanine floor rather than from the outlet of the 4 ft x 4 ft working section. It was therefore decided to mount the contraction and working section of the Low Noise tunnel on castors to enable ready fitting and removal, and thus easily provide close to optimum running conditions for the wind modelling working section. With this arrangement the maximum design speeds were :

	$\bar{U}_o$ ft/sec
Wind modelling working section without Low Noise tunnel contraction and working section	70
Wind modelling working section with Low Noise tunnel contraction and working section	52.6
Low Noise tunnel working section	134.7

The design specification required maximum possible tunnel speed variation capability and provision was made for either separate or joint control of the impeller blade pitch settings on the two fans.

The wind modelling working section was designed as five interchangeable 8 ft long modules. With later inclusion of the traversing gear and air supply lines, the working section assembly was evidently to become permanent, but the modular construction proved very convenient during the construction and assembly phases. To enable rapid fitting of honeycombs, gauzes or coarse grids, spacer ducts were specified upstream of the working section, between which frames carrying the required fitting could be bolted.

5.1.3 Access to the Working Section - Traversing Gear:

With the need to fit boundary layer generating apparatus, and possibly models, along the whole length of the working section, ease of access was considered essential, and so quick-fastening doors were planned to run the full length of both sides of the working section. On one side these doors were to be clear glass or perspex.

Earlier work in the 4 ft x 3 ft Aeronautical Tunnel had shown that for wind modelling work,at least two-dimensional, and preferably three-dimensional instrument traversing gear was required. Full working-section length traversing capability was therefore planned, with the imposed condition that the traversing gear should cause minimum flow blockage and minimum air leakage from the tunnel.

5.1.4 Rigidity of the Structure:

Generation of large scale simulated atmospheric turbulence in a wind tunnel tends to result in a certain amount of structural vibration. The working section therefore required rigidity with ample damping. Structural deflection criteria were selected to give a large factor of safety on mechanical and wind loading. To enhance structural damping, finished appearance and ease of model mounting in the tunnel, wood was chosen for the working section structural framework and floor, with aluminium alloy for the doors and door frames.

Anti-vibration mountings were specified for the fans, and a flexible rubber joint between the fan ducts and the rest of the tunnel. A second flexible joint was specified at the junction between the working section and the vertical corner section to allow for thermal expansion and prevent transmission of mechanical vibration.

5.1.5 Flow Requirements:

Ideally, a uniform steady flow of, say, less than 0.5% turbulent intensity was desired at the entrance to the working section. Working close to the fans, and the absence of a settling chamber and contraction were to prevent this condition being met, but provision was made for installation of flow redistributing guide vanes and honeycombs to remove at least large scale velocity fluctuations, non-uniformity and swirl.

5.1.6 Safety Features:

These were to include :

(i) a safety screen at the fan inlet;
(ii) overload cut-outs on the fan motors;
(iii) pneumatic-electric interlock to prevent the fans from starting on coarse pitch;
(iv) the fitting of sound absorbing panels around the laboratory and silencers in the tunnel to keep noise from the tunnel to an acceptable level.

5.2 DESIGN OF INDIVIDUAL WIND TUNNEL COMPONENTS

Drawings referred to in this section may be found in Appendix 8.

5.2.1 The Two-Stage Fan Unit:

The near-new Woods 33HP 48J½ aerofoil fan in the Low Noise tunnel was basically unsuited to the new facility, which required a fan with a much higher volume throughput, e.g. Woods 60J2 with 47BHP motors. Ideally, a single stage fan was wanted, with downstream guide vanes to straighten the flow, and fan speed control by, say, Ward-Leonard Drive as in the 4 ft x 3 ft aeronautical tunnel (Stevenson, 1968) rather than blade pitch adjustment, for tunnel speed control. These features would have given greater simplicity and quietness of operation.

As a compromise to include the existing fan in the new scheme, tunnel performance was boosted by fitting a second stage Woods 33HP 48J½ fan with the correct spacer duct, so that the system became a standard Woods 48J½-2 arrangement, with the fans contra-rotating to avoid the need

for downstream guide vanes. The design maximum efficiency operating condition for the new fan was Q = 48000 CFM at ~6.1 in. W.G. fan static pressure, with blade pitch 17° on both fans. This is equivalent to $\bar{U}_o$ = 128 ft/sec in the Low Noise tunnel working section. Pressure drop calculations for the various tunnel components, and performance estimates are given in Appendix 2, together with the Fan Performance Chart. Also summarised in Appendix 2 are actual tunnel performance data for various configurations of the tunnel. Estimated and measured tunnel air volume throughput figures show that with the complete, empty tunnel, the fans should not be loaded quite as heavily as the maximum efficiency loading given above.

Flow speed regulation in the tunnel was achieved by varying the pitch of the fan blades. Low pressure air (0 - 15 psig) fed through a rotary air seal on the boss of each impeller acts on a diaphragm which controls blade pitch via linkages connected to each blade (or wing) root. The air supply arrangement is illustrated schematically in Fig. 5.2, and the air supply lines and speed control panel can be seen in Fig. 5.3. The control panel was mounted on a table with castors to enable ready positioning near the desired part of the working section. 'Aro' couplings were mounted on the high pressure supply and low pressure delivery lines along the side of the tunnel to connect with the short leads from the control table. A further pair of long air lines were rigged to the mezzanine floor so that speed control could be made from the Low Noise working section.

As a makeshift means of obtaining separate fan blade pitch control, isolating valves were fitted to the air lines just before each fan. Further air line branches were taken off to each Fan Motor-Starter, and fed to pneumatic-electric interlock switches, which prevent the fans starting except on finest pitch. This protective device prevents overloading of the mains electrical supply and the star-delta fan starters. The fan speed control requires air supply pressure to be regulated to no greater than 15 psig .

A new lengthened fan chassis was designed, with additional anti-vibration mountings. The chassis side elevation is shown in DRG W1. The anti-vibration mountings were positioned so that the fan and spacer duct assembly sat level. Static and dynamic balance of each fan was checked and datum pitch settings corresponding to a coarse pitch of 17° were made. The tunnel inlet, fan units and starter boxes can be seen in Fig. 5.4.

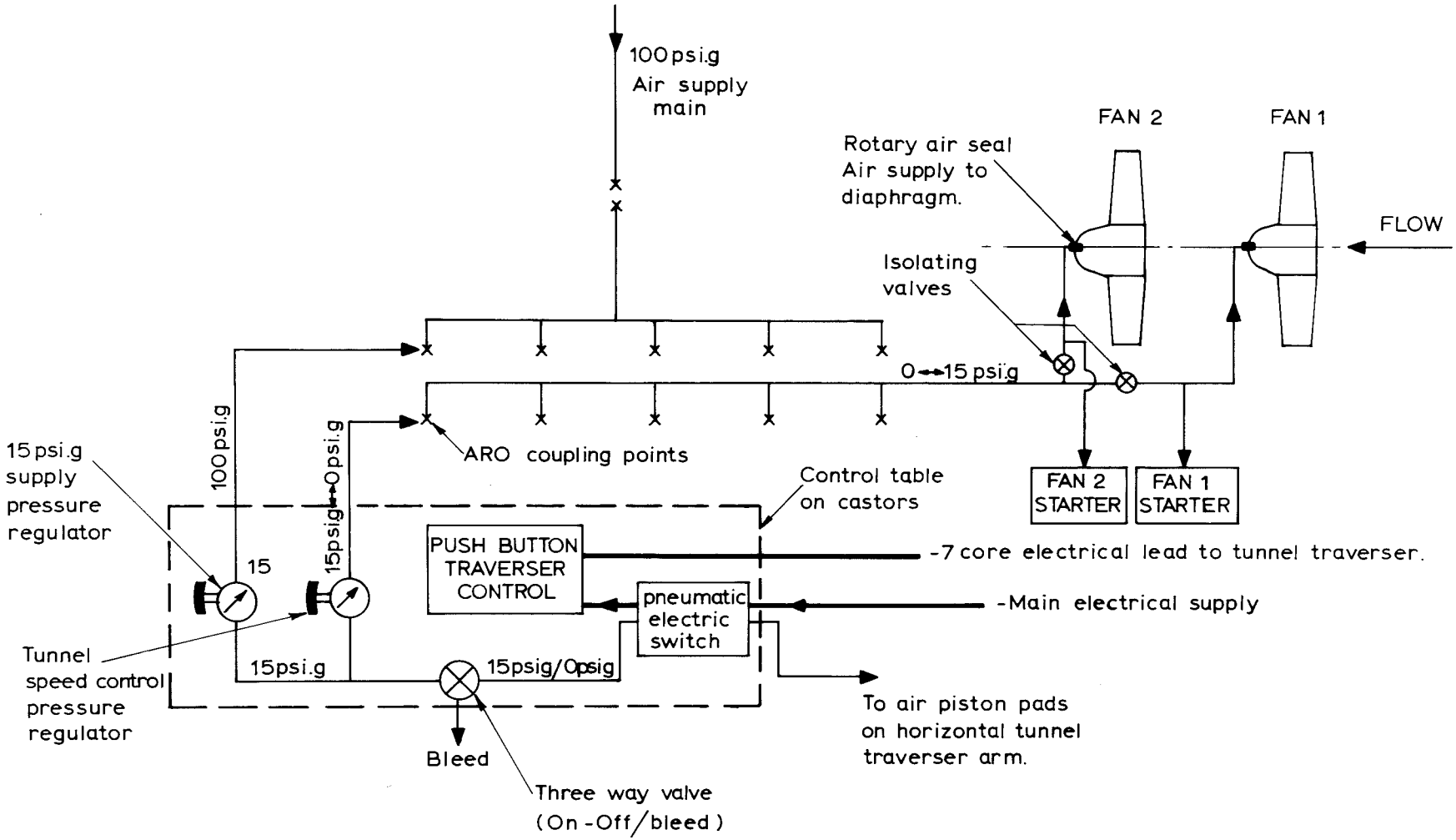

Fig.5-2 AIR SUPPLY TO WIND TUNNEL

Oblique view of lower working section towards vertical corner section

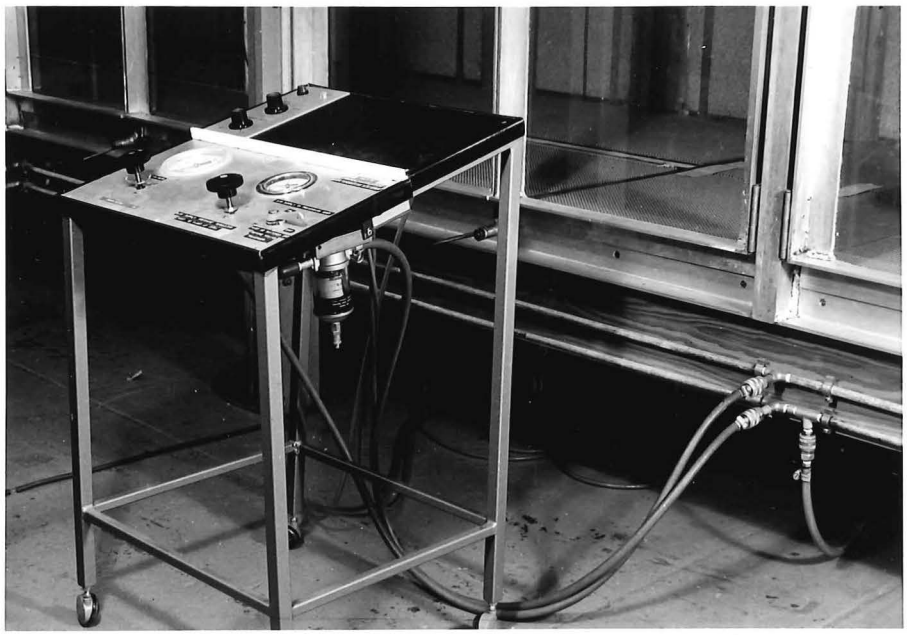

Wind tunnel control panel and air supply lines

Fig. 5.3

5.2.2 Round-to-Square Transition-Silencer:

The 4 ft diameter to 4 ft square transition downstream of the fans has a double skin with the 2 in intermediate space packed with AHI semi-rigid SF300 fibre glass batts. The outer skin is steel, and the inner skin punched aluminium sheet stiffened with wooden cleats on the back. The sound absorbing batts are coated to prevent entrainment of fibreglass particles into the flow. The equivalent cone angle of the transition silencer is 5.5^{o} which conforms with current diffuser design practice (Cockrell and Markland, 1963). A view of the fans and transition duct is shown in Fig. 5.4.

5.2.3 Wooden Spacer Ducts:

These are shown in DRGs W1 and W2. Designed in oregon framework with 3/4" M.D. particle board panelling, each duct was drawn up with 17" streamwise length. These lengths were later modified to 18" and 16" to make use of existing framework and an access door was built into the longer duct as shown in the tunnel view of Fig. 5.3.

5.2.4 Honeycombs and Honeycomb Frames:

Two 3 in streamwise thickness flow straightening honeycombs were constructed using CIBA 'Aeroweb' Type E383BU aluminium honeycomb. For these honeycombs the pressure drop coefficient was calculated (Ower and Pankhurst, 1966) as 0.45, for each honeycomb. The turbulent intensity generated by the honeycombs was calculated as 0.2% 12 ft downstream of the honeycombs (Pankhurst and Holder, 1952).

The use of honeycombs for flow straightening is well established, and in this application it was hoped that the small cell size would remove large lateral and vertical velocity fluctuations, and reduce streamwise velocity fluctuations. The expression given by Dryden and Schubauer (1947), Eqn. 4.3, for the turbulence damping by a wire gauze, should also be able to give a rough indication of the turbulence damping ability of a honeycomb. In Eqn. 4.3 it can be seen that K_o needs to be reasonably large for one screen to be effective in damping turbulence, and it is easily shown that two screens of $K_o = K_1$ would be more effective than one screen of $K_o = 2K_1$. In the present case, with $K_o = 0.45$, the effect of one screen is to reduce u' by 17% and of two screens to reduce u' by 31%. The honeycombs would be less effective than this in removing turbulence because of their relatively coarse mesh of 0.375 in., compared with usual wind tunnel screen mesh sizes of 0.03 - 0.05 in. The main purpose in fitting the

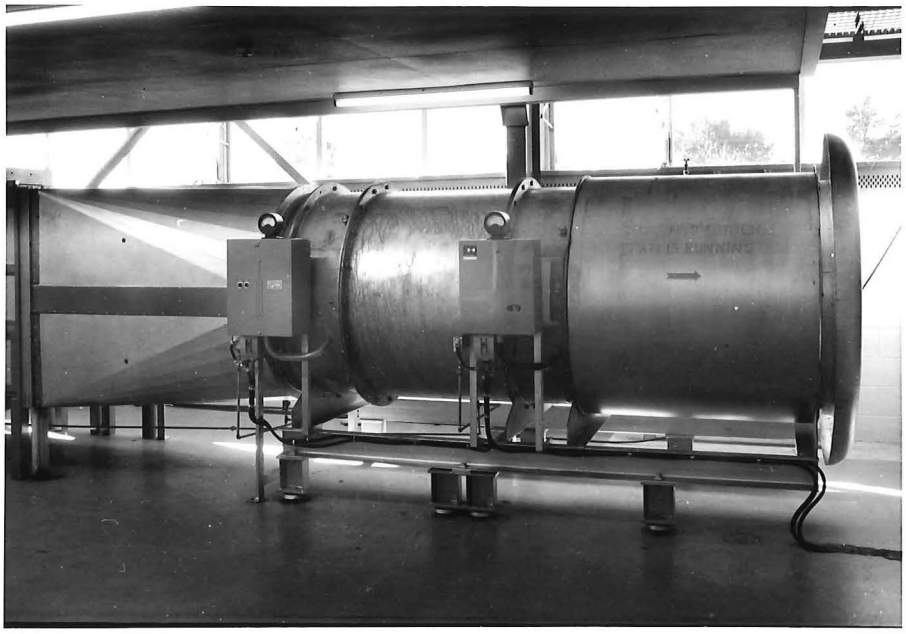

Fig.5.4 Bell mouth tunnel inlet and fan motor control boxes

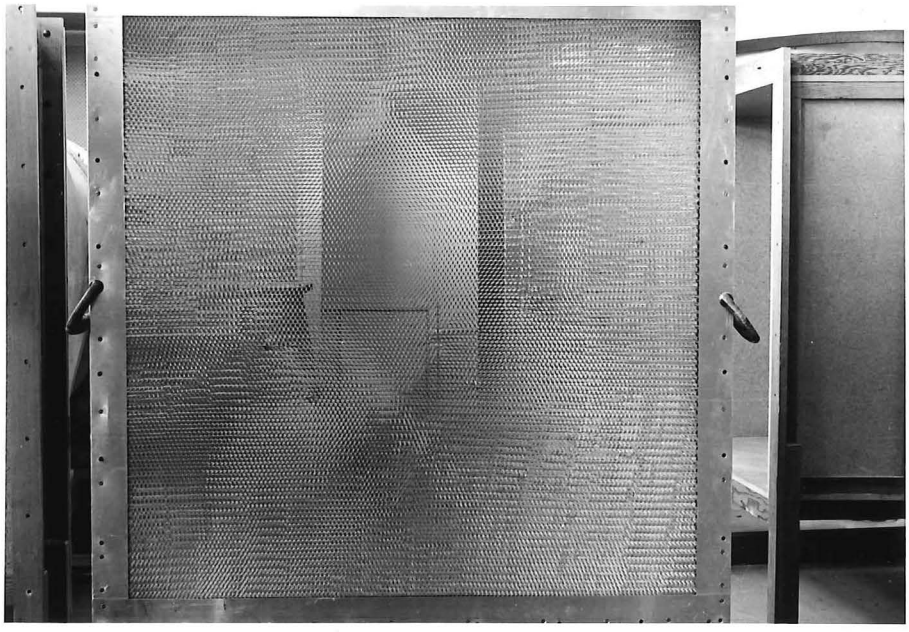

Fig. 5.5 Flow straightening honeycomb before insertion in wind tunnel

honeycombs was that of flow straightening, and the estimated pressure drop coefficient of 0.45 was high but unavoidable in the 4 ft x 4 ft duct upstream of the working section.

Use of fine wire gauze screens was considered for damping of turbulence and improvement of flow uniformity at the entrance to the working section, according to Equations 4.3 and 4.4. However, with expected gross lateral non-uniformity in the mean flow velocity at the working section entrance (found later to be ±30% about the mean), two gauzes of pressure drop coefficient $K_o = 2$ would have been required to reduce this lateral non-uniformity to less than 5% (Four screens of $K_o = 1$ would make this less than 3%). Such a large pressure drop coefficient, and the consequent performance loss were not considered acceptable. Gauze screens may be fitted at a later stage, if better lateral uniformity is required than that now provided by flow redistributing vanes and a coarse turbulence generating grid at the working section entrance. The extra loss could be offset by fitting an exhaust diffuser on the Low Noise working section. The use of turbulence damping screens in the conventional manner was prevented by the lack of streamwise space in which to include a contraction and large cross-section settling chamber, where screens would be fitted and losses minimised because of the low velocity.

In the initial assembly of the wind tunnel the honeycombs were fitted 36 in apart, with the most downstream honeycomb right at the working section entrance. The cell length of the honeycombs was 3 in, and with 0.375 in across flats of the hexagon cell, the cell length to mesh ratio was 8. This was considered adequate to remove residual swirl from the flow downstream of the second fan. Ideally, the contra-rotating impellers should produce no nett swirl, but a few degrees of swirl were found under some part-load conditions. A view of a honeycomb in its frame is shown in Fig. 5.5

The honeycomb frames, shown in DRG W3 were simply oregon frames in which the honeycombs were retained by 16G. aluminium plates screwed on the front and rear faces, so that the final opening size was 4 ft x 4 ft to match the tunnel duct size. Final drilling of the mounting bolt holes was done with the frames clamped in position in the tunnel in order to precisely locate the 4 ft x 4 ft opening. In normal use, honeycombs can be installed or removed in about 15 minutes.

5.2.5 Working Section Framework:

Several factors influenced the choice of timber and aluminium alloy construction for the working section framework:

(i) Ease of modification to the inside of the working section;
(ii) Ease of fixture of models in the working section;
(iii) Damping of sound and vibration;
(iv) Manoeuvrability of the finished framework was important, and it was desirable to keep structural weight and weight of the suspended roof panels low.

In regard to cost, little difference was involved between the method used, and steel construction.

During and after construction, the timber framework tended to warp owing to an insufficient seasoning time brought about by short supply conditions. Some difficulty was also encountered in obtaining a satisfactory weld quality in the argon arc welded aluminium frames, so that their final appearance was impaired. In retrospect, steel construction would have been more rapid and possibly less susceptible to pitfalls, but would have meant forfeiting the above listed advantages and would have been visually less attractive than the varnished wood, and aluminium.

The oregon working section framework was originally designed to take self-weight and fan stagnation air pressure loads, on the assumption of a single fan drive and about 3.8 in W.G. stagnation pressure. With later addition of the second fan unit the maximum static wind load in the tunnel became about 8 in W.G. Stresses and deflections were recalculated for the now completed working section framework, but maximum deflections in the framework, and wood panels were still less than 0.005 in, which was felt acceptable. Provision was made, however, to install a clamp across the longitudinal joists enclosing the roof panel to prevent excessive air leakage past the edges of the floating panel.

The working section framework is shown in DRGs W4 and W5 (assembly). Floor panels of 3/4 in M.D. particle board were screwed to the main floor joists, without glueing, to facilitate rapid removal and replacement. The framework and floor panels were sealed and varnished promptly to prevent further drying and distortion of the timber. Warping of some of the more heavily loaded timber did occur, and required correction before further fitting work took place. The five completed module frames were temporarily

bolted up in position to minimise further movement of the timber. Partial views of the frames are shown in Fig. 5.6. Note the presence of some of the wall panels, the roof panels and roof hoisting gear box units.

5.2.6 Working Section Roof and Walls:

Roof panels were constructed from oregon framework with a ¼ in tempered hardboard skin. Sealing of adjacent roof panels against each other and against the longitudinal roof joist at each side, was achieved by grooving the sides and ends of the roof panels and insetting a hard felt strip which sat proud of the timber. Roof panels set end-to-end for assembly can be seen in Fig. 5.6 and the roof panel is detailed in DRG W6.

The walls of the tunnel were wood-panelled on the side nearest the laboratory wall (north), and panelled with ¼ in armour plate glass on the other side (south). Identical aluminium alloy door frames were screwed (with sealant) to the oregon framework on both sides of the tunnel, as shown in DRG W7. The working section walls were effectively doors over its full length, with 20 doors each side. Use of suspended doors as on the 4 ft x 3 ft aeronautical tunnel (Stevenson, 1968), was rejected in favour of side-hinged doors, because of the restricted head room and the need for easy, rapid opening. The doors were designed for an opening angle of at least 120°. The doors were hinged with modified removable-pin 4 in butt hinges, which could be quickly dismantled for rapid removal of the doors.

The 1 in thick wood panels on the north side doors were laminated from ½ in M.D. particle board. These panels were slotted from top to bottom at 12 in intervals along the whole working section length to provide instrument access. Oregon slot-plugs were fitted in the slots. Wood panel doors are shown in DRG W8 and the slot-plugs in DRG W9. An oblique view of the wood panel doors is seen in Fig. 5.6. The glass panel doors of DRG W10 were more complicated to assemble. The window glass had to be packed out from its aluminium framework in some places to give a flush finish on the inside wall of the working section. The armour plate glass panels were glued to their frames using Araldite or Epiglue. The final strength of the glued joint was difficult to evaluate because

(i) the smooth glass and aluminium alloy surfaces gave a non-ideal bonding surface;

(ii) deflection of the glass panels under wind loading leads to stress concentration in the glued joints.

Fig. 5.6 Views of working section framework before and after erection of roof panels

Roof panels are resting on floor framework in photograph at left.

During commissioning of the tunnel two glued joints failed under a static loading on the door panel of 4 in W.G. These were reglued and no further trouble was experienced. As a precaution, a door was proof loaded to the equivalent of 8.4 in W.G. with cast iron weights, without failure. The glass door panel assemblies are visible in the middle distance, Fig. 5.3 .

Door catches were simply ramp-type clamps. A test mock-up was made in wood, and the 40 production clamps cast in bronze. The door catches, of which a sample is shown in Fig. 5.7, were spring loaded on their spindles for easy operation. Air sealing between the aluminium alloy door frames and the oregon working section frames was ensured by using a non-hardening jointing compound. Sealing between the doors and door frames was achieved with soft ½ in plastic foam draught excluder sealing strip. This sealant requires periodic replacement on doors that are frequently opened.

5.2.7 Roof Hinges, Hoisting Gear and Roof Clamps:

The design specification for the movable roof was a roof height variable from 3 ft to 4 ft 6 in. For normal use the roof was intended to be set at 4 ft height at the working section entrance, diverging as required up to a maximum of 6 in in 40 ft to maintain constant pressure in the simulated atmospheric boundary layer. A divergence of 6 in in 40 ft corresponds to a static pressure regain in the empty working section of ~5mm W.G. at a mean working section inlet speed of about 70 ft/sec. This range of static regain was ample to allow adjustment for zero streamwise pressure gradient in the model rural boundary layer. However, with say 4 in high floor roughness elements such as used by Davenport and Isyumov (1967) for an urban boundary layer simulation, it was calculated that a static pressure drop of as high as 14mm W.G. was possible with no roof divergence. Under these conditions, the roof height at the working section inlet may need to be lowered to about 3 ft 6 in to achieve zero streamwise pressure gradient, and a roof contraction insert would be required just upstream of the first roof panel. To cope with different settings of the roof, sliding hinges were designed to connect adjacent roof panels, as shown in DRG W11 and Figs. 5.6 and 5.8.

The roof panels were suspended from threaded steel rods giving 18 in travel. These roof hangers were connected to mountings shown in DRG W12 and Fig. 5.8. The six sets of roof hoisting gear each consisted of two interconnected worm and worm wheel gear boxes designed around Penfold $1\frac{1}{8}$ in centres worm and worm wheel sets, using Nylatron bearing material so that no oil bath lubrication was required. The roof hoisting gear is

Cast bronze door clamp

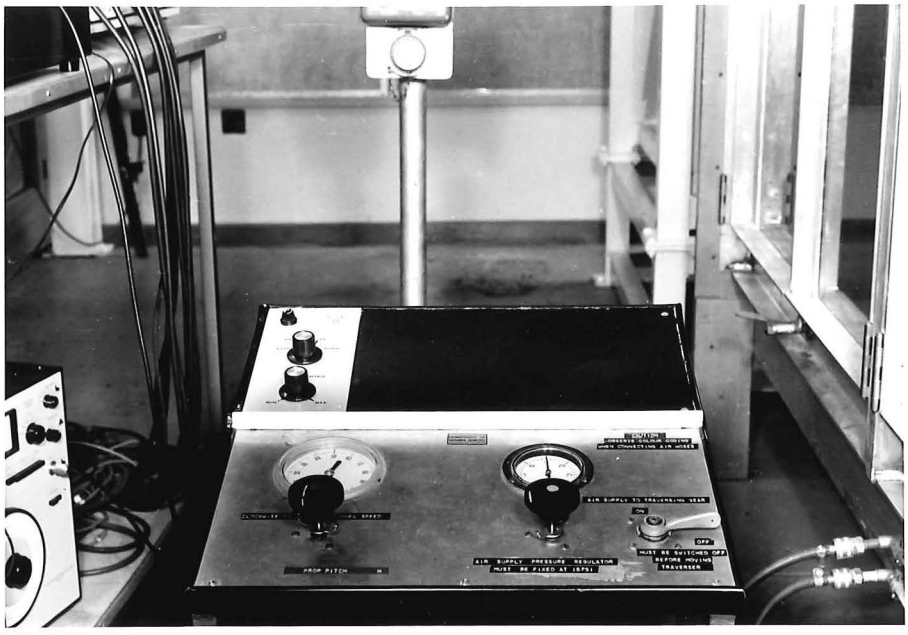

Tunnel control panel showing traverser control at top left

Fig. 5.7

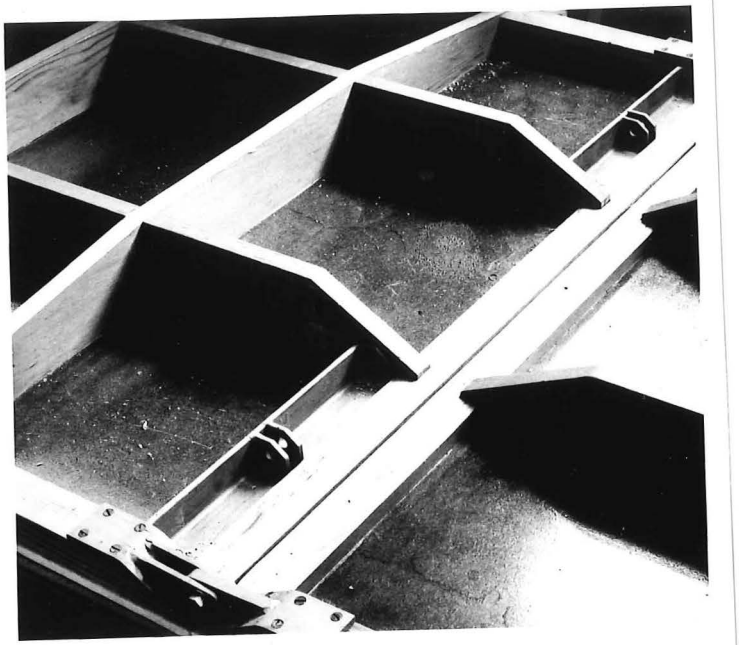

Abutting roof panels showing hinge and roof hanger mountings

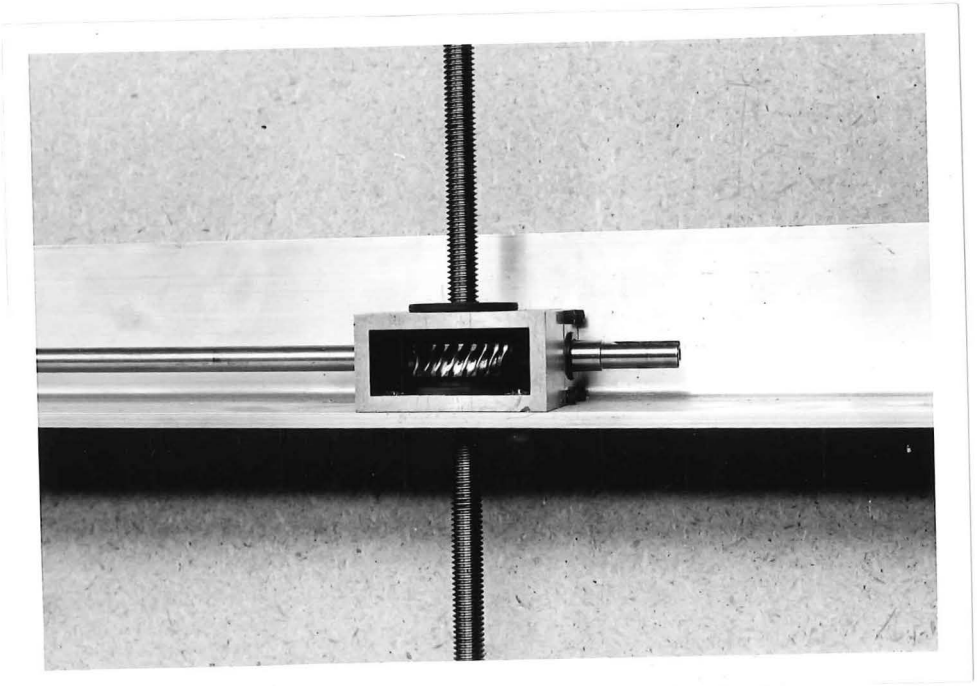

Roof hoisting gearbox detail

Fig. 5.8

mounted on an angle bracket bolted through the top flange of the working section module end frame. The squared end drive shaft for the hoisting gear sets is operated with an electric hand drill or hand-driven wood-working brace. The roof hoisting gear is detailed in DRGs W13 and W14 and may be seen in Figs. 5.8 and 5.9. Various other schemes were considered for raising and lowering the roof, including the chain driven and lever arrangements sketched schematically in Fig. 5.10. The scheme used, however, provided the best combination of compactness, good location and easy adjustment.

Roof clamps were fitted for the following reasons :

(i) to improve structural rigidity;

(ii) to prevent air leakage around the roof panel at high static air pressures, and at the same time ease the compressive load on the threaded roof hoisting hangers;

(iii) to spread the longitudinal roof joists each side of the tunnel, and thus reduce friction during roof adjustment.

These roof clamps operated on a G-clamp principle, but were attached to the side members to facilitate (iii) above. The clamps are shown in DRG W16 and can be seen in Fig 5.9.

This completes the description of the working section structure. An isometric assembly of one working section module appears in DRG W15.

5.2.8. Traversing Gear:

The decision to use motorised traversing gear inside the working section posed an interesting design problem, since at least streamwise and vertical traversing were required, with minimal blockage of the tunnel cross-section. A scheme such as sketched in Fig. 5.11 would have been bulky and made access for wiring, and fitting of motors, awkward. Further, any scheme which swept close to the floor as in Fig. 5.11 would prevent the fitting of surface roughness.

It was therefore decided to fit all the control equipment and drive system outside the working section, and gain access to the inside via a longitudinal slot. With boundary layer generating apparatus on the floor it was desirable that this slot be in the roof, but this proved impracticable with the suspended, movable roof construction. An access slot in the floor was finally chosen, with a motorised trolley running in the channel underneath.

Fig.5.9 Views of roof hoisting gear and roof panel clamps prior to construction of mezzanine floor.

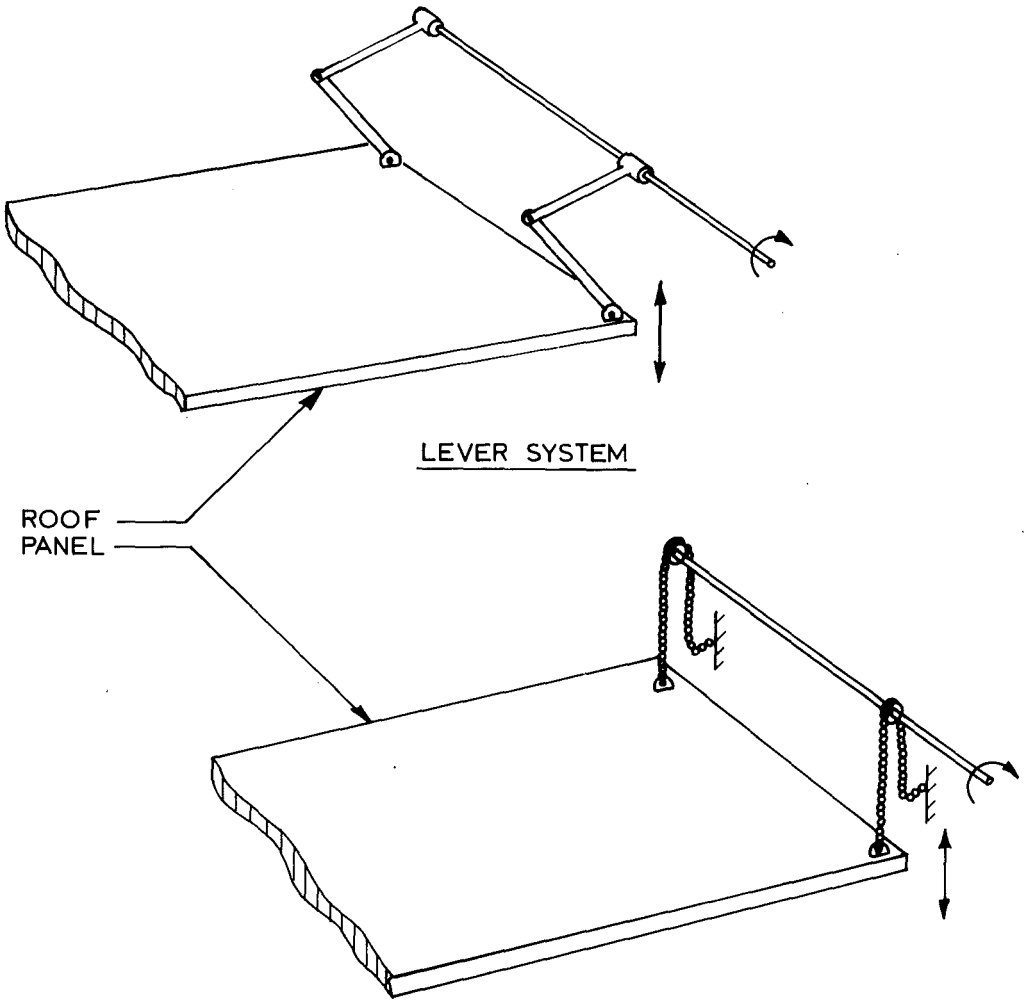

Fig.5.10 ALTERNATIVE SCHEMES FOR SUSPENSION ROOF PANEL

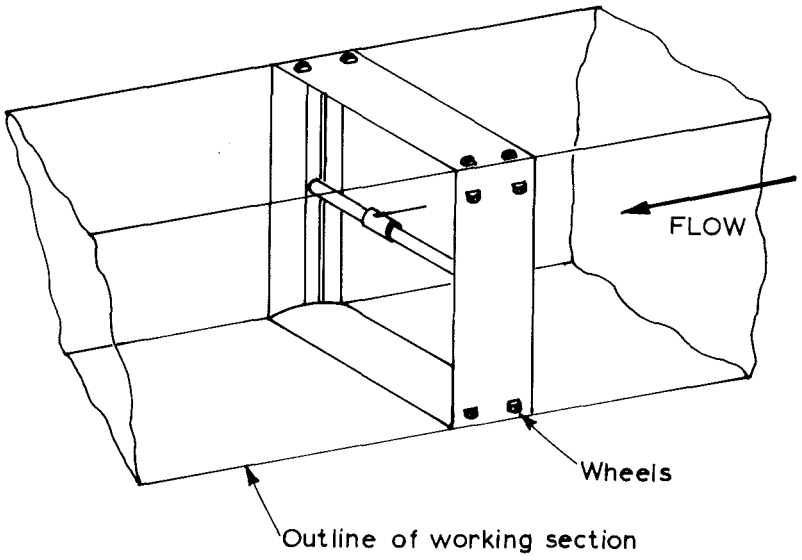

Square frame fits inside tunnel and runs on small wheels. Drive equipment shrouded inside streamlined skin of framework.

Fig.5.11 REJECTED TRAVERSER SCHEME.

Three major alternatives were considered for the vertical traversing system, as shown in Fig. 5.12. The hydraulically operated, telescopic vertical stanchion was attractive, but the 6 in depth of the space beneath the floor was insufficient to accommodate this scheme (see Fig. 5.6). The pivoted arm system would have necessitated longitudinal traversing during vertical positioning, an undesirable complication. The system selected utilised a vertical lead screw inside the stanchion, with a nut on the lead screw carrying a horizontal arm. This system had the advantages of simple operation from outside the working section, good streamlining and easy positioning. The vertical lead screw was driven through a bevel gear drive, using a 60 watt Singer sewing machine universal motor. Horizontal longitudinal traversing was achieved with a Parvalux 1/5 HP universal motor driving through a Penfold worm and worm wheel reduction onto one of the trolley axles.

The trolley itself has an aluminium chassis, and axles front and rear, carrying wheels to run on rails at the side of the underfloor channel, and modified Renold 212006 chain wheels which provide the drive onto a tensioned chain rack each side of the channel. The complete traversing trolley with motors, controls and vertical stanchion weighs 35-40 lb wt., and the tilting moment caused by wind drag on the traversing gear was calculated insufficient to cause tipping of the trolley. As a precaution, however, steadying springs were mounted on top of the trolley, and these run on 'Tufnol' low friction rubbing strips glued to the underside of the floor panels. DRGs W17, W18 and W19 show the components and assembly of the traversing trolley and vertical stanchion.

Two horizontal arms were built for the traverser. The first was a wing carrying a bank of pitot and static tubes, every third tube being a static tube. The pitot static wing is shown in DRGs W21 and W22. The second horizontal arm was simply a hot wire anemometer probe mounting bar as shown in DRG W23. With the relatively slender vertical stanchion, low frequency (<10 Hz) vibration was anticipated and air operated steadying pads were fitted to both the pitot static wing and the hot wire mounting bar. These pads were initially to be as shown in DRG W21, but this scheme was discarded in favour of the air piston arrangement of DRG W23. The pads press against the tunnel walls and use 15 psig air, which must be released before traversing can take place. A pneumatic-electric interlock ensures this. Tubes from the horizontal arms pass through the hole in the top of the trolley, visible in Fig. 5.13, and in the case of the pitot and static tubes connect to two multi-tube quick release couplings shown

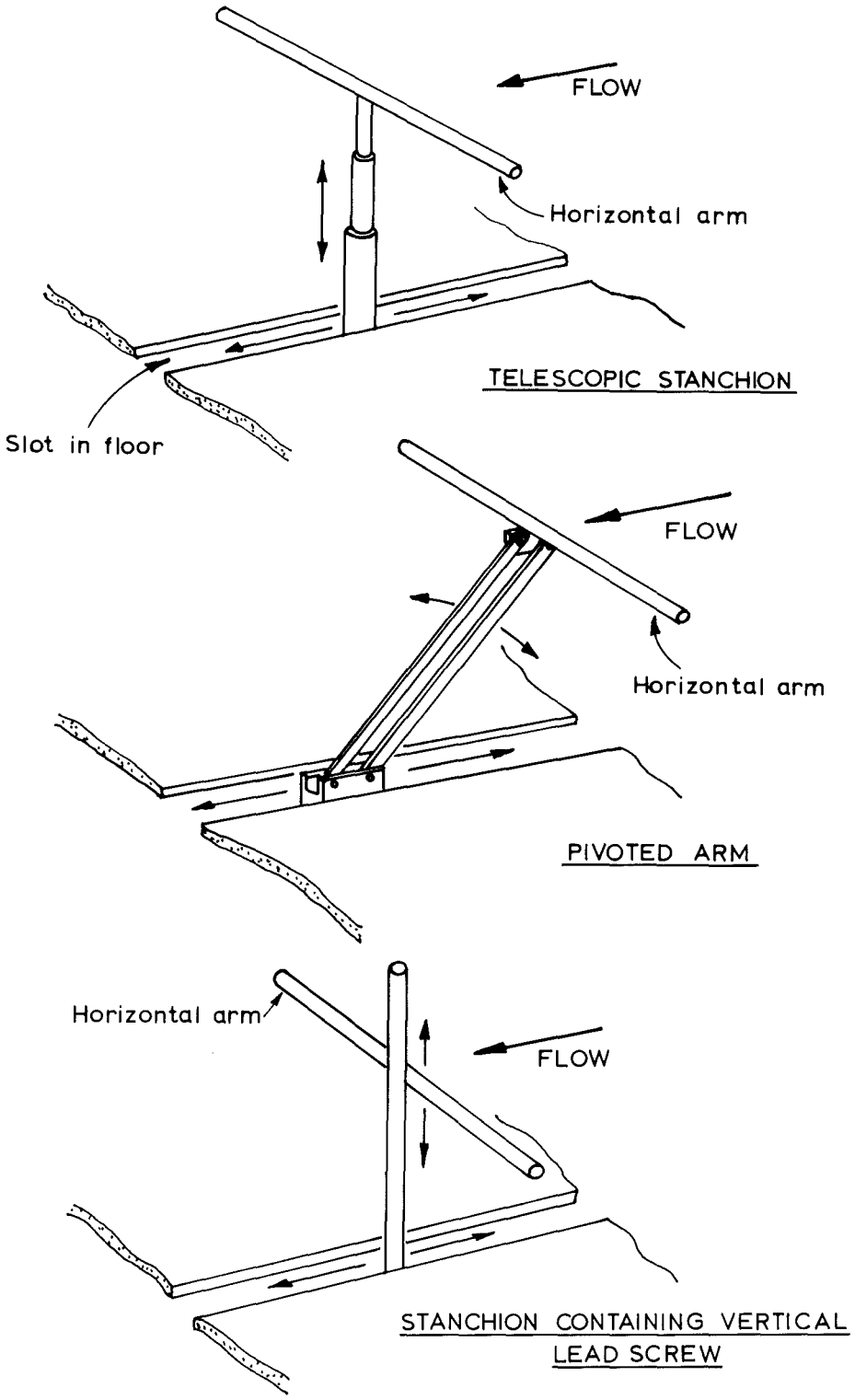

Fig. 5·12 ALTERNATIVE SCHEMES FOR VERTICAL TRAVERSING.

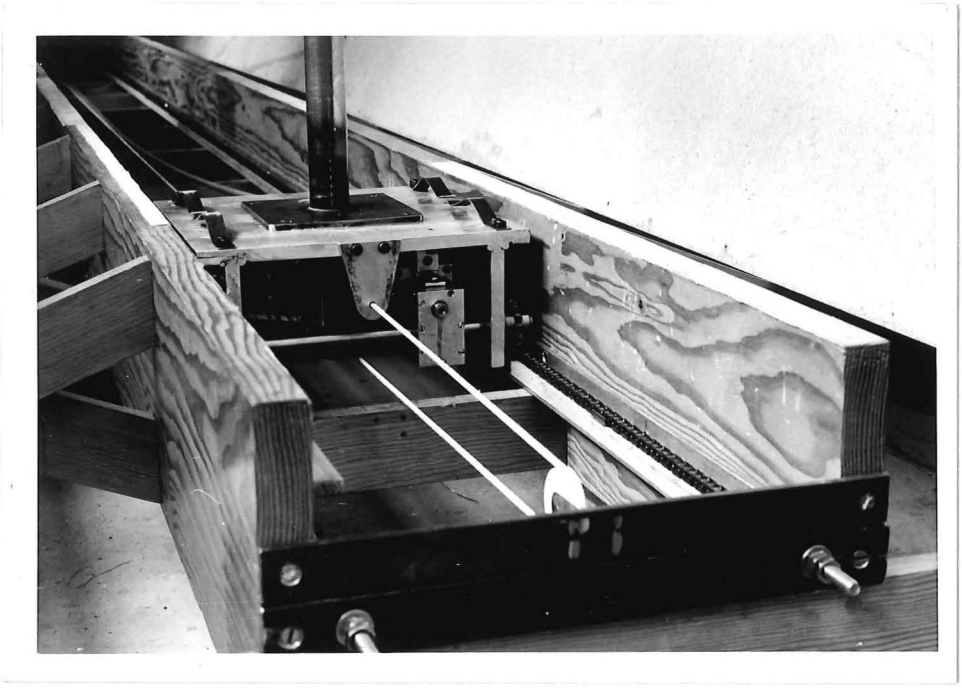

Fig. 5.13 Views of tunnel underfloor traverser trolley, near downstream end of travel.

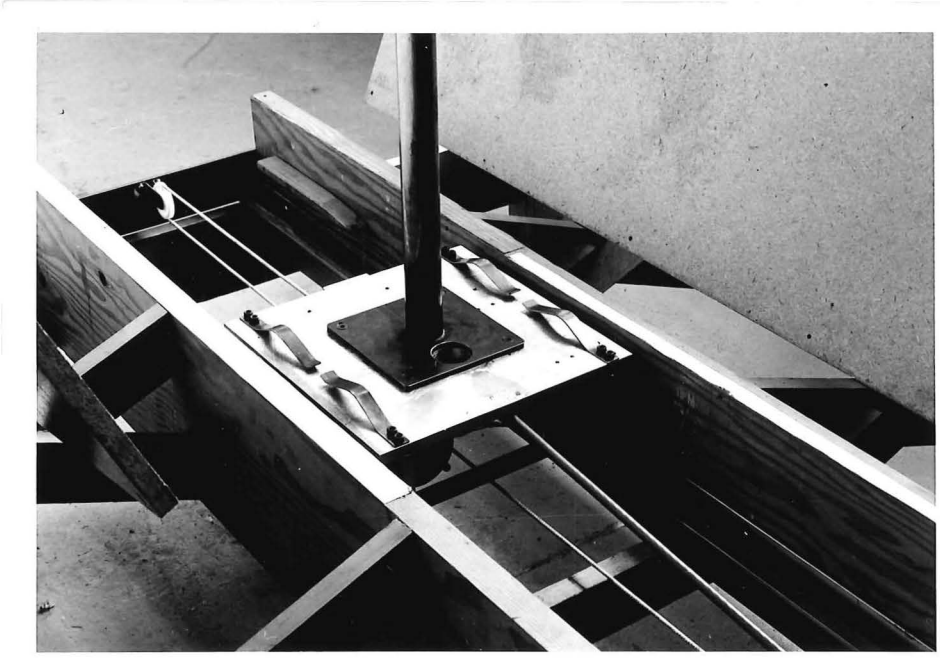

in DRG W24 and Fig. 5.14. The pitot static wing can be seen in Fig. 5.14 and the hot wire mounting bar in Fig. 8.1 (p.358)

Sealing of the floor slot each side of the traverser presented a problem and initially it was intended to use a hard but flexible rubber strip each side of the 3 in slot, so that the rubber strips overlapped to give a seal each side of the vertical stanchion. This scheme was dropped in favour of a heavy nylon zip running the full length of the working section, opening ahead of and closing behind the vertical stanchion. This proved very successful.

Access for the 7 core electric control cable to the underfloor trolley was achieved by fixing one point on the cable to an underfloor cross member about half way down the working section and feeding the cable to the trolley via a cable tensioning pulley bogey which runs on the chain rack between the underfloor trolley and the upstream end of the working section. Tension was maintained on the 7 core cable using a closed loop system shown schematically in DRG W20. The heavy Renold 212030 stock chain wheels on the pulley bogey prevent the bogey from jumping the track. This system operates faultlessly. An access hatch is built into the working section floor at its downstream end to enable rapid removal of the traversing trolley.

Fig. 5.13 shows two views of the traversing trolley close to the downstream end of the working section. In these views note:

(i) the wheels and sprockets of the drive system running on the rails and tensioned chain respectively;
(ii) the access hole in the top of the trolley;
(iii) the four trolley steadying springs;
(iv) the white Teflon tensioning cord and grey and core electric flex;
(v) a wedge of wood at the end of the trolley travel to operate power cut-off micro-switches;
(vi) the draw bolt chain tensioners. These had to be carefully adjusted to give equal pitch over the 40 ft traversing distance.

Fig. 5.15 shows the cable tensioning pulley bogey lifted off the chain rack, and a view down the working section with the pulley bogey sitting upstream of the trolley.

Fig. 5.14 Traverser vertical stanchion with pitot-static wing mounted. Note manometer couplings in foreground.

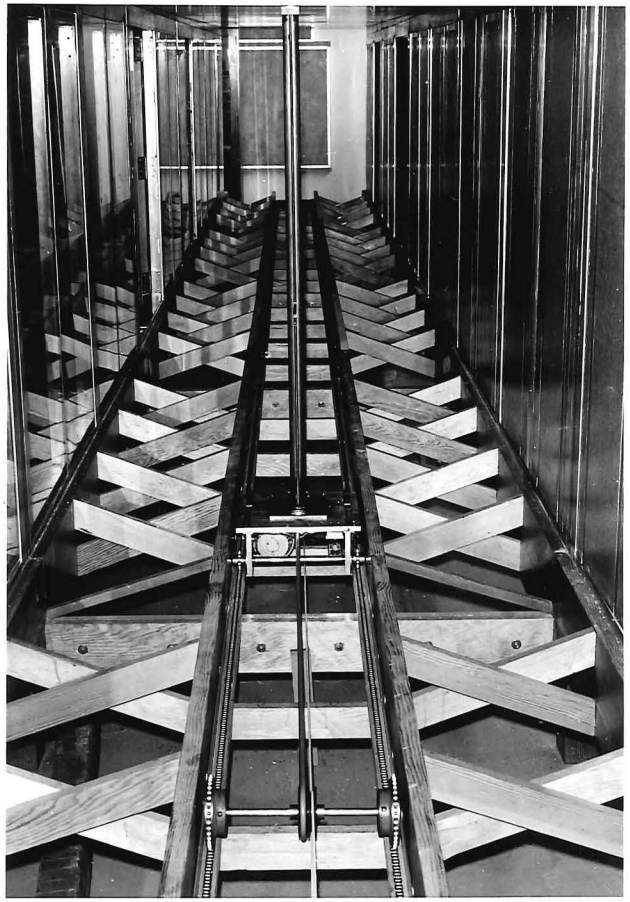

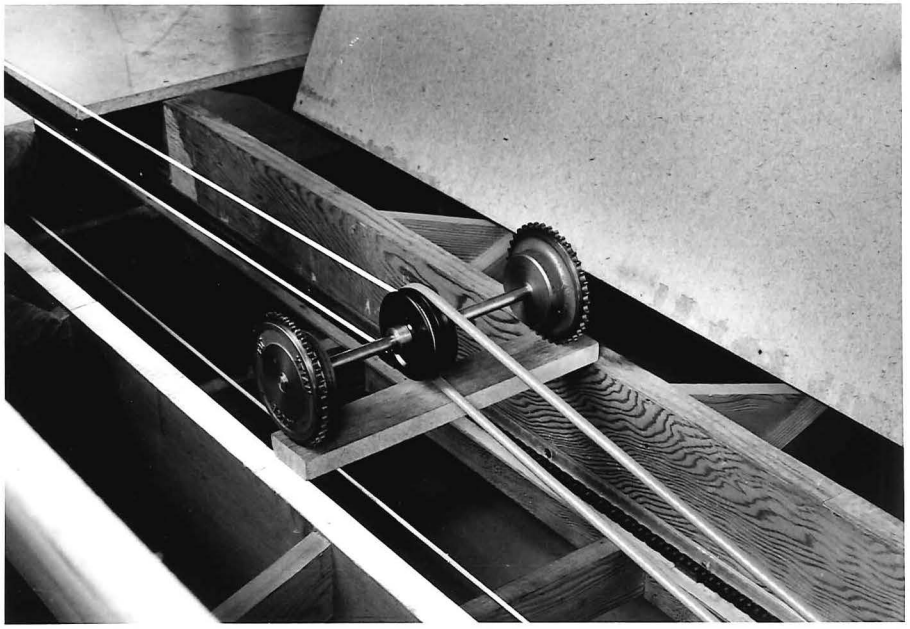

Fig. 5.15 Above: Pulley bogey removed from chain rack track. The thicker cable is the 7 core electric flex.
Left: View along working section with pulley bogey sitting upstream of traverser trolley.

The traverser control sits in the top left hand corner of the tunnel control panel shown in Fig. 5.7. A four position switch selects longitudinal or vertical traversing direction, while a second, rheostat control selects the variable traverse speed from zero to maximum. Note the horizontal arm pneumatic steadying pad air supply valve on the bottom right hand corner of the control panel. The trolley control circuit diagrams are shown at the end of Appendix 8.

5.2.9 The Corner Section:

Steel was considered most suitable for the construction of the vertical corner section. Design requirements for this section were :

(i) To reverse the flow direction with minimum loss;

(ii) To carry loading consisting of :

aerodynamic forces on the corner turning vanes;
wind static pressure, assumed 8 in W.G. maximum;
self-weight;
storage of disused equipment on top of the corner section.

With close to optimum performance obtainable with the flow discharging from the diffuser on the mezzanine floor, there was no need to make the corner section movable. Because of the shortage of construction space on the mezzanine floor, the corner section was, however, designed to be built in two parts, lowered in turn into position. The duct sizing on the lower and upper floors required diffusing from a 4 ft wide x 4 ft 6 in high cross-section to a 5 ft wide x 4 ft high cross-section. The first corner contracts from 4 ft x 4 ft 6 in to 4 ft x 4 ft, then a vertical diffuser expands to 5 ft x 4 ft, so that no change of section occurs in the second corner.

The main structure used RHS steel uprights with angle and channel framework onto which the 12G mild steel sheet skin was welded. The top corner was all steel angle framework. Joints on the inside skin were filled with fibreglass and buffed off. The two sections of the corner were bolted up with butyl rubber jointing compound. The mounting base was bolted to the floor with two 5/8 in Rawlbolts per flange. It was calculated that these bolts would withstand the tipping moment on the structure due to the turning forces on the wind, but this was barely necessary because the 30 cwt structure self-weight, and restraint of the bolted flange joint between the top corner and splitter silencer prevent tipping.

Turning vanes were designed with reference to Winter (1947), Ahmed and Brundrett (1968), Motson and Archer (1969) and others, as detailed in Appendix 3. The vanes were bent from 10G mild steel and had a chord length of 8.5625 in and gap to chord ratio of approximately 0.35. A removable perspex window was fitted on the rear wall of the corner section to allow access to the section between the sets of turning vanes.

The corner section is detailed in DRGs W25 to W36, with DRG W36 showing the final assembly. Views of the corner section under construction are shown in Fig. 5.16 and 5.17.

5.2.10 The Tunnel Assembly:

Construction of the tunnel was begun in December 1971 and with the equivalent of 1½ full-time technicians working on the construction, the lower section of the tunnel was ready to run at the end of April 1973. Construction of the mezzanine floor and corner section followed, and at the end of September 1973 the dual facility tunnel was completed. With extra technicians employed during the latter stages of the construction, the total labour involved is estimated at 7000 man-hours, excluding the mezzanine floor construction.

A summary of tunnel construction costs, including only materials and labour (excluding the mezzanine floor) for the complete facility, is given in Appendix 4. The total material cost was approximately $7,562, for the new construction. With labour costs estimated at approximately $24,500 for the new construction, the total new construction cost became approximately $32,060. Addition of estimated construction costs for the original Low Noise tunnel brings the total cost of the dual facility tunnel up to about $43,800. These figures include no costs for design time, or inflation over the years 1970 - 1973.

The tunnel is now in regular use for undergraduate and postgraduate research, and its performance, accepting some minor limitations, is satisfactory. The performance of the tunnel is discussed in 5.3. In 5.4 a possible future layout of the tunnel is suggested, to overcome the high noise level in the region of the fan inlet and to avoid the inconvenience of the poor flow uniformity at the discharge side of the fans. With more long term planning, a better designed facility would doubtless have evolved. The need to have the research rig operational as early as possible, and the unpredictable nature of developments in a research effort, tend to thwart the achievement of the optimum design solution.

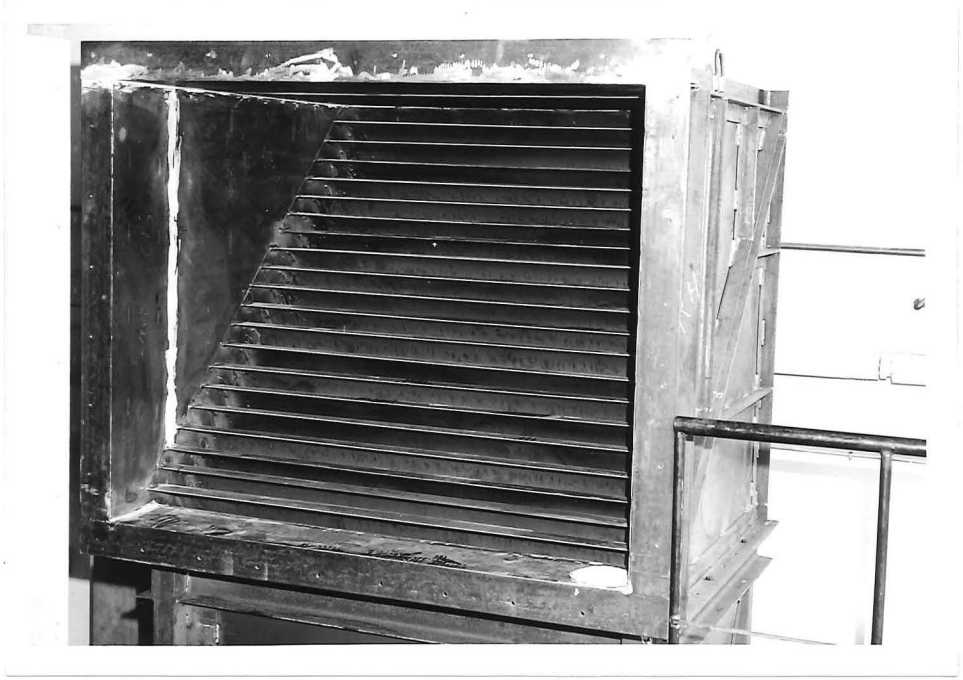

Above : Fig. 5.17 Outlet of corner section top corner.

Left : Fig. 5.16 Bottom corner of corner section and vertical diffuser

Views of corner section under construction

5.2.11 The Mezzanine Floor:

Preliminary design of the mezzanine was carried out by a Departmental design technician and the author. The approved design was detailed by the design technician, with whom the author supervised the construction.

Steel RHS columns were erected each side of the proposed floor span and longitudinal channels placed on top of the columns, to carry transverse 10 in x 2 in Rimu joists. 3/4 in flooring grade particle board flooring was used. The first 3 ft of the floor at the east end of the mezzanine was left open and a steel grill fitted to allow free passage of air down to the tunnel inlet. Vinyl floor covering was fitted and safety fences erected around the edge of the floor.

The mezzanine floor design loading was taken as 40 lb/ft^2, with a factor of safety of 4 on all components. Point loads due to the load bearing legs of the Low Noise tunnel sections were allowed for by the positioning of the transverse timber joists.

The ceiling on the underside of the mezzanine floor acts as an acoustic absorber. It was panelled with 3/16 in pegboard. Above the peg-board was a 1 in gap, then 1 in thick tissue-covered AHI SF300 semi-rigid fibreglass batts, and finally an 8 in space to the underside of the particle board mezzanine floor panels. Tests of several arrangements of the sound absorbent batts were made using a 6 in diameter impedance tube to determine the most effective arrangement of the silencing material. These tests are detailed in Appendix 5. Lighting beneath the mezzanine floor is provided by a continuous row of 11 65W ceiling mounted fluorescent tubes on the south side of the working section, and four further tubes on the north (laboratory wall) side.

The addition of the mezzanine floor has increased both the tunnel versatility, and the available working space in the laboratory. These features will help to accommodate an expanding low speed aerodynamics research programme.

5.3 COMMISSIONING OF THE WIND TUNNEL

5.3.1 Flow Uniformity at the Entrance to the 4 ft x 4 ft Working Section:

Initial tests were run with both honeycombs fitted upstream of the 4 ft x 4 ft working section, and with the flow discharging from the end of

the 4 ft x 4 ft working section. An early traverse across the working section showed that there was gross non-uniformity in the mean flow, with a momentum deficit in the centre of the tunnel, as illustrated by Fig. 5.18. The velocity contours for the same traverse, made 2 ft into the working section, are shown in Fig. 5.19, where it can be seen that there was mean velocity variation across the working section of approximately ±30% of the mean, with a standard deviation on the mean velocity of 14%. This non-uniformity presented a considerable challenge, since there was a distance of only 3 ft upstream of the working section in which to fit corrective devices.

High loss gauze screens were not acceptable, as noted in 5.2.4, and flow redistributing guide vanes were designed to correct the flow uniformity. Prior to fitting an experimental set of guide vanes, velocity head traverses were made at selected locations upstream of the working section, as shown in Fig. 5.20. It can be seen from this figure that the effect of the fans is to create a high velocity region near the wall of the fan duct and a massive deficit in momentum in the centre, due mainly to the influence of the fan bosses and motors. Uniformity of flow across the tunnel inlet is fair, but there is evidence of flow separation at the wall. Downstream of the fans, a large correction in flow uniformity occurs between the round-to-square transition and the start of the working section. The effect of the honeycombs on flow uniformity is uncertain. It appears that a smaller correction in flow uniformity occurs through the second honeycomb than through the first. The steep radial velocity gradients in the flow in this region (e.g. Fig. 5.20b) led to momentum transfer back into the centre of the duct and it may be possible that this process was inhibited rather than helped by the honeycombs, which have a straightening effect on the flow. Comparison of the effects of the first and second honeycombs under these flow conditions is therefore not really possible.

The need to start the atmospheric wind modelling programme promptly led to the discarding of plans for a three-dimensional guide vane system in favour of a device which would correct lateral non-uniformity only. Since the atmospheric boundary layer modelling programme was to involve generation of a non-uniform vertical velocity profile, the initial vertical non-uniformity was less important, although the lateral uniformity correction device could be expected to cause some improvement in vertical uniformity. The technique used was to remove the upstream honeycomb and install a set of vertical deflector vanes as shown in Fig. 5.21. The 3/4 in particle

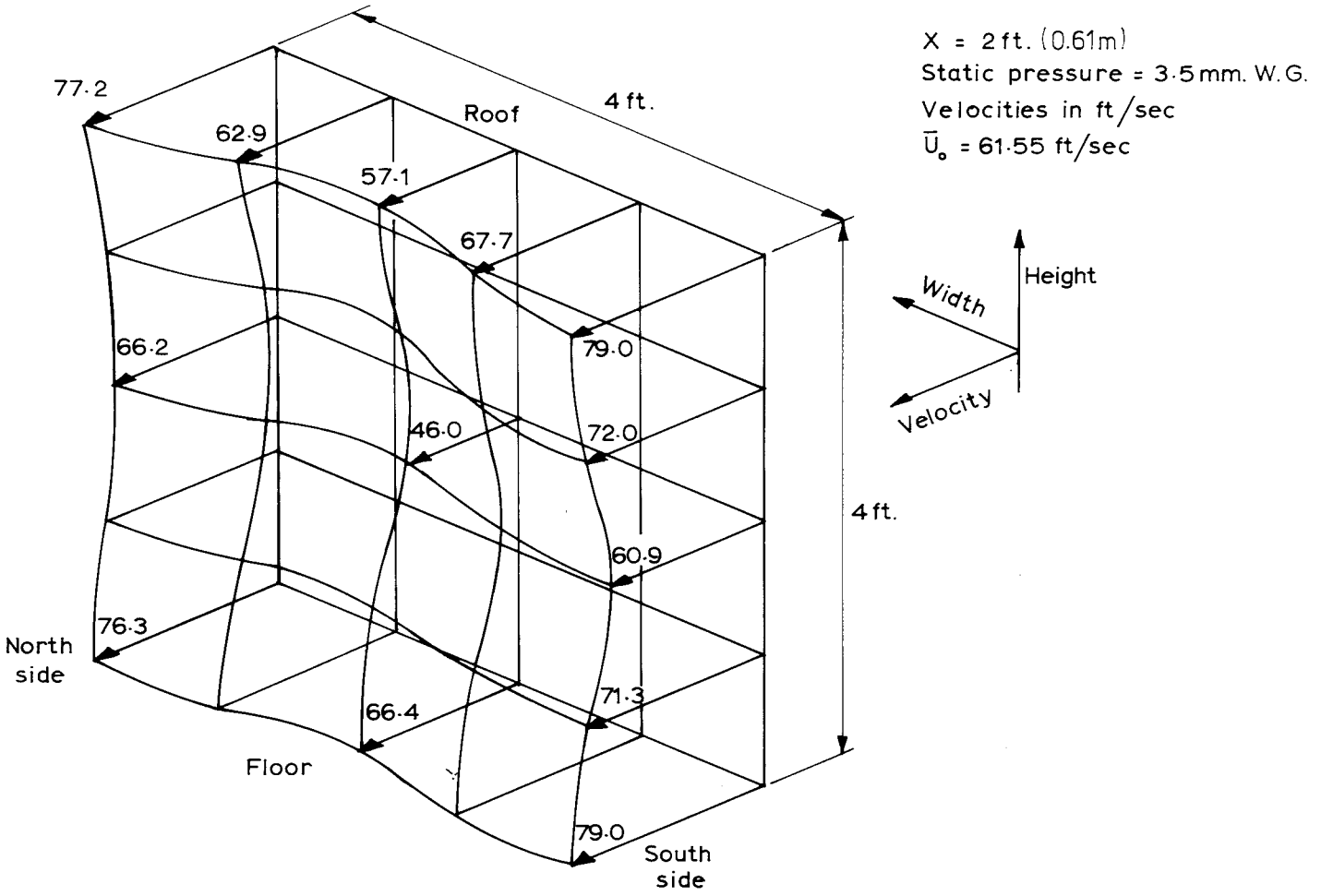

Fig. 5.18 SCHEMATIC VIEW OF INITIAL VELOCITY DISTRIBUTION IN 4 FT. x 4 FT. WORKING SECTION.

X = 2ft.(0.61m)
Static pressure = 3·5mm. W.G.
Velocities in ft/sec.
Spatial mean. $\bar{U}_o$ = 61·55 ft/sec

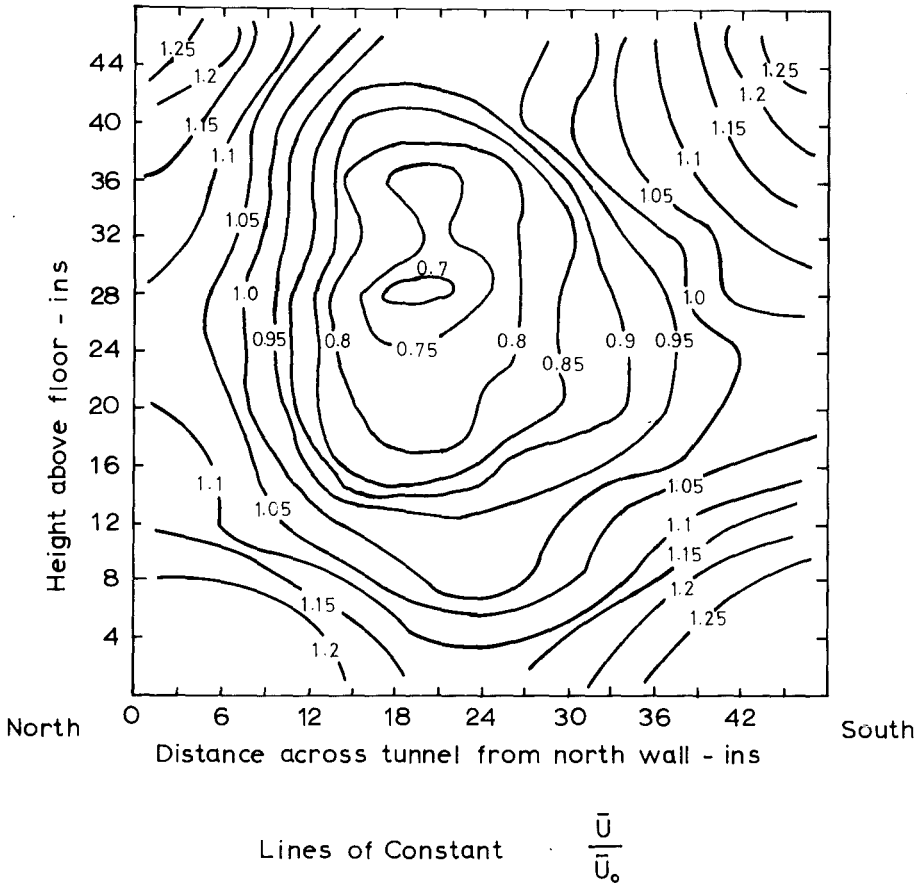

Lines of Constant $\frac{\bar{U}}{\bar{U}_o}$

Fig. 5·19 INITIAL VELOCITY DISTRIBUTION IN 4FT x 4FT WORKING SECTION.

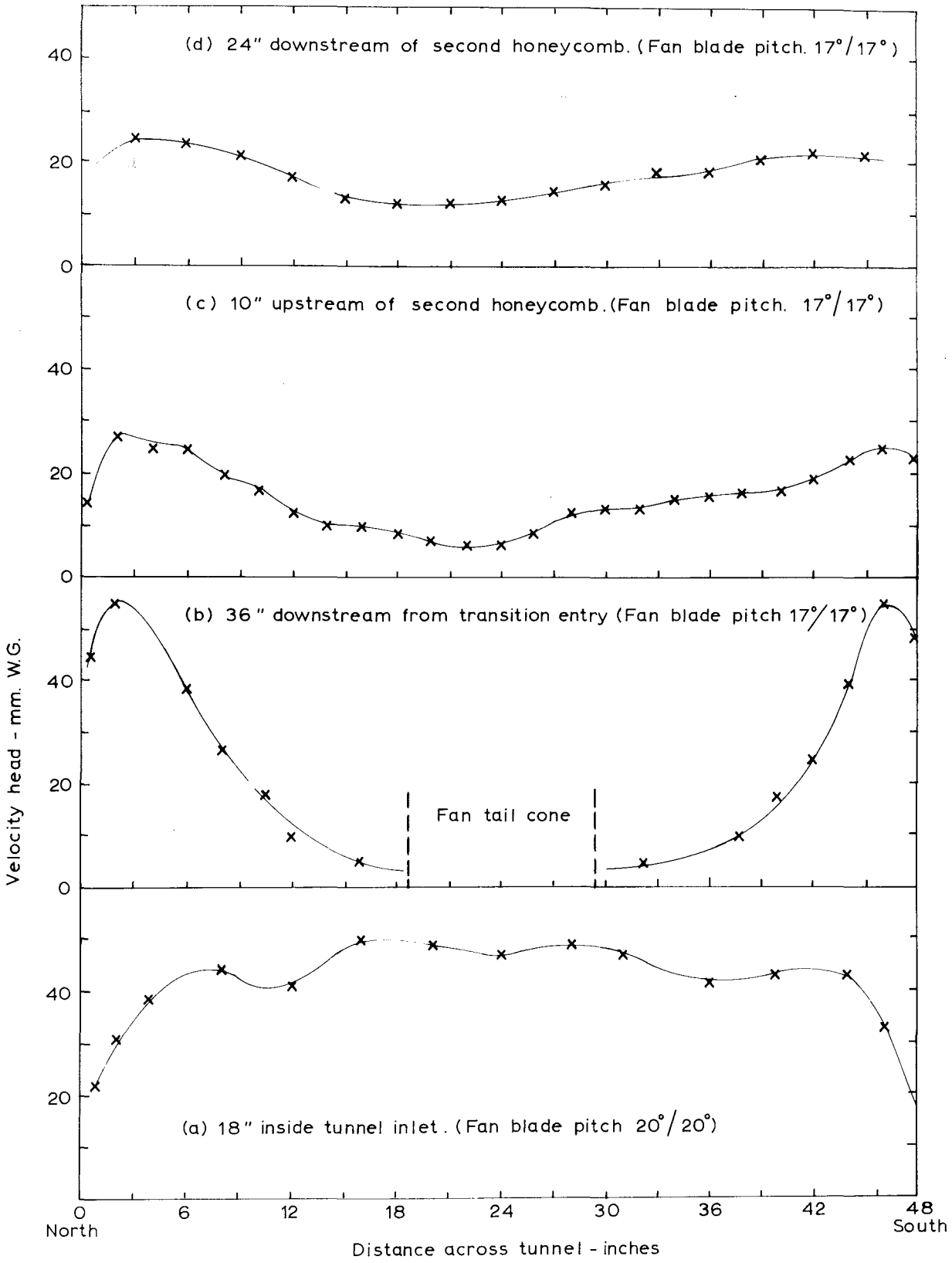

Fig. 5·20 VELOCITY HEAD ACROSS TUNNEL AT HALF DUCT HEIGHT.

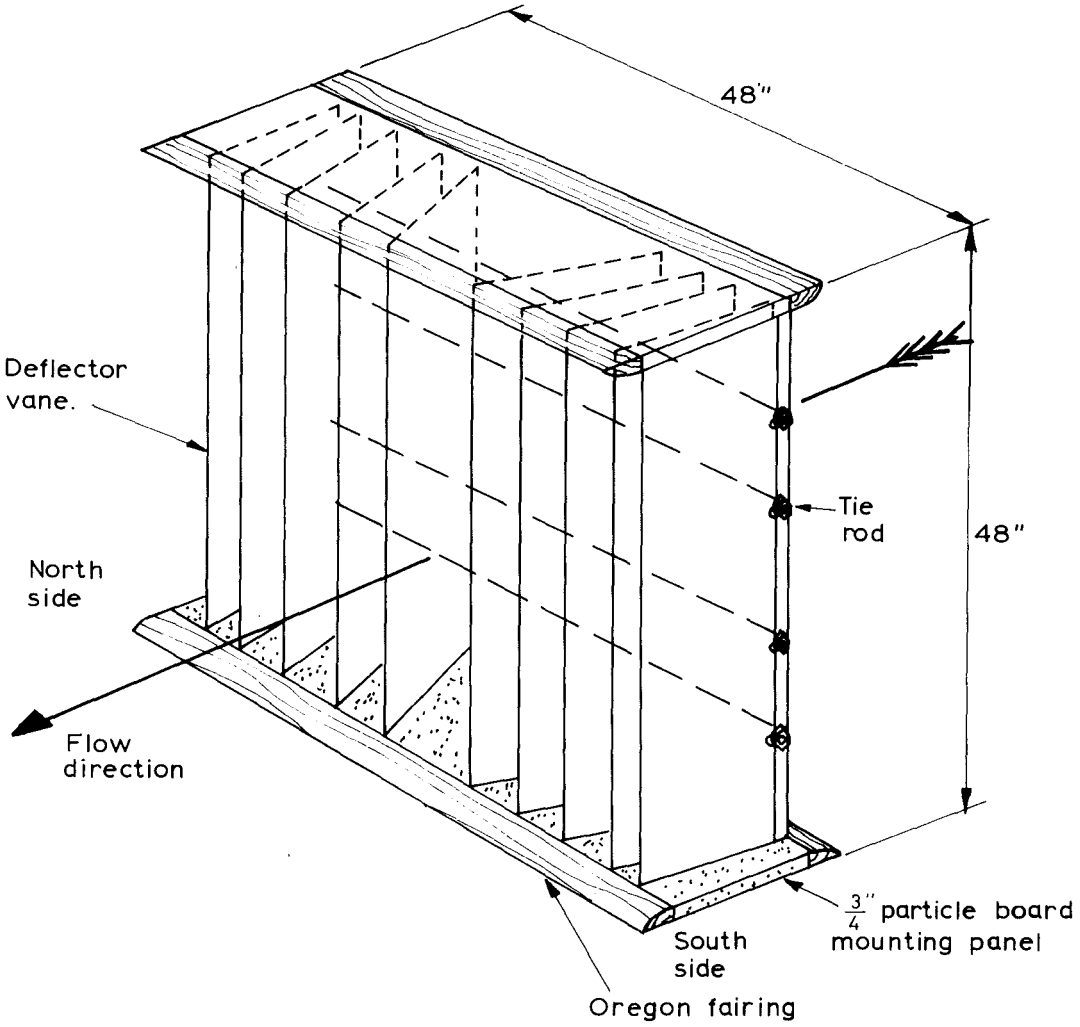

Fig. 5.21 FLOW DEFLECTOR VANES FOR CORRECTION OF LATERAL UNIFORMITY AT ENTRANCE TO WORKING SECTION.

board floor and roof panels were slotted to carry the 10G steel plates. The leading edge of each plate is bent approximately parallel to the tunnel axis and slotted in four places to carry ½ in steel tie rods which prevent flutter. Consideration was given to mounting each plate on stub axles projecting through the floor and ceiling of the spacer duct, to enable independent control of each vane from outside the tunnel. Available time ruled out this idea which should perhaps be implemented in the future, with a suitable alternative means of preventing flutter.

Four deflector vane patterns were tested, the patterns determined using an approximate continuity calculation. The pattern finally used is shown in Fig. 5.22. This still left some non-uniformity at X = 8 ft (8 ft downstream of the working section entrance), but at the start of the test section, X = 30 ft, lateral uniformity was acceptable. Fig. 5.23 shows that at X = 30 ft, outside the region of the approximately 6 in thick wall boundary layers, mean velocity was uniform to within ±2-4% of the mean, and over the whole working section uniform to within ±8%, a vast improvement on the initial condition. This was considered good enough to proceed with the atmospheric boundary layer modelling work, as it was expected that the coarse turbulence generating grid (see DRG W37) to be fitted at the working section entrance would further improve flow uniformity.

5.3.2 Mean Flow Swirl in the Working Section:

With a single stage fan system, use of downstream guide vanes to straighten the flow may increase the pressure development of the impeller by 10 - 30%. With a contra-rotating two-stage fan unit, as used in the present work, the second stage receives the rotating or swirling flow from the first impeller and ideally discharges the flow free from swirl so that no guide vanes upstream or downstream are used. Static pressure development with such a system should be approximately double that obtained with a similar single stage unit with the best possible downstream guide vane arrangement. A contra-rotating two-stage fan unit cannot, however, be expected to produce swirl-free flow under all load conditions (for fixed blade pitch relativity between the two stages). In the atmospheric wind modelling tunnel the first stage impeller rotates clockwise viewed from the tunnel inlet.

Initial swirl measurements made with a yawmeter and with both honeycombs installed in the tunnel are summarised in Table 5.2. Note that the honeycombs remove residual swirl from the flow. With one fan

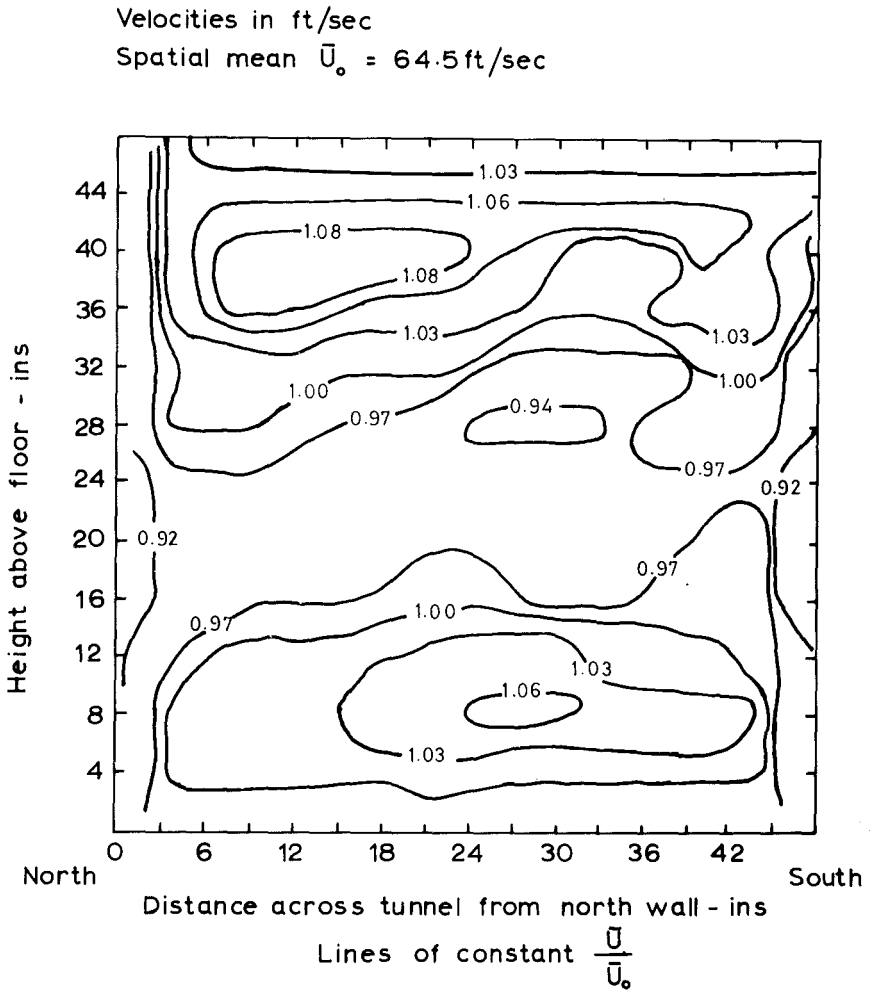

Fig.5·23 MEAN VELOCITY DISTRIBUTION AT X = 30FT, WITH DEFLECTOR VANES AND HONEYCOMB UPSTREAM OF WORKING SECTION AS IN Fig. 5·22.

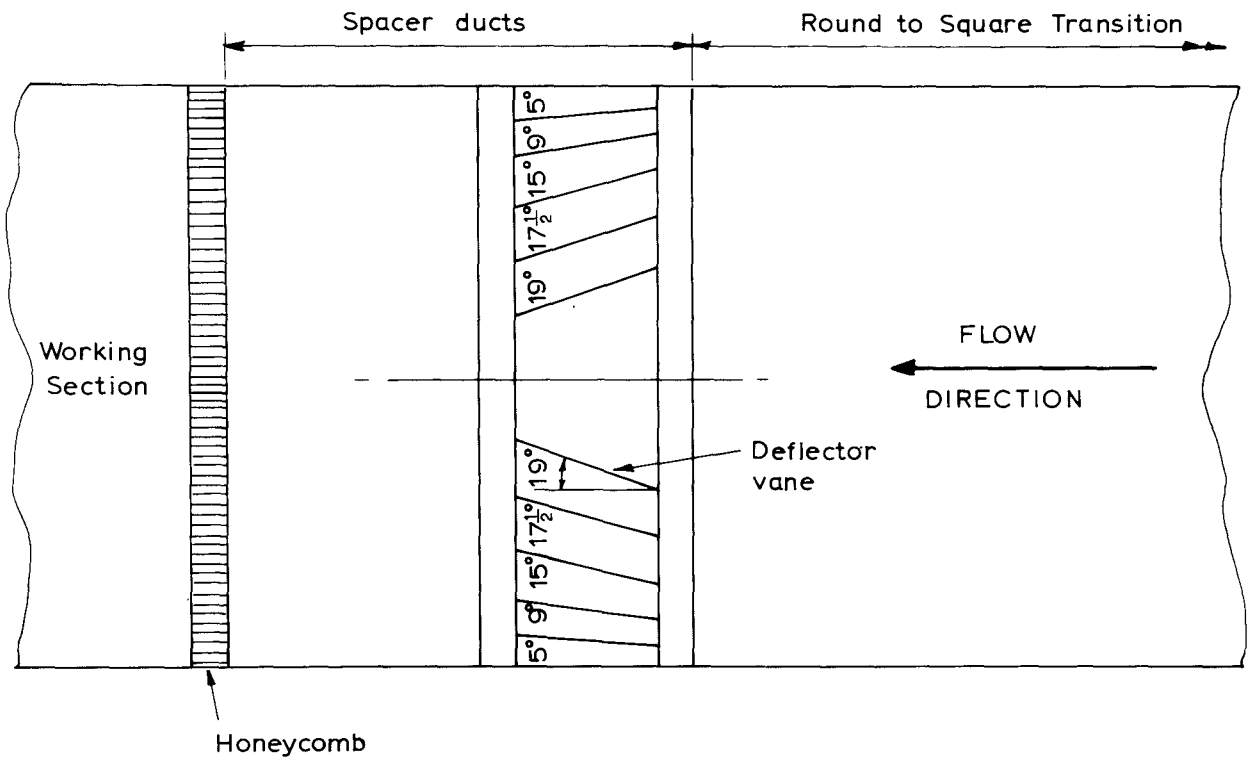

Fig. 5·22 FINAL DEFLECTOR VANE PATTERN.

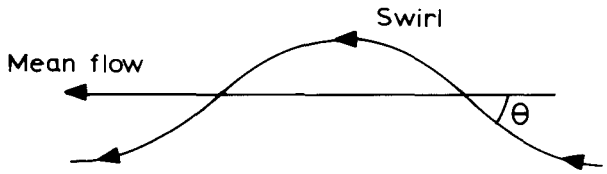

Right hand helix Swirl down tunnel +
Left " " " " " −

C = Coarse pitch
M = Medium pitch
F = Fine pitch
P = Fan powered
I Fan idling

TUNNEL ARRG^T	LOCATION	FAN BLADE PITCH SETTINGS		SWIRL ANGLE
		FAN 1	FAN 2	θ°
Both honeycombs fitted upstream of 4ft. x 4ft. working section.	36in. downstream from entry to Round-to-Square Transition. Near wall.	C/P	C/P	$\lvert\theta\rvert<3°$*
		C/P	C/I	+25°
	36in. downstream from entry to Round to Square Transition. 18in. radially from tunnel axis.	C/P	C/P	$\lvert\theta\rvert<3°$*
		C/P	C/I	+15°
		M/P	M/P	~-10°
		F/P	F/P	~+5°
	10in. upstream of 2nd Honeycomb.	C/P	C/P	~0°
	Xin. = 10ft in Working Section	C/P	C/P	~0°
Coarse Grid & Flow Deflector Vanes fitted upstream of 4ft x 4ft Working Section Measuring at X = 30ft.		20°	20°	~0°
		16°	20°	~-6°
		F	F	~+4°

* θ negative

TABLE 5.2 SWIRL MEASUREMENTS IN LOWER PART WIND TUNNEL.

idling (no power) there is strong residual swirl, and with both fans under power and on coarse pitch, there is a slight over-correction of swirl by the second fan. During the atmospheric wind modelling programme, further swirl measurements were made at X = 30 ft in the working section, because it was suspected that mean flow swirl was upsetting hot wire anemometer calibration. These measurements are also summarised in Table 5.2. The deflector vanes and coarse turbulence generating grid tend to be less effective in removing swirl than the honeycombs. Note in particular that with Fan 1 on ~16° blade pitch and Fan 2 on 20° blade pitch, about 6° left hand helix swirl persists into the working section. At these blade pitch settings, the fan motor speeds are, however, exactly balanced.

Normally, small differences in load on the two fan stages results in slightly different fan speeds. This difference in fan speeds appears to cause more favourable flow over part of the impeller area causing :

(i) a higher velocity zone which rotates around the axis of the tunnel at a 'beat frequency' of 0.5 - 0.05 Hz depending on the difference in impeller speeds. This makes instrument observations less easy;

(ii) acoustic beating at a higher harmonic of the velocity beat frequency.

These mean velocity fluctuations caused by interaction of the fan stages were reduced to within ±2% by the addition of the coarse turbulence generating grid, and still further by the addition of the Low Noise tunnel on the mezzanine floor, as the fan loads were progressively equalised. Complete elimination of this fan interaction problem can only be achieved by equalisation of the fan loads and thus speeds. In the present work, this required setting of Fan 1 to ~16° blade pitch and Fan 2 to 20°. A very steady flow speed resulted but, as noted above, left residual swirl in the flow. With the coarse grid installed in the tunnel there was no space to fit a honeycomb, so the fans were run to give swirl-free flow rather than perfectly steady flow.

The swirl problem tends to occur on part load or when the fan blade pitch settings are different. This performance limitation of the wind tunnel will be best eliminated by installing conventional downstream guide vanes immediately after the second stage impeller.

5.3.3 Pressure Loss Coefficients of Various Tunnel Components:

The pressure loss coefficient, K_w, was evaluated for several sections, using

$$\bar{P}_1 + \tfrac{1}{2}\rho\bar{U}_1^2 = \bar{P}_2 + \tfrac{1}{2}\rho\bar{U}_2^2 + H_L$$

where H_L = head loss = $K_w \cdot \tfrac{1}{2}\rho\bar{U}_w^2$

$\bar{P}_1, \bar{P}_2$ = average static pressure upstream and downstream of section in question, respectively.

$\bar{U}_1, \bar{U}_2$ = spatial mean velocity upstream and downstream respectively.

$\bar{U}_w$ = spatial mean velocity in 4 ft x 4 ft working section.

Details of the measured K_w values for various sections are given in the appropriate places in Appendix 2, to compare with the design estimates. Below, only a summary of measured pressure loss coefficients is given. The original design estimates are also shown :

Section	$K_{w\ meas.}$	$K_{w\ est.}$
Tunnel inlet (with silencer shroud)	0.73	-
Tunnel inlet (without silencer shroud)	0.39	0.81
Honeycomb	0.40	0.45
Working section (4 ft x 4 ft)	0.16	0.18
Bottom corner + vertical diffuser	0.21	0.24
Top corner	0.16	0.13
Silencer + 3rd diffuser	0.59	0.66

It can be seen that most of these loss coefficients are lower than those originally estimated in Appendix 2, typically by 10 - 12%. The inlet loss is, however, less than 50% of that estimated (without the shroud) in the normal operating condition. The above measured pressure loss coefficients are used to give corrected estimates of the total pressure loss coefficient for the different tunnel configurations in Appendix 2.

5.3.4 Tunnel Performance Measurements:

Measurements of air volume flow rate in the 4 ft x 4 ft working section, with various tunnel configurations, showed that the fans were not delivering the volume of air predicted by the Fan Performance Chart. The volume throughput was typically low by ~13% and this was initially attributed to underestimation of the tunnel losses. Measurement of tunnel losses showed, however, that flow resistance in the tunnel was, if anything, lower than estimated. Subsequent fitting of ammeters to the

fan motor power supplies showed that Fan 2 would not load up fully and thus causes the performance deficit. This is discussed further, below, in (b).

(a) Tunnel Performance Data: Since the tunnel was to be run with flow discharging from the third diffuser, on the mezzanine floor, during atmospheric wind modelling work, the fans on the $17^{o}/17^{o}$ maximum blade pitch setting were not fully loaded and maximum blade pitch was therefore increased to $20^{o}/20^{o}$. Maximum pitch should normally be reset to $17^{o}/17^{o}$ when the Low Noise contraction and working section are fitted, to prevent overloading of the fan motors. The tunnel performance for various tunnel configurations is detailed in Appendix 2. Here two sample results only are given :

(i) Flow discharging from 3rd Diffuser:

For the results given below, the coarse turbulence generating grid and flow deflector vanes were fitted upstream of the 4 ft x 4 ft working section.

Corrected total pressure loss coefficient $K_{w\ total} = 4.44$

Fan blade pitch setting = $20^{o}/20^{o}$.

Measured Q = 58,560 CFM at 2.42 in W.G. fan static pressure.

Ideal Q = 67,500 CFM at 3.15 in W.G. fan static pressure.

(Ideal Q from Woods 48J½-2 Fan Performance Chart).

Measured volume throughput is 13% low.

(ii) Flow Discharging from Low Noise Working Section:

Coarse turbulence generating grid and flow deflector vanes again fitted upstream of 4 ft x 4 ft working section.

Corrected total pressure loss coefficient $K_{w\ total} = 11.94$

Fan blade pitch setting = $20^{o}/20^{o}$.

Measured Q = 47,600 CFM at 5.77 in W.G. fan static pressure.

Ideal Q = 51,500 CFM at 6.76 in W.G. fan static pressure*

(* at this duty the 33BHP fan motors would be overloaded slightly).

Measured volume throughput is about 8% low.

The measured performance in this test is close to the design maximum efficiency load calculated in Appendix 2 for this tunnel configuration with fan blade pitch $17^{o}/17^{o}$. This was:

Q = 48,000 CFM at 6.15 in W.G. fan static pressure.

In (ii) the measured volume throughput was only about 8% low compared

with deficits of about 13% in most other tests. In (ii) however, Fan 1 was drawing a 7% current overload and exceeding design performance. Generally performance of the tunnel was considered adequate, but steps should be taken in the future to rectify the performance deficit, as suggested in (b).

(b) Fan Motor Loading vs Tunnel Performance: Observations of fan motor currents showed that under all configurations, Fan 1 drew a larger current than Fan 2, and the motor current in Fan 2 could be made to exceed that in Fan 1 only by making the impeller blade pitch substantially greater on Fan 2 than on Fan 1. Figs. 5.24 and 5.25 show a summary of fan motor current readings with the tunnel discharging from the 3rd diffuser (Fig. 5.24) and from the Low Noise 2.5 ft x 2.5 ft working section, (Fig. 5.25). Note from these figures that motor current I_2 is always less than I_1 for equal blade pitch. This difference is fairly small for motor loads corresponding to ~16° blade pitch. For coarser pitch I_1 climbs rapidly to full load current (46.9 amps) while I_2 increases only very slightly. Further, for both tunnel configurations, driving the tunnel with Fan 1 alone results in overload current at coarsest pitch, while driving the tunnel with Fan 2 alone gives $I_{2\ max}$ = 36 amps only, at coarsest pitch, with discharge at the 3rd diffuser (or $I_{2\ max}$ = 37 amps with discharge at the Low Noise working section exit). In these single-fan tests, Fan 1 gave a correspondingly higher volume throughput.

It is clear from Figs. 5.24 and 5.25 that Fan 2 is unwilling to work as hard as Fan 1. Woods (1960) suggests that Fan 2 should draw, if anything, a little more current than Fan 1, at full load, in a properly balanced system. The fault here probably relates, at part load, to the different entry conditions at each impeller, which could result in a 2 - 4 amp current difference between the two fan motors. However, the 8 - 14 amp current difference occurring at full load conditions is very large and would have to be caused by some gross aerodynamic fault, such as stall on one impeller.

Fan 2 at no time reaches full load current, despite there being sufficient flow resistance to enable it to do so. It also appears unlikely that Fan 2 is running stalled at full load in the present arrangement. The author therefore suggests that there may be an electrical fault causing the performance deficit, rather than an aerodynamic fault. A trouble-shooting programme is being undertaken at the time of writing, and the Fan 2 motor and power supply wiring will be checked out. Should

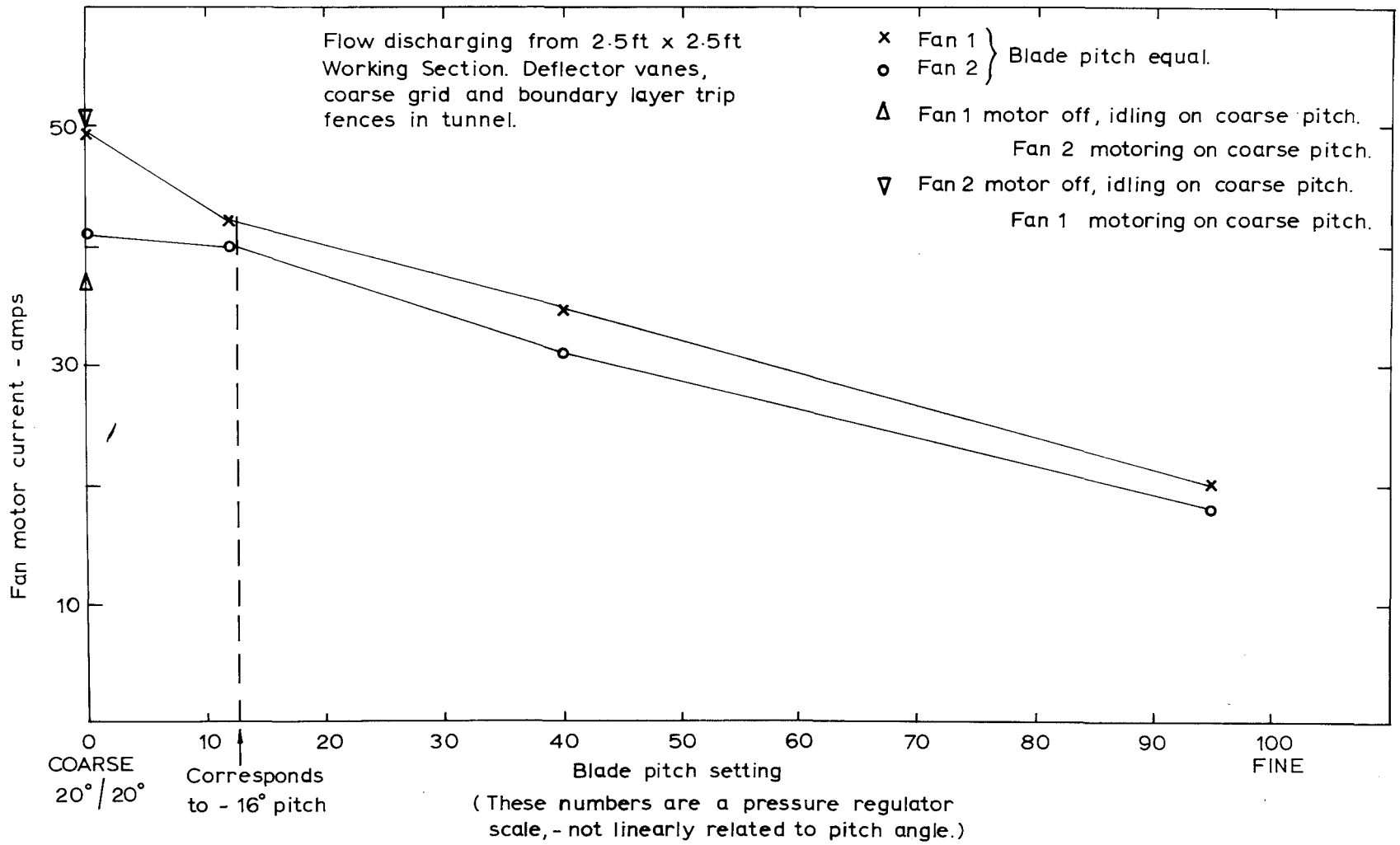

Fig. 5·25 FAN MOTOR CURRENTS VS. IMPELLER BLADE PITCH SETTINGS.

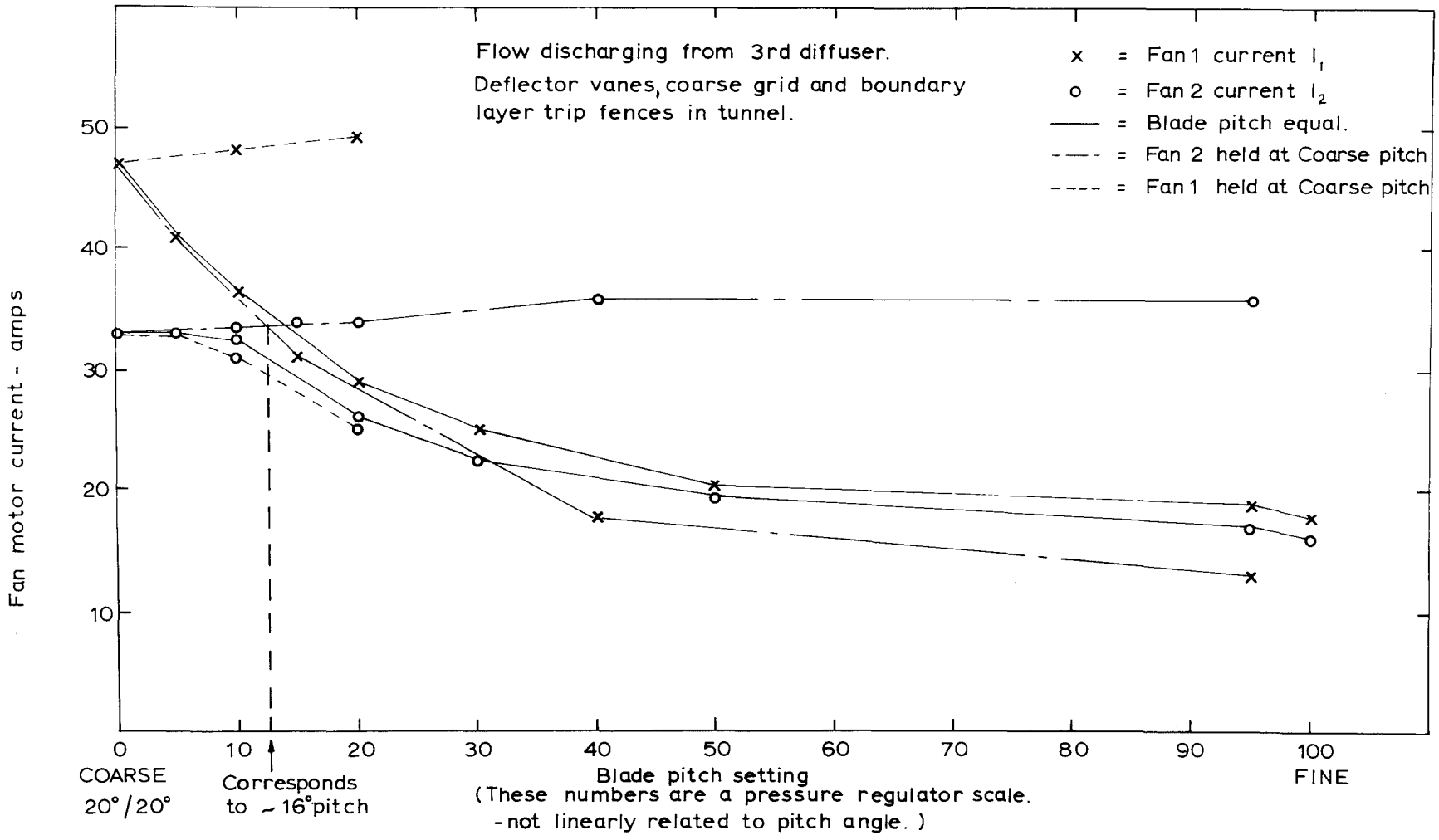

Fig. 5.24 FAN MOTOR CURRENTS VS IMPELLER BLADE PITCH SETTINGS.

there be no apparent electrical fault, the first step in establishing an aerodynamic cause for the problem will be to change over Fans 1 and 2 to check whether Fan 2 will draw full load current with a different entry condition.

5.3.5 Turbulent Intensity and Energy Spectra in the 4 ft x 4 ft Working Section:

Turbulence measurements were made in the clear 4 ft x 4 ft working section, with one honeycomb and the deflector vanes fitted upstream of the working section. $u'/\bar{U}$ turbulent intensity was measured at X = 1m, 2m, 5m and 10m and results are shown in Fig. 5.26. Hot wire anemometry equipment was set up as for the flow modelling work of Chapter 6. (See Appendix 6). It can be seen from Fig. 5.26 that there is considerable lateral non-uniformity in the turbulent intensity at X = 1m, but uniformity improves with distance down the working section. e.g. for points at z = 30, 60, 90cm (outside the floor boundary layer)

At X = 1m: mean $u'/\bar{U}$ = 0.109

with standard deviation = 0.027 or 25% of the mean.

At X = 10m: mean $u'/\bar{U}$ = 0.056

with standard deviation = 0.002 or 4.2% of the mean.

These results may be compared with Fig. 6.8 where turbulent intensity results are shown for the same streamwise locations in the working section after the addition of the coarse turbulence generating grid in place of the honeycomb at X = 0. The later results with a mean value of $u'/\bar{U}$ of 0.133 at X = 1m and a standard deviation of 3.4% about this mean, show better uniformity of the turbulent intensity across the wind tunnel cross-section. The effect of the grid on mean flow uniformity was also beneficial.

Energy spectra for the u velocity component are shown in Fig. 5.27. These are plotted at X = 10m and z = 5cm and 60cm. The spectrum at z = 5cm has a broad peak centred on $k_p \simeq 0.80\ m^{-1}$, while that at z = 60cm has a peak at $k_p = 0.60 m^{-1}$. The corresponding turbulent length scales at these two heights are $L_{u_x} = 0.18$m and 0.24m respectively. (Using Eqn. 2.57). Reference to Table 6.1 shows that L_{u_x} was larger before the turbulence grid was fitted. This observation is consistent with the grid removing large scale turbulence generated by the fans, so that at X = 10m,

$$\left(\frac{u'}{\bar{U}}\right)_{\text{with grid}} < \left(\frac{u'}{\bar{U}}\right)_{\text{without grid}} \quad \text{and} \quad L_{u_x\ \text{with grid}} < L_{u_x\ \text{without grid}}$$

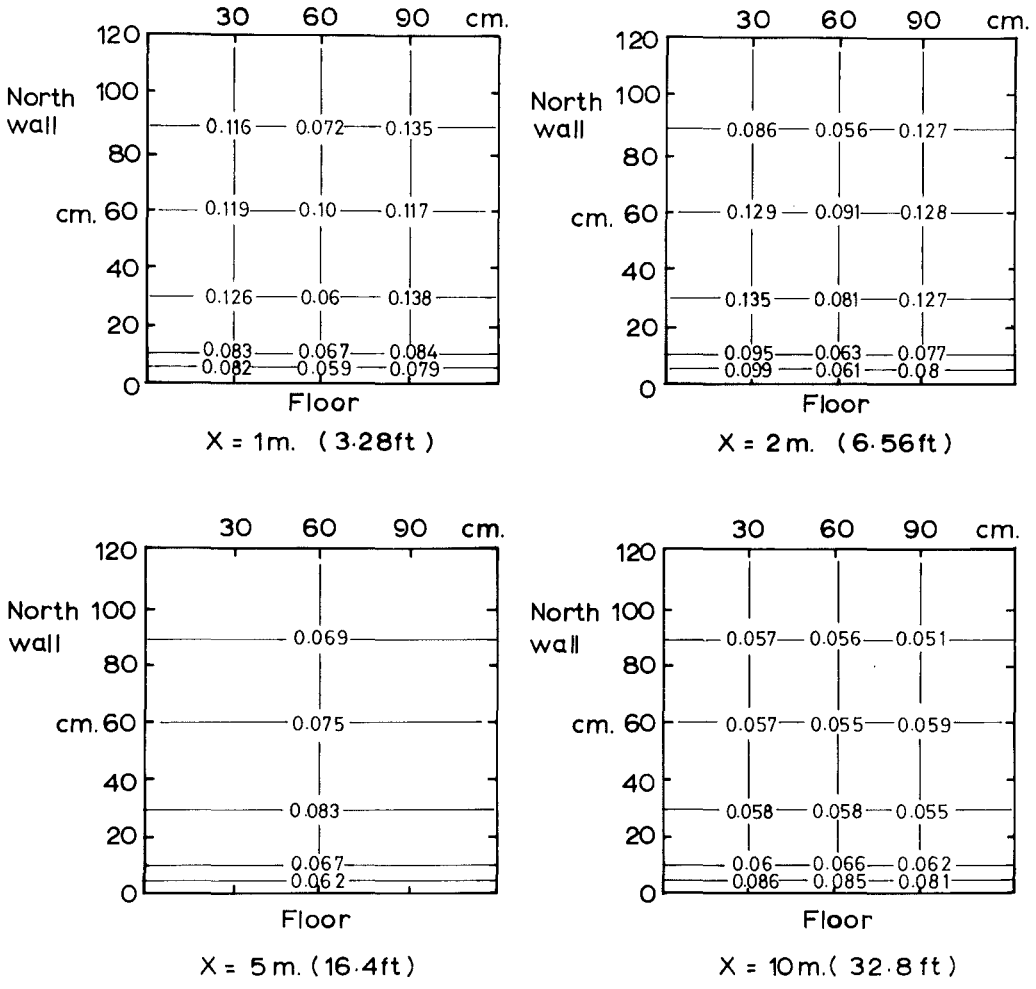

(Flow towards reader)

X = Distance downstream of working section entrance.

Fig. 5·26 $\frac{u'}{U}$ TURBULENT INTENSITY IN THE CLEAR 4FT. x 4FT. WORKING SECTION.

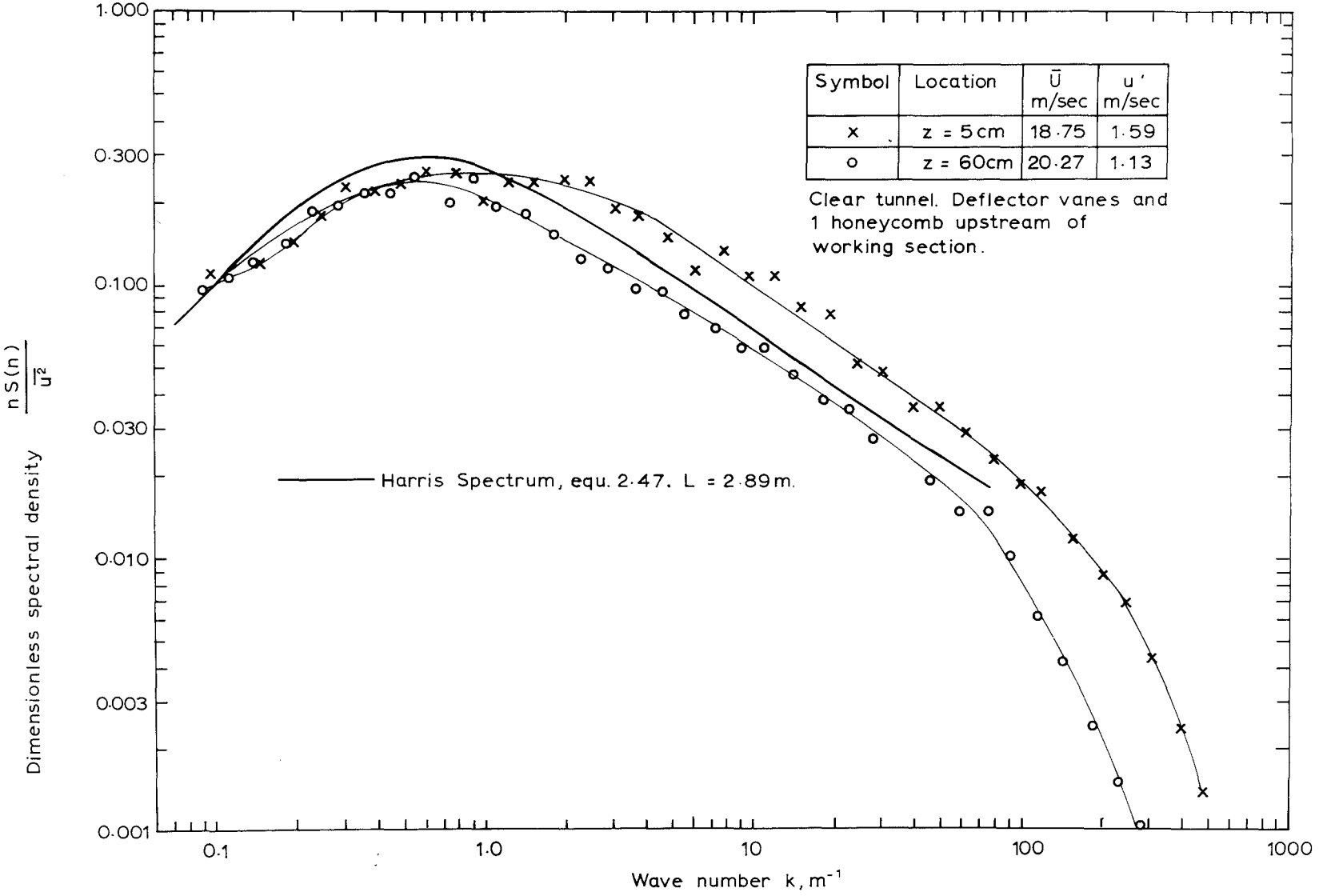

Fig. 5·27 ENERGY SPECTRUM FOR u VELOCITY COMPONENT AT X = 10 M.

The spectrum shape at X = 10m in Fig. 5.27 comes fairly close to Harris' approximate von Karman model of Eqn. 2.47.

5.3.6 Performance of Various Wind Tunnel Components:

To complete this chapter, aspects of the tunnel performance not previously discussed are dealt with briefly below :

(a) Tunnel Inlet: Initially a sound absorbing shroud was built around the tunnel inlet. This was previously used by Tang (1971). Entrance loss measurements (Appendix 2) showed, however, that the presence of the shroud increased $K_{entrance}$ from 0.24 to 0.45 (based on local mean velocity). In the interests of better tunnel performance, the shroud was therefore removed and replaced with a flat sound absorbent panel built against the east wall of the laboratory.

(b) Round to Square Transition Silencer: Converting the transition to act also as an absorptive silencer caused a small decrease in the noise level outside the tunnel. Sound measurements were made before and after modifying the transition duct and are shown in Fig. 5.28. The effectiveness of the silencer is probably overestimated by the figures of Fig. 5.28, as the Low Noise contraction and working section were connected up for the later test, but not for the earlier test. The higher fan loading in the second test would have been accompanied by a decrease in fan noise (see Fan Performance Chart, Appendix 2). The reduction on the noise level outside the tunnel due to the transition-silencer was probably not more than 2dBA. It is planned to erect suspended sound absorbant panels surrounding the tunnel inlet, but sufficiently removed from it not to increase the entrance loss. These should decrease sound levels to a more suitable level for several-hour daily exposure times.

(c) The Honeycombs: Handling of the honeycombs during installation and removel required great care, as the ends of the cells were easily damaged, the material thickness being only 0.003 in. Pieces of lint, paper, etc. caught on the upstream face of the honeycombs were periodically removed by vacuum cleaning. Once the honeycombs were removed, ingested material generally found its way to the tunnel outlet. This was regrettably instanced by a pair of technician's spectacles, exhausted in fragments.

(d) The Roof Hoisting Gear: This functioned well, but care had to be taken to loosen off the roof clamps completely before adjustment of roof height. Stepwise adjustment moving along the working section is advisable to prevent racking of adjacent roof panels. A complete roof

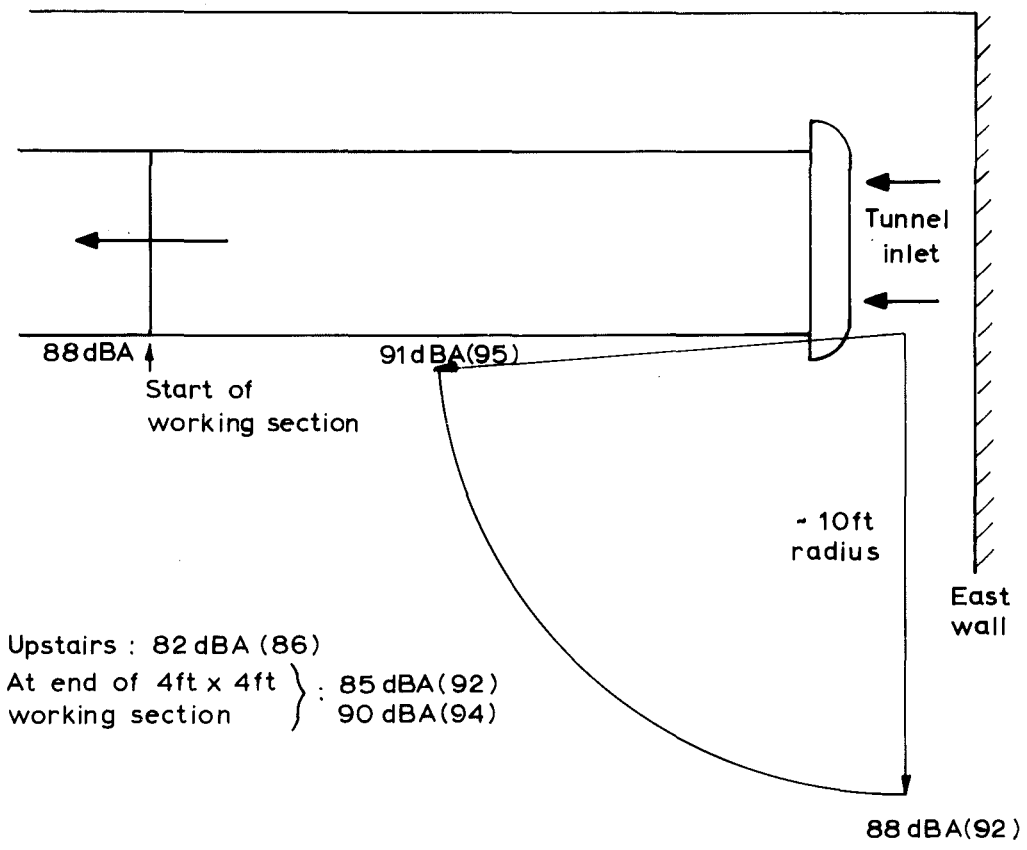

Linear reading at 10ft radius was ≒ 100dB. Readings in brackets are from earlier test with lower flow resistance and no silencing in the round to square transition.

Fig.5·28 SOUND LEVEL MEASUREMENTS OUTSIDE TUNNEL.

adjustment including clamping up may be achieved in about 20 minutes when an electric drill is used to drive the hoisting gear sets. The vertical, threaded roof hangers should be cleaned and relubricated with heavy oil (SAE 80) about once a year.

(e) Traversing Gear: This performed well in all respects, but for two problems with the vertical traverser :

(i) accumulation of airborne dirt on the vertical lead screw;

(ii) unsatisfactory location of the horizontal arm.

After about three months of operation, the vertical traverser 2:1 bevel gear drive was replaced by a 10:1 reduction worm and worm wheel drive, and a 10 T.P.I. vertical lead screw installed in place of the initial 20 T.P.I. screw. This overcame a tendency for the vertical traverser to labour on upward journeys, but residual eccentricity after screw cutting the 4 ft long lead screw caused low frequency vibration of the vertical stanchion, and accentuated the looseness of location of the horizontal arm. Vibration was largely eliminated by stiffening the vertical stanchion, and the horizontal arm was steadied quite satisfactorily by the air operated pads. However, a new chain driven vertical traverser was designed, and is being installed at the time of writing. In the new scheme, a chain runs on sprockets at top and bottom of the stanchion and operates a horizontal arm carrier which is rigidly restricted to slack-free vertical movement by bearings running on an auxiliary vertical guide bar. (See Fig. A6.4, p.509).

The traversing gear saved countless hours of manual instrument positioning in the experimental work, and fitting a new tunnel with such equipment must be considered essential where large numbers of multi-point traverses are anticipated.

(f) Tunnel Speed Control: Backlash in the air diaphragm fan blade pitch adjusting mechanism makes it essential to adjust tunnel speed with reference to a pitot-static tube signal, say, rather than the air gauge on the control panel. Future consideration should be given to arranging a feedback tunnel speed control which utilises a velocity head signal from the working section in the control system, to enable 'dialling up' a desired tunnel speed.

5.4 CONCLUSIONS

The completed wind tunnel is a useful dual purpose experimental facility and has extended the versatility of the aeronautical laboratory. Performance of the tunnel as it stands is acceptable, but consideration

should be given to making the following improvements, listed in a suggested order of priority :

(i) erection of sound absorbing panels around the tunnel inlet (situated not closer than 6 ft to the periphery of the bell mouth);

(ii) correction of the inability of Fan 2 to draw full load current, thus improvement of tunnel air volume throughput;

(iii) construction of a diffuser to fit on the outlet from the Low Noise working section (or its acoustic termination), suggested dimensions:

Length	10 ft (4.28m)
Inlet cross-section	2.5 ft x 2.5 ft (0.76m x 0.76m)
Outlet cross-section	4 ft x 4 ft (1.22m x 1.22m)

Addition of a diffuser such as this would increase volume flow rate by about 20% with lower fan power requirements. Details of tunnel performance with this suggested outlet diffuser are given in Appendix 2;

(iv) addition of downstream guide vanes after the fans to eliminate residual swirl from the mean flow at all load conditions;

(v) installation of a 'closed loop' tunnel speed control to enable pre-setting a desired speed;

(vi) relocation of the fans on the mezzanine floor, just after the top corner (as shown in Fig. 5.29). This would be a major alteration which would place the lower working section at a negative gauge pressure and make sealing against air leakage a more important factor. Two advantages would, however, be present:

(a) with the fans drawing air through the wind modelling working section, the space upstream of the working section could be used for a settling chamber and contraction, to give a more uniform, less turbulent flow at the working section entrance;

(b) the present noise level (about 90dBA 10 ft from the tunnel inlet) would be reduced.

Relocation of the fans on the mezzanine floor would require strengthening of the floor joists to carry the 3000 lb wt load of the 2 stage fan unit assembly, and evaluation of possible effects on the performance of other components of the tunnel.

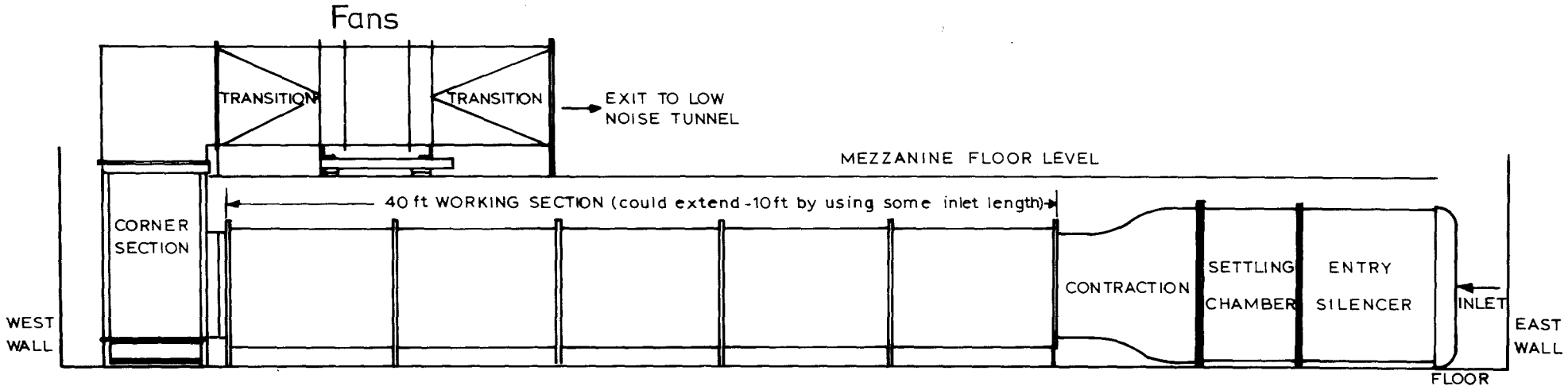

Fig. 5-29 POSSIBLE FUTURE LAYOUT OF WIND TUNNEL.

CHAPTER 6

THE ATMOSPHERIC WIND SIMULATION PROGRAMME

The object of the atmospheric wind modelling work in this project was to produce a wind tunnel simulated neutrally stable rural atmospheric boundary layer, of linear scaling as large as 1:400 if possible. In Chapter 4 it was shown that this could not be achieved in the 4 ft x 3 ft working section of the aeronautical wind tunnel, and the new wind modelling facility was therefore constructed. In Chapter 3 the review of previous wind modelling efforts showed that a linear scaling of 1:400 in the simulated atmospheric flow in the 40 ft (12.2 m) long working section of the new tunnel, would only be achieved if a 'step change + boundary layer growth' scheme were used to produce accelerated boundary layer growth. On the basis of the discussion of 3.6, the first 9.15 m of the working section length were set aside for the production of an approximately 1 m deep boundary layer, leaving approximately 3 m for a test section. In 6.1 the approach to the flow modelling exercise is stated. The method used involved stepwise addition of boundary layer generating devices to a basic scheme, and various layouts tested are described in 6.3. The final simulated boundary layer is described in 6.4 and discussed in relation to previous simulations reviewed in 3.5.

6.1 THE APPROACH TO THE ATMOSPHERIC WIND MODELLING EXERCISE

It was decided to aim for a simulated boundary layer characteristic of flow over terrain of roughness length, z_o, about 5 cm, corresponding to a mean velocity profile power law exponent of 1/6 (see Fig. 2.7, p.30). It was pointed out in 3.6 and 4.3 that a feature of pure graded blockage boundary layer generation schemes, and 'step change + boundary layer growth' schemes reviewed, was the decrease in integral length scale of turbulence with height occurring in the flow at the test section, contrary to the requirement of Eqn. 2.63 (p.64). In the atmosphere there can be sufficient upstream fetch for considerable quantities of turbulent energy to have diffused to the outer part of the boundary layer as large scale, low intensity turbulence. In the accelerated growth wind tunnel boundary layer there is normally insufficient distance for equilibrium to be established between turbulent energy production, diffusion and dissipation, so that at the test section it is usual for the mean velocity profile and turbulence structure to be slowly changing. In particular, there is the observed tendency for turbulent intensity and length scale to be too small in the outer part of the boundary layer.

Accepting that horizontal homogeneity can probably not be achieved in a working section less than about 30 m long, if linear scaling of about 1:400 is wanted, some means is required to produce a flow that at some point in the working section satisfactorily simulates atmospheric mean velocity profile and turbulence structure. To overcome the deficit in turbulent energy in the outer part of the boundary layer, a device is required at the entrance to the working section, to produce intense turbulence of relatively large scale at all heights. This initial disturbance will provide a base level of large scale low intensity turbulence downstream at the test section. To provide initial thickening of the boundary layer (with boundary layer thickness based on mean velocity profile), a tripping device near the start of the working section is required. Downstream from the working section entrance, continuous generation of turbulence must occur close to the ground, to maintain a sufficiently high level of turbulent intensity in the surface layer. Surface roughness is therefore required, of a suitable size to ensure satisfactory distributions of mean velocity and shear stress with height.

To achieve the above requirements, it was decided to work as follows:

(i) A coarse square mesh grid of 1½ in (3.81 cm) bars, with $\phi = 0.5625$ would be placed at the entrance to the working section. The performance of this grid was estimated in 4.2.1. The finer, 1½ in bar, configuration was used as the grid was required to improve mean flow uniformity as well as generate the base level of turbulence.

(ii) A solid or permeable trip fence of suitable height would be placed 2 ft (0.61 m) downstream from the coarse grid.

(iii) Surface roughness in the form of 'Torro' baseboard would cover the floor from X = 2 ft (0.61 m) to X = 30 ft (9.15 m).

(iv) Additional surface roughness in the form of Torro blocks or progressively lower trip fences would be used as required further downstream, to obtain a satisfactory boundary layer mean velocity profile and turbulence structure at the start of the test section.

The use of subsidiary trip fences in (iv) meant that the downstream surface roughness would not be uniform, but it was considered that there is a similarity to nature in this method, where atmospheric flow passes over a rural terrain consisting of fields interspersed with windbreaks or rows of farm buildings. The general boundary layer simulation plan left wide scope for modification by alteration of grid bar spacing, trip fence

height and spacing, and surface roughness configuration. Later modification for urban boundary layer generation would be easily achieved.

In the atmospheric boundary layer modelling work, S.I. units were used following metrication, and in the work described in this Chapter and Chapters 7, 8 and 9, S.I. units are used.

6.2 EXPERIMENTAL APPARATUS.

6.2.1 Flow Measuring Equipment:

Measurements in the flow were made with two linearised DISA hot wire anemometer sets using either two 55F31 miniature single wire probes located in different parts of the tunnel, or a single 55A32 crossed-wire probe (X probe). The single wire probes were oriented with the wire in a vertical plane and perpendicular to the mean flow direction, to read $\bar{U}$ and u'. The X probe was generally oriented with the plane of the wires vertical (as in Fig. A6.2, p.501) to measure $\bar{U}$, u', w', $-\overline{uw}$ and u and w component energy spectra. The plane of the wires could be rotated to horizontal to measure the v component of turbulence and related quantities. Fig. 6.1 shows schematically how the hot wire anemometer sets were connected up, and Fig. 6.2 shows a photographic view of the instruments. Hot wire signals were fed to the DISA 55D30 DC meters and 55D35 RMS meters to extract the mean velocity and RMS velocity fluctuation respectively. Leads were also taken off to the DISA TCA unit for measurement of auto and cross-correlations, and to a Bruel & Kjaer Type 2114 1/3 Octave Bandwidth Spectrometer and Type 2305 Level Recorder for spectral analysis. A Tektronix Type 502A oscilloscope was used to check anemometer gain stability and display the hot wire signals.

Details of the operation procedure for the hot wire anemometers are given in Appendix 6. In Appendix 6 sources of error in calibration of the hot wire anemometers are examined, and effects of high turbulent intensity and inclination of the mean flow to the streamwise (x) direction on the hot wire signal are analysed. The effect of mean flow swirl on the X probe signal is also discussed, and estimates are given of the readable accuracy of various instruments used. Integral length scales of turbulence, derived from the hot wire data, were calculated using the methods described in 2.5.9, and methods for estimating the linear scaling of the wind tunnel simulation are described in Appendix 7.

Hot wire probes are shown mounted for the later work with model fences, in Fig. 8.1 (p.358). Also visible is the reference pitot-static tube, whose signal was read out on a Schiltknecht Micromanometer.

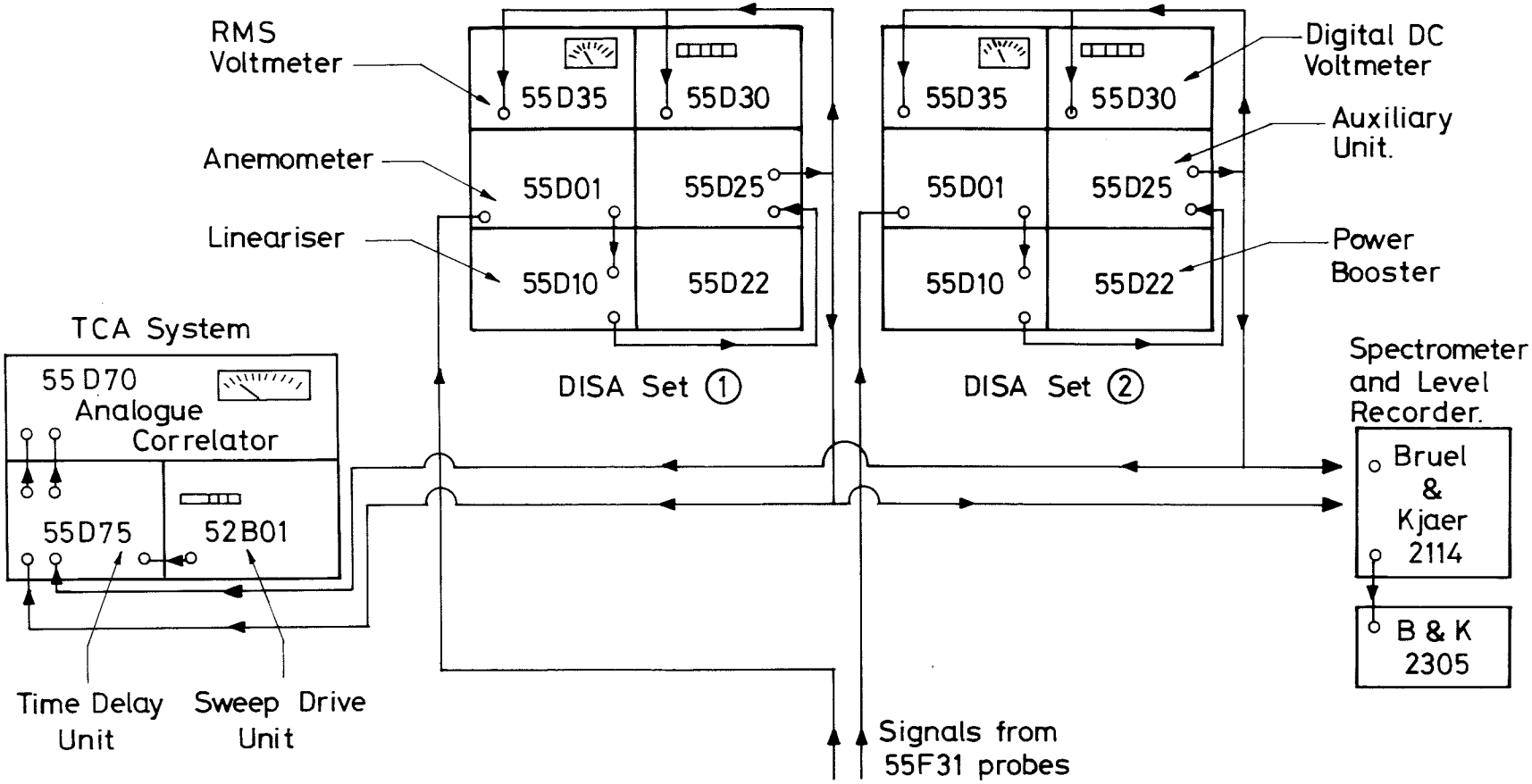

Fig.6-1 CONNECTION DIAGRAM FOR HOT WIRE ANEMOMETERS (SCHEMATIC ONLY.)

(Connection for Reynolds Stress Measurement shown in Fig.A6-2)

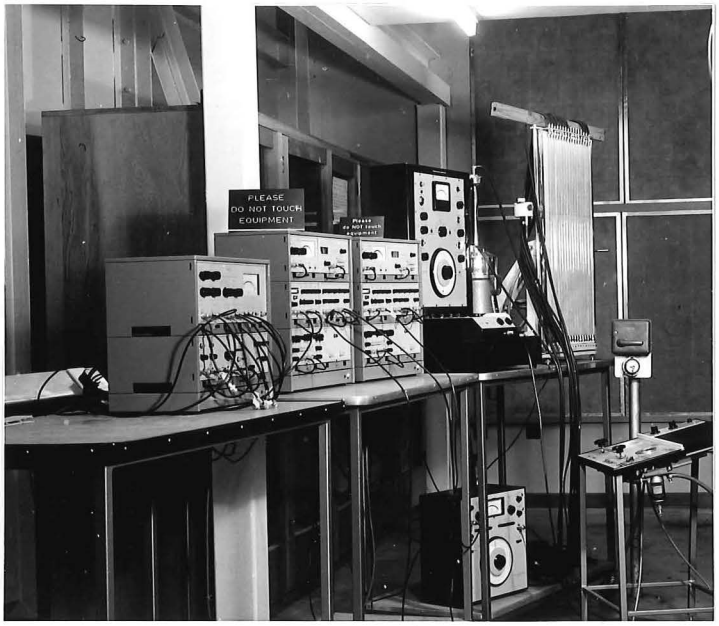

Fig. 6.2 Flow Measuring Equipment: From left - DISA TCA system, 2 DISA 55D00 hot wire anemometer sets with linearisers, Bruel & Kjaer 2114 spectrometer and 2305 level recorder (beneath), Schiltknecht micromanometer, multitube manometer

Fig. 6.3 Coarse turbulence-generating grid before installation in wind tunnel

6.2.2 The Turbulence Generating Grid:

The coarse turbulence generating grid is shown in DRG W37, and in Fig. 6.3. It was designed with the bars movable in their locating slots to enable:

(i) combination of 1½ in bars to provide a 3 in bar width in the grid;

(ii) non-uniform bar spacing to be set up if required for mean velocity profile generation.

This necessitated a biplane construction; wood was used, as it was light and adequately rigid.

6.2.3 The Initial Trip Fence:

Three aluminium fences were built, using 16G sheet, and three alternative fence heights were selected - 5 cm, 10 cm and 15 cm. 3/16 in diameter fence posts were glued to the rear face of each fence, and these fitted holes drilled in the wind tunnel floor, 0.61 m from the initial coarse grid.

6.2.4 The Torro Blocks and Baseboard:

60,000 white Torro building blocks, 1¼ in x 5/8 in x 3/8 in, were generously donated to the project by Torro International (N.Z.) Limited, together with sufficient green Torro baseboard to cover the whole working section floor. The 5 in x 5 in pieces of baseboard were glued to 4 ft modular lengths of 1/8 in hardboard which were, in turn, nailed lightly to the tunnel floor. The Torro blocks were used to build solid and permeable trip fences, and as individual roughness elements on the floor.

Torro blocks, counterpart of the British 'Lego' materials, are a very convenient tool in wind tunnel modelling work, and have been used in the Lego form by Armitt and Counihan (1968), Counihan (1969, 1973) and Teunissen (1972). The bulk of the blocks obtained in the present work will not be used until urban boundary layer modelling work is started.

6.2.5 Lateral Location of Flow-Measuring Probes:

With each successive arrangement of the boundary layer generating apparatus, lateral flow uniformity was briefly checked with a pitot-static tube traversed at three or four heights above the tunnel floor. Turbulence measurements were restricted to locations S25 and N25; i.e. 25 cm each side of the tunnel centre-line. Centre-line turbulence measurements were avoided because of possible, but unlikely, upstream effects created by the traverser

stanchion. The laterally uniform layout of boundary layer generating grid, fences and floor roughness enhance lateral uniformity of the flow downstream, and it was felt that the locations chosen for the hot wire probes would be adequate for detection of any lateral non-uniformity in the downstream turbulence structure.

6.3 ATMOSPHERIC WIND MODELLING PROCEDURE.

In Figs. 5.23, 5.26 and 5.27, the mean velocity distribution, turbulent intensity levels, and energy spectra for the u velocity component at X = 10 m were given for the clear working section. Starting with these flow conditions, stepwise modifications were made to the flow by addition of components of the boundary layer generating apparatus, until the final simulated atmospheric boundary layer was achieved. The procedure involved fitting first the coarse grid at the working section entrance, then adding the Torro baseboard surface roughness, and finally adding various trip fence arrangements with both uniform and non-uniform spacing of the horizontal bars of the grid. Each sub-heading in this section describes a new arrangement used to improve the boundary layer structure. Not all the different layouts tested have been reported. Where a new layout provided no improvement to a basic feature of the flow, such as mean velocity or turbulent intensity profile, only brief mention is made.

Initially there was a lack of standardisation in streamwise measurement locations, although distances of 2 m, 5 m and 10 m from the working section entrance (X = 0) were usually used. Location of trip fences later dictated to a certain extent where measurements could be made, and as the final layout was approached, measurements were restricted to positions X = 9 m and X = 11 m. It was aimed to achieve correct boundary layer structure at X = 9 m. Until the final layout was obtained, measurements were restricted to mean velocity, u and w turbulent intensities, $-\rho\overline{uw}$ Reynolds stress and u component energy spectra, correctness of these quantities being considered basic to the simulation. (See 3.4) For a given layout, during the developmental stage, not all the above measurements were made at each streamwise and lateral location tested, and the graphed experimental data show the test locations. Testing at one key location, such as the start of the test section, was often sufficient to show whether the trend in a given quantity, e.g. Reynolds stress, was satisfactory.

With the exception of Layout 2, tests were carried out with the maximum flow speed in the working section, such that $\bar{U}_{Ref} \simeq 18.3$ m/sec at

z = 60 cm, corresponding to fan blade pitch settings of $20^{o}/20^{o}$. With Layout 2, fan blade pitch settings of $16^{o}/20^{o}$ were used. All tests were run with the flow discharging from the third diffuser, on the mezzanine floor.

6.3.1 Layout 1: Uniform Coarse Mesh Grid + Clear Working Section:

Originally, it was intended to use a coarse grid of graded permeability, designed using the methods of Chapter 4, to generate both a mean velocity profile and a base level of turbulence in the working section. Non-uniformity in the flow entering the working section prevented the use of the Cowdrey or adapted Owen and Zienkiewicz grid design techniques. While the large scale turbulence generated by the fans would have given a good base level of turbulence in the working section, Figs. 5.23 and 5.26 (pp.197 & 206) show that the residual non-uniformity in mean velocity, and non-uniformity in turbulent intensity, respectively, necessitated the use of the grid at X = 0 to improve flow uniformity, even at the possible expense of a reduction in integral scale of turbulence in the flow.

The performance figures for the finer, 1½ in bar configuration of the coarse grid, shown in Table 4.1 (p.145) indicate that with a uniform approach flow, this grid would give turbulent intensity and length scale of 0.022 ($u'/\bar{U}$) and 11.6 cm (L_{u_x}) respectively, downstream at the start of the test section (X = 9.15 m). These values were expected to be modified by the turbulence from the fans in the approach flow. Removal of the second honeycomb to fit the coarse grid meant that all the wind modelling work was done with the flow deflector vanes and coarse grid in place of the two honeycombs.

With Layout 1, flow measurements were restricted to mean velocity, u component turbulent intensity and u component energy spectra. Initial pitot-static rake traverses of mean velocity at X = 2 m and 10 m were made with no roof divergence. A roof divergence of 14 cm in 12.2 m (~0.7^{o}) was set before hot wire anemometer measurements were made.

Results and Discussion:

(a) Mean Velocity Distribution: The contour graphs of Figs. 6.4 and 6.5 indicate the uniformity of the flow at X = 2 m and 10 m respectively. Comparing these graphs with Fig. 5.23 (p.197), it is evident that the grid improved flow uniformity at both X = 2 m and X = 10 m in comparison with the original 'clear tunnel + honeycombs' configuration. The improvement in mean flow uniformity over the central region of the tunnel at X = 10 m is marked, but the contours of equal velocity show clear evidence of boundary layer growth on both the floor, and the north wall of the working section, where

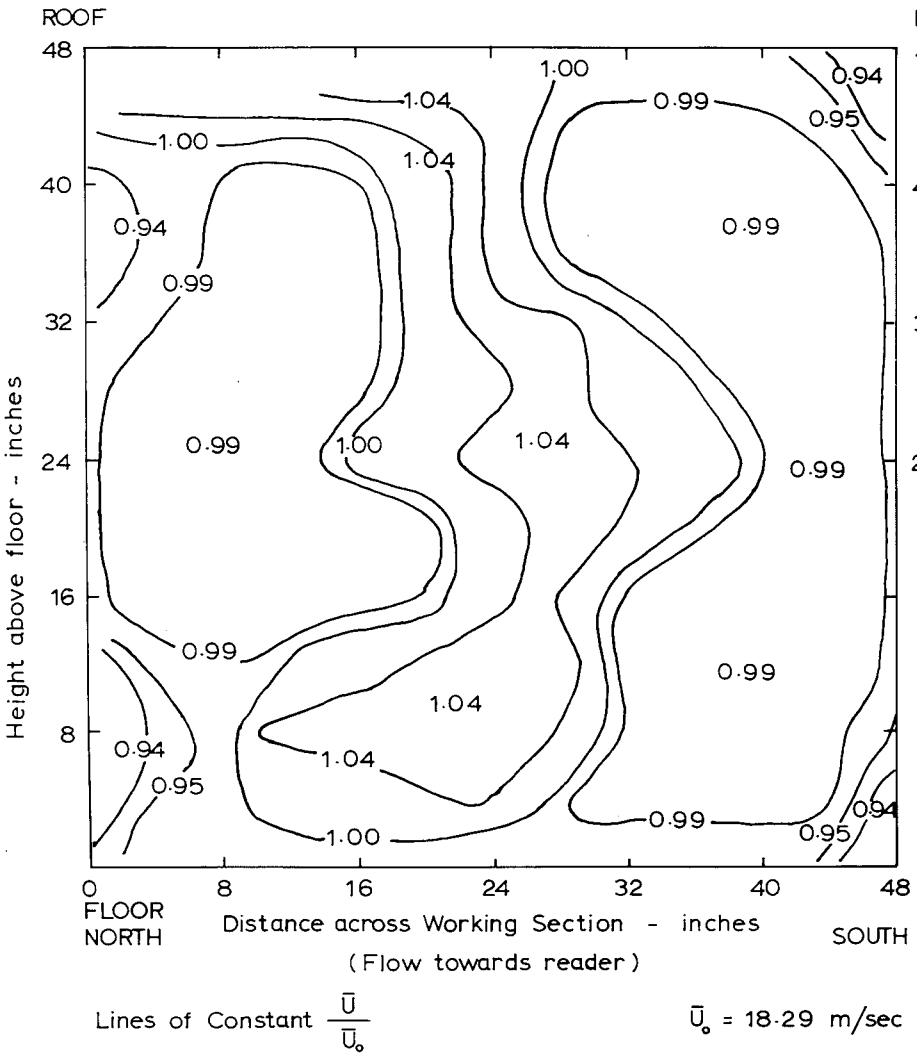

Fig. 6·4 MEAN VELOCITY DISTRIBUTION AT X = 2m.
LAYOUT 1.

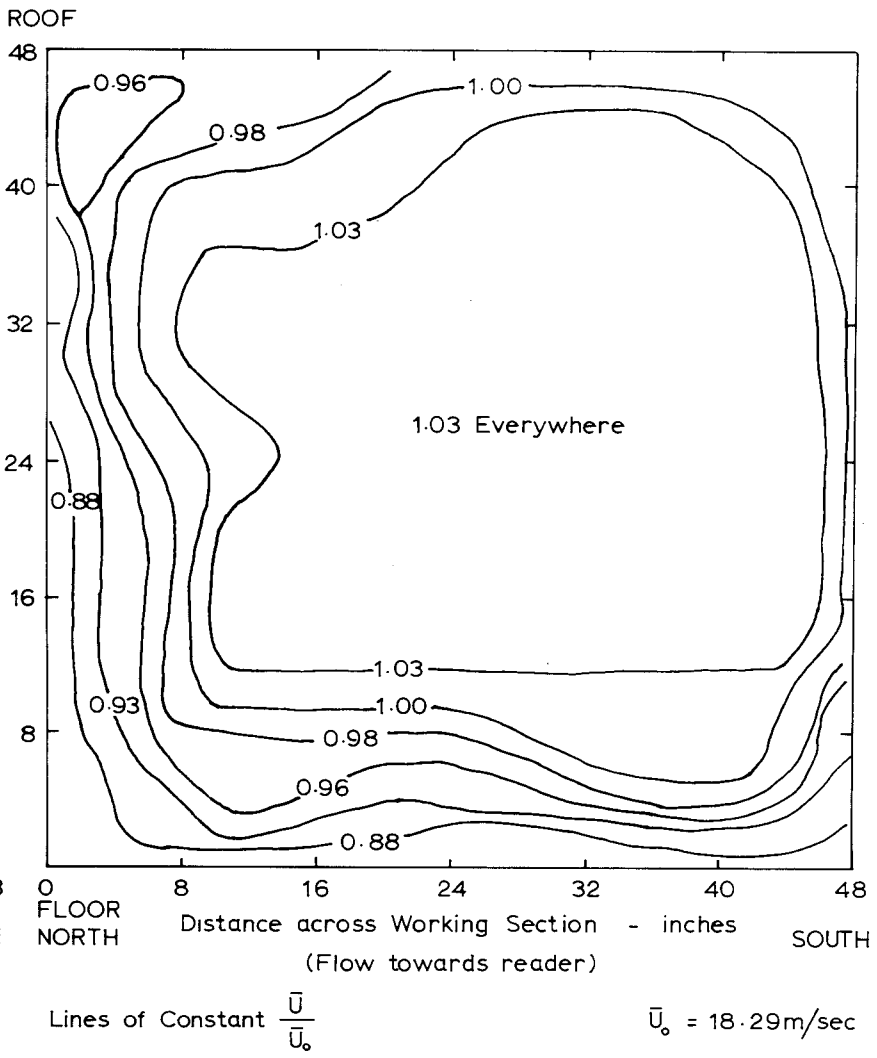

Fig. 6·5 MEAN VELOCITY DISTRIBUTION AT X = 10m.
LAYOUT 1.

the inside surfaces of the wood panel doors, with the plugged instrument slots, constitute greater surface roughness than the glass window panels of the south wall. The boundary layer growth on the floor was of course desirable for the atmospheric boundary layer simulation, but that on the walls was not wanted. In the future, tests could be run with the air-sealing strips removed from between the north wall doors. With a positive gauge static pressure in the working section, the gaps left between the doors should act as suction slots and reduce boundary layer growth.

At X = 10 m, Fig. 6.5 shows about 2% lateral non-uniformity in the first 20 cm above the floor, excluding the north wall boundary layer region. It was hoped that turbulence generating features, later fitted on the floor downstream of the coarse grid, would further improve mean flow uniformity by enhancing momentum transfer into the north wall boundary layer region. Fig. 6.6 shows the approximately logarithmic mean velocity profile at X = 10 m, with the roughness length, z_o, evaluated approximately by extrapolation as 0.00012 cm.

Fig. 6.4 shows that at X = 2 m, the upstream deflector vanes have produced a small over-correction to the original velocity defect in the centre of the tunnel. This occurred because the second honeycomb was removed in order to fit the grid, but flow uniformity is regained with further distance downstream.

Addition of the coarse grid resulted in a noticeable decrease in the long period fluctuations on mean velocity that occur because of interaction of the two fan impeller stages. This improvement in flow steadiness was attributed to the high pressure loss coefficient of the coarse grid:

i.e. for the honeycomb removed, $K_w = 0.4$ (measured)

for the coarse grid, $K_w = 2.1$ (estimated from Baines and Peterson, 1953, data, and measured).

The grid did, however, cause a reduction in spatial mean flow velocity from about 19.9 m/sec to 18.3 m/sec, because of its higher loss. (See Appendix 2).

The mean velocity distribution after addition of the coarse grid was considered acceptable at the test section, and it remained to see how the turbulence structure of the flow had been affected.

(b) Turbulent Intensity Measurements: These tests were carried out with a single DISA 55F31 hot wire probe, which was traversed on a coarse mesh pattern as shown in Fig. 6.7. Within the limits of this traversing pattern

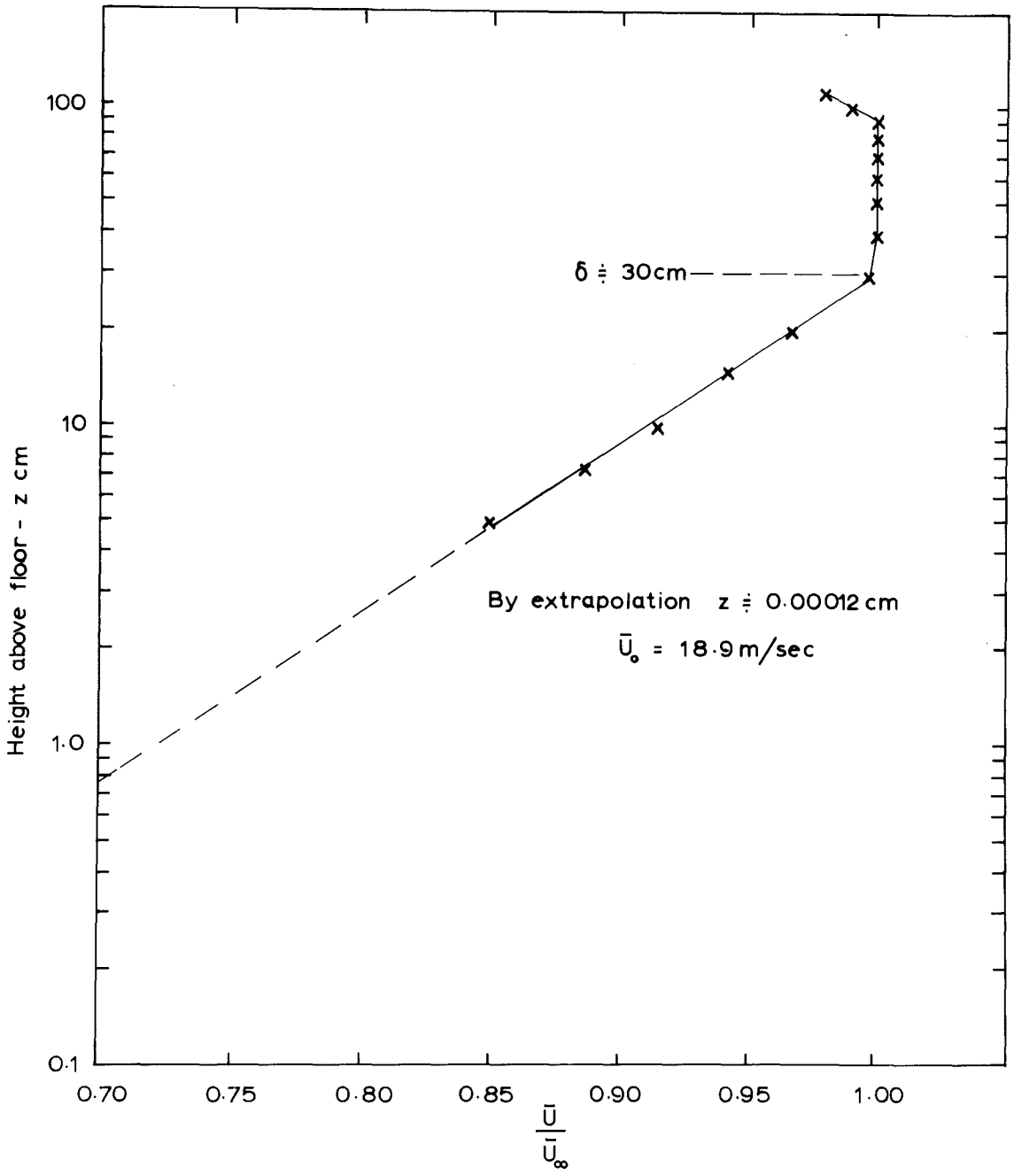

Fig. 6·6 CENTRELINE MEAN VELOCITY PROFILE AT X = 10M OVER BARE TUNNEL FLOOR - LAYOUT 1.

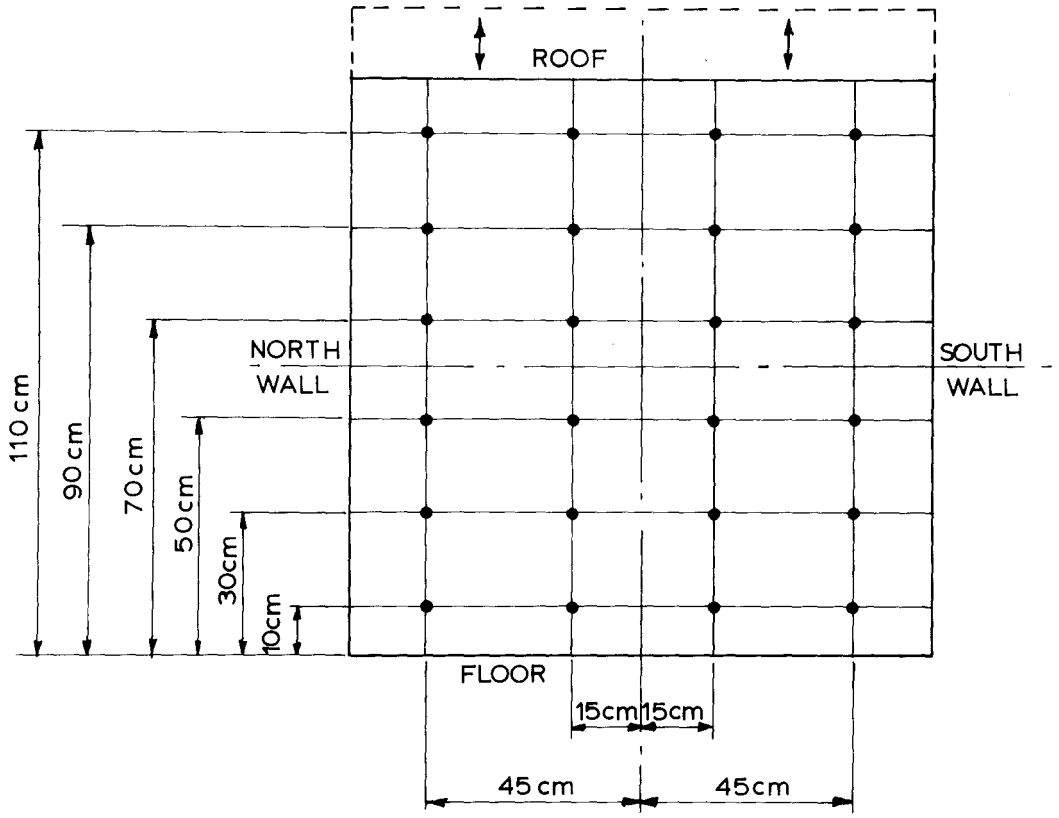

Fig. 6·7 GRID PATTERN FOR HOT-WIRE TRAVERSE IN PLANES NORMAL TO THE FLOW DOWNSTREAM OF UNIFORM COARSE BAR GRID IN CLEAR TUNNEL — LAYOUT 1

mean flow uniformity appeared unchanged by the introduction of the 0.66^{o} roof divergence. (Mean flow velocity, of course, decreased in proportion to the increasing working section area with streamwise distance, so that at X = 10 m, $\bar{U}_o$ = 16.8 m/sec.)

Fig. 6.8 shows plots of $u'/\bar{U}$ turbulent intensity for distances X = 1 m, 2 m, 5 m, 10 m from the working section entrance. Note in Fig. 6.8:

(i) the marked improvement in lateral and vertical uniformity of the turbulent intensity, particularly near the grid, where the scatter about the spatial mean $u'/\bar{U}$ value of 0.132 at X = 1 m, is ±6%, compared with the clear tunnel turbulent intensity of Fig. 5.26 (p.206), where the scatter about the mean $u'/\bar{U}$ value of about 0.1 at X = 1 m was ±40%.

(ii) The decay of turbulent intensity with downstream distance, except close to the floor, where a gradual increase in $u'/\bar{U}$ in the floor boundary layer is apparent between X = 5 m and X = 10 m.

(iii) By comparison with Fig. 5.26, the spatial mean turbulent intensity at X = 1 m is higher than without the coarse grid fitted, but the turbulence downstream of the grid shows more decay with distance than in the flow before the grid was fitted. This probably occurred because the grid removed some of the more permanent large scale velocity fluctuations in the flow. (Averaging time on the hot wire anemometer RMS meter was such that velocity fluctuations of frequency at least as low as 0.2 Hz were sensed).

With the grid at the working section entrance, turbulent intensity in the central region of the tunnel at X = 10 m was reduced to 0.036, a satisfactory value for the outer part of a simulated atmospheric boundary layer.

Fig. 6.9a shows the decay of the spatial mean turbulent intensity, between z = 30 cm and 50 cm, with downstream distance. This turbulence decay follows Batchelor's initial period decay law (Eqn 4.9) quite closely, with X_o set at 3M as estimated for this grid in 4.2.1. For large distances from the grid, e.g. X > 6 m, the intensity of turbulence tends higher than predicted by either Eqn. 4.9 (p.141) or Eqn. 4.14 (p.141). This may be due to the residual influence of large scale velocity fluctuations from the fans, not removed by the grid.

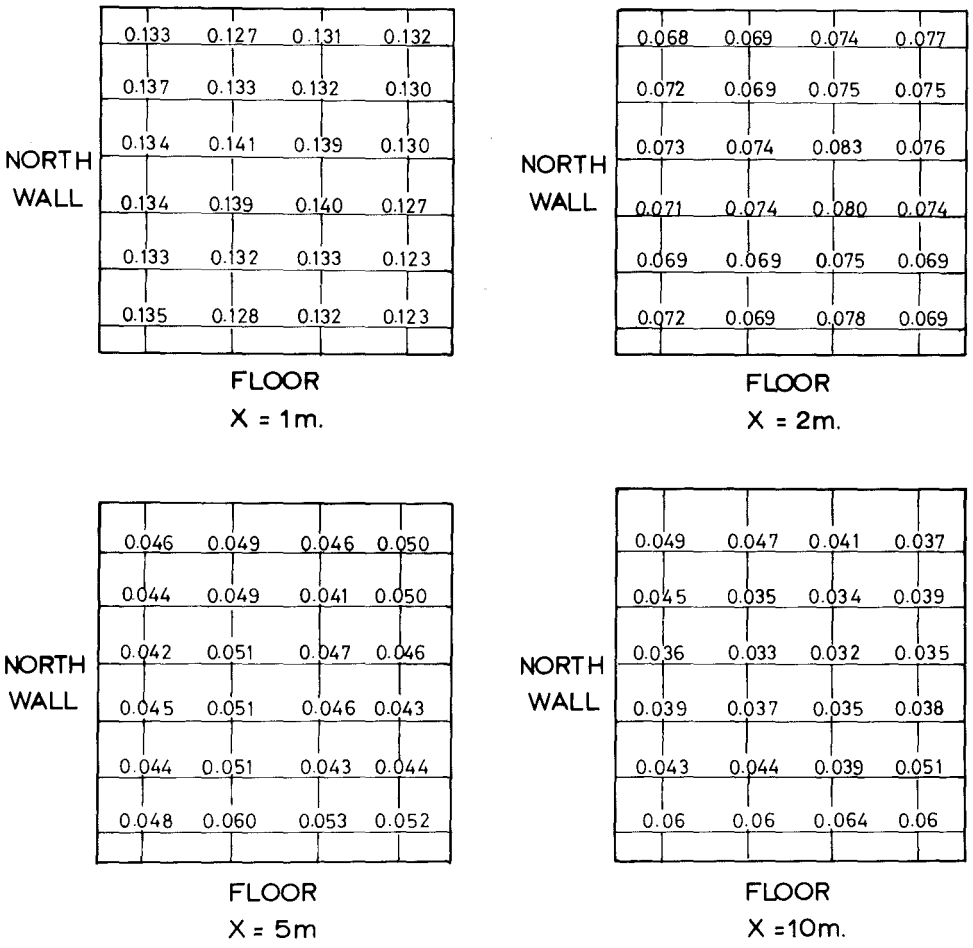

Fig. 6·8 $\frac{u'}{U}$ TURBULENT INTENSITY DOWNSTREAM OF COARSE SQUARE MESH BAR GRID - LAYOUT 1.

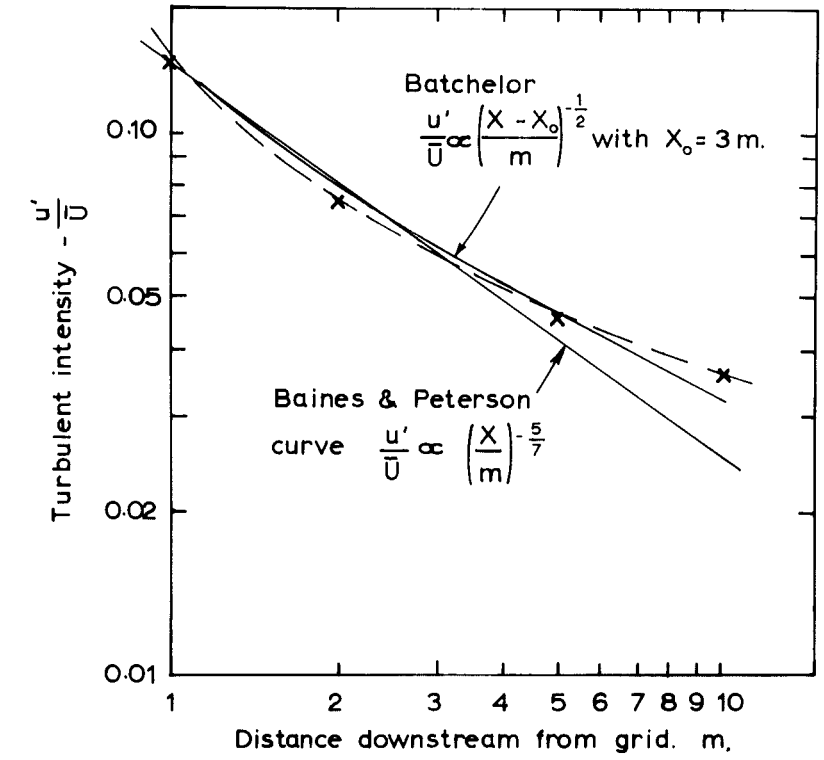

Fig. 6·9(a) DECAY IN $\frac{u'}{\bar{U}}$ DOWNSTREAM OF GRID. - LAYOUT 1

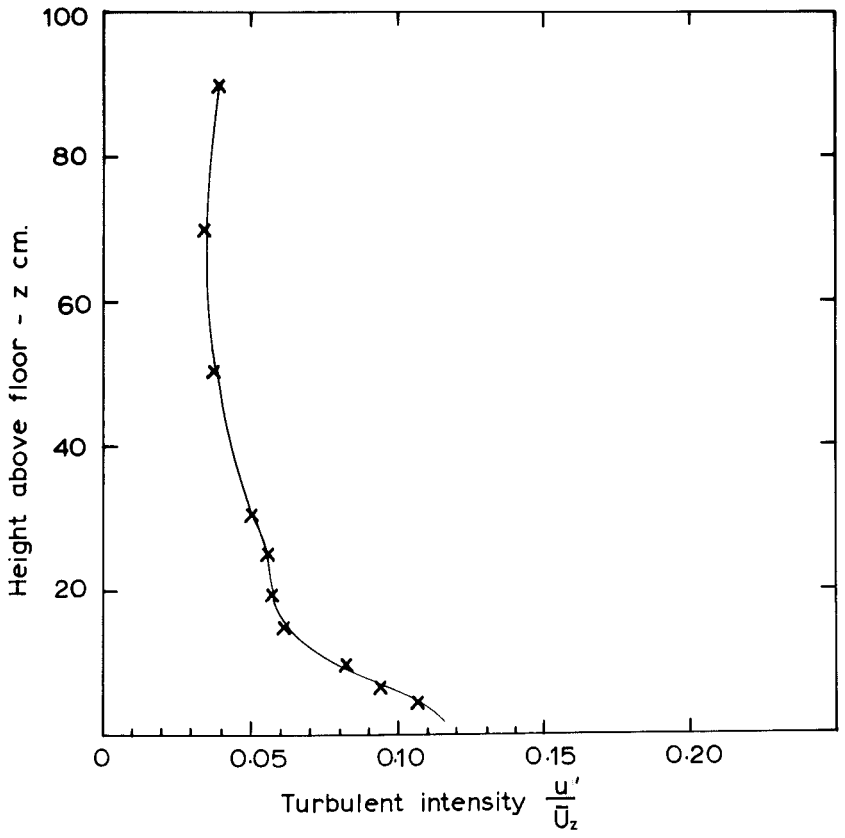

Fig.6·9(b) TURBULENT INTENSITY PROFILE AT X=10M, S15, LAYOUT 1.

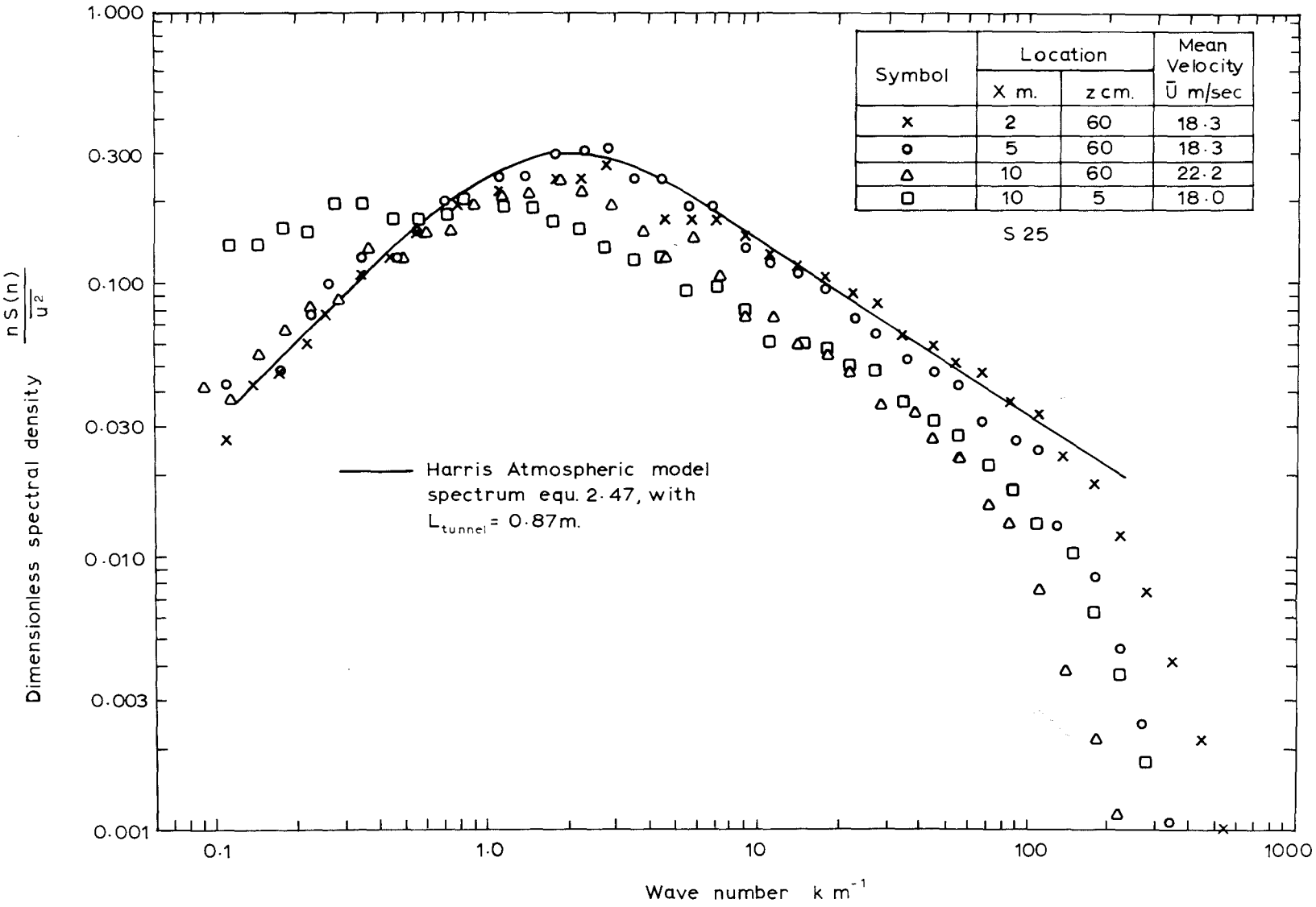

Fig. 6·10 ENERGY SPECTRA FOR u VELOCITY COMPONENT - LAYOUT 1.

Fig. 6.9b shows the variation in turbulent intensity with height at X = 10 m. As the floor is approached, the increase in local turbulent intensity is less than that required in a rural boundary layer, as can be seen by comparing with Fig. 2.10 (p. 45).

(c) u Velocity Component Energy Spectra: These are shown in Fig. 6.10, plotted in the form $\frac{nS(n)}{u^2}$ vs. k . Harris' model spectrum, Eqn. 2.47 (p. 55) is plotted for comparison, and it can be seen that there is fairly good spectral shape agreement with this model, except close to the floor, where flattening of the spectral peak occurs, and a less distinct region of -2/3 slope. In Table 6.1, the turbulent integral length scale calculated from the spectrum is summarised for each case, together with the linear scaling between wind tunnel and atmosphere, calculated according to the methods set down in Appendix 7.

In Table 6.1 (shown on following page), note that at z = 60 cm, no linear scaling can be realistically estimated, as comparison of turbulent length scales between wind tunnel and atmosphere leads to linear scaling between 1:3000 and 1:13000, depending on the method used. This would place the 60 cm height at least 1800 m off the ground in the atmosphere, where, in a rural boundary layer, $z_G \simeq 300$ m, i.e. the 60 cm height, when scaled up, lies far outside the atmospheric boundary layer.

Within the approximately 30 cm deep floor boundary layer, meaningful linear scales can be calculated. Teunissen's (1970) criterion for variation of atmospheric turbulent length scale, Eqn. 2.63 (p. 64) here predicts a linear scaling d_m/d_a = 1:130 at X = 10 m and z = 5 cm. Equations 2.60 (p.61) and 2.61 (p.62) which are based on matching of spectrum peaks on the wind tunnel and model atmospheric spectra, predict much larger atmospheric turbulent length scale near the ground than Eqn. 2.63, and thus also predict smaller linear scaling. Teunissen (1970) gives field results supporting the accuracy of Equn. 2.63, and it appears that Eqn. 2.61, and to a lesser extent, Eqn. 2.60, over-estimate L_{u_x} near the ground. This was discussed in 2.5.9. Interpreting the values of linear scaling at X = 10 m and z = 5 cm in Table 6.1 conservatively, it appears that the turbulence structure close to the floor corresponds to a linear scaling of about 1:500 or larger, but further out in the boundary layer small eddy sizes make the linear scaling extremely small. This is the same problem that was encountered in the work with bar grids in the 4 ft x 3 ft aeronautical tunnel, viz: the difficulty in obtaining large enough turbulent length scale in the outer part of the boundary layer.

TABLE 6·1 LAYOUT 1

Location		Spectral Peak Wave No.	Turbulent Length Scale	Linear Scaling $d_m : d_a$ based on -				
				$\frac{\delta_m}{\delta_a}$	$\frac{z_{o_m}}{z_{o_a}}$ †	L_{ux_m} / L_{ux_a}		
X m.	z cm.	k_p m^{-1}	$L_{u_x} = \frac{0.146}{k_p}$			Equ.2·60	Equ.2·61	Equ.2·63
2	60	2·5	5·8 cm.	—	—	*	*	*
5	60	2·0	7·3	—	—	~1:2500	~1:5000	~1:13000
10	60	1·64	8·9	—	—			
10	5	~0·66	22·1	1:830	1:1000	1:500	1:800	1:130

* These values have no practical meaning.

† $z_{o_m} \doteq 0.0001$ cm.
z_{o_a} from Fig. 2·7.

At z = 60 cm, an increase in L_{u_x} should occur with downstream distance. This increase is not great, since k_p does not decrease substantially between X = 2 m and X = 10 m, but the spectra of Fig. 6.10 show a general shift to lower wave number as X increases, indicating increasing scale. The length scale at X = 10 m and z = 60 cm compares well with that estimated for the flow downstream of the grid in Table 4.1 (p.145), where L_{u_x} was estimated at about 12 cm, compared with the value estimated from the measured spectrum, of about 9 cm. The value $L_{u_x} \simeq 9$ cm, at X = 10 m and z = 60 cm, is less than the value $L_{u_x} = 24$ cm measured at this location in the clear tunnel, as commented on in 5.3.5. The grid has therefore had the expected effect of improving uniformity of the flow, at the expense of a decrease in turbulent length scale in the flow entering the test section far downstream of the grid.

Summary:

(i) The addition of the coarse grid at the working section entrance appeared to have the desired effect of improving uniformity of mean velocity and turbulent intensity in the plane normal to the streamwise direction, and providing a suitable level of turbulent intensity in the region of the flow (in the test section) corresponding to the outer part of the required simulated boundary layer.

(ii) The improvement in flow uniformity was achieved at the expense of a decrease in the length scale of turbulence in the free stream region of the flow in the test direction.

(iii) Boundary layer growth on the floor of the working section resulted in a logarithmic mean velocity profile at X = 10 m, with $z_o \simeq 0.0001$ cm and $\delta = 30$ cm. This was approximately equivalent to a 1/9 power law profile.

(iv) Energy spectra showed quite good similarity to Harris' (1968) atmospheric model. Turbulent length scale estimates from the energy spectrum at X = 10 m and z = 5 cm suggest a linear scaling, within the floor boundary layer, of the order of 1:500. Comparison of turbulent length scales in the flow with atmospheric models, showed that a major aim of modifications to the flow would be to increase turbulent length scale in the region high above the floor.

6.3.2 Layout 2: Uniform Coarse Mesh Grid + Torro Baseboard:

The smooth wall boundary layer of Layout 1 could possibly be used as a small scale model of atmospheric flow over sea or mudflats, but is not very useful. As a first step to improve the boundary layer structure, it was decided to fit the Torro baseboards to the floor of the working section, to examine their effect on boundary layer thickness, and profiles of mean velocity and turbulent intensity. Layout 2 is shown in Fig. 6.11.

In the tests described below, it was found that alteration to fan blade pitch settings affected steadiness of the flow, and lateral uniformity of mean velocity and turbulent intensity in the working section. Experiments were run with blade pitch 16^{o} on Fan 1 and blade pitch 20^{o} on Fan 2. As pointed out in 5.3.2, this setting gave a steady mean flow speed as fan motor loads were equal. In all subsequent tests the fans were run with equal blade pitch settings. While this meant that the fan motor loads were unbalanced, this mode was preferred because :

(i) The 'equal pitch' operation gave best overall uniformity of mean velocity and turbulence parameters.

(ii) The balanced load, 'unequal pitch', operation gave a more constant wind speed, but mean flow swirl in the working section as shown in Table 5.2. This swirl caused problems in calibration of the X probe and errors in early Reynolds stress measurements.

Measurements with this layout were restricted to mean velocity, turbulent intensity and Reynolds stress profiles, and u component energy spectra.

Results and Discussion:

(a) Mean Velocity Profiles: Log/linear plots of mean velocity vs height are shown in Fig. 6.12. $\bar{U}_{\infty}$ is again the velocity at $z = \delta$, corresponding to $\bar{U}_{G}$ in the atmosphere. From Layout 2 onwards the most downstream measurement point (except for flow self-preservation checks) was X = 9 m, about 15 cm short of the end of the Torro baseboard floor covering. In Fig. 6.12 the growth of a turbulent boundary layer mean velocity profile characteristic of a rougher surface than the bare floor is readily seen. The profile tends toward an approximate power law form of exponent $\alpha \simeq 0.29$, at X = 9 m, where the roughness length determined approximately by extrapolation is $z_{o} \simeq 0.05$ cm.

Values of α and z_{o}, suggested above for the X = 9 m location, can only be approximate, as it is possible that a zero-plane displacement form should

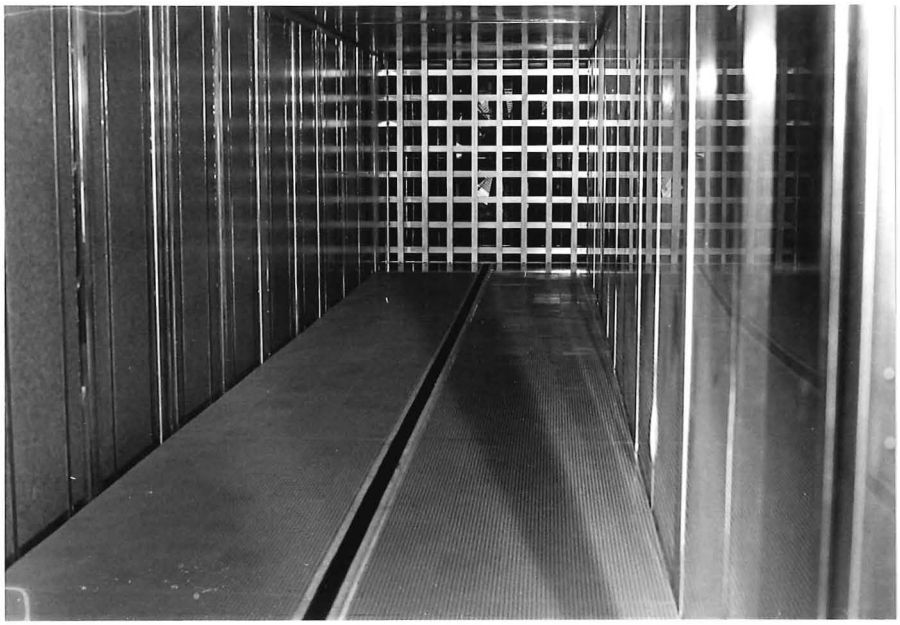

View towards upstream end of working section

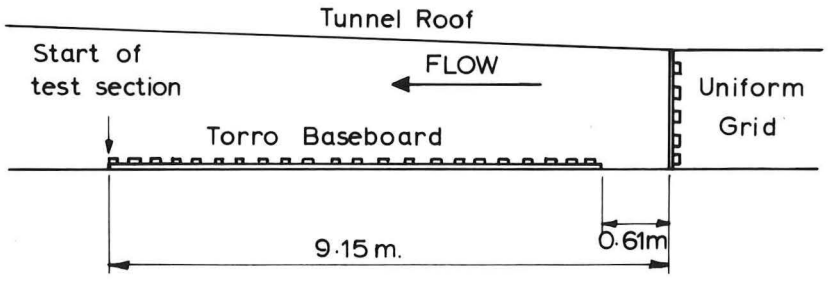

Fig. 6·11 LAYOUT 2. (Schematic only - not to scale.)

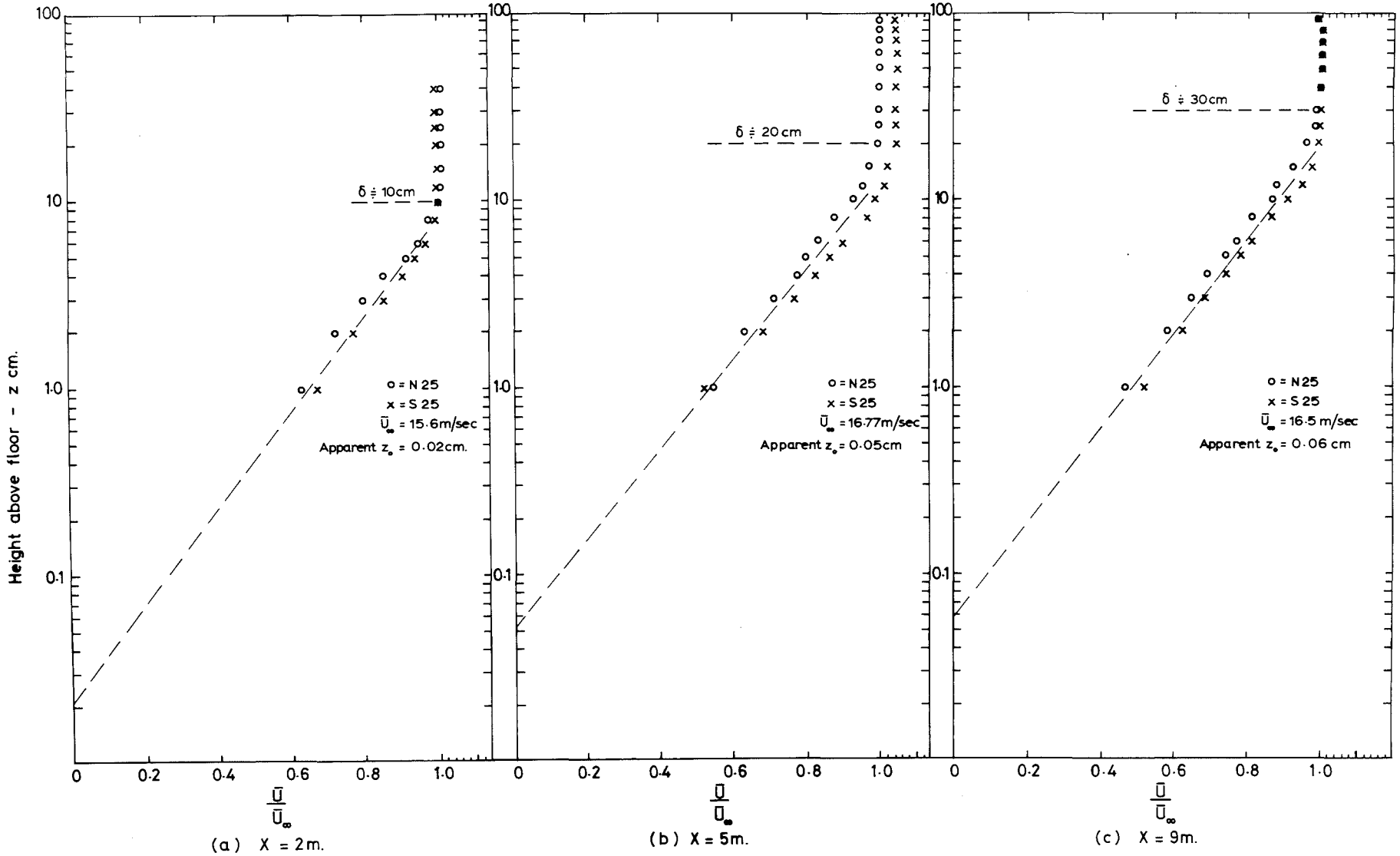

Fig 6·12 MEAN VELOCITY PROFILES - LAYOUT 2.

be used for the mean velocity profile, such as Eqn. 2.15 (p. 21) or its power law equivalent. However, the 1/8 in roughness element height on the Torro baseboard is not great, and it was felt that basing estimates of z_o on Eqn. 2.13 (p. 20) would be sufficiently accurate at this developmental stage of the work.

It appears from Fig. 6.12 that a long fetch of Torro baseboard floor roughness, sufficient to give a 1 m boundary layer depth, would be a suitable model roughness for a rural/suburban boundary layer simulation. The restricted working section length prevented use of this surface alone in the present work. In Fig. 6.12 it is seen that the boundary layer depth at X = 9 m is about the same as that with the smooth tunnel floor at X = 10 m in 6.3.1. Greater boundary layer depth should have occurred with the rougher floor surface, and it appears that the difference in fan blade pitch settings in the two layouts, in changing flow uniformity in the working section, affected the apparent boundary layer depth.

(b) Turbulent Intensity Profiles: These are shown in Figs. 6.13 and 6.14. Note in Fig. 6.13:

(i) the increase in $u'/\bar{U}_\infty$ turbulent intensity with increasing boundary layer thickness in the region z = 10 - 30 cm;

(ii) the previously observed decrease in free stream intensity with distance downstream. If free stream turbulent intensity is assumed to occur at $z = \delta$ and above, then on this basis $\delta_{x=9m} = 35$ cm;

(iii) the increasing lateral non-uniformity in $u'/\bar{U}_\infty$ with distance downstream. This non-uniformity corresponded to that in the mean velocity, regions of lower turbulent intensity in Fig. 6.13 corresponding to regions of higher mean velocity in Fig. 6.12.

In Fig. 6.14 plots of $u'/\bar{U}_\infty$, $v'/\bar{U}_\infty$, $w'/\bar{U}_\infty$ are compared at X = 9 m. Note from this graph :-

(1) Near the 'ground' (z = 2 cm), u':v':w' ≃ 2.0: 1.39: 1.0. This corresponds reasonably well with the atmospheric model of Eqn. 2.30 (p.42) which gives u':v':w' = 1.93:1.54:1.0.

(2) Within limits of experimental accuracy, free stream values of u', v', w' are equal. This indicates the presence of approximate isotropy, and supports the previously observed agreement of the u component energy spectrum with Harris' approximate von Karman isotropic form, Eqn. 2.47.

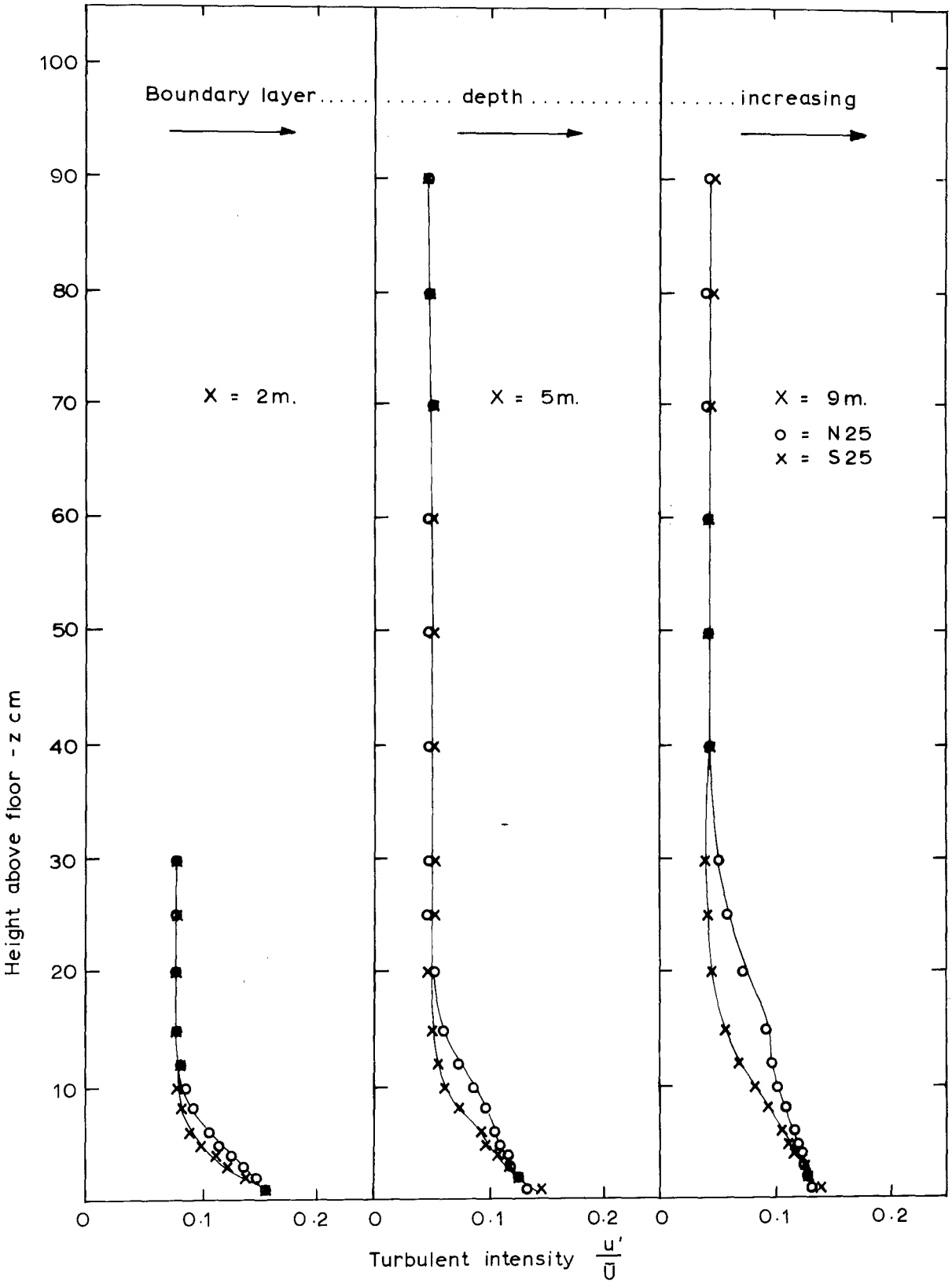

Fig. 6.13 $\frac{u'}{\bar{U}}$ TURBULENT INTENSITY - LAYOUT 2.

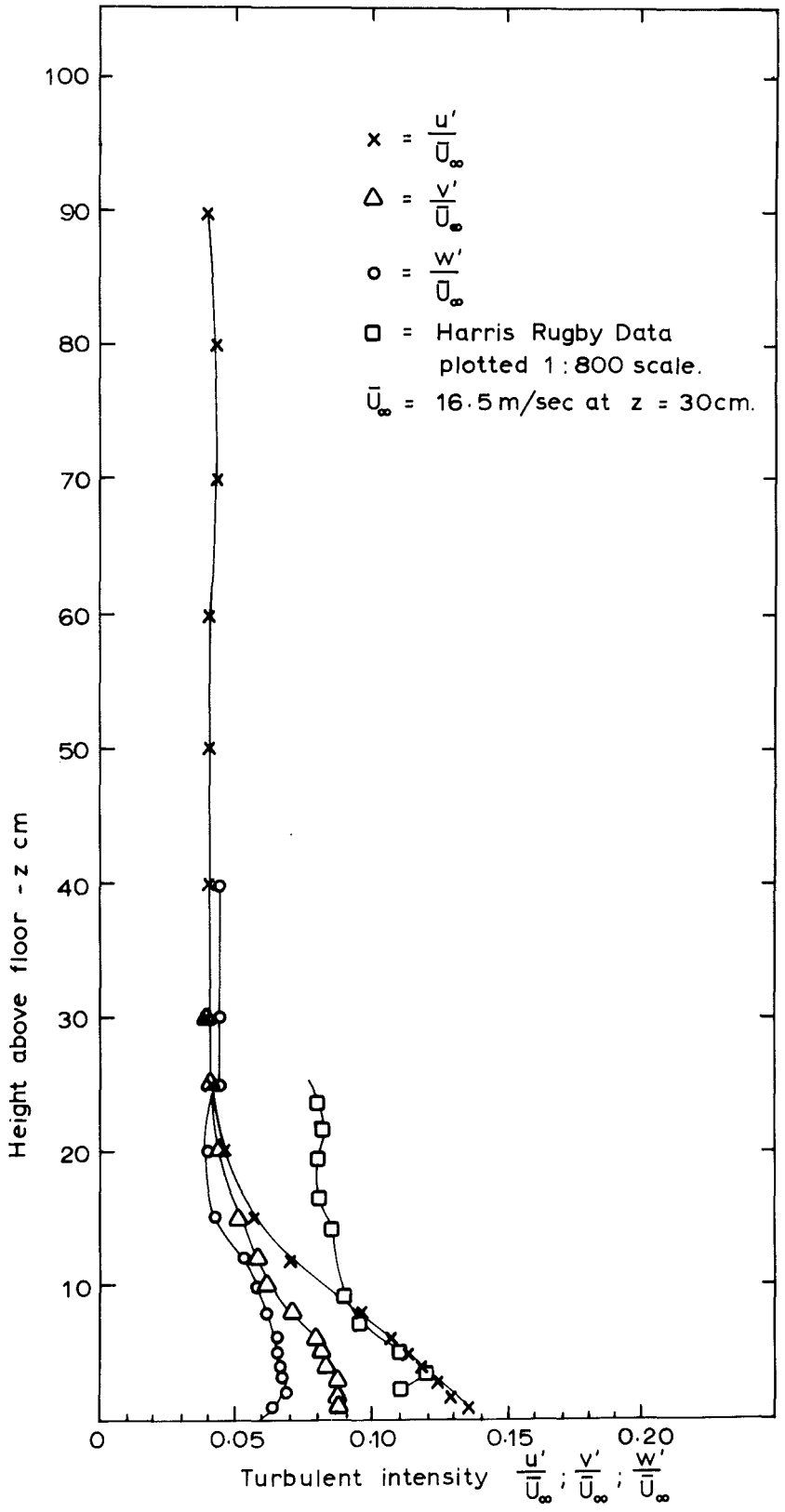

Fig. 6.14 TURBULENT INTENSITY AT X = 9m, S 25 , FOR u, v, w VELOCITY COMPONENTS - LAYOUT 2.

(3) Below z = 10 cm there is good agreement between $u'/\bar{U}_\infty$ and Harris' (1970) Rugby data plotted to a scale of 1:800. Harris' data are close to rural boundary layer design turbulent intensity profiles illustrated in Fig. 2.10. Further out in the wind tunnel boundary layer there is a deficit in turbulent intensity (for a 1:800 scale model).

(c) Reynolds Stress Profiles: In Fig. 6.15 the shear stress $-\rho\overline{uw}$ is plotted in the form $-\overline{uw}/\bar{U}_\infty^2$. In 2.4.4. it was established that a reasonable value of $(u_*/\bar{U}_\infty)^2$ for a rural boundary layer is 0.0025. If it is assumed that $u_*^2 = -\overline{uw}_{max}$, then the wind tunnel simulated atmospheric boundary layer should have $-\overline{uw}/\bar{U}^2_{\infty max} \simeq 0.003$, provided that $\bar{U}_\infty$ corresponds to $\bar{U}_G$. In Fig. 6.15, $-\overline{uw}/\bar{U}^2_{\infty max}$ is approximately 0.0035, based on a linear scaling of 1:1000 and $z_G \simeq 300$ m. This maximum stress value is acceptable, but there is no evidence of a definite constant stress layer. The increase in Reynolds stress with boundary layer growth between X = 5 m and X = 9 m can be seen.

The value of $(u_*/\bar{U}_\infty)^2$ derived from the logarithmic mean velocity profile of Fig. 6.12(c) is 0.0048, somewhat higher than the measured Reynolds stress. This suggests the use of a zero plane displacement in the velocity profile of Fig. 6.12(c). For instance, with d = 0.4 cm (about the height of the roughness elements), z_o = 0.03 cm, and $(u_*/\bar{U}_\infty)^2$ becomes 0.0035.

The Reynolds stress measurements of Fig. 6.15 must be considered approximate, as difficulties in calibration were encountered in early shear stress measurements using the hot wire anemometer. (See Appendix 6.7.3c)

(d) u Velocity Component Energy Spectra: These are shown in Fig. 6.16. There is quite good shape similarity over the approximate 30 cm boundary layer depth, but the usual flattening of the peak and absence of a distinct -2/3 slope region, in the $nS(n)/\overline{u^2}$ vs k plot, occur as z decreases. As z increases, the spectrum shifts to slightly lower wavenumbers. Harris' (1968) spectrum, Eqn. 2.47, is plotted for comparison with the spectra at z = 10 cm, 20 cm and 50 cm. There is acceptable similarity to the Harris spectrum in the upper part of the boundary layer. The flattening of the spectral peak close to the 'ground' is also observed with atmospheric data, e.g. see Teunissen (1970, Fig. 6) and Davenport (1963).

In Table 6.2, the length scale of turbulence calculated from the spectrum is summarised for each height, together with the linear scaling

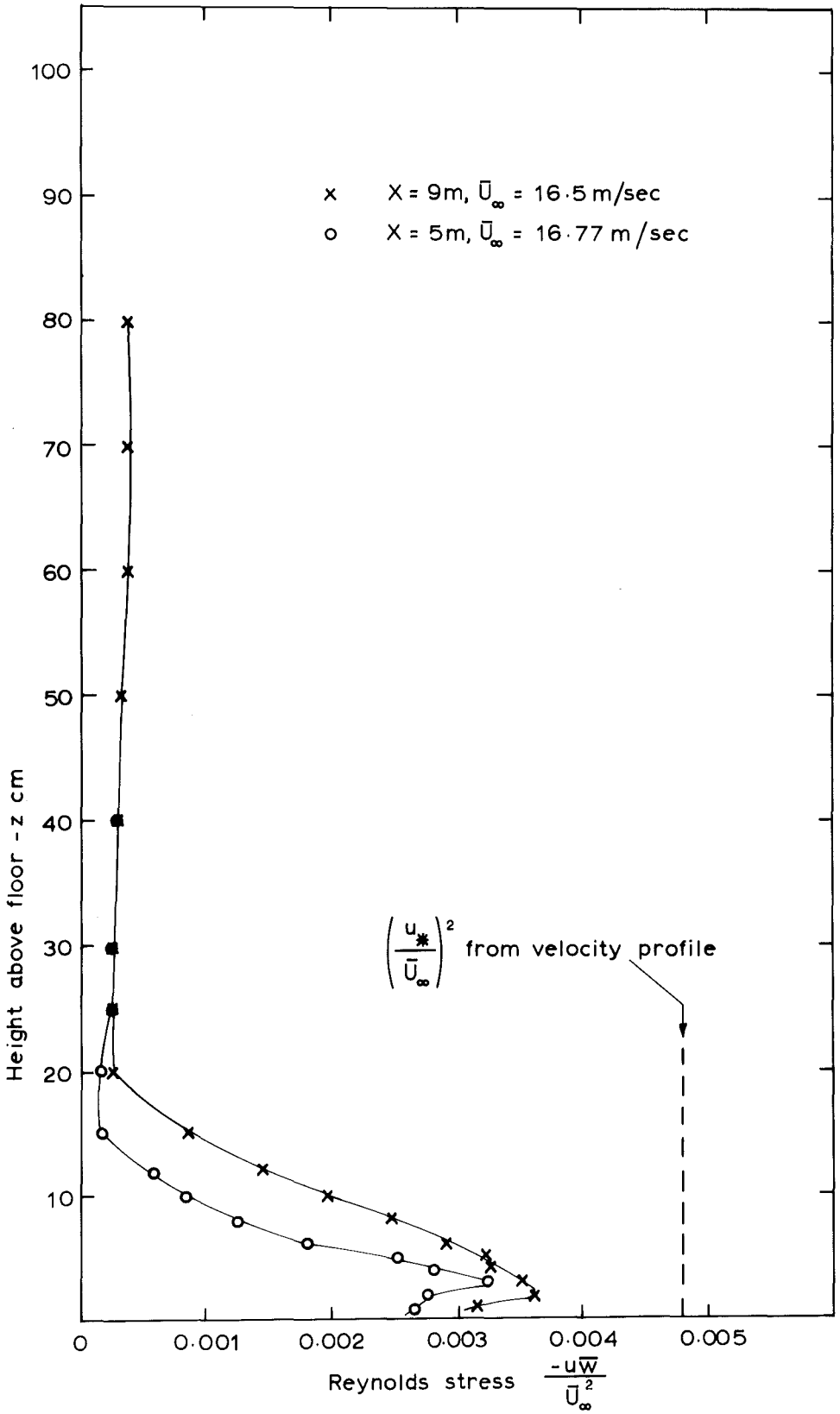

Fig. 6·15 REYNOLDS STRESS PROFILE AT S 25. - LAYOUT 2.

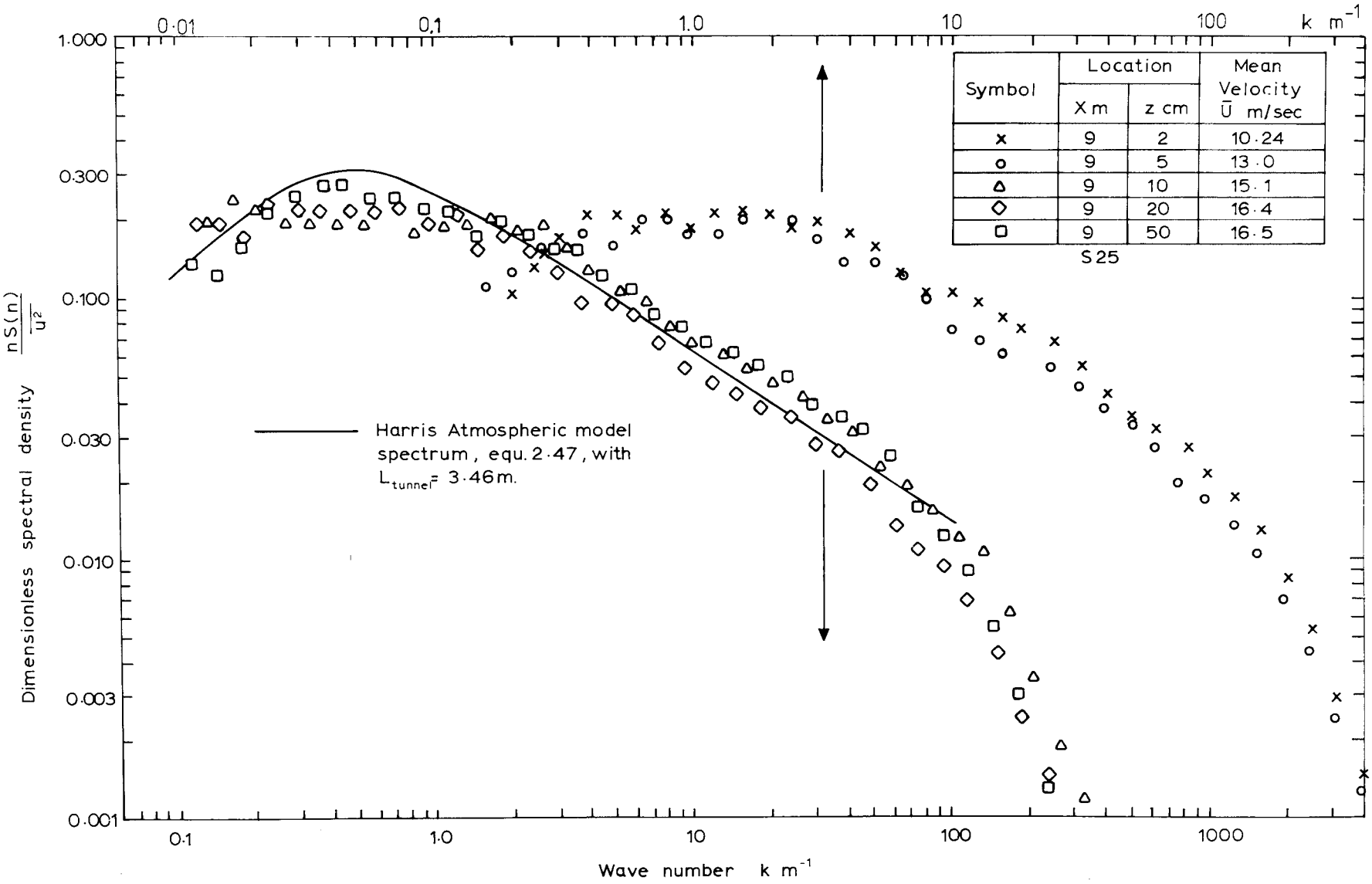

Fig. 6·16 ENERGY SPECTRA FOR u VELOCITY COMPONENT - LAYOUT 2.

TABLE 6·2 LAYOUT 2

Location		Spectral Peak Wave No.	Turbulent Length Scale	Linear Scaling $d_m : d_a$ based on -				
				$\frac{\delta_m}{\delta_a}$	$\frac{z_{o_m}}{z_{o_a}}$	L_{ux_m} / L_{ux_a}		
X m.	z cm.	k_p m^{-1}	$L_{ux} = \frac{0.146}{k_p}$			Equ.2·60	Equ.2·61	Equ.2·63
9	2	~1·2 *	~11	1:1200	1:1000	~1:1100	~1:2200	~1:180
9	5	~1·0 *	~15	1:1200	1:1000	~1:1060	~1:2160	~1:270
9	10	0·59	24·7	1:1200	1:1000	1:620	1:1170	1:200
9	20	0·59	24·7	1:1200	1:1000	1:740	1:1400	1:400
9	50	0·46	31·7	—	—	1:520	1:950	1:600

* Broad spectral peak makes these very approximate.

between wind tunnel and atmosphere calculated according to the methods given in Appendix 7. The methods comparing boundary layer depth and roughness lengths in wind tunnel and atmosphere lead to linear scaling of about 1:1200 and 1:1000 respectively. Methods comparing length scales of turbulence between wind tunnel and atmosphere predict different linear scale depending on the atmospheric model chosen. Teunissen's (1970) model, Eqn. 2.63, again predicts large linear scaling near the floor, but a decrease with height. Equns 2.60, and 2.61, the length scale expressions derived from the Davenport and Harris model atmospheric spectra, suggest smaller linear scaling near the floor, but an increase with height. Thus, taking Equns 2.60 and 2.63 as more realistic (see 2.5.9), a suitable linear scaling for the whole boundary layer of 1:600 is conservatively suggested. Close to the floor estimates of L_{u_x} from the spectral peak were very approximate due to the flat, ill-defined peak on the spectrum trace.

On balance, a linear scaling for the simulation of about 1:1000, or slightly larger, appears reasonable.

Summary:

(i) The addition of the Torro baseboard surface roughness downstream of the uniform coarse grid had the desired effect of increasing turbulent intensity, roughness length and equivalent power law exponent, in the boundary layer. The boundary layer depth at X = 9 m became 30 - 35 cm, compared with a depth of about 30 cm at X = 10 m without the Torro baseboard surface roughness.

(ii) The still developing mean velocity profile at X = 9 m was characteristic of flow over a suburban area (when plotted with no zero plane displacement). With the approximate power law exponent of 0.29, comparison of boundary layer depths between wind tunnel and atmosphere, using Fig. 2.7 (p.30) indicated a linear scaling of about 1:1200. Interpreted as a rural boundary layer simulation, turbulent intensities, Reynolds stress level near the floor, length scales of turbulence and boundary layer thickness were characteristic of an atmospheric flow linearly scaled down by a factor of 1:1000 or slightly larger.

(iii) Use of a 0.4 cm zero plane displacement in the mean velocity profile plots would give better agreement between measured Reynolds stress values and those estimated from the mean velocity profile slope, and would change the approximate power law profile exponent at X = 9 m from 0.29 to about 0.23.

6.3.3 Layout 3: Uniform Coarse Grid + 15 cm Solid Trip Fence + Torro Baseboard Surface Roughness:

The need to increase boundary layer thickness and turbulent intensity and shear stress levels in the outer part of the boundary layer was seen as the major requirement of the next modification to the flow. Values of turbulent length scale in Table 6.2 also indicated the need for further increase in length scales in the outer part of the boundary layer. The results of 6.3.2 indicated that a naturally grown boundary layer on the Torro baseboard would have a higher velocity profile power law exponent than 1/6, but the Torro baseboard was retained, recognising that addition of trip fences would further change the non-equilibrium profile at X = 9 m. The Torro baseboard was also valuable for mounting trip fences.

Trip fences have been used to introduce shear, turbulence and boundary layer thickening in previous atmospheric boundary layer simulations, as reviewed in 3.5. Usual practice is to use a single trip fence at the start of the working section, to accelerate boundary layer growth. A solid fence causes a strong upward displacement of the flow, and the formation of a separation zone behind the fence. A region of high shear is introduced at the top of the fence (see 9.1.5, p.406), so that the top of the fence behaves as a point source of turbulence, and a field of large velocity fluctuations is initiated, diffusing vertically upwards and downwards in the assumed two-dimensional flow as the flow moves downstream. Downstream effects from a trip fence are commonly assumed to disappear 40H to 50H downstream of the barrier (H = fence height). In the present work, effects were still noticeable 90H - 100H downstream.

Davenport and Isyumov (1967) found that a 30 cm high solid trip fence at the entrance to a 152 cm high working section caused excessive levels of turbulent intensity 20 - 25 m downstream at the test section. There the trip fence caused about 20% blockage of the working section. In the present work, it was decided to use, initially at least, a relatively lower trip fence. A 15 cm solid fence, giving about 12% blockage of the working section, was installed at X = 0.61 m, as shown in Fig. 6.17. (A 10 cm initial trip fence was also tested, and increased the boundary layer thickness at X = 9 m to about 60 cm, with corresponding increases in turbulent intensities. The effect of the 15 cm trip fence was, however, even more favourable, and results for only the 15 cm trip fence are given).

Measurements with this layout were restricted to mean velocity, turbulent intensity and Reynolds stress profiles, and u component energy spectra.

Close-up view of grid and initial trip fence

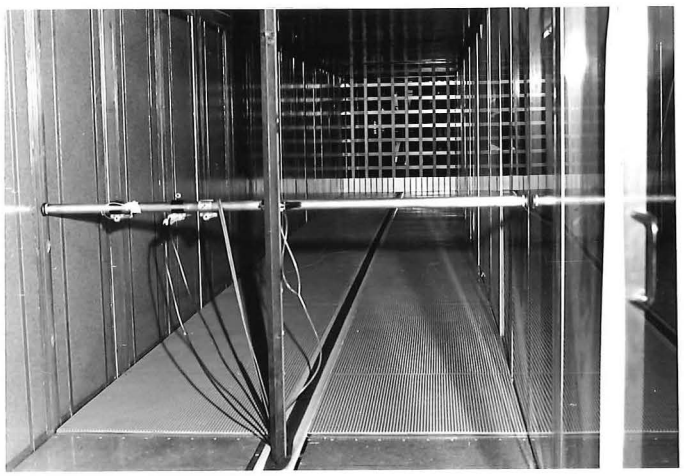

View towards upstream end of working section

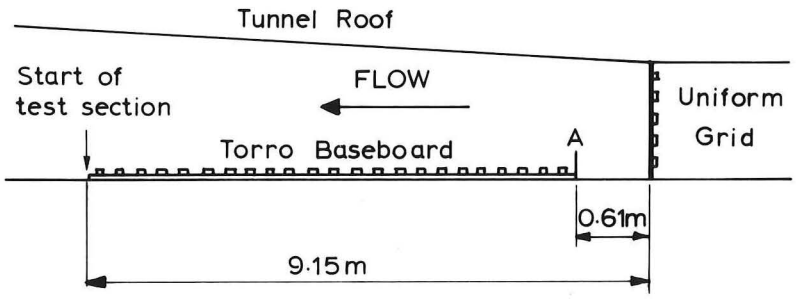

Fence A = Solid aluminium 15cm. high.

Fig. 6.17 LAYOUT 3 (Schematic only-not to scale.)

Flow self-preservation checks were made at X = 11 m.

Results and Discussion:

(a) Mean Velocity Profiles: For Layout 3 and all subsequent tests, the fans were operated on the same blade pitch settings, $20^{o}/20^{o}$, for optimum flow uniformity (and apparently slightly greater boundary layer depth). The addition of the 15 cm trip fence increased the boundary layer depth at X = 9 m to about 90 cm. Mean velocity profiles for Layout 3 are shown in Fig. 6.18.

Fig. 6.18 shows that there is good lateral uniformity at X = 9 m, and obvious boundary layer growth between X = 5 m and X = 9 m. Retardation of the flow velocity between X = 5 m and X = 9 m close to the floor is probably due to the effect of the Torro baseboard surface, but further out is probably related to the change in tunnel cross-section area. The log/linear plot of Fig. 6.18a does not show a very clear straight line portion near the floor. While this may be due to the non-equilibrium nature of the velocity profile, replotting with a 0.4 cm zero plane displacement as in Fig.6.18b improves the linearity of the lower portion of the profile. Although the velocity profile at X = 9 m deviates from the design 1/6 power law curve, between $z \simeq 2$ cm and $z \simeq 50$ cm, it would probably be acceptable as an open country velocity profile, provided the turbulent structure of the flow were correctly scaled. Comparing Fig. 6.18 with Fig. 6.12, it is seen that the trip fence has had the desired effect of transferring mean flow momentum upwards, increasing mean velocities in the upper part of the working section, at the expense of those near the floor.

(b) Turbulent Intensity Profiles: These are shown in Fig. 6.19. In Fig. 6.19a the change in $u'/\bar{U}_{\infty}$ and $w'/\bar{U}_{\infty}$ between X = 5 m and X = 9 m as the boundary layer thickens can be seen, and the decrease in w' with distance downstream from the trip fence is evident. The profiles at X = 9 m suggest a boundary layer thickness of 80 - 90 cm as with the mean velocity profiles. In Fig. 6.19b $u'/\bar{U}_{\infty}$ and $w'/\bar{U}_{\infty}$ are plotted for X = 9 m. Teunissen (1970) suggests a constant value of u' and w' in the atmospheric surface layer, with w' = 0.52u' (Eqn. 2.32). In reality u' and w' must decrease with height above the surface layer as shown for u' in Fig. 2.8 (p.40). The relative magnitudes of u' and w' in Fig. 6.19b are of the correct order, particularly near the floor, and the $u'/\bar{U}_{\infty}$ profile plots close to Harris' (1970) data scaled down about 1:350 scale. It is somewhat doubtful comparing wind tunnel data with one particular set of field data

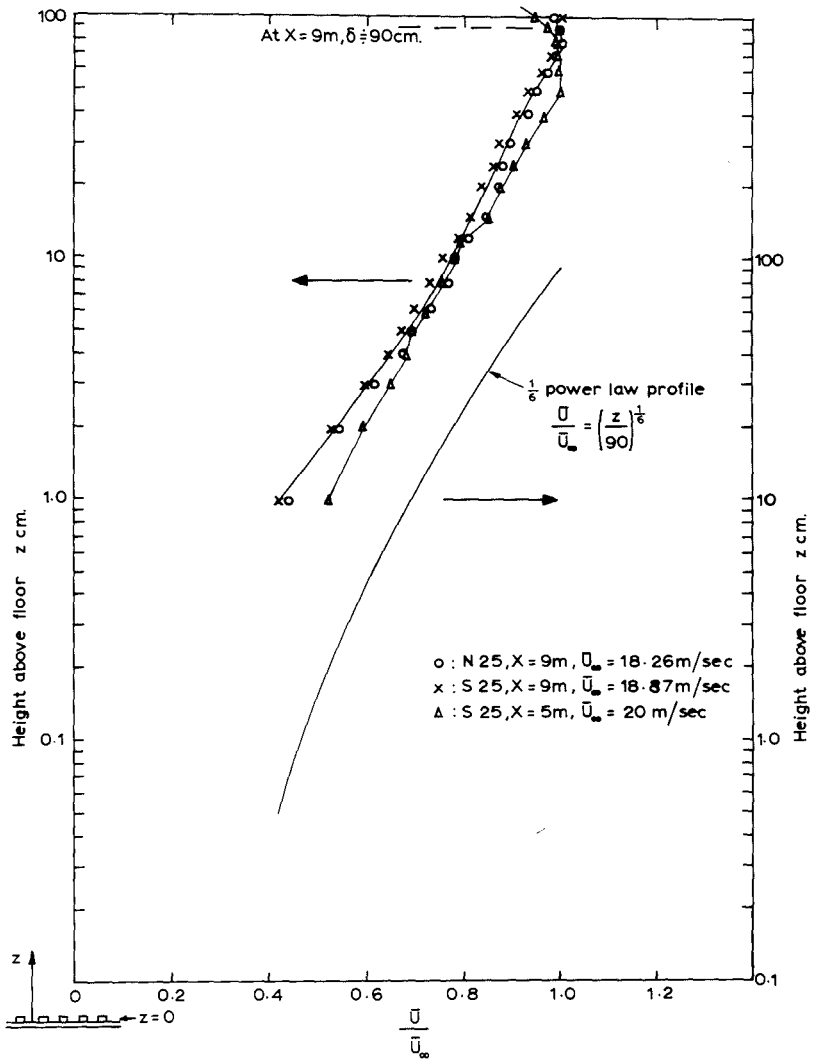

Fig. 6·18a. MEAN VELOCITY PROFILES - LAYOUT 3

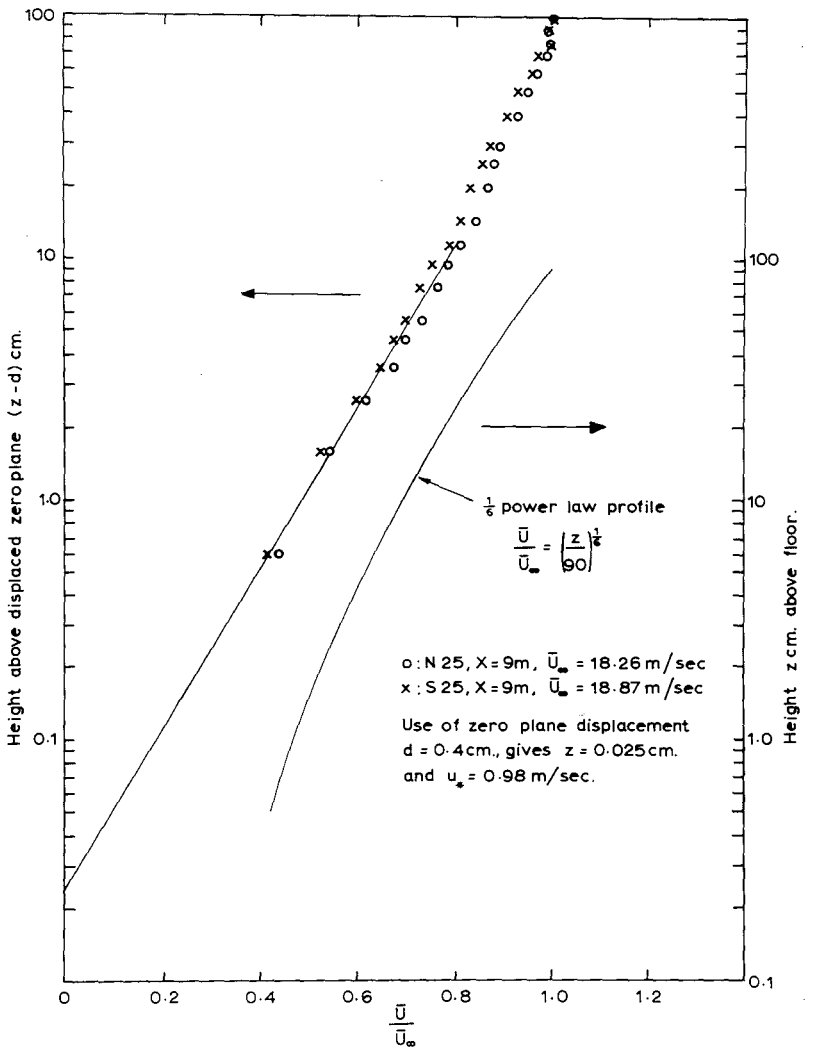

Fig. 6·18b MEAN VELOCITY PROFILE - LAYOUT 3 PLOTTED WITH 0·4CM. ZERO PLANE DISPLACEMENT.

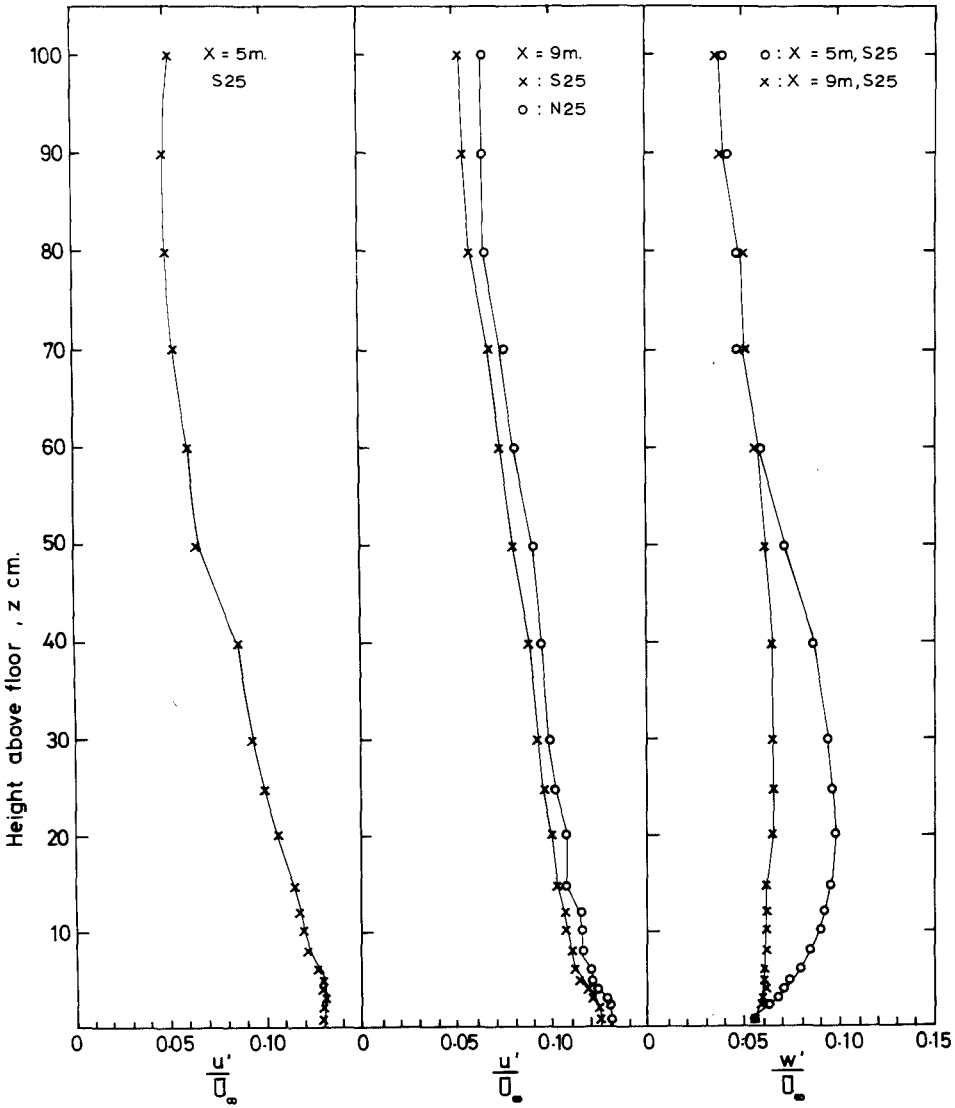

Fig. 6·19a. $\frac{u'}{U_\infty}$ AND $\frac{w'}{U_\infty}$ TURBULENT INTENSITY - LAYOUT 3.

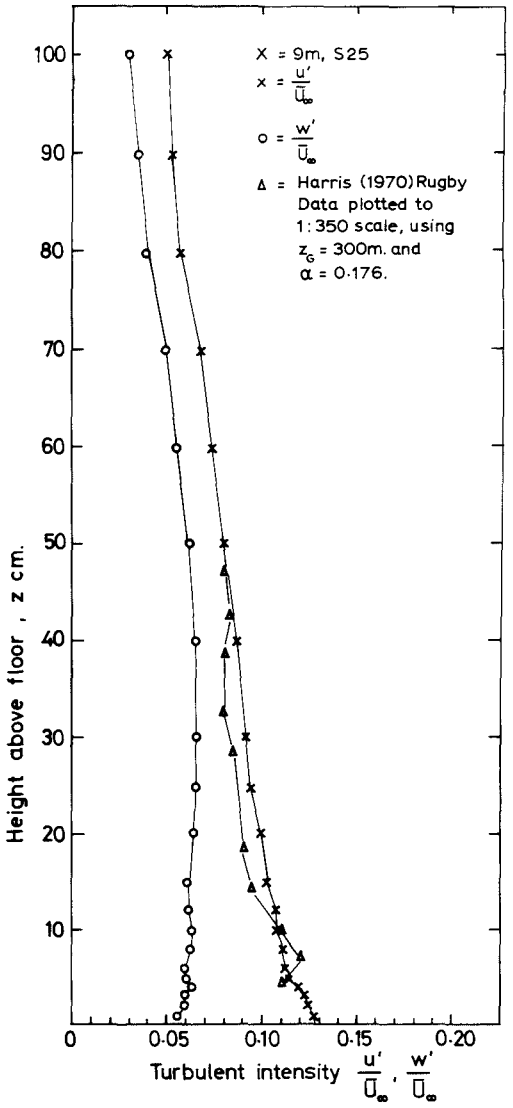

Fig. 6·19b. TURBULENT INTENSITY LAYOUT 3.

as done in Fig. 6.19b. Harris' (1970) atmospheric measurements do, however, fall close to Davenport's (1961) Sale data and the ESDU (1972) turbulent intensity design curve for z_o = 5 cm, as shown in Fig. 6.42b (p.289). They are therefore suitable to compare with the wind tunnel simulated flow. Harris himself commented that his (1970) turbulence intensities were a little lower than expected near the ground.

Comparison of Fig. 6.19 with Fig. 6.14 shows that addition of the trip fence has had the desired effect of increasing turbulent intensity further out in the boundary layer, thus effectively increasing the linear scaling of the simulated atmospheric flow.

(c) Reynolds Stress Profiles: The Reynolds stress profile at X = 9 m is shown in Fig. 6.20. Comparing with Fig. 6.15, it can be seen that the addition of the trip fence has produced a substantial increase in Reynolds stress, corresponding to the increased boundary layer depth. The stress is constant within about 5% between z = 5 cm and z = 30 cm, with a maximum value of ~0.005. This value appears too large for a rural boundary layer simulation where $-\overline{uw}/\bar{U}^2_{\infty max}$ is usually taken as about 0.003. However, the increase in linear scaling caused by the addition of the trip fence, as shown by Table 6.3, may be such that $\bar{U}_{z=90cm}$ ($=\bar{U}_\infty$) is no longer equivalent to $\bar{U}_G$, i.e. the wind tunnel boundary layer has become only a partial depth model of the atmospheric boundary layer. Under these conditions

$$\frac{-\overline{uw}}{\bar{U}^2_{\infty true}} < \frac{-\overline{uw}}{\bar{U}^2_{z=90cm}},$$

and it would be more realistic to use dimensionless Reynolds stress = $-\overline{uw}/\bar{U}^2_{10\ max}$, assumed equal to k_{10}, where $\bar{U}_{10}$ is the mean velocity at the scale 10 m height in the tunnel. Once the linear scaling of the simulation, and thus the scale 10 m height, are established, the acceptability of the Reynolds stress measurements can be more easily verified. e.g. in the present case, Table 6.3 shows that Eqn 2.63 (p. 64), predicts a linear scaling for the simulation of ~1:100 near the floor, in the surface layer

$\therefore$ scale 10 m height in the tunnel is z = 10 cm.

from Fig. 6.18a, $\bar{U}_{10}/\bar{U}_\infty = 0.78$

$$\therefore \quad -uw/\bar{U}^2_{10\ max} = 0.005 \times 0.78^2$$
$$= 0.003.$$

This is a low to average value of $-\overline{uw}/\bar{U}^2_{10\ max}$ for a rural boundary

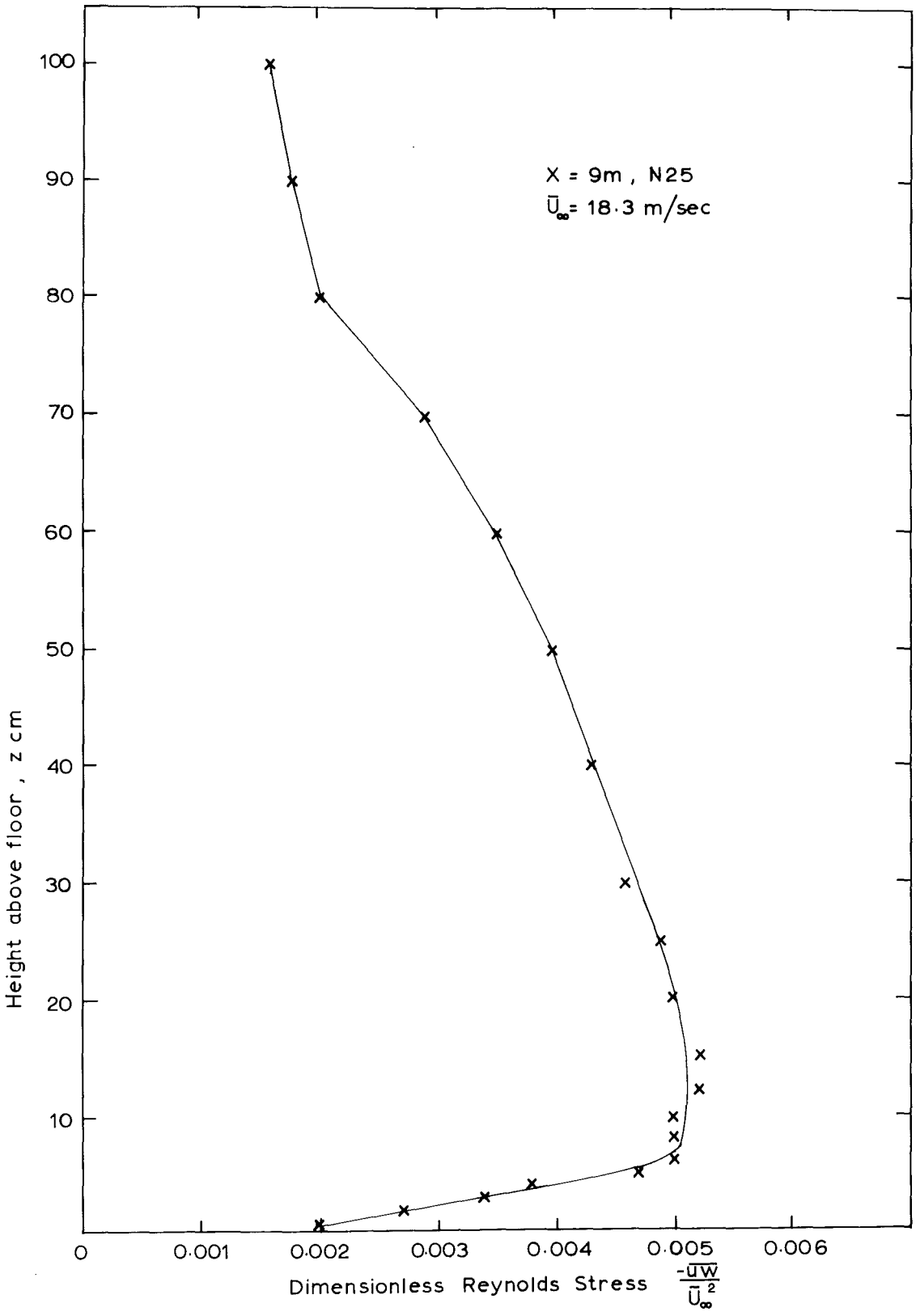

Fig. 6·20 REYNOLDS STRESS PROFILE - LAYOUT 3.

layer. Thus depending on the linear scaling of the simulation, a value of $-\overline{uw}/\bar{U}_\infty^2$ of 0.005 may be acceptable. This is discussed further in 6.4.3. In general, however, it would be expected that the trip fence would introduce shear into the flow characteristic of a rougher surface than the intended model rural terrain, and high shear stress values would therefore follow.

Estimating surface drag from the slope of the mean velocity profile in Fig. 6.18,

with no zero plane displacement, $(u_*/\bar{U}_\infty)^2 = 0.0042$.

with " " " $d = 0.4$ cm, $(u_*/\bar{U}_\infty)^2 = 0.0028$.

The latter value corresponds to the value of $-\overline{uw}/\bar{U}_\infty^2$ at z = 2 cm in Fig. 6.20, i.e. the shear stress close to the surface. With the non-equilibrium nature of the model boundary layer, estimation of surface drag from the mean velocity profile is uncertain at best, and more reliance should be placed on the actual Reynolds stress measurements. In Fig. 6.20 the maximum stress value of 0.005 is characteristic of the shear introduced by the trip fence, while the value $-\overline{uw}/\bar{U}_\infty^2 = 0.002$ close to the surface is more characteristic of the Torro baseboard roughness.

(d) u Velocity Component Energy Spectra: These are shown in Fig. 6.21. There is better similarity of shape between the spectra at different heights at X = 9 m, than at X = 5 m, and at X = 9 m there appears to have been a small decrease in spectral peak wave number at each height compared with the spectra of Fig. 6.16, Layout 2. Acceptable similarity to Harris' model spectrum, Eqn. 2.47, is present at X = 9m.

In Table 6.3, turbulent length scales and linear scaling estimates are summarised for Layout 3. Comparing Table 6.3 and Table 6.2, it is seen that the linear scaling of the simulation has increased markedly in Layout 3, and there is greater consistency between different methods of assessing $d_m:d_a$ than in Layout 2. Eqn. 2.63 again results in large linear scale estimates near the surface, when wind tunnel and atmospheric turbulent length scales are compared, while Eqn. 2.60 leads to linear scale estimates close to that given by a comparison of boundary layer depths in wind tunnel and atmosphere (using Fig. 2.7). Eqn. 2.61 leads to conservative estimates of linear scaling, through the choice of an 1800 m scaling length in matching the Harris spectrum to atmospheric data. (See 2.5.9.) On balance, Table 6.3 indicates a linear scaling of about 1:400 for the boundary layer as a whole.

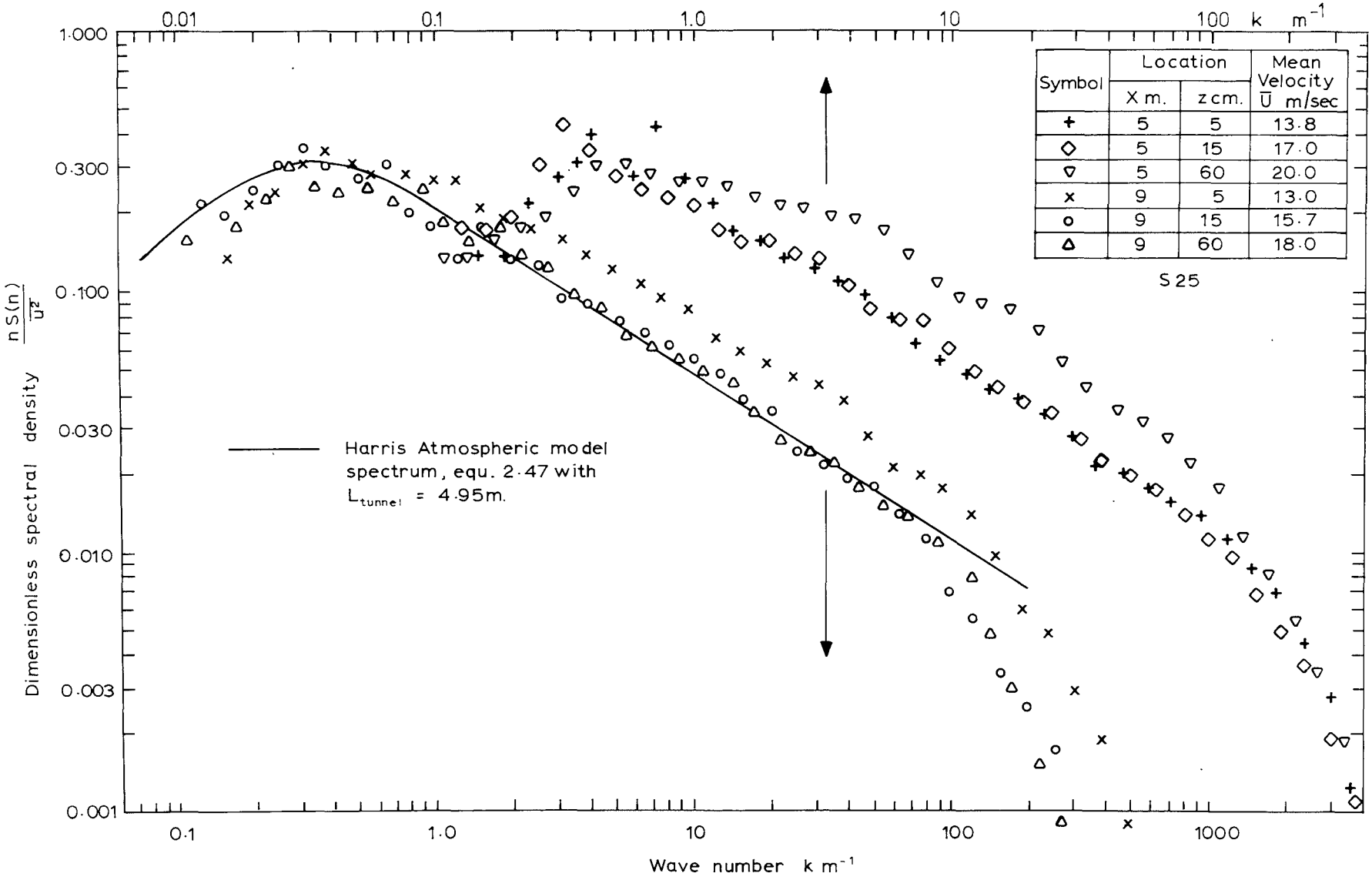

Fig. 6·21 ENERGY SPECTRA FOR u VELOCITY COMPONENT - LAYOUT 3.

TABLE 6·3 LAYOUT 3

Location		Spectral Peak Wave No. k_p m^{-1}	Turbulent Length Scale-cm $L_{u_x} = \frac{0.146}{k_p}$	Linear Scaling $d_m : d_a$ based on -				
				$\frac{\delta_m}{\delta_a}$	$\frac{z_{o_m}}{z_{o_a}}$	L_{uxm} / L_{uxa}		
X m.	z cm.					Equ.2·60	Equ.2·61	Equ.2·63
9	5	0·49	29·8	1:300	-1:300	1:400	1:700	1:70
9	15	0·33	44·2	1:300	-1:300	1:300	1:520	1:90
9	60	0·36	40·6	1:300	-1:300	1:415	1:800	1:435

Table 6.3 also shows that a trend has appeared for L_{u_x} at z = 60 cm to be less than L_{u_x} at z = 15 cm. While the turbulent length scale at z = 60 cm is larger than that in Layout 2, a greater relative increase has occurred at z = 15 cm, where L_{u_x} is slightly higher than required.

(e) Flow Self-Preservation at X = 11 m: Fig. 6.22 shows mean velocity profiles measured at X = 11 m in comparison with the average mean velocity profile at X = 9 m. The acceleration of the flow below z = 10 cm is clearly seen, and was due to the passage of the flow over a 1.85 m length of smooth floor downstream from the end of the Torro baseboard. The depth of the internal boundary layer characteristic of the smoother surface is 8 - 10 cm at X = 11 m. This smooth floor boundary layer growth was later largely eliminated in model tests by extending the Torro baseboard to X = 11.6 m. Lateral uniformity at X = 11 m was better than would appear from the normalised plot of Fig. 6.22. Velocities at N25 and S25 were identical below z = 50 cm.

The turbulent intensity profiles of Fig. 6.23 show a reduction in intensity below z = 10 cm, corresponding to the smooth floor internal boundary layer growth, but intensities near the floor would still be acceptable for a rural boundary layer simulation. The lateral non-uniformity in turbulent intensity profile at X = 11 m disappears if it is plotted in the form $u'/\bar{U}_z$ vs z.

Energy spectra were very similar to those of Fig. 6.21, with approximately the same peak wave numbers at respective heights, but even better agreement with the atmospheric model of Equation 2.47 and a more extensive region of -2/3 slope in the $nS(n)/\overline{u^2}$ vs k plots.

Summary:

(i) Addition of the 15 cm trip fence produced an increase in depth of the simulated boundary layer to approximately 90 cm at X = 9 m. The mean velocity profile showed better conformity to the 1/6 power law design profile when plotted with a 0.4 cm zero plane displacement, but velocities were generally a little high in the lower half of the boundary layer.

(ii) At X = 9 m, profiles of $u'/\bar{U}_\infty$, $w'/\bar{U}_\infty$ and $-\overline{uw}/\bar{U}_\infty^2$ were satisfactory for a rural boundary layer with z_o = 5 - 10 cm in full scale, but the maximum Reynolds stress value tended high.

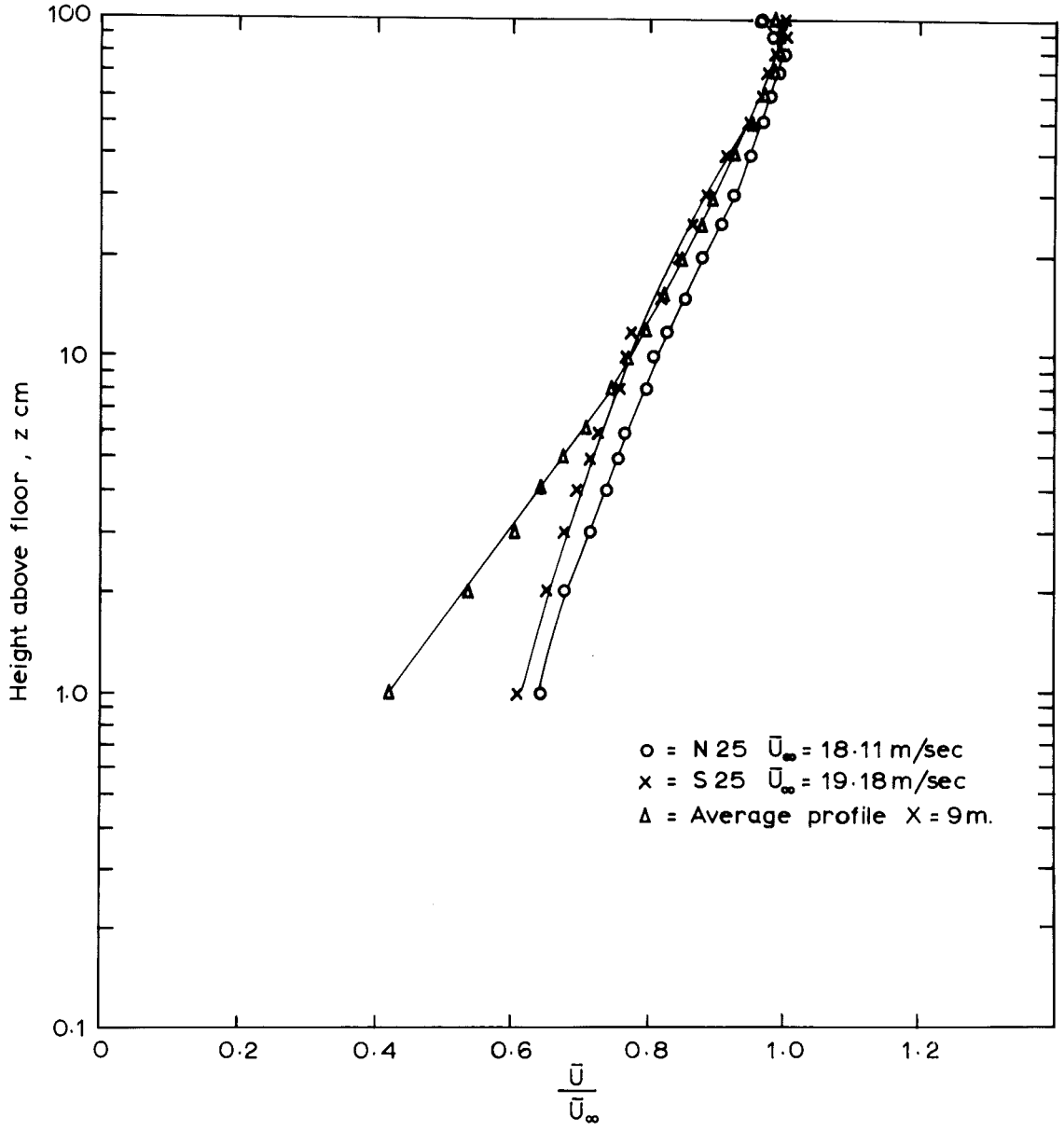

Fig. 6·22 MEAN VELOCITY PROFILES X = 11M.- LAYOUT 3.

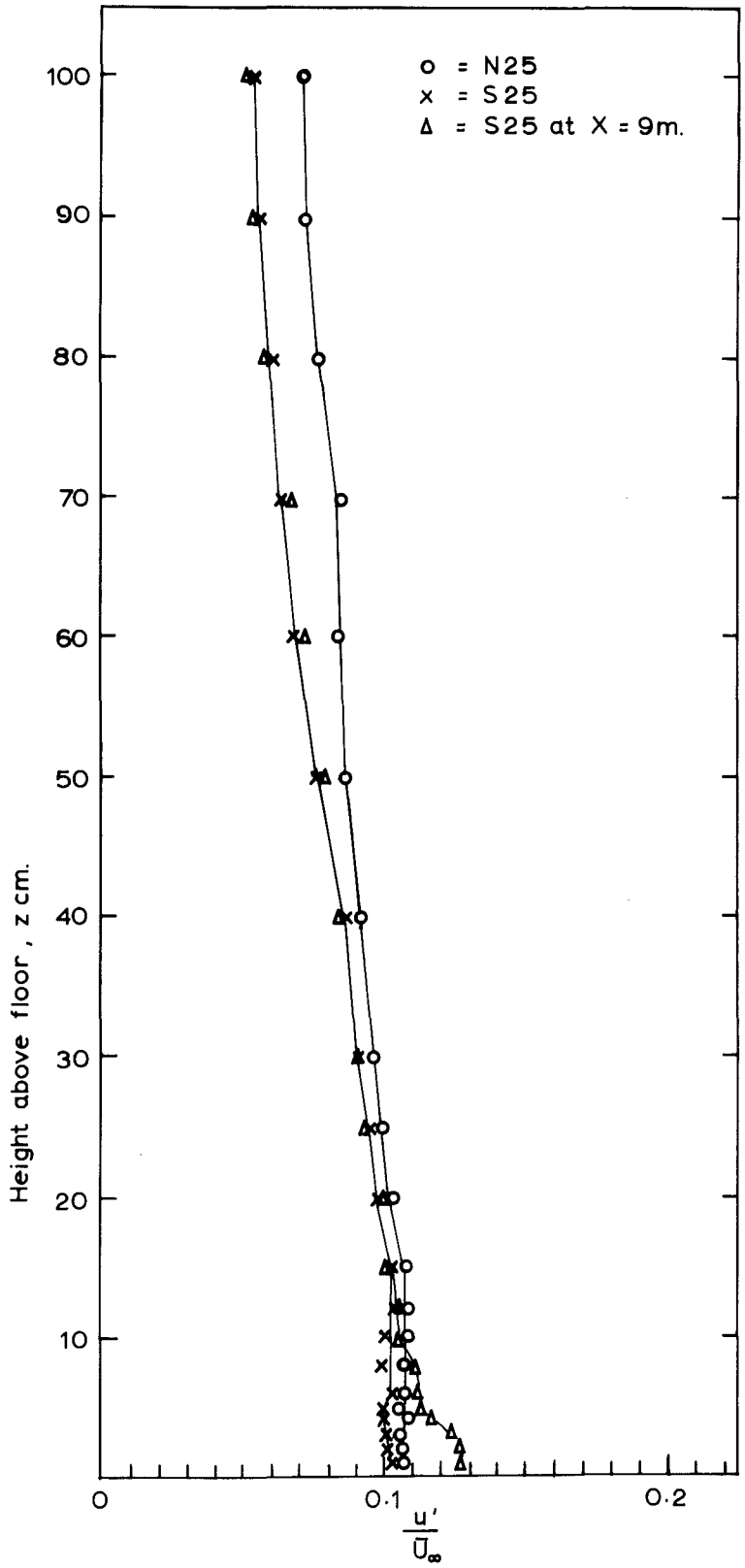

Fig. 6·23 TURBULENT INTENSITY PROFILES
X = 11 M. - LAYOUT 3.

(iii) u velocity component energy spectra showed improved similarity to each other over the tunnel height, and to the Harris model spectrum. Turbulent length scales derived from the spectra in the tunnel indicated a linear scaling between wind tunnel and atmosphere of between 1:300 and 1:400, in agreement with scaling based on boundary layer depth and turbulent intensity profiles.

(iv) At X = 5 m, large scale velocity fluctuations generated by the trip fence made measurements more difficult. Reynolds stress profile, energy spectra and boundary layer depth at this location were all inferior to those at X = 9 m.

(v) If imperfection in the mean velocity profile at X = 9 m were acceptable, the boundary layer generated at this point by Layout 3 would be a reasonable rural boundary layer simulation scaled a little larger than 1:400.

6.3.4 Layout 4: Uniform Coarse Grid + 15 cm Solid Trip Fence + 6.7 cm 34% Permeable Trip Fence + Torro Baseboard.

The model rural boundary layer structure of Layout 3 was achieved with relatively few modifications to the original bare working section. It was decided to make no further flow measurements with Layout 3, for the time being at least, but rather attempt to further modify the boundary layer with the aim of :

(i) improving the mean velocity profile;
(ii) further increasing the linear scale of the simulation.

To this end combinations of trip fences were tested in the working section and subsequently bar spacing in the coarse grid varied. In this section, the effect of the addition of a second trip fence is examined. A 34% permeable Torro block fence was added at X = 5 m. Measurements with Layout 4 were restricted to mean velocity, turbulent intensity and Reynolds stress profiles, and u component energy spectra. This layout is shown in Fig. 6.24.

Results and Discussion:

(a) Mean Velocity Profiles: The effect of adding the second trip fence is seen in Fig. 6.25. Boundary layer depth is still about 90 cm and lateral uniformity good, but there has been a reduction in mean velocity in the lower half of the boundary layer as desired, in comparison with the profile of Layout 3. Again, better conformity with the design 1/6 power

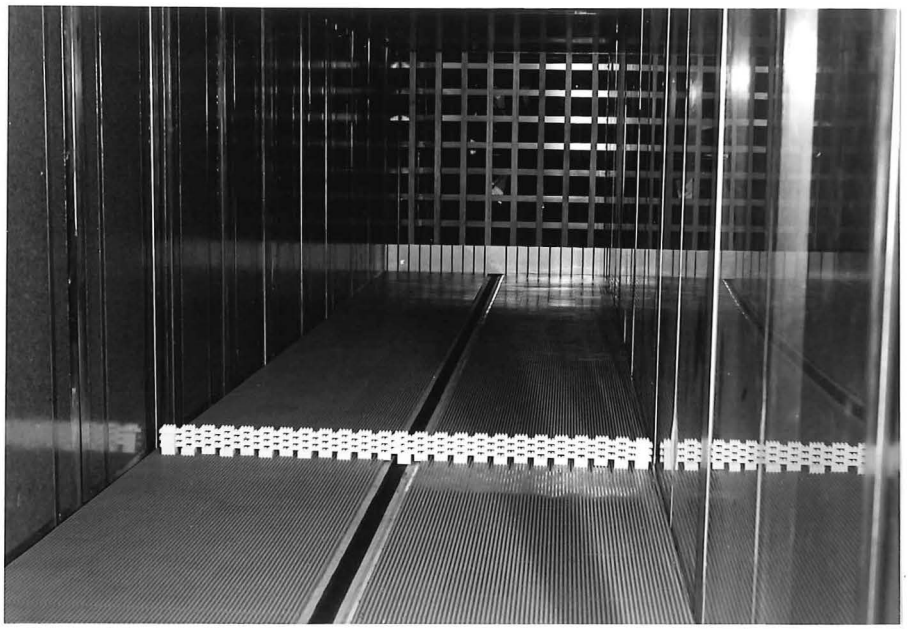

View towards upstream end of working section

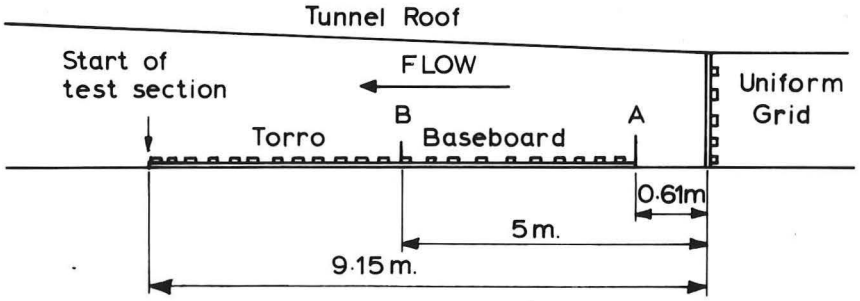

Fence A : Solid Aluminium , 15 cm. high.
Fence B : 34 % Permeable , Torro Blocks , 6·7 cm. high.

Fig. 6·24 LAYOUT 4. (Schematic only-not to scale.)

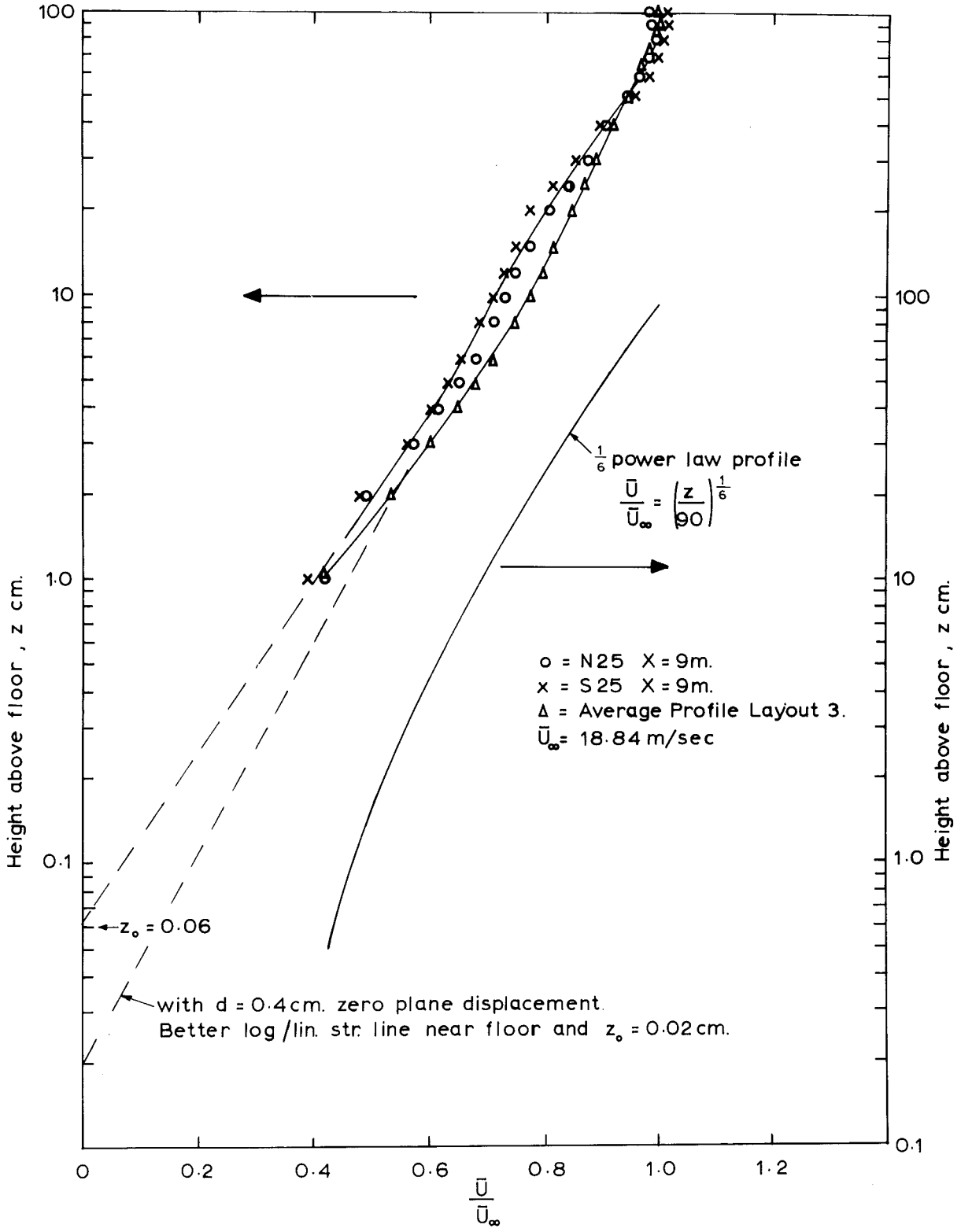

Fig. 6.25 MEAN VELOCITY PROFILES - LAYOUT 4.

law velocity profile would be obtained with a 0.4 cm zero plane displacement, as shown in Fig. 6.25.

(b) Turbulent Intensity Profiles: These are shown in Fig. 6.26. The addition of the 6.7 cm fence has increased the turbulent intensity in the middle region of the boundary layer, suggesting an increase in linear scale for the simulation. Harris' (1970) Rugby data are plotted to a scale of 1:175 for comparison with the $u'/\bar{U}_\infty$ data. With the closer proximity of a trip fence, the w' component is increased somewhat, and remains too high above z = 70 cm. Near the floor $w' \simeq 0.5u'$ as desired.

(c) Reynolds Stress Profile: The measured Reynolds stress profile was found to be inaccurate because of a calibration fault with the X probe and was not repeated as Layout 4 was later superseded.

(d) u Velocity Component Energy Spectra: At each height the spectra at X = 9 m were similar to those of Layout 3 in Fig. 6.21, and are shown in Fig. 6.27. Slightly more scatter at low frequency was noticed on the spectrum plot than for Layout 3, but variation in k_p with height was slightly better. Harris' atmospheric model spectrum is plotted for comparison in Fig. 6.27, with $k_p = 0.3\ m^{-1}$.

Table 6.4 contains estimates of turbulent length scales, and linear scaling between wind tunnel and atmosphere for each tunnel measurement height. Methods involving comparison of turbulent length scales between tunnel and atmosphere give linear scale estimates a little larger than those of Table 6.3, but still around 1:300. Using Eqn 2.63 as the atmospheric model for turbulent length scale variation again leads to large linear scaling near the floor, and Eqn 2.61 gives a very conservative estimate of linear scaling at all heights. Consistency between linear scaling estimates at different heights is better than in Table 6.3.

Summary:

(i) Addition of the 6.7cm 34% permeable trip fence at X = 5 m to the arrangement of Layout 3, improved the mean velocity profile at X=9m, and increased turbulent intensities in the outer part of the boundary layer so that the linear scaling, based on the turbulent intensity (and Reynolds stress) profile, became approximately 1:200.

(ii) Energy spectra were similar to those of Layout 3, with slightly improved consistency between different estimates of linear scaling. For the whole boundary layer depth at X = 9 m, the representative linear scaling was about 1:300.

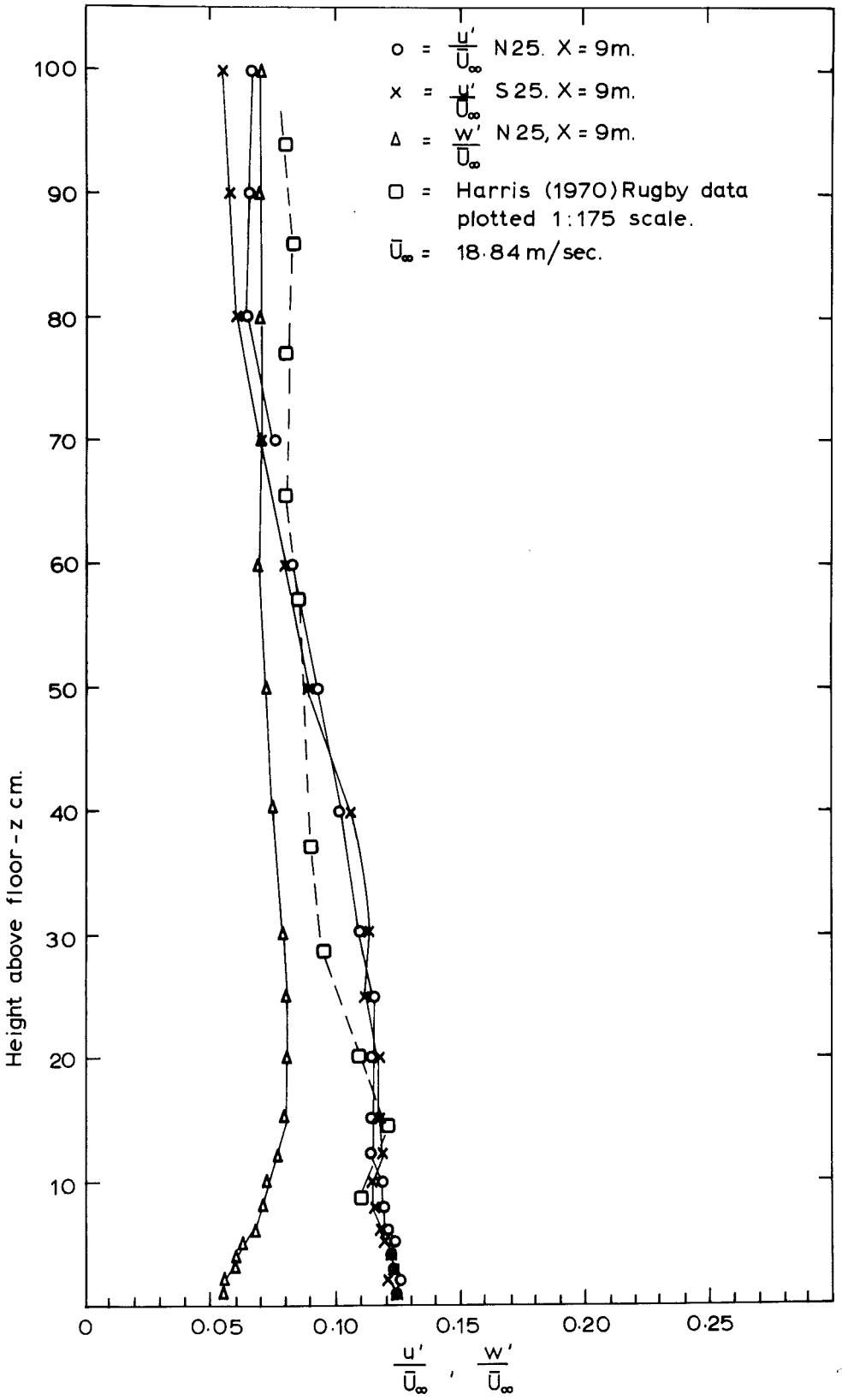

Fig. 6.26 TURBULENT INTENSITY PROFILES - LAYOUT 4.

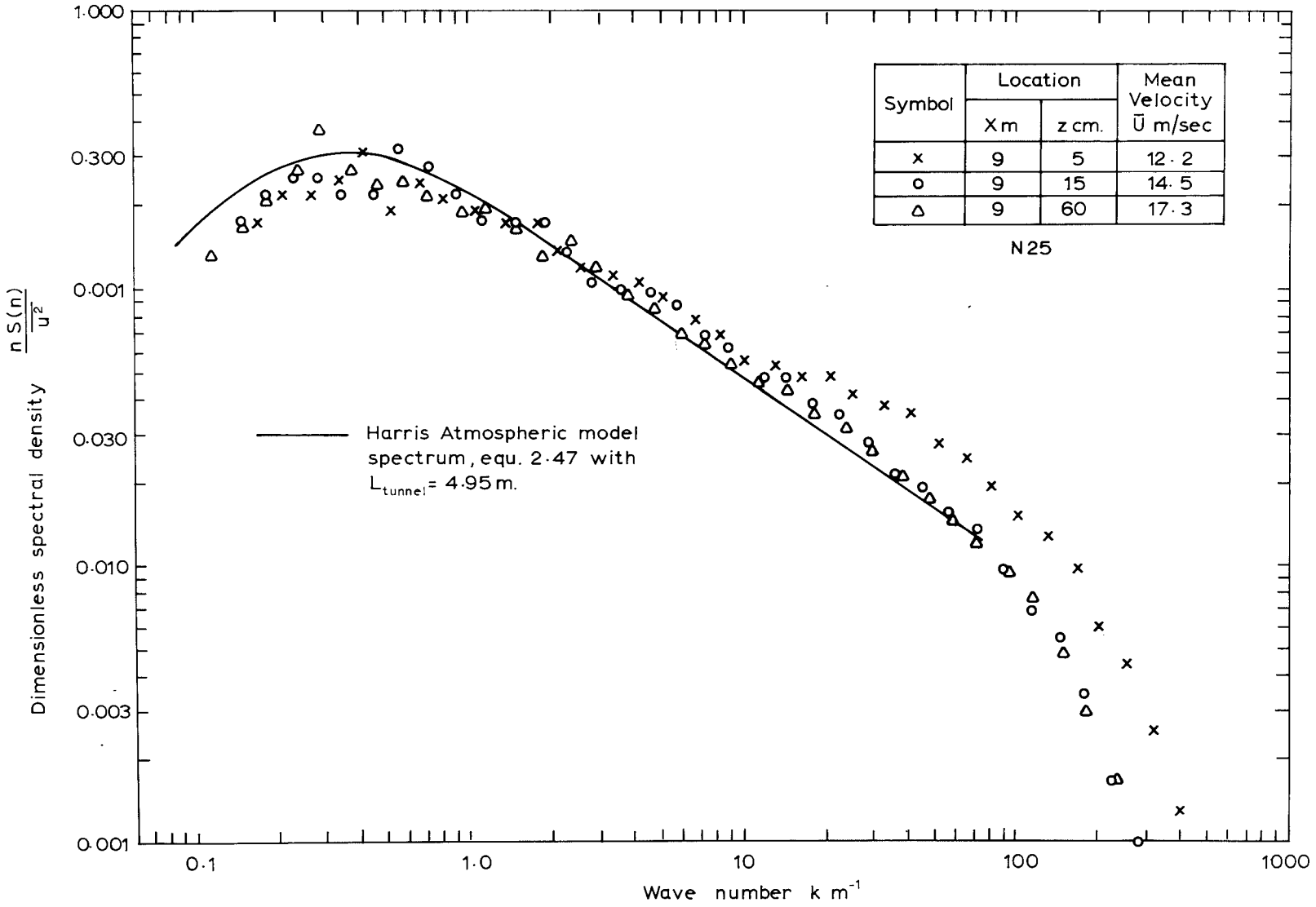

Fig. 6·27 ENERGY SPECTRA FOR u VELOCITY COMPONENT - LAYOUT 4.

TABLE 6·4 LAYOUT 4

Location		Spectral Peak Wave No. k_p m^{-1}	Turbulent Length Scale cm. $L_{u_x} = \frac{0.146}{k_p}$	Linear Scaling $d_m : d_a$ based on -				
X m.	z cm.			$\frac{\delta_m}{\delta_a}$	$\frac{z_{o_m}}{z_{o_a}}$ *	L_{uxm} / L_{uxa}		
						Equ.2·60	Equ.2·61	Equ.2·63
9	5	0·46	31·7	1:300	-1:300	1:360	1:660	1:60
9	15	0·4	36·5	1:300	-1:300	1:380	1:690	1:130
9	60	0·3	48·7	1:300	-1:300	1:350	1:640	1:300

* Assuming 0·4cm zero plane displacement.

6.3.5 Layout 5: Uniform Coarse Grid + Torro Blocks Surface Roughness:

The simulated atmospheric boundary layer of Layout 4 was probably adequate as an approximate 1:300 scale rural boundary layer. Before attempting further improvements by the addition of trip fences or by modification to the coarse grid, a further layout of fairly uniform surface roughness was tested, to check whether a sufficiently deep boundary layer could be generated without the use of trip fences. Starting with the uniform grid and Torro baseboard of Layout 2, Torro blocks were fitted to the Torro baseboard floor as shown in Fig. 6.28. The area density of blocks on the floor was 1/6 and the new height of the roughness elements a three-fold increase over that of the Torro baseboard alone. Flow measurements were again restricted to mean velocity, turbulent intensity and Reynolds stress profiles, and u component energy spectra.

Results and Discussion:

(a) Mean Velocity Profiles: These are shown in Fig. 6.29. This figure shows that Layout 5 gave a boundary layer depth of 50 - 60 cm compared with 30 - 35 cm for the Torro baseboard alone, in Layout 2. (Equn 2.19 indicates that the change in boundary layer depth was due in part to the difference in fan blade pitch settings in these two tests.) The mean velocity profile contains some lateral non-uniformity - about 10% up to $z = 10$ cm, with higher speeds at S25, as with Layout 2. Plotted with no zero plane displacement, extrapolation of the profile gives a roughness length at $X = 9$ m of $z_o \simeq 0.2$ cm, or about four times that in Layout 2. This corresponds to the increase in roughness element height. The enhanced boundary layer growth evident in Fig. 6.29 was desirable, but the new roughness length, and equivalent power law exponent of about 0.4 (below $z = 15$ cm), were characteristic of suburban or urban terrain, rather than rural terrain.

(b) Turbulent Intensity Profiles: The initial trip fence of Layout 3 aided lateral mixing, and in its absence lateral non-uniformity reappeared in the mean velocity profile, and in the turbulent intensity profile as shown in Fig. 6.30. This non-uniformity is seen to be more prominent in the u component intensity than in the w component intensity. Compared with Layout 2 (Fig. 6.13), Layout 5 shows a predictable increase in turbulent intensity in the thickened region of the boundary layer, away from the floor. The increase in turbulent intensity between Layouts 2 and 5 is less than that achieved by the addition of the trip fence in Layout 3 (see Fig. 6.19, p.247)

(c) Reynolds Stress Profile: This is shown in Fig. 6.31. General

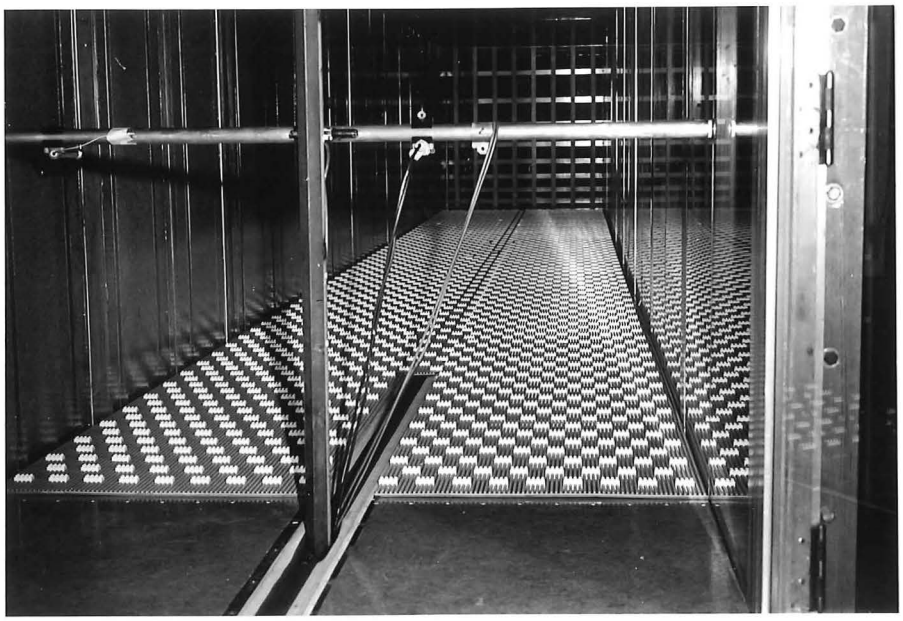

View towards upstream end of working section

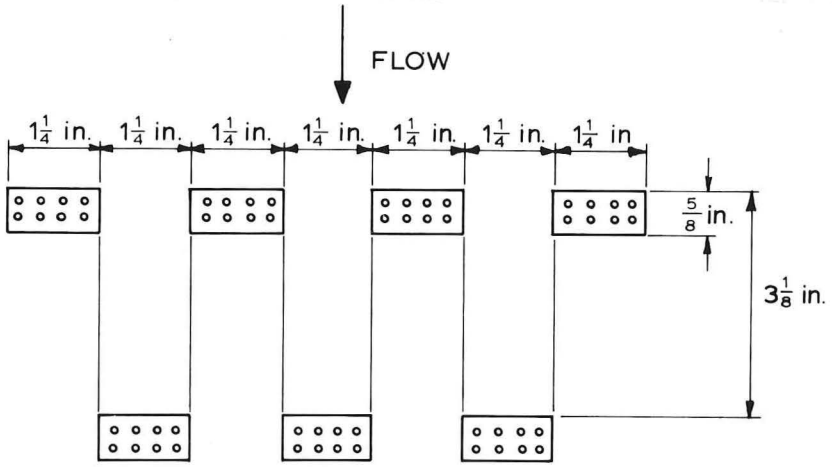

Torro Block Pattern.

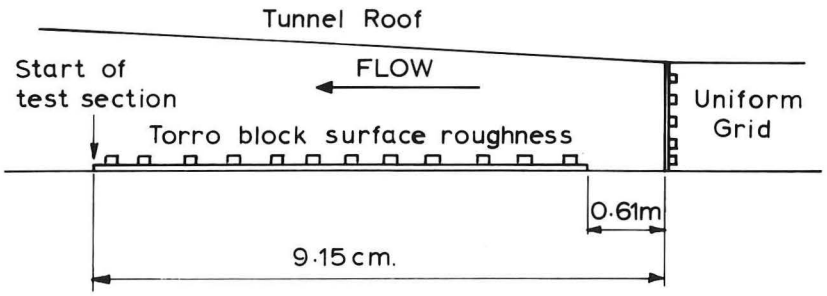

Fig. 6·28 LAYOUT 5 (Schematic only - not to scale.)

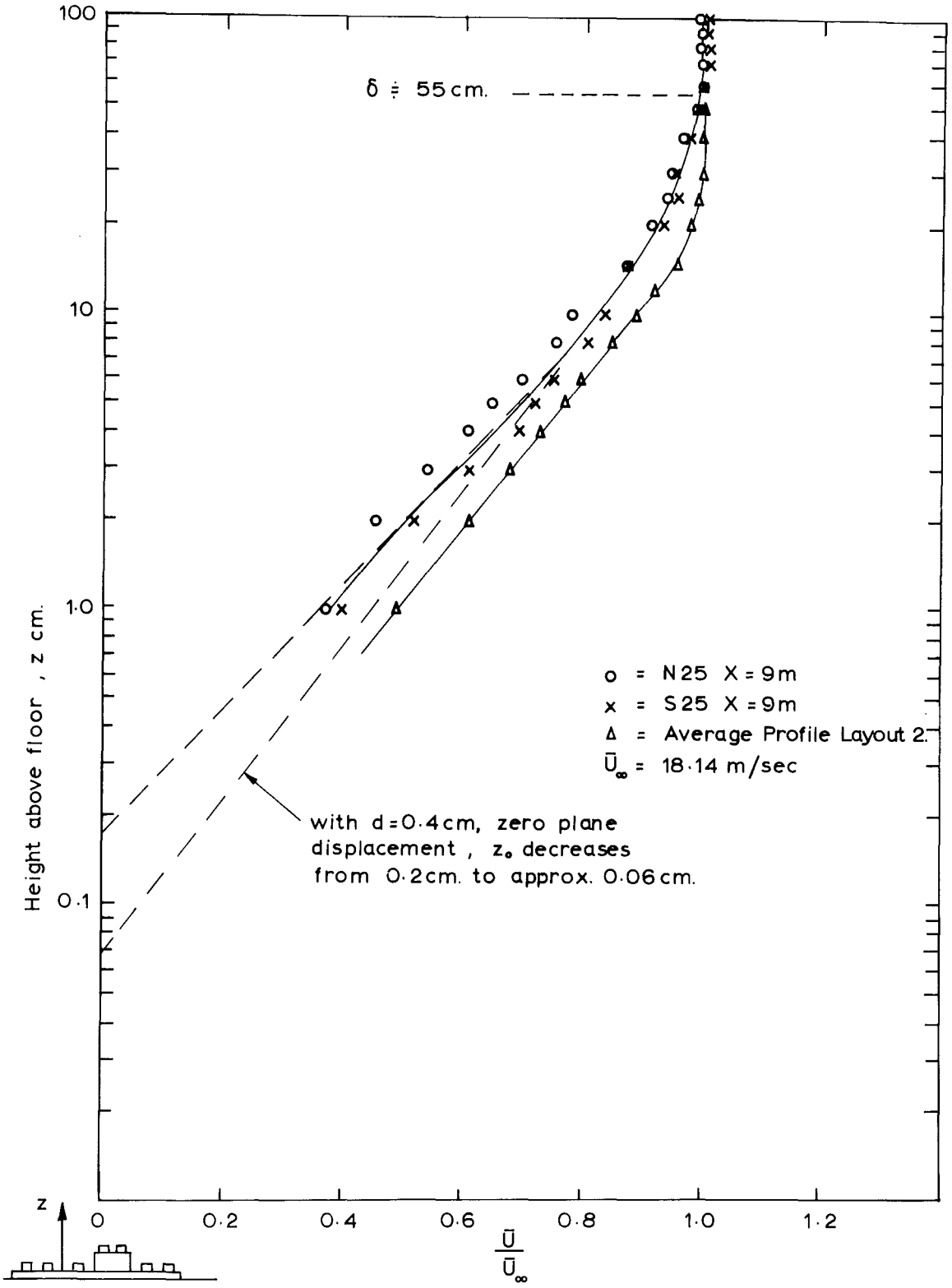

Fig. 6·29 MEAN VELOCITY PROFILES - LAYOUT 5.

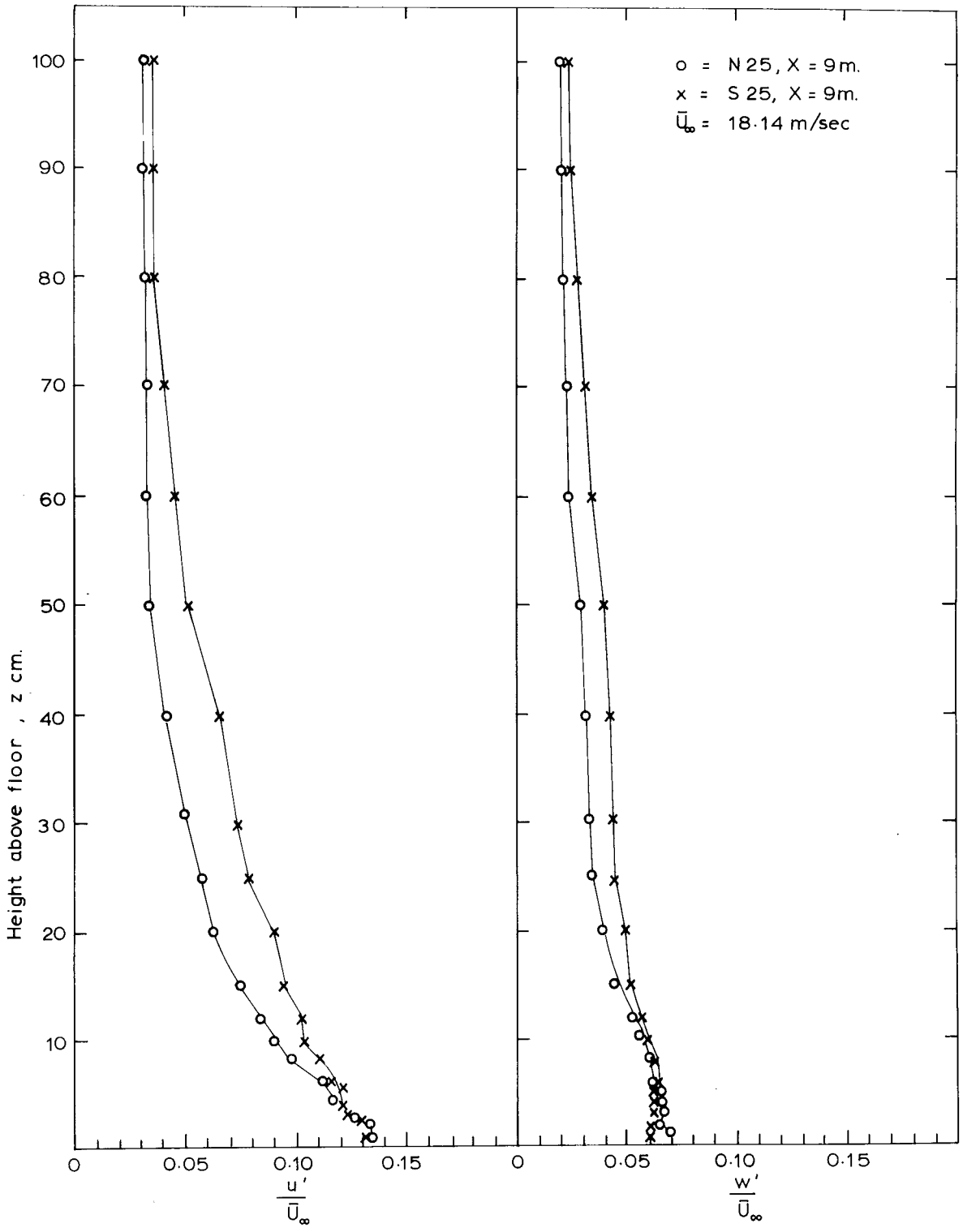

Fig. 6·30 TURBULENT INTENSITY PROFILES - LAYOUT 5.

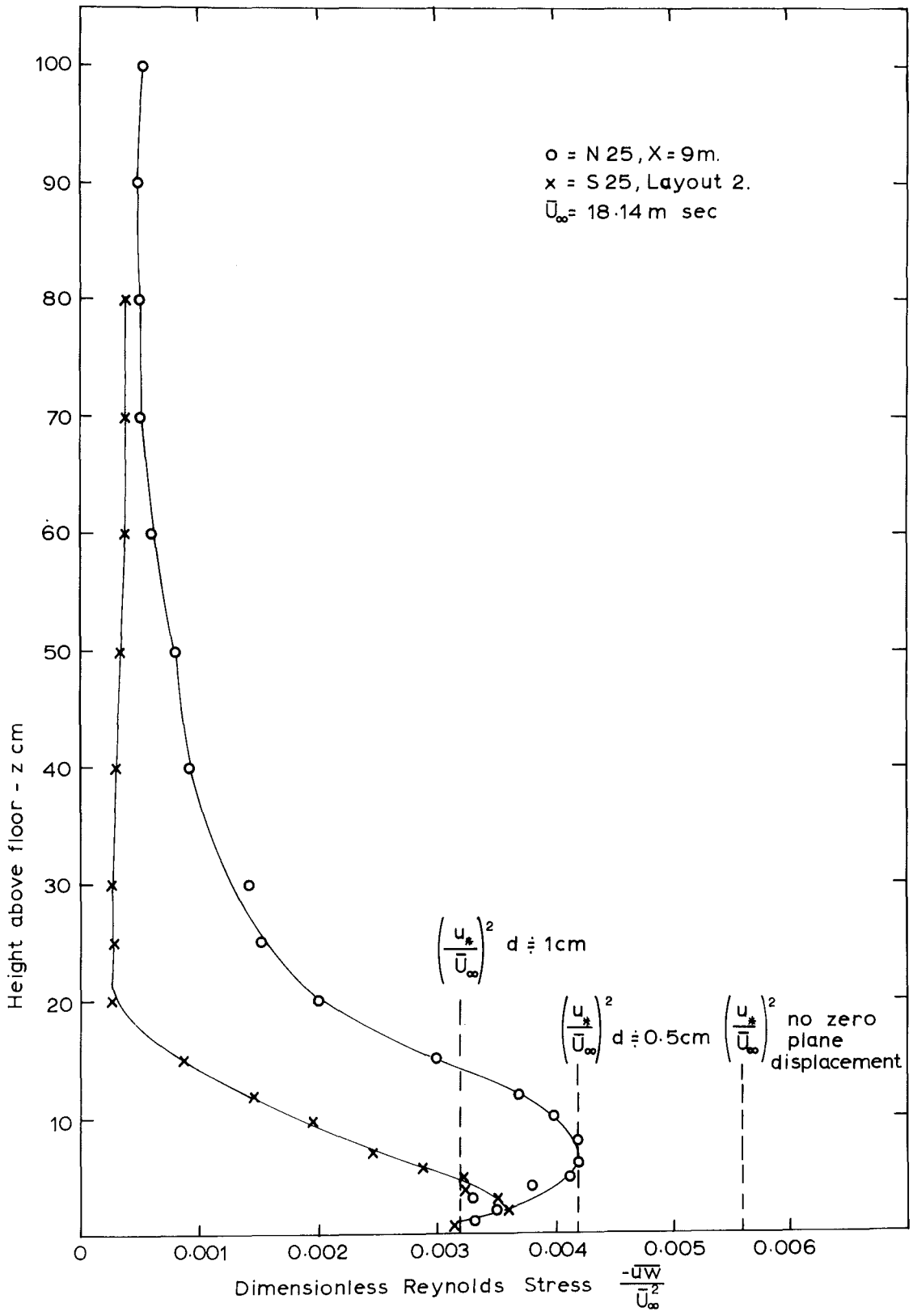

Fig. 6·31 REYNOLDS STRESS PROFILE - LAYOUT 5.

similarity of form is present between Layout 5 and Layout 2 and there is the expected increase in shear stress at all levels in the boundary layer. The maximum value $-\overline{uw}/\bar{U}^2_{\infty max} = 0.0042$, is too high for a rural boundary layer simulation, and like the mean velocity gradient, is more characteristic of an urban or suburban terrain. If, with due regard for the non-equilibrium nature of the boundary layer, surface shear stress is calculated from the slope of the straight line portion of the log/linear mean velocity profile, it is found that

with a zero plane displacement of d = 0.5 cm $(u_*/\bar{U}_\infty)^2 = 0.0042$
and $z_o \simeq 0.06$ cm.

with no zero plane displacement $(u_*/\bar{U}_\infty)^2 = 0.0056$ and $z_o \simeq 0.2$ cm.

It is therefore possible that the mean velocity profile of Fig. 6.29 would be better plotted with, say, a 0.5 cm zero plane displacement. The corresponding power law exponent for the lower part of the profile would be approximately 0.3.

(d) u Velocity Component Energy Spectra: These showed close similarity in shape to those measured over the Torro baseboard (Fig. 6.16) and are not presented here. Table 6.5 shows turbulent length scales and linear scaling estimates for Layout 5. These are similar to those for Layout 2 in Table 6.2, but note that k_p at z = 15 cm is lower in Layout 5, probably due to the influence of the surface roughness. A reasonable assessment of Table 6.5 is a linear scaling for the simulation, at X = 9 m, of about 1:1000, for an urban boundary layer of 520 m depth (see Fig. 2.7, p. 30).

Summary:

(i) The greater surface roughness of the Torro block pattern caused a predictable increase in boundary layer thickness, turbulent intensity, shear stress and roughness length by comparison with Layout 2 (the Torro baseboard roughness). The only significant change in the spectra was a reduction in the peak wave number at z = 15 cm.

(ii) Layout 5 showed that much greater boundary layer thickness could be obtained by addition of roughness to the basic Torro baseboard, and with the use of greater roughness, e.g. roughness elements 4 - 5 Torro blocks high, the 90 cm boundary layer depth, obtained in Layouts 3 and 4 with trip fences, could probably be achieved. However, lateral non-uniformity persisted in the flow when uniform roughness schemes such as

TABLE 6·5 LAYOUT 5

Location		Spectral Peak Wave No. k_p m^{-1}	Turbulent Length Scale, cm $L_{u_x}=\frac{0.146}{k_p}$	Linear Scaling $d_m : d_a$ based on -			
X m.	z cm			$\frac{\delta_m}{\delta_a}$	$\frac{z_{o_m}}{z_{o_a}}$	$L_{u_{xm}} / L_{u_{xa}}$	
						Equ.2·60	Equ.2·63
9	5	0·96	15·2	1:1000	-1:1000	-1:2000	-1:270
9	15	0·39	37·4	1:1000	-1:1000	-1:440	1:130
9	60	0·46	31·7	1:1000	-1:1000	-1:740	1:600

Layouts 2 and 5 were used, and resulting profiles of mean velocity and shear stress were characteristic of suburban/ urban terrain roughness scaled ~1:1000. It was therefore decided to persist with the basic Torro baseboard surface roughness, using trip fences and alterations to the coarse grid to modify the flow.

6.3.6 Layout 6: Non-uniform Grids + Surface Roughness:

Various combinations of non-uniform grid and surface roughness were tested to examine the influence of grid bar spacing on mean velocity profile. As an initial test, a grid was designed using the Cowdrey method (see Chapter 4) with K_o = 0.6 and a power law exponent of 1/7 . Predictably, this grid did not perform satisfactorily because of the vertical non-uniformity in the flow upstream of the grid, the velocity defect in the central part of the tunnel persisting downstream as shown in Fig. 6.32. Maximum deviation from the design profile was about 10%.

It was recognised that trial and error velocity profile grid design was necessary, and several arrangements were tested, with the Torro block surface roughness of Layout 5, then with the Torro baseboard surface roughness of Layout 2, and finally with the 15 cm trip fence at X = 0.61 m in combination with Torro baseboard roughness. These arrangements are summarised in Table 6.6.

Since the trial and error establishment of grid design was to suit an initially non-uniform flow, the detailed results are of little significance as far as adaption to another wind tunnel is concerned. Quantitative results are therefore shown only for the final, most promising arrangement. In arrangements 6/1 to 6/4, the Torro block surface roughness dictated the mean velocity profile at X = 9 m up to a height of 20 cm, although some correction towards the design 1/6 power law profile was obtained above z = 20 cm. Arrangements 6/5 to 6/8 were also unsatisfactory. As shown by Fig. 6.33, the mean velocity profile for Arrangement 6/8, greater boundary layer depth was obtained than in Layout 2, but the surface roughness dominated the profile near the floor. Arrangements 6/1 to 6/8 indicated that use of a trip fence was desirable to generate the required higher turbulent intensity in the middle region of the boundary layer, and to produce the desired mean velocity gradient near the floor. Arrangements 6/9 to 6/15 showed more promise, and led to the final grid design of Arrangement 6/15, for which results are given below.

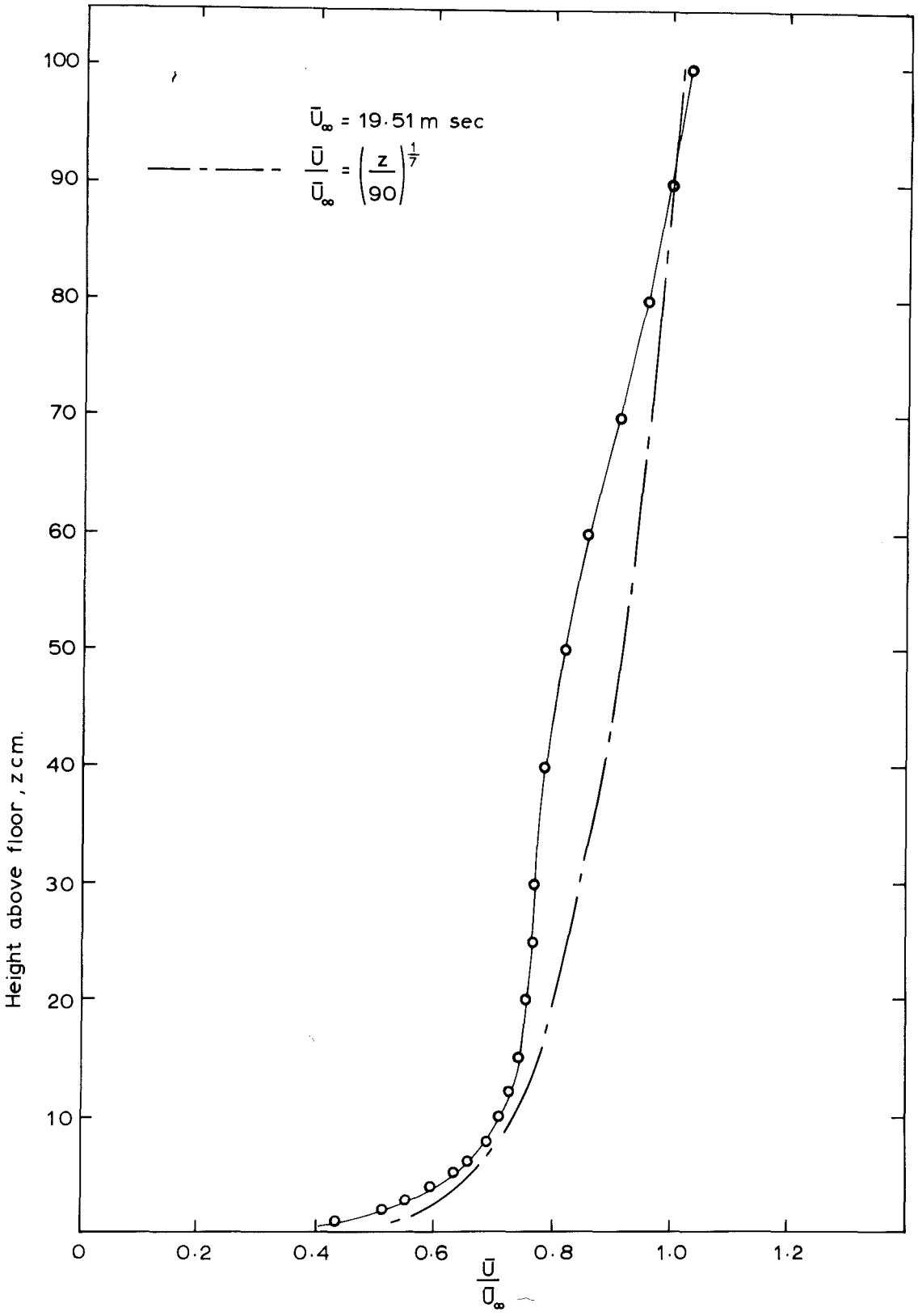

Fig. 6·32 MEAN VELOCITY PROFILE AT X = 9m, N25, USING COWDREY $\frac{1}{7}$ POWER LAW GRID WITH K_o=0·6. + TORRO BASEBOARD SURFACE ROUGHNESS.

TABLE 6·6 LAYOUTS 6

Various Coarse Grid & Downstream Roughness Configurations : Horizontal bars $1\frac{1}{2}$ in. width.
: Grid has 6 vertical $1\frac{1}{2}$ in. bars at 6in. centres.

SPACING BETWEEN ADJACENT BARS (INCHES)

Arrgt. No.	Non-uniform Grid + Surface Roughness Configuration	FLOOR	BAR 1	BAR 2	BAR 3	BAR4	BAR 5	BAR 6	BAR 7	BAR 8	ROOF
6/1	Grid + Torro blocks surface roughness	1	2	$2\frac{1}{2}$	3	$3\frac{3}{4}$	$4\frac{1}{2}$	$5\frac{3}{4}$	$6\frac{3}{4}$	$6\frac{3}{4}$	
6/2	" + " " " "	0	$2\frac{1}{2}$	3	$3\frac{3}{4}$	$4\frac{1}{2}$	$5\frac{1}{2}$	$5\frac{1}{2}$	$5\frac{5}{8}$	$5\frac{5}{8}$	
6/3	" + " " " "	0	$2\frac{1}{2}$	4	$4\frac{3}{4}$	6	$6\frac{1}{4}$	$5\frac{1}{4}$	4	3	
6/4	" + " " " "	$2\frac{1}{4}$	$4\frac{1}{2}$	$5\frac{1}{2}$	$6\frac{1}{2}$	5	$3\frac{1}{3}$	$3\frac{1}{3}$	$3\frac{1}{3}$	$2\frac{1}{4}$	
6/5	Grid + Torro baseboard surface roughness	1	2	$2\frac{1}{2}$	$3\frac{1}{2}$	5	6	6	6	4	
6/6	" + " " " "	1	$1\frac{1}{2}$	2	$3\frac{1}{2}$	6	6	6	6	4	
6/7	" + " " " "	1	1	$1\frac{1}{2}$	3	$6\frac{3}{4}$	$6\frac{3}{4}$	6	6	4	
6/8	" + " " " "	$2\frac{1}{4}$	$2\frac{1}{4}$	3	5	5	$5\frac{1}{2}$	$5\frac{1}{2}$	$5\frac{1}{4}$	$2\frac{1}{4}$	
6/9	Grid + 15cm.trip fence + Torro baseboard roughness	$2\frac{1}{4}$	$4\frac{1}{2}$	$4\frac{1}{2}$	$5\frac{1}{2}$	$5\frac{1}{2}$	$4\frac{1}{2}$	4	3	$2\frac{1}{4}$	
6/10	" + " " " + " " "	$2\frac{1}{4}$	$2\frac{1}{4}$	$5\frac{1}{2}$	$6\frac{3}{4}$	$5\frac{1}{2}$	$4\frac{1}{2}$	4	3	$2\frac{1}{4}$	
6/11	" + " " " + " " "	$2\frac{1}{4}$	$2\frac{1}{4}$	$2\frac{1}{4}$	$2\frac{1}{4}$	$5\frac{1}{2}$	8	$8\frac{1}{4}$	3	$2\frac{1}{4}$	
6/12	" + " " " + " " "	$2\frac{1}{4}$	$2\frac{1}{4}$	$2\frac{1}{4}$	$2\frac{1}{4}$	5	$6\frac{1}{2}$	$6\frac{1}{2}$	$6\frac{3}{4}$	$2\frac{1}{4}$	
6/13	" + " " " + " " "	$2\frac{1}{4}$	$2\frac{1}{4}$	$3\frac{1}{2}$	$4\frac{1}{2}$	5	$5\frac{1}{2}$	$5\frac{1}{2}$	$5\frac{1}{4}$	$2\frac{1}{4}$	
6/14	" + " " " + " " "	$2\frac{1}{4}$	$2\frac{1}{4}$	3	5	5	$5\frac{1}{2}$	$5\frac{1}{2}$	$5\frac{1}{4}$	$2\frac{1}{4}$	
6/15	" + " " " + " " "	$2\frac{1}{4}$	$2\frac{1}{4}$	3	5	$5\frac{1}{2}$	$5\frac{1}{2}$	$5\frac{1}{4}$	5	$2\frac{1}{4}$	Final Arrgt.

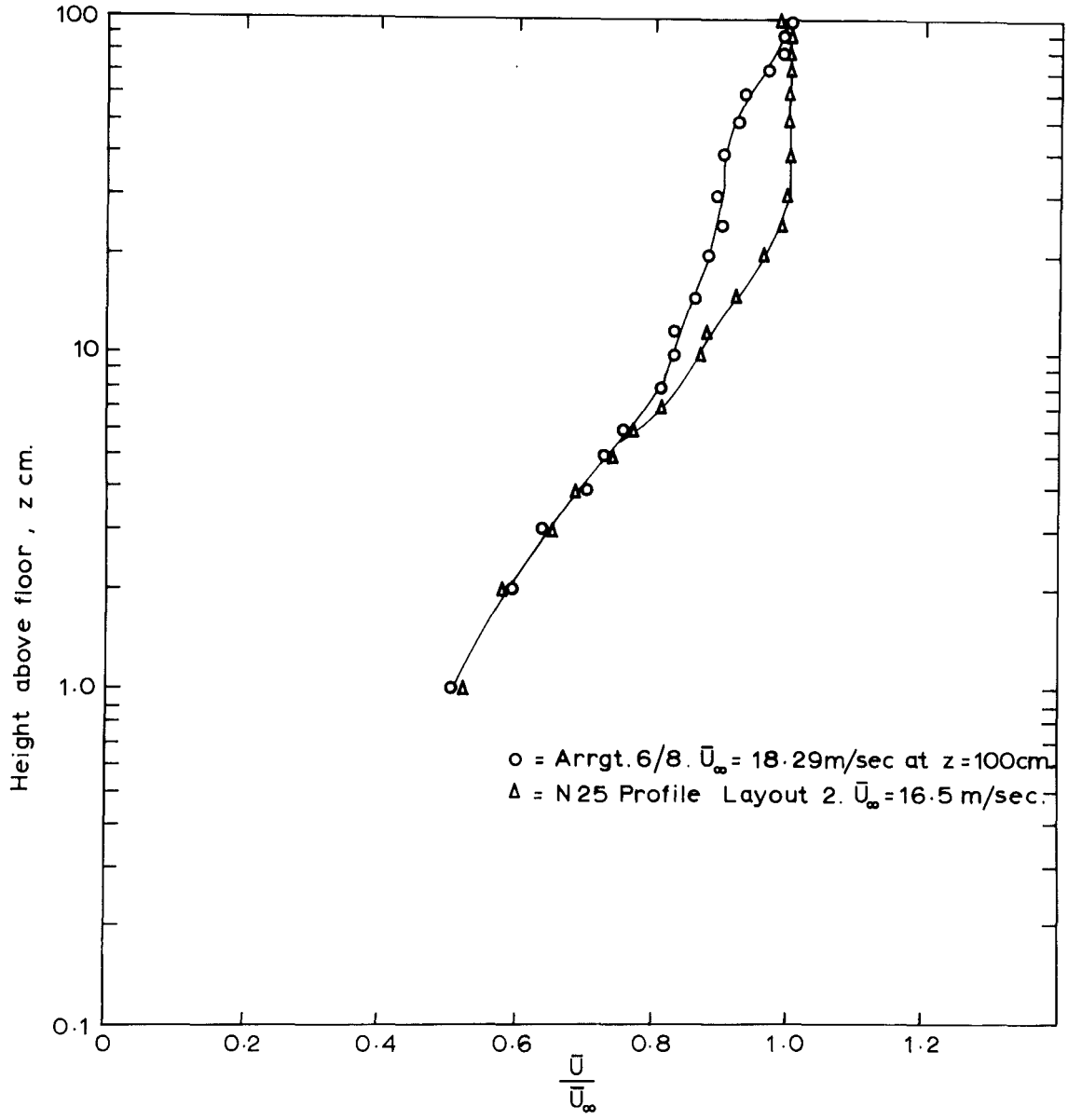

Fig. 6.33 MEAN VELOCITY PROFILE AT X = 9m, N25, DOWNSTREAM OF NON-UNIFORM GRID ARRG^T 6/8 PLUS TORRO BASEBOARD SURFACE ROUGHNESS.

Results and Discussion: Arrangement 6/15:

(a) Mean Velocity Profiles: These are shown in Fig. 6.34. For clarity, only measurements at N25 and S25 are shown. Profiles at the tunnel centreline and N35 lay between those shown. Figs. 6.33 and 6.34 show that the 15 cm trip fence dominates the generation of the velocity profile. Fig. 6.33 shows that with Torro baseboard alone, downstream of the grid, the velocity profile of Layout 2 (uniform grid) is distinctly different from that of Arrangement 6/8 (non-uniform grid). Fig. 6.34 shows that addition of the 15 cm trip fence at X = 0.61 m markedly reduced the difference between the mean velocity profiles obtained with the uniform and non-uniform grids (Arrangements 6/8 and 6/15 very similar grids). Above z = 7 cm, the mean velocity profiles at X = 9 m in Arrangement 6/15 were very close to a 1/7 power law form, but close to the floor the Torro baseboard retarded the flow more than desired. Later use of smaller trip fences further down the working section tended to remove (temporarily) the effect of the Torro baseboard on the surface layer mean velocity gradient.

(b) Turbulent Intensity Profiles: These are shown in Fig. 6.35. Compared with results where the uniform grid was used, in Layout 3, an increase in $u'/\bar{U}_\infty$ is apparent in the boundary layer above z = 20 cm, and an increase in $w'/\bar{U}_\infty$ between z = 20 cm and z = 70 cm. These increases in turbulent intensity correspond to the higher initial shear at the working section entrance, and indicate an increase in linear scaling between wind tunnel and atmosphere.

(c) Reynolds Stress Profiles: These are shown in Fig. 6.36. The increase in shear caused by the non-uniform grid bar spacing is manifested at X = 9 m as increase in the constant stress layer depth to about 50 cm, with $-\overline{uw}/\bar{U}^2_{\infty max}$ approximately the same as in Layout 3.

Originally it was hoped to achieve the design mean velocity profile at X = 9 m with lower values of $-\overline{uw}/\bar{U}^2_\infty$ by use of the non-uniform grid and surface roughness alone. However, it became evident that as the grid was altered to bring the velocity profile closer to the design 1/6 power law form, shear stress increased to approach that occurring when trip fences were used. It was also clear that the high shear was necessary if the accelerated growth boundary layer was to be grown in a distance 10 times its final depth.

Summary:

Tests with non-uniform grids + surface roughness alone were not

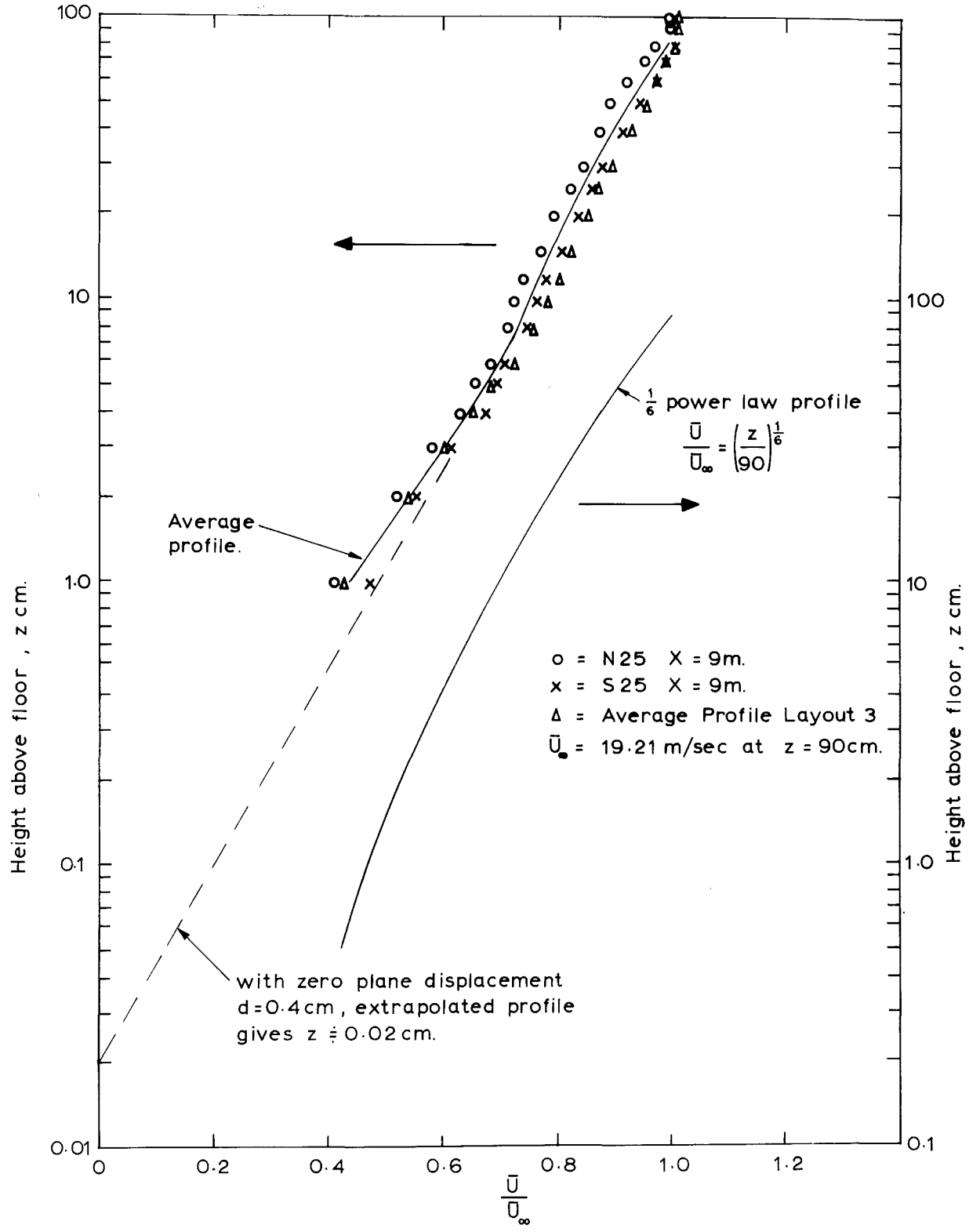

Fig. 6·34 MEAN VELOCITY PROFILES ARRGT. 6/15

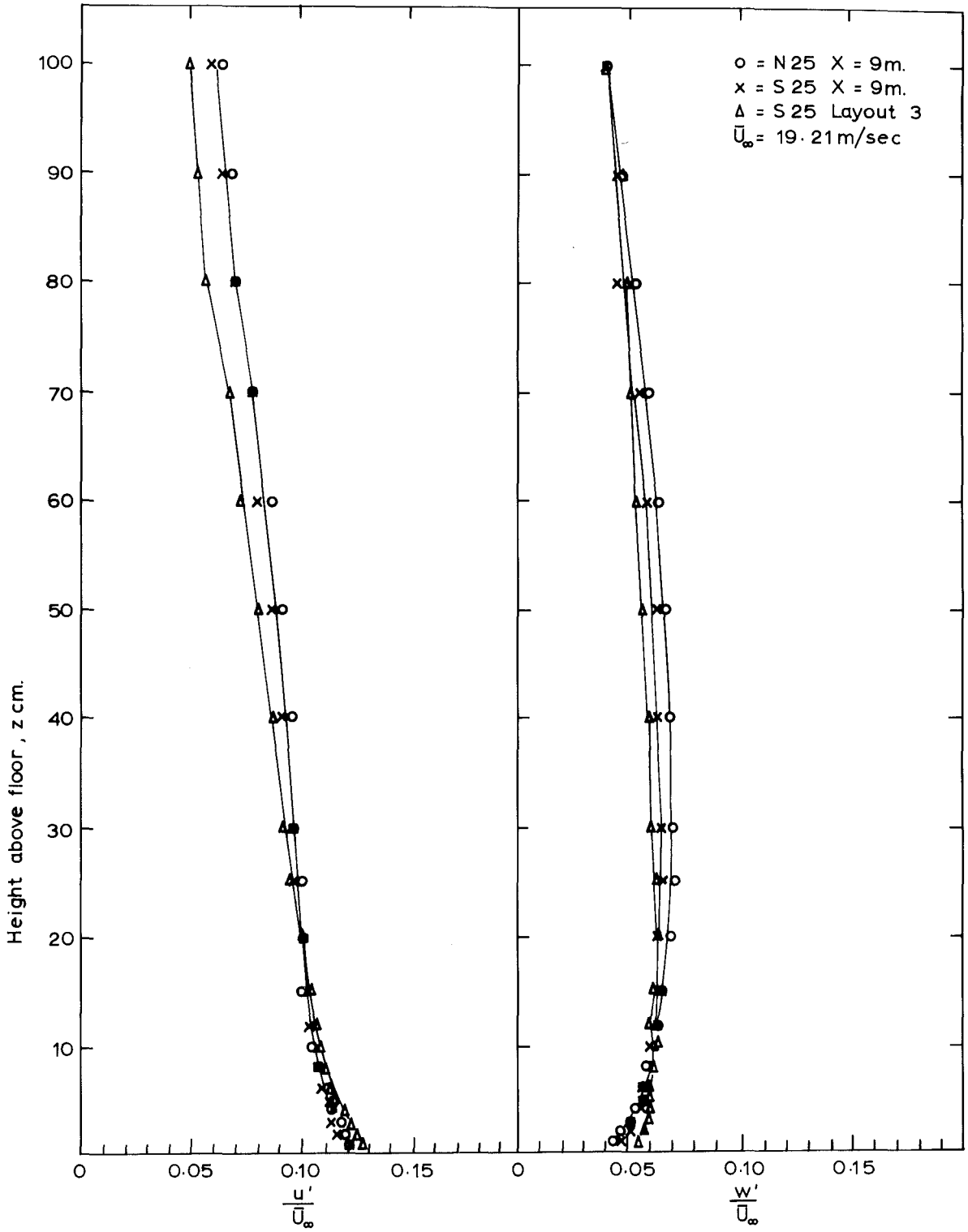

Fig. 6·35 TURBULENT INTENSITY PROFILES ARRGT. 6/15.

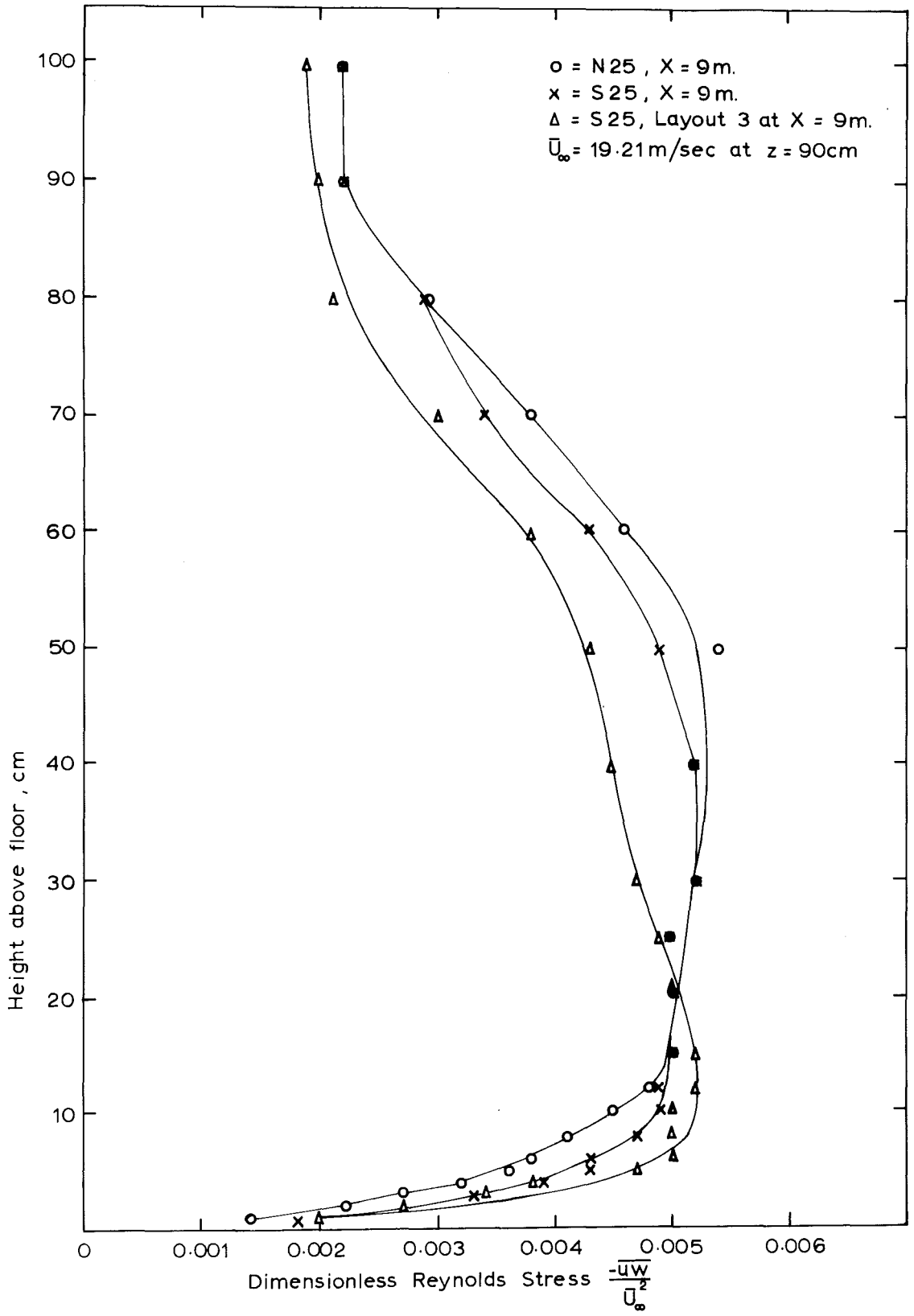

Fig. 6·36 REYNOLDS STRESS PROFILE - ARRGT. 6/15

productive. However, results of Layout 3 were improved by the use of a non-uniform grid with the 15 cm trip fence at X = 0.61 m and Torro baseboard surface roughness. The modification to the grid produced a small improvement in the mean velocity profile by transferring mean flow momentum from the lower and central region of the working section to the upper part. Corresponding increases in turbulent intensity and Reynolds stress occurred in the outer part of the boundary layer, suggesting increased linear scaling for the simulation, compared with Layout 3. For arrangement 6/15, $d_m:d_a$ would have been about 1:300, as in Layout 4.

6.3.7 Layouts 7 - 14: Non-uniform Grid + Torro Baseboard + Various Trip Fence Combinations:

The grid bar spacing of Arrangement 6/15 was retained for all subsequent boundary layer generating layouts, in which different trip fence combinations were mounted on the Torro baseboard. 8 such schemes were tested with generally only minor alterations to the boundary layer structure occurring. Some results are given for four representative cases. Results for the other schemes (Layouts 7 - 10) are not presented. Layouts 7 - 14 are described in Table 6.7.

In Layouts 7 - 10, addition of the subsidiary trip fences at X = 2.5 m and X = 5 m tended to increase turbulent intensity in the surface layer of the simulated atmospheric flow. Addition of the fence at X = 2.5 m in Layout 8, altered the velocity profile form of Fig. 6.34 to a 0.16 power law form. Substitution of the initial 10 cm 34% permeable fence for the 15 cm solid fence (Layout 8 to Layout 9) resulted in lower turbulent intensities at X = 9 m, but did not significantly alter the mean velocity profile.

The four final layouts tested are described in Table 6.7 and in Fig. 6.37. Results for these Layouts are restricted to profiles of mean velocity, turbulent intensity and Reynolds stress. More detailed results for Layout 14 appear in 6.4. This layout was used in later model studies.

Results and Discussion: Layouts 11 - 14

(a) Mean Velocity Profiles: These are compared for the four layouts in Fig. 6.38. All would probably be acceptable for a rural boundary layer simulation. However, Layouts 13 and 14 gave profiles closest to the design 1/6 power law and are an improvement over Layouts 3 and 4.

TABLE 6·7 LAYOUTS 7-14

Layout No.	Grid Type	Surface Roughness	Trip Fence at			
			X = 0·61m.	X = 2·5m.	X = 5m.	X = 7·5m.
7	Arrgt 6/15	Torro baseboard	Aluminium 15cm., $\Phi = 0$	———	Torro blocks $3\frac{1}{3}$cm, $\Phi = 0.34$	———
8	"	" "	"	Torro blocks $6\frac{2}{3}$cm, $\Phi = 0.34$	"	———
9	"	" "	Torro blocks 10cm., $\Phi = 0.34$	"	"	———
10	"	" "	"	Torro blocks 5cm, $\Phi = 0.34$	"	Torro blocks $2\frac{1}{2}$cm., $\Phi = 0$
11	"	" "	Torro blocks 10cm., $\Phi = 0.43$ *	Torro blocks $3\frac{1}{3}$cm., $\Phi = 0.34$	"	"
12	"	" "	Aluminium 5cm., $\Phi = 0$	"	"	"
13	"	" "	Torro blocks 10cm. $\Phi = 0.34$	"	"	"
14	"	" "	Aluminium 10cm, $\Phi = 0$	"	"	"

* see Fig. 6·37

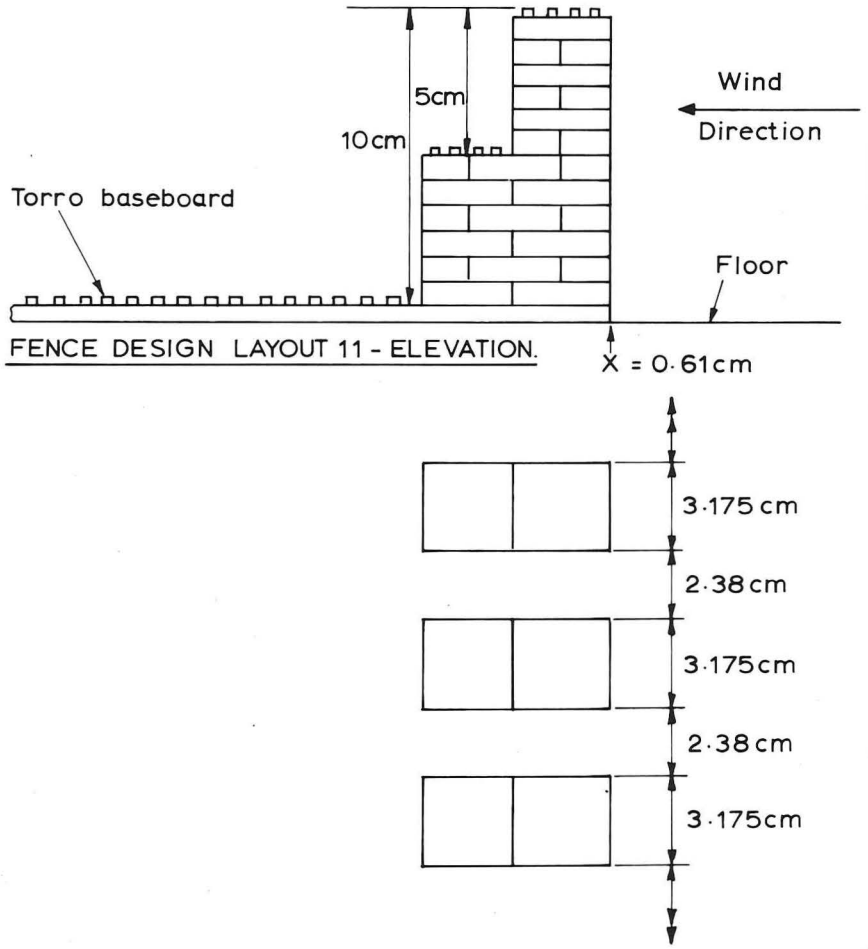

FENCE DESIGN LAYOUT 11 - ELEVATION.

Fig. 6·37 LAYOUTS 11 - 14.

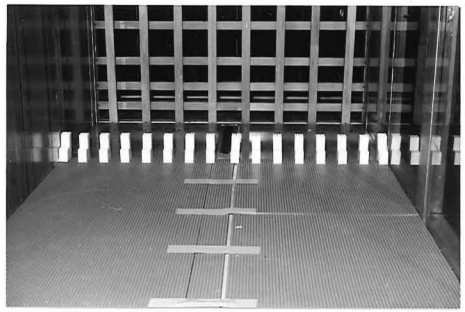

Layout 11 - close to initial Torro block trip fence.

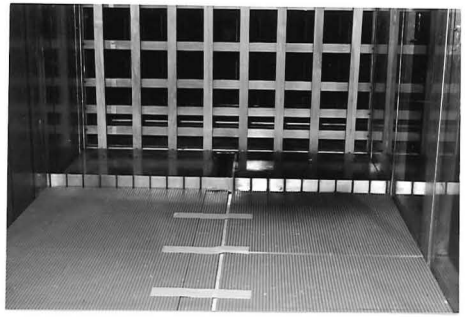

Layout 12 -close to initial trip fence.

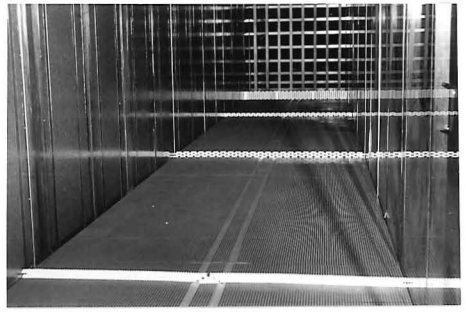

Layout 13

Layout 14

Views towards upstream end of working section

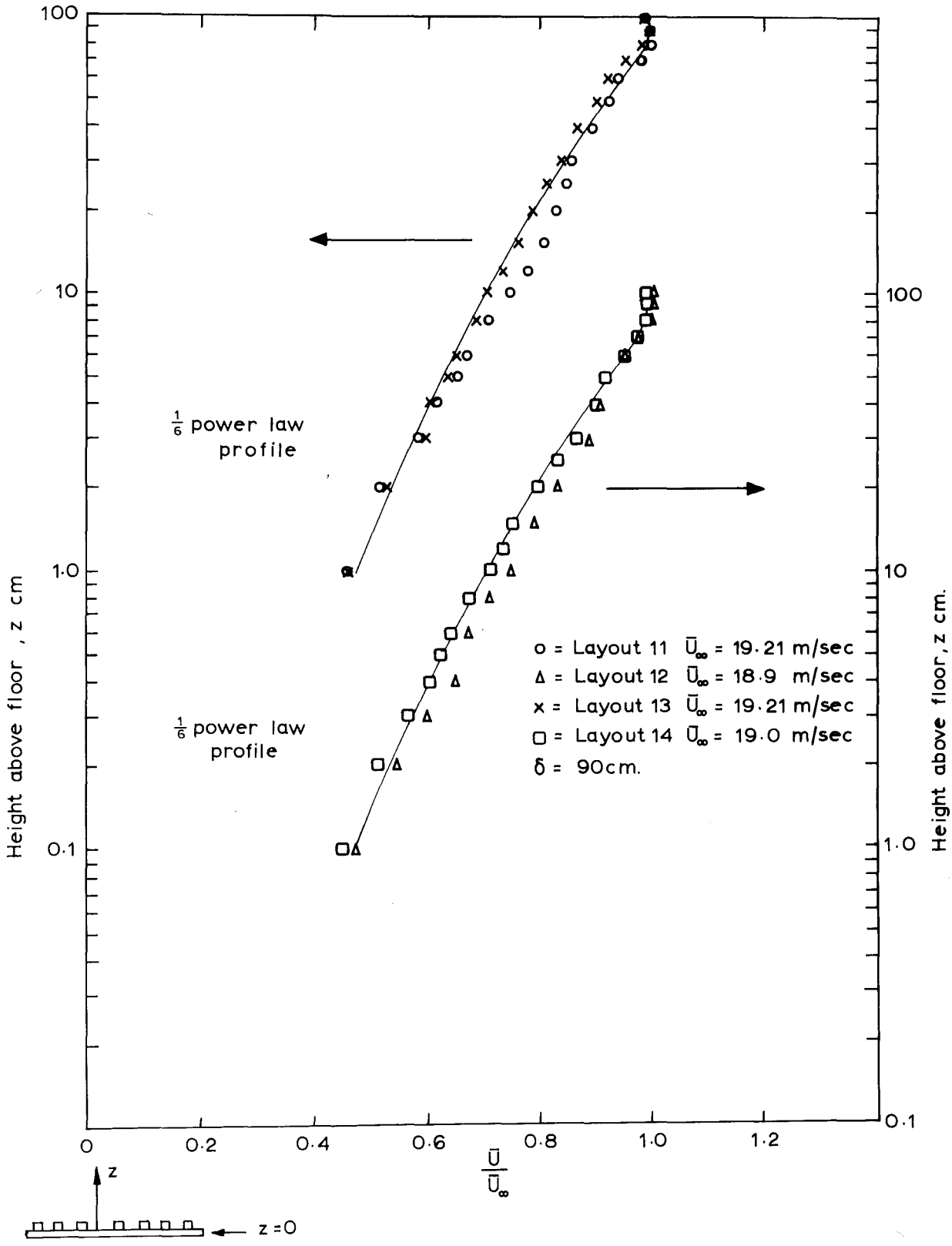

Fig. 6·38 MEAN VELOCITY PROFILES X = 9m , N25 LAYOUTS 11-14.

(b) Turbulent Intensity Profiles: These are shown in Fig. 6.39. The $u'/\bar{U}_\infty$ profiles of Fig. 6.39a are similar for the four layouts, but closer comparison shows that Layouts 11 and 12 gave very similar profiles, with slightly lower intensities than the very similar results from Layouts 13 and 14. It is interesting that far downstream, the effect of the initial 5 cm solid fence was similar to that of the 10 cm high 43% permeable Torro Block post fence.

As with the mean velocity profiles, the turbulent intensity profiles of Layouts 13 and 14 were considered more satisfactory because of their slightly higher intensities in the middle and outer parts of the boundary layer, indicating larger linear scaling for the simulation.

The $w'/\bar{U}_\infty$ profiles of Fig. 6.39b reflect the same trends as the $u'/\bar{U}_\infty$ profiles.

(c) Reynolds Stress Profiles: In Fig. 6.40 it is seen that the various Reynolds stress profiles at X = 9 m exhibit close similarity up to z = 15 cm, but differences exist above that height. Layout 12, where the initial 5 cm solid trip fence was used, gives the lowest maximum stress and lower stress at all heights. Less shear far downstream would be expected with this lower fence.

In contrast to the turbulent intensity profiles, the Reynolds stress profiles are most similar for Layouts 11 and 14, while Layout 13 exhibited a lower maximum stress but a greater depth of approximately constant stress. Profiles for Layouts 13 and 14 are interesting in relation to wind protection by windbreaks. Layout 14, with the initial solid fence shows the highest maximum shear stress, characteristic of the high shear imparted by a solid fence, but the initial permeable fence of Layout 13 leaves higher average shear in the flow far downstream of the fence. This may support the observation that the far field effectiveness of a permeable fence is greater than that of a solid fence.

In the lowest 15 cm of the boundary layer, the shear stress profiles are dominated by the lower trip fences and Torro baseboard.

Summary:

Mean velocity profiles for Layouts 13 and 14 were closest to the design 1/6 power law form, and the corresponding turbulent intensity profiles suggested slightly larger linear scaling for Layouts 13 and 14 than for 11 and 12. Layout 14 was finally used for tests of model fences.

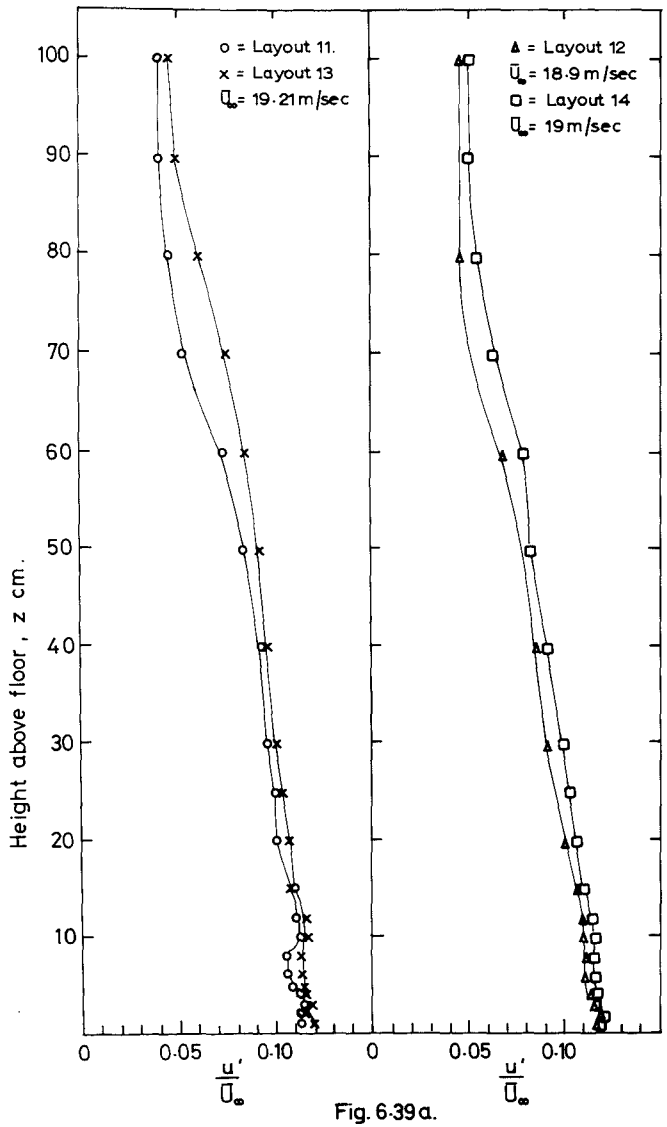

Fig. 6·39a.

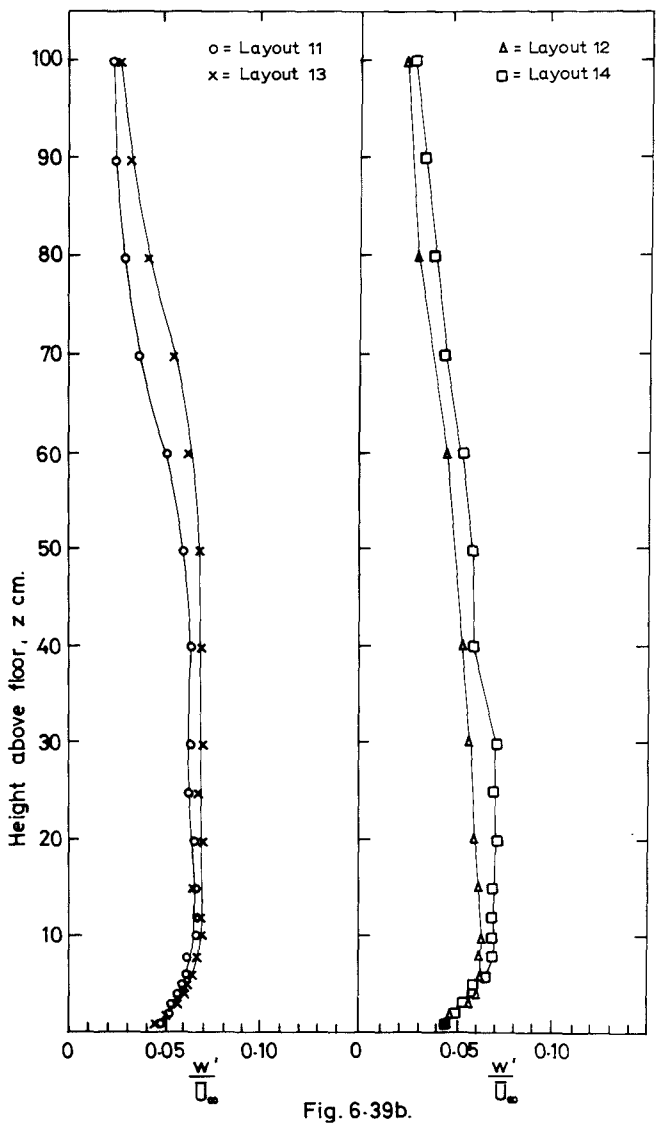

Fig. 6·39b.

Fig. 6·39 TURBULENT INTENSITY PROFILES, X = 9m, N25 - LAYOUTS 11-14.

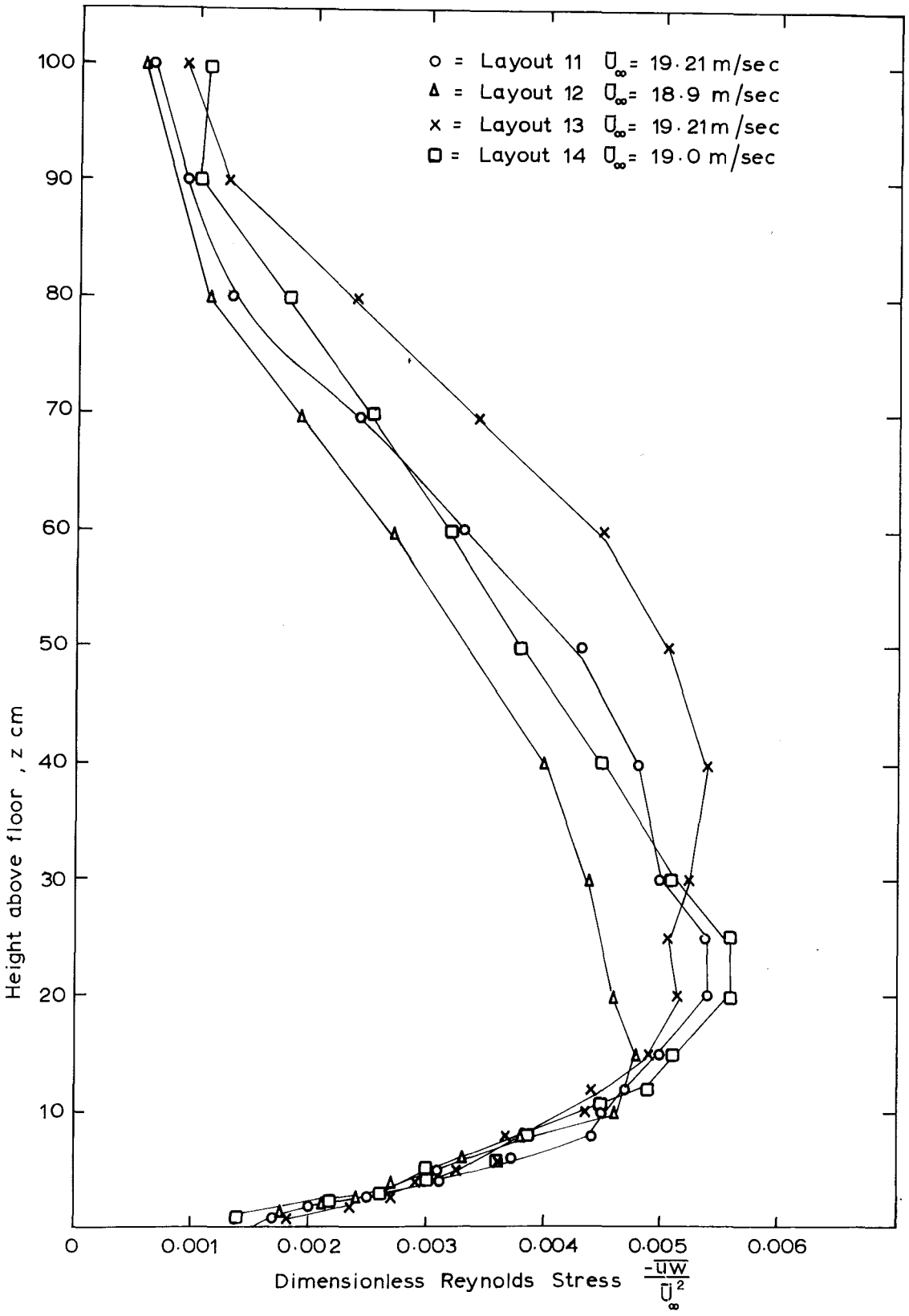

Fig. 6.40 REYNOLDS STRESS PROFILES AT X = 9m , N 25
LAYOUTS 11-14.

6.4 LAYOUT 14: NON-UNIFORM GRID + TORRO BASEBOARD + 4 TRIP FENCES: DETAILED RESULTS AND FINAL EVALUATION

In this section detailed results are presented for Layout 14 (described in Table 6.7 (p.279). Detailed measurements were made for both Layouts 13 and 14, but Layout 14, using the solid initial trip fence, showed better lateral uniformity in profiles of mean velocity and Reynolds stress, and less scatter of points in auto and cross-correlation plots. Evaluation of the simulated atmospheric boundary layer is therefore referred to Layout 14. In addition to measurements of profiles of mean velocity, u and w component turbulent intensities, and Reynolds stress already made, the following measurements were carried out :

(i) v velocity component turbulent intensity;
(ii) u and w component energy spectra;
(iii) auto-correlation coefficients;
(iv) lateral and vertical cross-correlations of the u velocity compt.
(v) self-preservation of the flow at X = 11 m.

With the development of computing facilities in the Mechanical Engineering Department, future measurements should include cross-spectral density functions, and probability distributions for the fluctuating velocity components. v component energy spectra can be measured with the present equipment.

6.4.1 Mean Velocity Profiles:

These are shown in Fig. 6.41. Fig. 6.41a indicates that lateral uniformity in Layout 14 is good, the worst lateral non-uniformity being ±3.8% about the lateral mean at z = 15 cm. This was considered quite acceptable for an atmospheric boundary layer simulation, and compares favourably with previous work, e.g. that of Armitt & Counihan (1968), Counihan (1969) and Campbell and Standen (1969).

In Fig. 6.41b mean velocity profiles at X = 9 m are compared for Layout 14 and Layout 3. The increase in power law exponent is obvious, but it is debatable whether the fairly close obedience to the design 1/6 power law profile was necessary, and worth the large number of extra arrangements. It is felt that the turbulence structure of this simulated atmospheric flow is the vital part in the modelling process, and the turbulence structure is only characterised by the mean velocity profile in an equilibrium boundary layer. In the non-equilibrium 'step change + boundary layer growth'

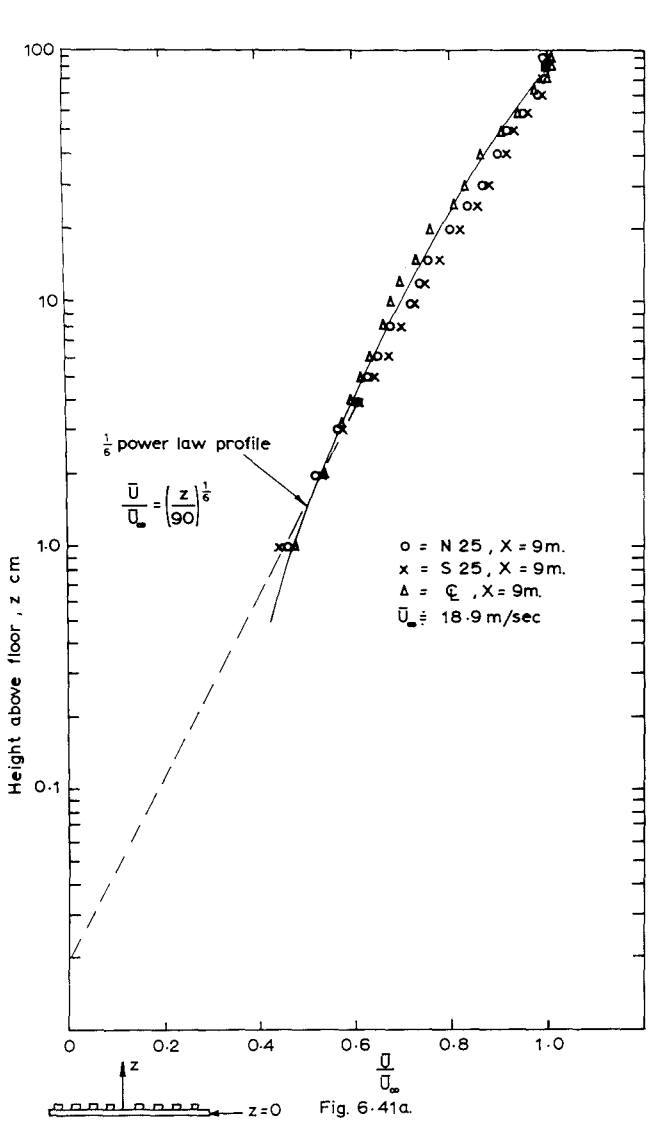

Fig. 6·41a.

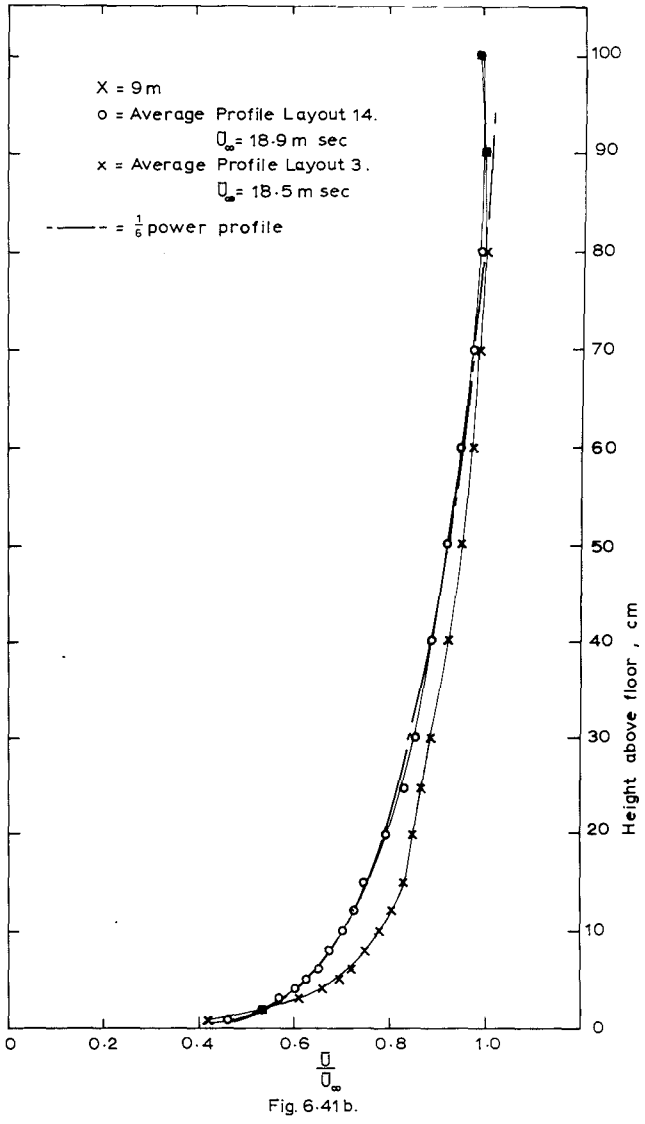

Fig. 6·41b.

Fig.6·41 MEAN VELOCITY PROFILES - LAYOUT 14.

atmospheric model, it would be expected that with substantially correct turbulence structure in the test section, a velocity profile with power law exponent within say ±10% of the design value would be sufficiently accurate for engineering applications.

While the power law mean velocity profile form conveniently describes the boundary layer as a whole, a logarithmic profile should be expected close to the ground. A straight line portion close to the floor is approximately exhibited by Fig. 6.41a, particularly for N25 and S25. For Layout 14, extrapolation of the logarithmic portion of the profile gives z_o = 0.02 cm. The actual Torro baseboard roughness element height is 0.32 cm or 16 z_o. It must be emphasised that this evaluation of z_o refers only to the X = 9 m location, since z_o changes with downstream distance in the non-equilibrium boundary layer. In fully rough flow, z_o increases with distance in flow over uniform roughness, as shown by Fig. 6.12 (p.234), and as found by Ludwig and Sundaram (1969).

In the present work there was insufficient working section length for horizontal homogeneity to be achieved. With the Torro baseboard alone, z_o reached a value of ~0.05 cm at X = 9 m, compared with z_o = 0.02 cm in Layout 14. Thus, the addition of trip fences and modification to the grid reduced z_o below the value it would have achieved over the Torro baseboard alone, so that the trip fences and graded grid were not exactly matched to the floor roughness. This is common in accelerated growth boundary layers.

Evaluation of the linear scaling between wind tunnel and atmosphere by considering the ratio z_{om}/z_{oa} (see Appendix 7) should be considered approximate owing to the fact that z_o is slowly changing with distance downstream.

6.4.2 Turbulent Intensity Profiles:

These are shown in Fig. 6.42. Plots of $u'/\bar{U}_\infty$, $v'/\bar{U}_\infty$ and $w'/\bar{U}_\infty$ are presented in Fig. 6.42a. From this figure it can be established that in the first 2 cm above the floor, Layout 14 gives

$$u'; v': w' = 2.34: 1.54: 1.0.$$

This compares quite well with the model of Eqn 2.30 (p.42) which gave, for the atmospheric surface layer:

$$u': v': w' = 1.92: 1.54: 1.$$

Further out in the tunnel boundary layer, e.g. between z = 20 cm and z = 90 cm,

$$u': v': w' = 1.5: 0.8: 1.0.$$

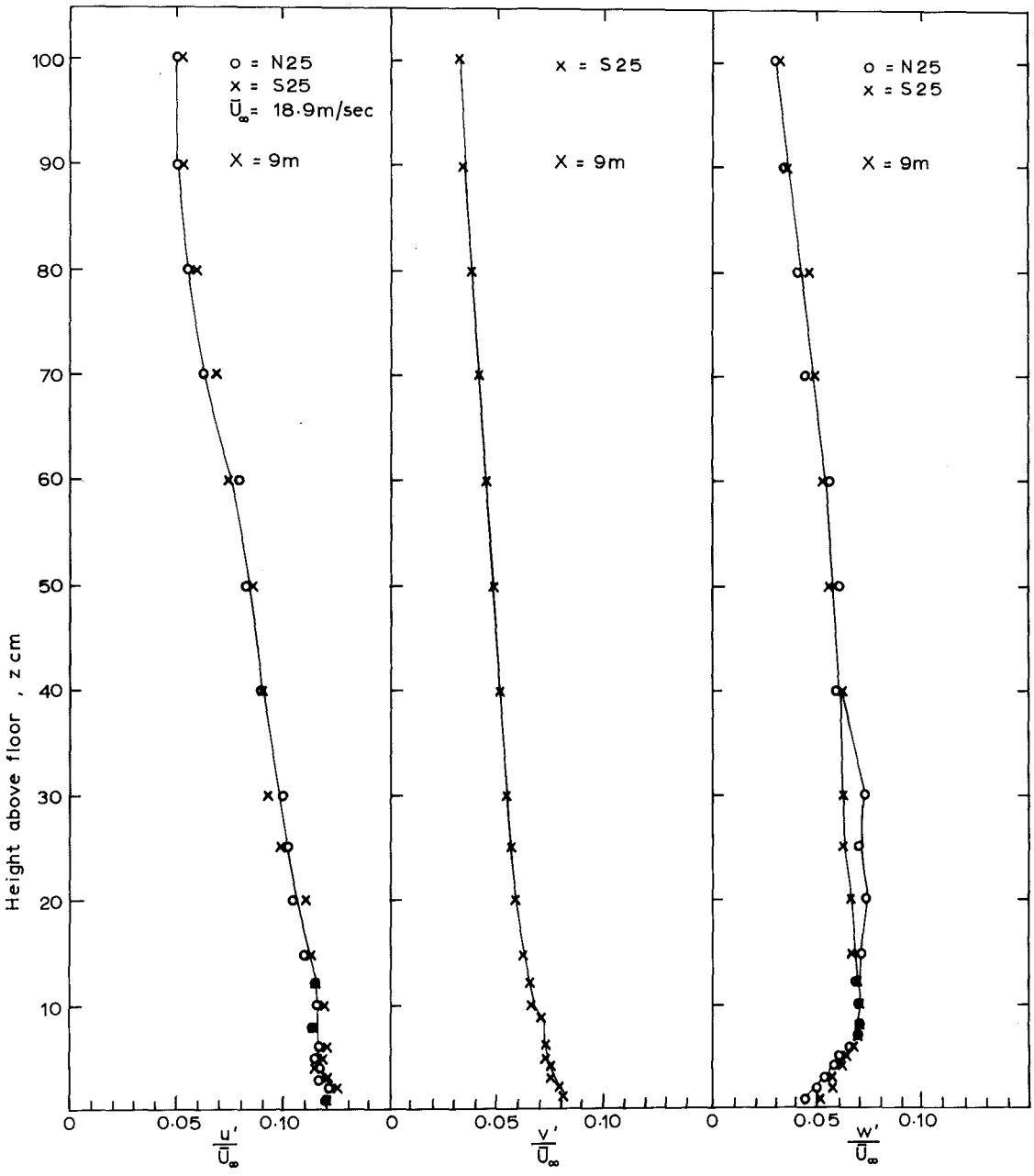

Fig. 6·42a. TURBULENT INTENSITY PROFILES - LAYOUT 14.

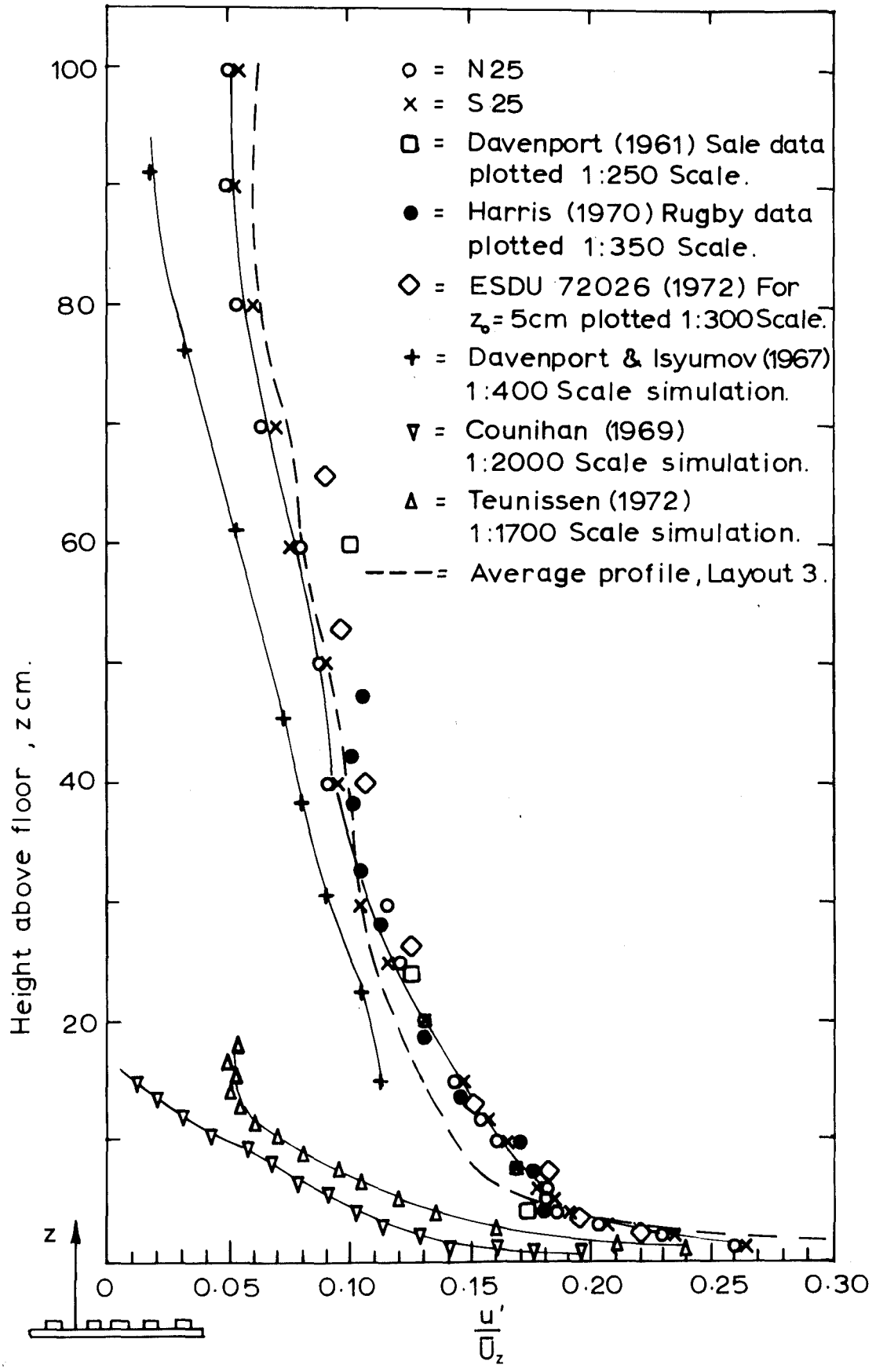

Fig. 6·42 b. u VELOCITY COMPONENT TURBULENT INTENSITY AT X = 9m LAYOUT 14.

This indicates that w' is somewhat high in the outer part of the boundary layer. This probably arises through the use of trip fences to thicken the boundary layer, and accompanies the high shear stress values that occur in the accelerated boundary layer growth process. Counihan's (1969) accelerated growth rural boundary layer results show a similar excessive value of w' in relation to v'. It was decided that the profiles of u, v, and w component turbulent intensities of Layout 14 were acceptable, with the caution that the high w' values could affect results of tests where vertical momentum transfer is important, e.g. vertical forces on bridge decks, wind reduction by shelter fences.

In Fig. 6.42b, the u component turbulent intensity is plotted in the form $u'/\bar{U}_z$ vs z, for more realistic comparison with field data and data from other simulations. The height co-ordinate has not been plotted in normalised (z/δ) form, in order to show differences in scale between different simulations. The intensity profile compares very favourably with the field data of Harris (1970) and Davenport (1961), and with the design curve for turbulent intensity over rural terrain with z_o = 5 cm given by ESDU (1972). All of these are scaled about 1:300. Lateral uniformity and profile shape are better than in the simulations of Armitt and Counihan (1968), Campbell and Standen (1969), Templin (1969) and Teunissen (1972), probably because of the greater two-dimensionality of the boundary layer generating apparatus.

Davenport and Isyumov (1967) did not give data for different lateral positions in the flow, but their 1:400 scale turbulent intensity profile is shown for comparison in Fig. 6.42b. The shape is similar to that for the profile of Layout 14, and would require scaling up to a linear scale of 1:270 to match the present results. Counihan's (1969) turbulent intensity data matched Harris' (1968) Rugby data best when plotted to a scale of 1:2000, and are shown to 1:2000 scale in Fig. 6.42b. (Counihan's turbulent length scale data were characteristic of a linear scaling nearer 1:4000).

Teunissen (1972) required a 2.54 cm trip fence in combination with his air jet scheme and Lego baseboard roughness, to generate sufficient turbulent intensity in the 17.8 cm, 0.16 power law profile boundary layer. Teunissen's data are plotted to the 1:1715 scale of his simulation in Fig. 6.42b. The $u'/\bar{U}_z$ profile of Layout 14 is a closer fit to field data and gives larger linear scaling than the equivalent profile for Layout 3, shown by the dotted line in Fig. 6.42b.

It was concluded from Fig. 6.42b that the turbulent intensity profiles were scaled 1:300 or slightly larger, between wind tunnel and atmosphere.

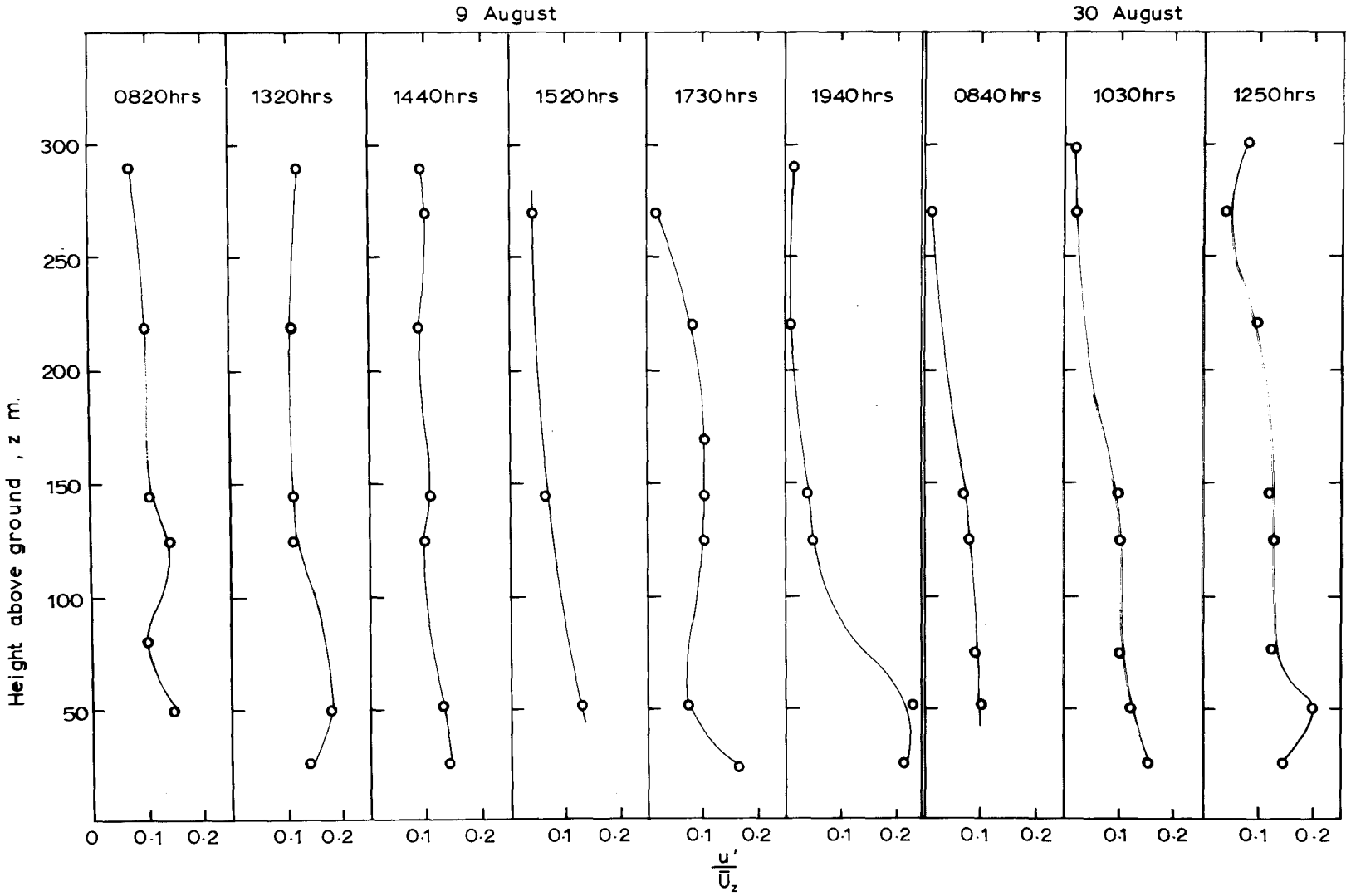

Fig. 6·43 TURBULENT INTENSITY PROFILES MEASURED IN THE 300m LAYER ON 9 AUGUST AND 30 AUGUST, 1961, BY IVANOV (1965).

(These graphs show the statistical variability of field data.)

6.4.3 Reynolds Stress Profiles:

These are shown in comparison with previous simulation data in Fig. 6.44. The height co-ordinate has not been normalised with boundary layer depth, in order to show scale differences between the simulations. Comparison of Layout 14 with Layout 3, Fig. 6.20 (p.249), shows a maximum dimensionless Reynolds stress about 10% higher in Layout 14.

Ludwig and Sundaram (1969) (see 3.3.1) state that the lowest 100 m of the atmospheric boundary layer, assumed horizontally homogeneous and free from pressure gradients, constitutes an approximate constant stress layer. An aim of the present work was to create such a constant stress surface layer in the simulated boundary layer. Plate (1971) suggests that achievement of a constant stress layer should not be a major criterion for the success of the simulation and frequently reports of atmospheric boundary layer simulations do not include Reynolds stress data, or, where these are included, typically only a maximum is compared with an atmospheric surface drag coefficient. This is no doubt due to the absence of atmospheric Reynolds stress measurements with which to compare wind tunnel data.

In 2.4.4 it was pointed out that except over smooth surfaces, the maximum value of $-\rho\overline{uw}$ in the atmospheric surface layer is likely to occur above the surface, and therefore exceed the normally measured surface shear stress. If, however, the usual assumption is made, that $-\rho\overline{uw}_{max} = \tau_o$, then wind tunnel Reynolds stress measurements may be compared with measured values of the atmospheric surface drag coefficient, k_{10}. Fig. 2.7 shows that for a rural boundary layer profile of 1/6 power law form, $k_{10} \simeq 0.006$. Now assuming $\bar{U}_\infty = \bar{U}_G$, and $k_\infty = -\overline{uw}/\bar{U}^2_{\infty\,max}$, the value of k_∞ appropriate to $k_{10} = 0.006$ is $k_\infty = 0.0025$, as suggested by Plate (1971). Counihan (1969) used $k_\infty = 0.0025$ as a simulation criterion, and Fig. 6.44 shows that both Counihan (1969) and Teunissen (1972) obtained Reynolds stress profiles with $-\overline{uw}/\bar{U}^2_\infty \simeq 0.0025$. Using $k_{10} = k_\infty(\bar{U}_\infty/\bar{U}_{10})^2$,

Counihan's 1:2000 scale simulation gives $k_{10} = 0.0123$
Teunissen's 1:1715 scale simulation gives $k_{10} = 0.008$.

The value of k_{10} in Counihan's simulation is seen to be high for a 1/7 power law profile rural boundary layer (see Fig. 2.7, p30).

For Layout 14, in the present work, Fig. 6.44 shows a maximum value for $-\overline{uw}/\bar{U}^2_\infty$ of 0.0056, with $-\overline{uw}/\bar{U}^2_\infty = 0.0053 \pm 0.0003$ in the approximately constant stress depth from z = 12 cm to z = 35 cm. As for Layout 3,

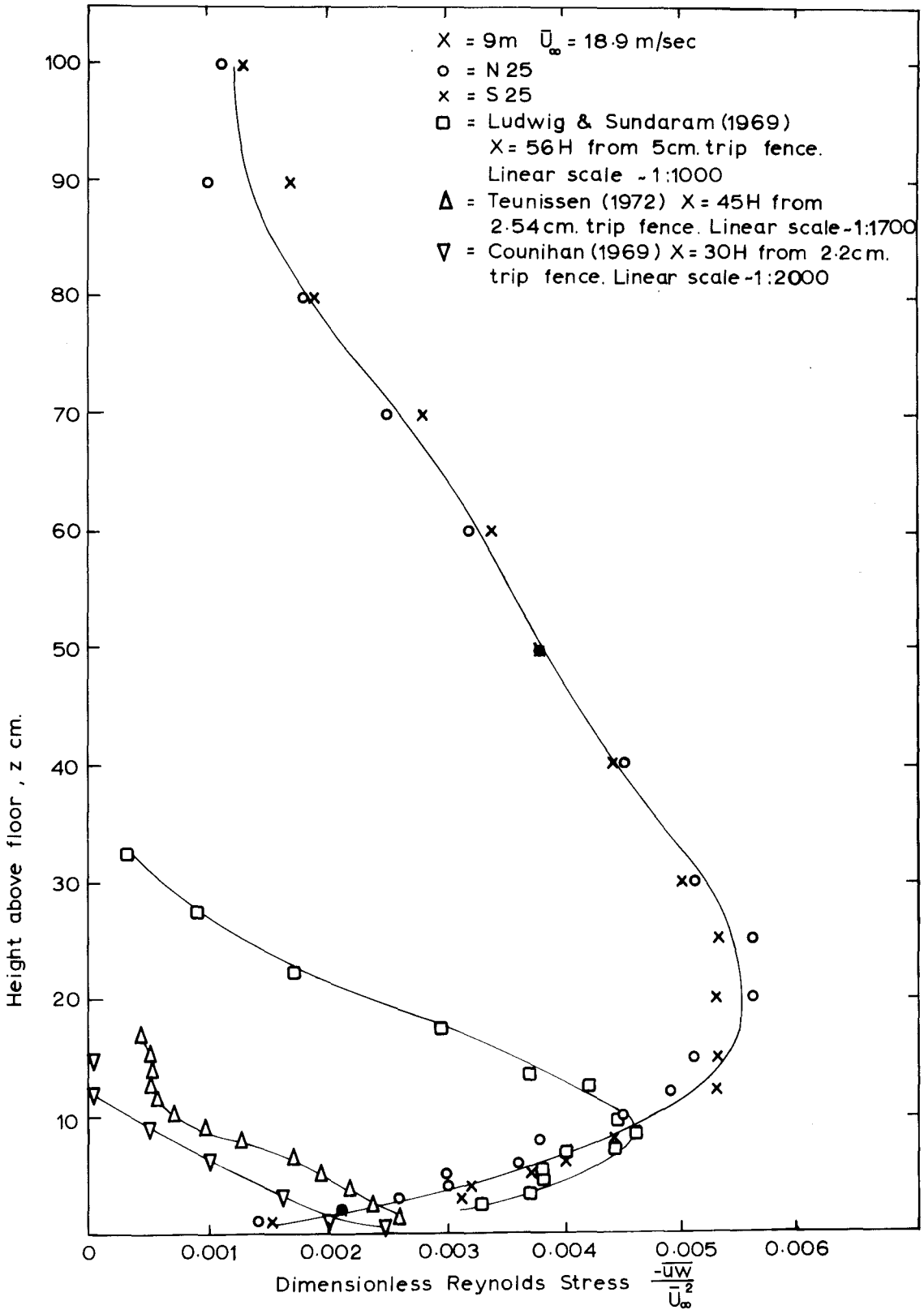

Fig. 6·44 REYNOLDS STRESS PROFILE - LAYOUT 14.

(Fig. 6.20), the maximum stress appears too high for a rural boundary layer. With a linear scaling, based for the meantime on boundary layer depth and turbulent intensity profiles of 1:300, $\bar{U}_{10}/\bar{U}_G$ in Layout 14 is 0.58, so that $-\overline{uw}/\bar{U}^2_{10max} \simeq 0.017$. If this maximum stress is again assumed equal to k_{10}, Fig. 2.7 shows that the shear stress in the boundary layer is characteristic of woodland or suburban terrain. The maximum shear stress, $-\overline{uw}/\bar{U}^2_\infty = 0.0056$, can be made to appear acceptable, as in 6.3.3c, by basing linear scaling for the simulation on comparison of length scales of turbulence using Eqn 2.63. For instance, Table 6.9 suggests a possible linear scaling of 1:50 near the floor. Under these conditions, the wind tunnel boundary layer becomes only a partial depth atmospheric model with $\bar{U}_\infty \neq \bar{U}_G$, so that

$$\bar{U}_{10}/\bar{U}_\infty = 0.78$$

$$\therefore \quad -\overline{uw}/\bar{U}^2_{10max} = \frac{0.0056}{0.78^2} = 0.0092$$

This value of maximum dimensionless Reynolds stress would be acceptable for rural terrain, but the simulated boundary layer would represent only the lowest 45 m of the atmospheric boundary layer, with a constant stress depth of 15 m. However, a linear scaling of 1:50 for the boundary layer as a whole, is incompatible with data from correlation measurements, with some of the spectral information and with turbulent intensity measurements, so that the above rationalisation of Reynolds stress level is really unacceptable.

As pointed out in 6.3.3.c, the high dimensionless shear stress in the simulated boundary layer appears to occur because the graded blockage at the grid, and the trip fences, are effectively larger roughness than that characteristic of the surface in an ideal 1:300 scale rural boundary layer. Thus, $-\overline{uw}/\bar{U}^2_{\infty max}$ is characteristic of the disturbance to the flow generated by the grid and trip fences, while the value of $-\overline{uw}/\bar{U}^2_\infty$ close to the floor is characteristic of the smaller roughness of the Torro baseboard. For instance, at the surface in Layout 14,

$$k_\infty = -\overline{uw}/\bar{U}^2_\infty \simeq 0.002$$

This corresponds to $u_* = 0.85$m/sec. If now u_* is estimated from the slope of the logarithmic mean velocity profile near the floor, $u_* = 0.79$ m/sec. The latter value of u_* agrees with that estimated from the surface Reynolds stress rather than the value of u_* derivable from $-\overline{uw}/\bar{U}^2_{\infty max}$.

If data from the turbulent intensity profiles are taken together with $u_* \simeq 0.8$ m/sec, then at $z \simeq 2$ cm :

$$u' : v' : w' : u_* = 2.85 : 1.9 : 1.24 : 1.$$

By comparison, Eqn. 2.30 gives, for the atmospheric surface layer

$$u' : v' : w' : u_* = 2.50 : 2.0 : 1.30 : 1.$$

This is acceptable agreement. Above the floor region, however, the accelerated boundary layer growth process increses w', hence $-\overline{uw}/\bar{U}_\infty^2$, above their desired values.

The problem of uncharacteristically high Reynolds stress levels in accelerated growth boundary layers appears to occur as the linear scale of the simulation increases. This is seen in Fig. 6.44 where the small, ~1:2000 scale simulations of Counihan and Teunissen have a suitable maximum stress level, but the 1:1000 scale simulation of Ludwig and Sundaram shows a maximum value of $-\overline{uw}/\bar{U}_\infty^2$ of 0.0046 (equivalent to $k_{10} = 0.024$) and the present simulation shows a higher maximum still, at a linear scale of ~1:300. The review of 3.5 showed that similarly high maximum Reynolds stress values occurred in the 1:250 scale rural boundary layer simulation of Armitt and Counihan (1968). In the simulations of Counihan (1969), Ludwig and Sundaram (1969) and Teunissen (1972), the ratio of trip fence height to final boundary layer depth, H/δ, was about 0.15 in each case. In the work of Armitt and Counihan (1968) H/δ was about 0.12, and in the present work 0.11, although in these latter cases, other turbulence generating devices (vortex generators and grid respectively) would have made H/δ effectively similar to H/δ in the smaller scale simulations. It therefore appears that the larger the linear scaling of the simulation, the higher will be the maximum value of $-\overline{uw}/\bar{U}_\infty^2$ when a high shear device such as a trip fence is used at the working section entrance, even if downstream measurement location is chosen so that H/δ is held sensibly constant with increasing linear scale.

This problem was briefly examined by considering a mixing length model for the shear stress generated by the action of the trip fence on the flow. Referring to Fig. 6.45, a flow, assumed initially uniform, passes over a trip fence of height H. The maximum Reynolds stress, considered a short distance downstream from the trip fence occurs across the separation streamline where mean velocity gradient is highest (see Arie and Rouse, 1956, or Plate, 1971). The shear stress maximum, measured at the start of the test section far downstream, should be approximately proportional to the high shear stress just downstream of the fence. The normalised Reynolds stress expression is :

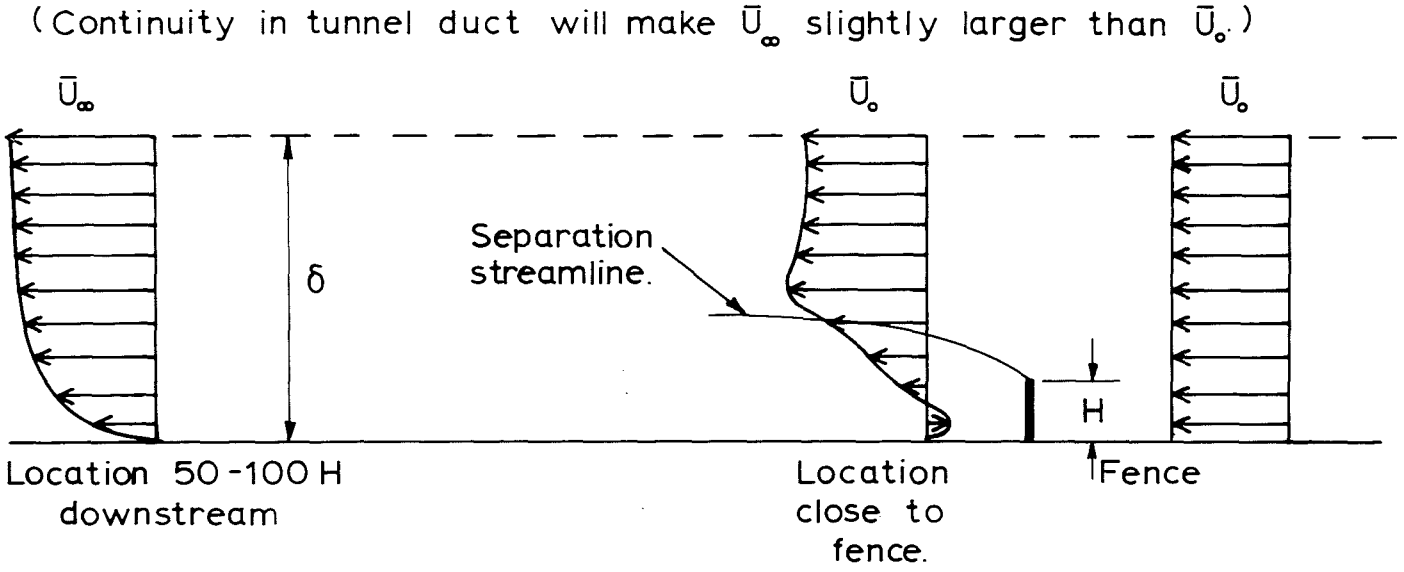

Fig. 6·45 SHEAR INTRODUCED BY TRIP FENCE.

$$\frac{-\overline{uw}}{\bar{U}_\infty^2} = \frac{\tau}{\rho \bar{U}_\infty^2} = \frac{\ell^2}{H^2} \left| \frac{d\left(\frac{\bar{U}}{\bar{U}_\infty}\right)}{d\left(\frac{z}{H}\right)} \right| \frac{d\left(\frac{\bar{U}}{\bar{U}_\infty}\right)}{d\left(\frac{z}{H}\right)} \qquad \ldots.(6.1)$$

Experimental results (e.g. Arie and Rouse, 1956) show that at Reynolds numbers $\bar{U}\, H/\nu$, greater than about 10^4, in uniform approach flow

$$\frac{d\left(\frac{\bar{U}}{\bar{U}_\infty}\right)}{d\left(\frac{z}{H}\right)}$$

at any point (x/H, z/H) in the leeward flow is independent of $\bar{U}$. Under these conditions

$$\frac{d\left(\frac{\bar{U}}{\bar{U}_\infty}\right)}{d\left(\frac{z}{H}\right)}$$

should also be independent of H. Hence, from Equn. 6.1, if $-\overline{uw}/\bar{U}^2_{\infty max}$ close to the fence (and thus presumably $-\overline{uw}/\bar{U}^2_{\infty max}$ far downstream) is to remain constant as H increases with the increasing linear scale of the simulation, the mixing length, ℓ, must be directly proportional to H. If as appears to be the case, $-\overline{uw}/\bar{U}^2_{\infty max}$ increases with the linear scaling of the simulation, ℓ must increase more rapidly than H. i.e.

$$\frac{d(\ell/H)}{dH} > 0.$$

It would be expected that the mixing length in the fence generated shear would increase with increasing fence height, but there is no ready explanation for the required non-linear relationship between fence height and mixing length.

The above simplified arguments cannot be developed further without further experimental examination of this problem. Effects of boundary layer structure in the flow approaching the trip fence, and effects of other turbulence generating devices, need to be isolated from the basic problem of the fence generated shear. Reynolds stress measurements are required at a given location (x/H) downstream of fences of various heights mounted on a flat plate in a flow which is as nearly uniform as possible, and results could be examined for variation in $-\overline{uw}/\bar{U}^2_\infty$ with H and $\bar{U}_\infty$. In the absence of other causes for the apparent increase in $-\overline{uw}/\bar{U}^2_{\infty max}$ with increasing H, it is possible

that the more permanent nature of the larger scale eddies generated by a higher fence may be responsible for $-\overline{uw}/\bar{U}_{\infty}^2$ persisting at a higher level far (50H - 100H) downstream.

The obvious solution to a linear scaling dependent scale effect on $-\overline{uw}/\bar{U}_{\infty max}^2$, is to avoid the use of high-shear devices, but this reduces the chance of achieving the required thick boundary layer in a distance of, say, 10δ from the start of the working section. All the accelerated boundary layer growth simulations reviewed in 3.5 did require the use of a tripping device to thicken the boundary layer, or give sufficiently high turbulent intensity in the outer part of the boundary layer. It may evolve that the only way to avoid uncharacteristically high levels of Reynolds stress in large scale simulations, say $d_m/d_a > 1{:}300$, is to revert to pure boundary layer growth, with the consequent greater working section length required.

6.4.4 Correlation Coefficients and Turbulent Length Scales:

In Fig. 6.46, the auto-correlation coefficient is plotted against delay time, τ. The auto-correlation coefficient was measured using the DISA TCA system with the duplicated input signal measured with a 55F31 single wire probe. Maximum delay time possible was 100 msec. The relatively larger magnitude of ρ_{uu_τ} at z = 15 cm in Fig. 6.46, over the delay time range, corresponds to the low peak wave number on the u component spectrum observed at z = 15 cm. The auto-correlation data at z = 60 cm tended to show a subsidiary peak at τ = 25 msec.

From 2.5.1, Taylor's Hypothesis was assumed applicable for wave numbers $k >> 0.0016m^{-1}$ in the atmosphere, or in a 1:300 scale simulation, $k >> 0.48m^{-1}$ in the wind tunnel. The spectra in Fig. 6.49 show that on this basis, part of the low frequency region of the energy spectrum is therefore excluded. Estimates of L_{u_x} from the auto-correlation data will therefore be only approximate, and may not reflect the large scale, low frequency content of the turbulence. Close to the floor, where definite anisotropy exists, results of applying Taylor's Hypothesis must be considered uncertain. Turbulence length scale values derived from the auto-correlation data are summarised in Fig. 6.46.

In Fig. 6.47 lateral correlation curves of ρ_{uu_y} vs y are shown for the u velocity component. These curves show a steady increase in length scale with height, as desired, and the lateral length scales calculated from the correlation data are summarised in Fig. 6.47. Harris (1970) suggests

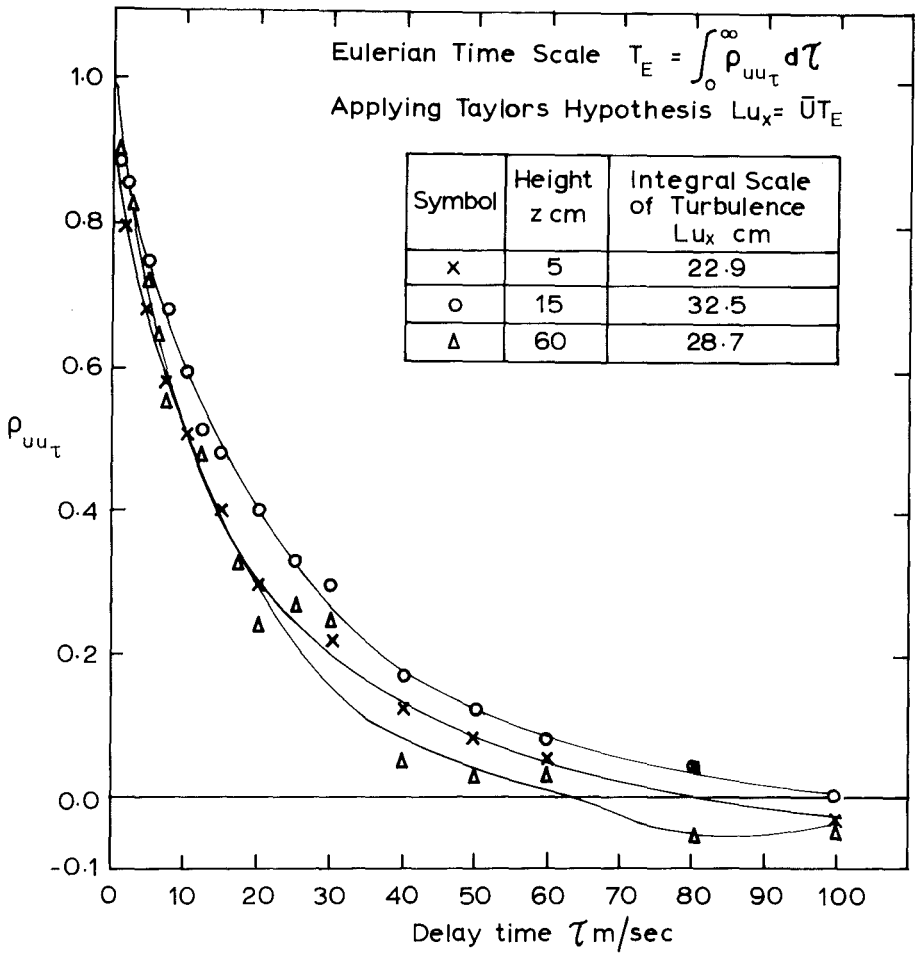

Fig. 6·46 AUTOCORRELATION COEFFICIENT X = 9m, N 25 - LAYOUT 14.

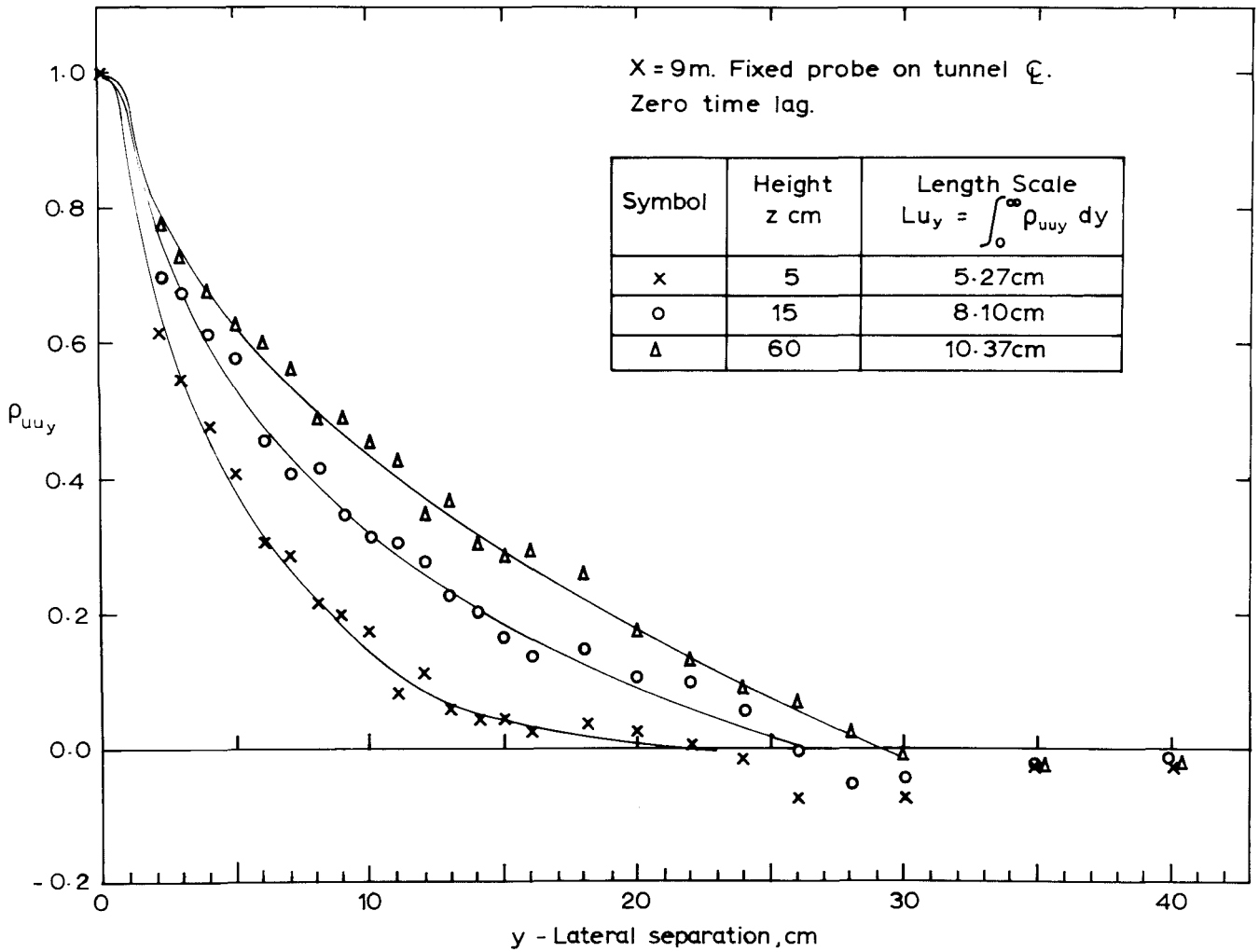

Fig. 6·47 LATERAL CORRELATION COEFFICIENT OF u VELOCITY COMPONENT. - LAYOUT 14.

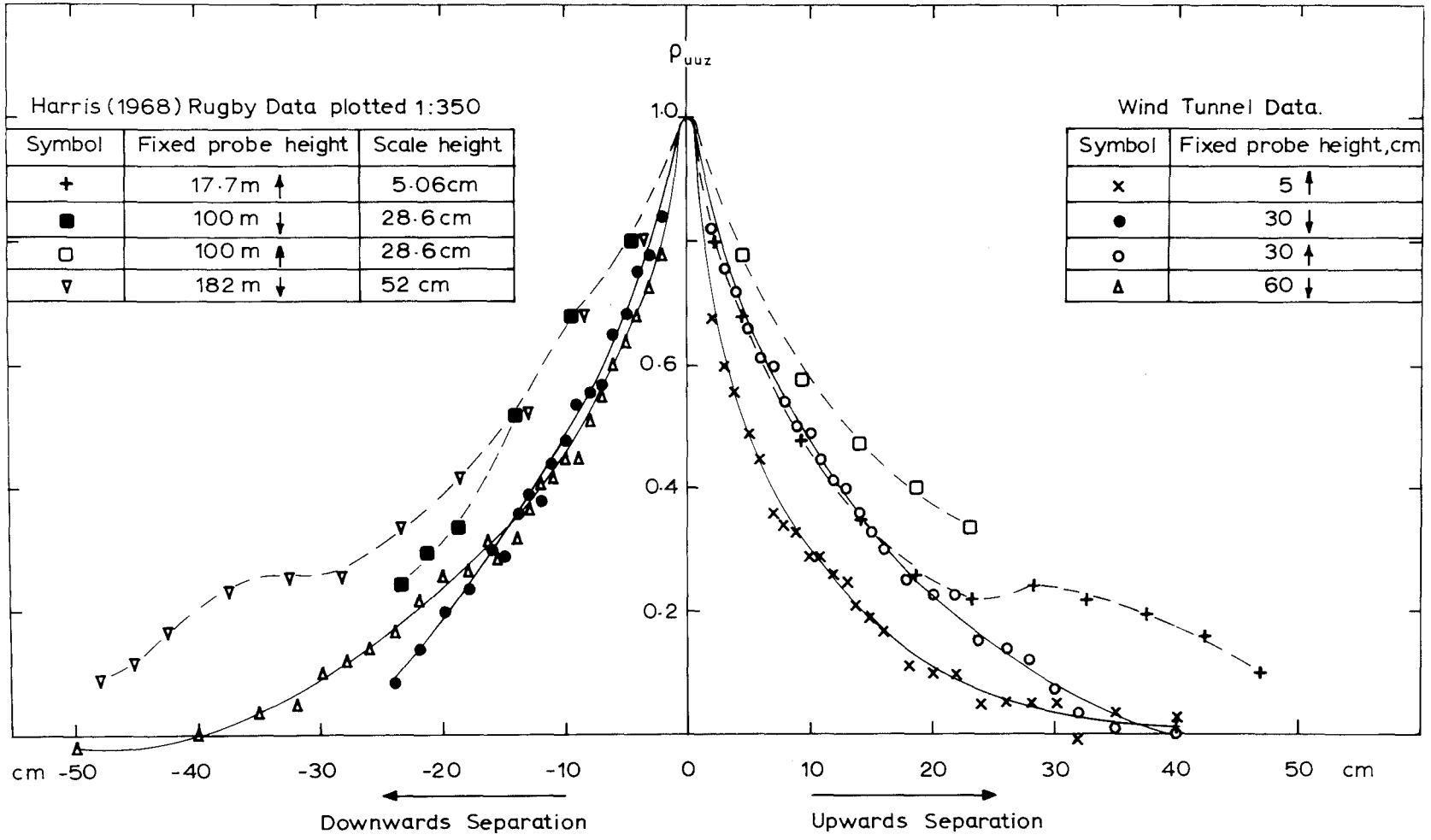

Fig. 6·48 VERTICAL CORRELATION COEFFICIENT OF u VELOCITY COMPONENT AT X = 9m, S25-LAYOUT 14.

that $L_{u_x} = 4\ L_{u_y}$ close to the ground (from measurements 10 m above ground at an airfield site), but that high above the earth's surface, in the middle to outer part of the boundary layer, the homogeneous isotropic relationship $L_{u_x} = 2\ L_{u_y}$ should be approached. This behaviour is shown approximately by the length scale data of Figs. 6.46 and 6.47.

The vertical length scales derived from the vertical correlation curves ρ_{uu_z} vs z of Fig. 6.48, show the desired increase with height. The asymmetry measuring upwards and downwards from z = 30 cm was expected, and is similar to that found by Harris (1970) in field tests. The length scale L_{u_z} measured with a downwards separation at z = 60 cm appears low, like the streamwise length scale L_{u_x}, but it is probably smaller than L_{u_z} evaluated with the travelling probe moving upwards from z = 60 cm (not measured). Again, approximate isotropy in the outer part of the boundary layer would give $L_{u_x} \simeq 2\ L_{u_z}$. In the present work, the measured u', v' and w' data indicate that anisotropy still exists in the region around z = 60 cm, so that it would be expected that L_{u_z} would be less than $0.5\ L_{u_x}$.

For comparison with the wind tunnel data, similar correlation curves to a smaller scale were found in the work of Counihan (1969) and Teunissen (1972). The only field data found were those of Harris (1968) and these are shown for comparison with the present measurements in Fig. 6.48. Harris' data have been plotted to a linear scale of 1:350 to agree with that used in the turbulent intensity plots of Fig. 6.42b. However, with the vertical correlation coefficient plot, it is evident that a better fit would have been obtained with the Harris data plotted to a scale of 1:600 or 1:650. Teunissen (1972) also compared some of Harris' (1968) data with his wind tunnel simulation correlation curves, and found his wind tunnel values of ρ_{uu_z} tended low relative to the scaled field data.

Turbulent length scale data derived from Figs. 6.46, 6.47 and 6.48 are summarised in Table 6.8 for comparison with those derived from energy spectra.

6.4.5 u and w Velocity Component Energy Spectra:

These are shown in Figs. 6.49 and 6.50. Comparing the u component spectra of Fig. 6.49 with those of Fig. 6.21 (p. 251) for Layout 3, there has been little change in the spectra at z = 5 cm and z = 60 cm, but the peak of the spectrum at z = 15 cm has moved to a lower wave number, such that it is almost at the low frequency cut-off point for the spectral analyser.

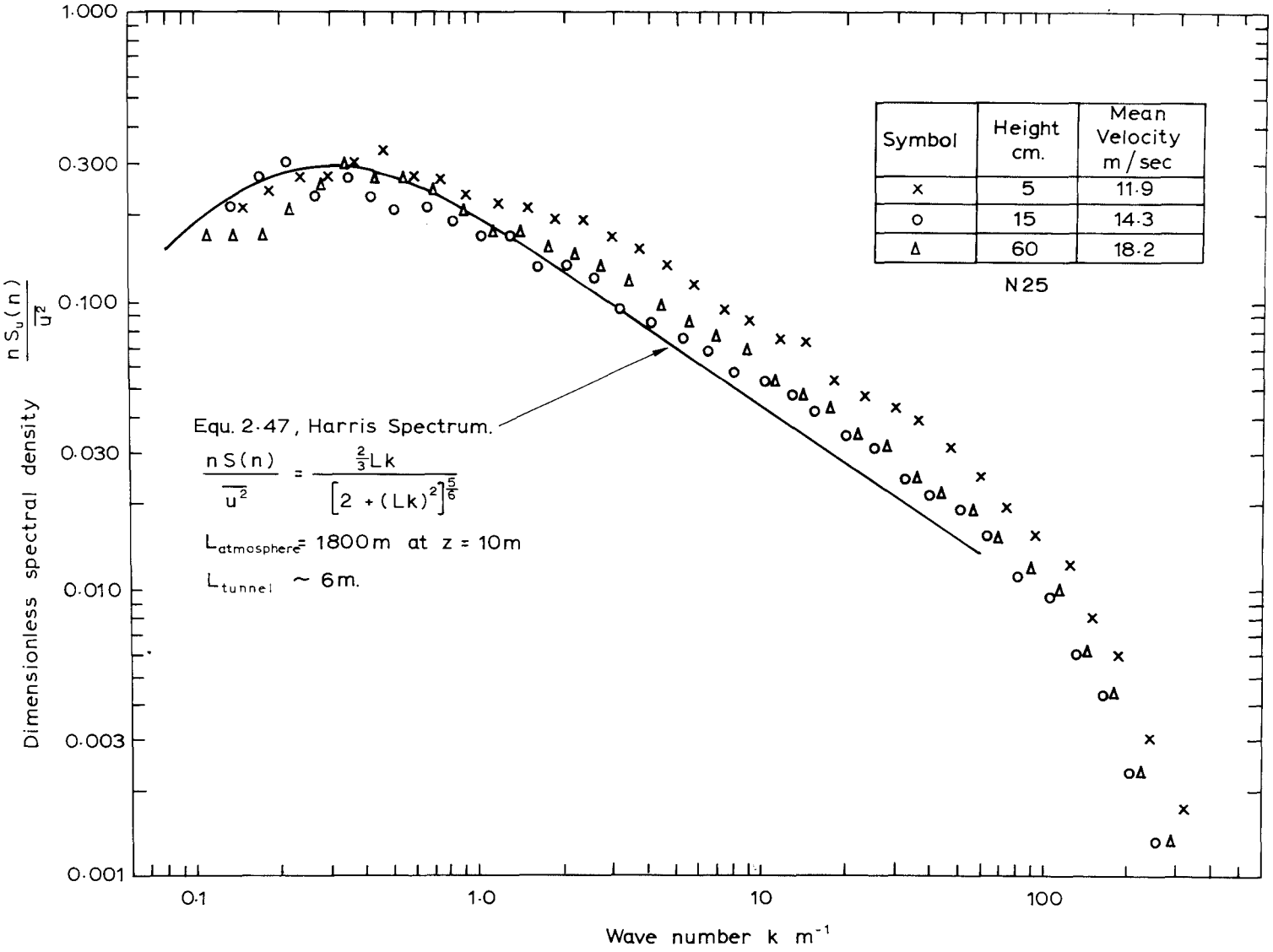

Fig. 6·49 ENERGY SPECTRUM FOR THE u VELOCITY COMPONENT. X = 9m, LAYOUT 14.

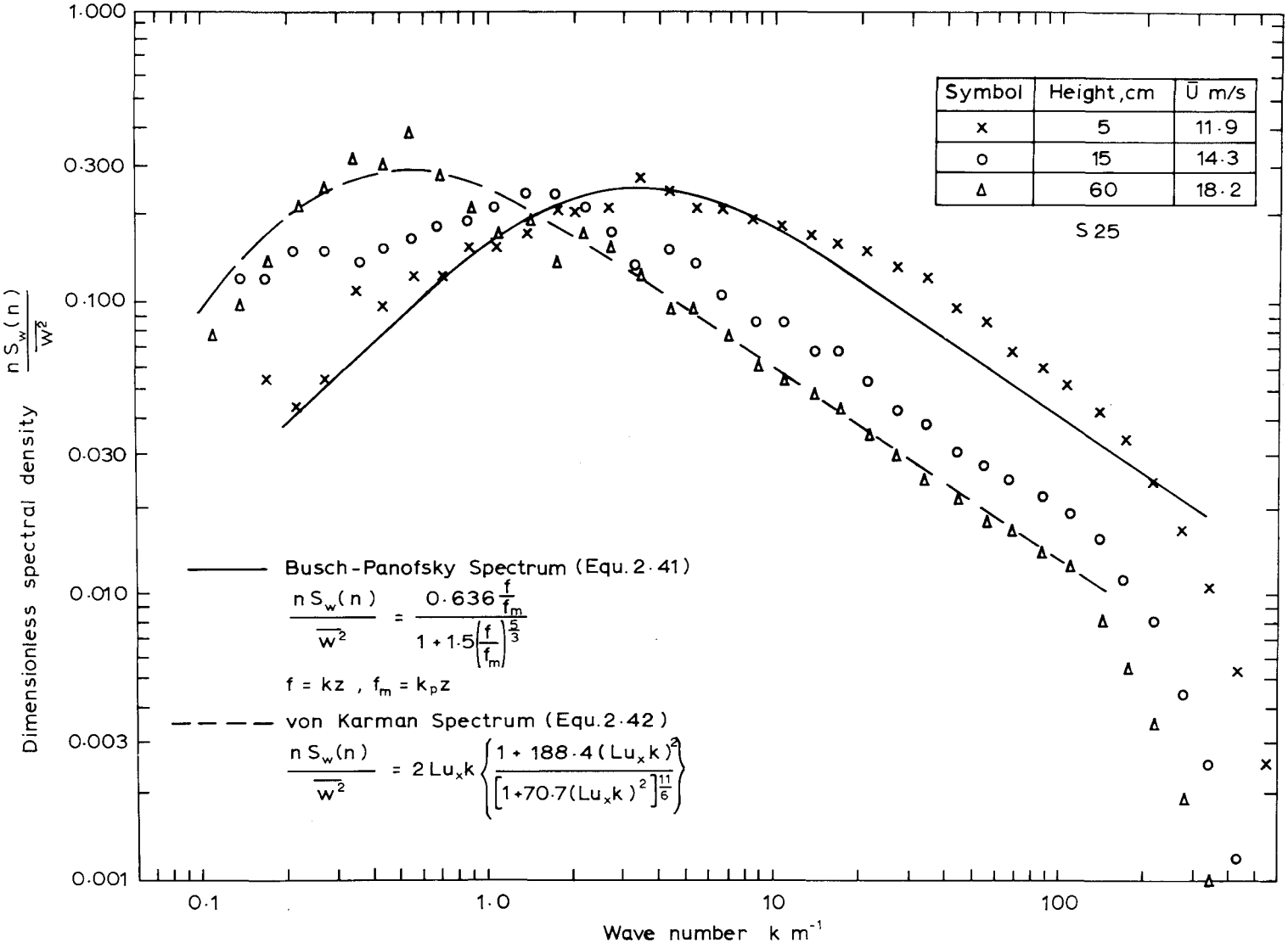

Fig. 6·50 ENERGY SPECTRUM FOR THE w VELOCITY COMPONENT X = 9m.- LAYOUT 14.

This decrease in peak wave number and corresponding increase in L_{u_x}, occurring only at z = 15 cm, is undesirable without corresponding changes at z = 5 cm and 60 cm. The fit with Harris' atmospheric model spectrum is still tolerably good, but low frequency cut-off on the spectral analyser prevented comparison for wave numbers much lower than the peak wave number.

The w component spectra of Fig. 6.50 show considerable variation with height above the floor, as expected in the atmosphere, and comparison with the two atmospheric model equations, Equations 2.41 and 2.42 (p.50) is made. In Fig. 6.50, the von Karman spectrum of Eqn. 2.42 gives a good match with the wind tunnel spectrum at X = 9 m, z = 60 cm. At z = 5 cm and 15 cm, the Busch-Panofsky model of Eqn. 2.41 gives the best fit. At z = 60 cm, where Eqn. 2.58 (p.61) is valid (i.e. above the surface layer), L_{w_x} has been calculated from the value of k_{p_w} and is shown in Table 6.8. Estimation of L_{u_x} from k_{p_w} at z = 60 cm, using Eqn. 2.58 gave excellent agreement with the estimate of L_{u_x} from k_{p_u} using Eqn 2.57, as shown in Table 6.8.

Generally the u and w component spectra were considered to have acceptable shape for a simulated rural boundary layer. Based on an approximate -2/3 slope in the spectrum $\frac{nS_u(n)}{\bar{U}^2}$ vs k, the u component spectrum shows an inertial subrange (assuming local isotropy) of about two orders of magnitude on the k axis. Therefore, there is little likelihood of viscous effects being important in the range of energy containing eddies. e.g. for the worst case, at z = 5 cm,

$$\left(\frac{u'}{\nu k_p}\right)^{\frac{3}{8}} = 112.86$$

$$>> 1.$$

$\therefore$ Batchelor's criterion for the existence of an inertial subrange is satisfied.

Length scales of turbulence calculated from spectral peaks are plotted against z in Fig.6.51, to compare with the variation in atmospheric length scale predicted by Equations 2.60 and 2.63. These length scales are also tabulated to compare with values derived from the correlation data, in Table 6.8.

TABLE 6·8 LAYOUT 14.

Location		Spectral Peak Wave No. u Component	Spectral Peak Wave No. w Component	Integral Length Scales of Turbulence, cm.						
				Derived from Spectra			Derived from Correlation Curves			
X m	z cm.	k_{p_u} m^{-1}	k_{p_w} m^{-1}	$L_{u_x} = \frac{0.146}{k_{p_u}}$	$L_{u_x} = \frac{0.212}{k_{p_w}}$	$L_{w_x} = \frac{0.106}{k_{p_w}}$	L_{u_x}	L_{u_y}	L_{u_z}	Assuming Isotropy $L_{u_x} = 2L_{u_y}$
9	5	0·43	3·3	34	——	(3·2)*	22·9	5·27	↑ 8·0	——
9	15	0·22	1·44	66·4	——	(7·35)*	32·5	8·1	——	——
9	60	0·33	0·48	44·2	44·2	22·1	28·7	10·37	↓ 11·73	20·74

* Very approximate because of isotropy assumption, plotted in Fig. 6·51.

6.4.6 Linear Scaling of the Simulation:

Table 6.8 shows considerable variation between length scales, L_{u_x}, derived using different methods. In Fig. 6.51, the measured length scales of turbulence are compared with atmospheric models, assuming for the atmosphere a 1/6 power law mean velocity profile with z_G = 283 m (see Fig. 2.7). The variation of L_{u_x} with height is not very satisfactory, with L_{u_x} at z = 15 cm tending too high in relation to L_{u_x} at z = 5 cm and z = 60 cm.

It is uncertain whether derivation of turbulent length scales from energy spectra, or from correlation data, is more accurate. Teunissen (1972) discusses this point, and notes that the accuracy of auto-correlation measurements, at large τ, is lost when A.C. coupled correlation equipment is used. Teunissen preferred evaluation of L_{u_x} from the spectral peak, accepting the inaccuracy near the surface of assuming isotropy, because length scales of turbulence in the atmosphere are generally derived from the spectral peak in field measurements, even at low altitude, and the use of the same procedure in the wind tunnel appeared reasonable.

Working from the spectrum chart record in the present work involved uncertainty where:

(i) the spectral peak was flat - i.e. in measurements near the surface;

(ii) the spectral peak was at such a low frequency as to be nearly off the chart record, e.g. see Fig. 6.52.

The chart record for the spectrum of the u component at z = 15 cm, shown in Fig. 6.52, shows that with the scatter occurring at low frequency, the peak frequency is uncertain to within about ± 3 Hz. e.g. had the spectral peak at z = 15 cm been at 6.3 Hz, L_{u_x} derived from the spectral peak would have been 33 cm in agreement with that derived by auto-correlation.

Using the DISA 55D70 Analogue Correlator, however, also involved uncertainties, and averaging times of 30 - 100 sec were required in order to obtain a sufficiently steady value of the auto-correlation and cross-correlation coefficients to record. With large time delays in auto-correlation or large separations in cross-correlation, it was found that even with a 100 sec averaging time the meter reading fluctuated considerably. Readable accuracy deteriorated from about ±2% at zero time delay in auto-correlation down to ±100% for $|\rho_{uu_\tau}| < 0.02$, at large time delays.

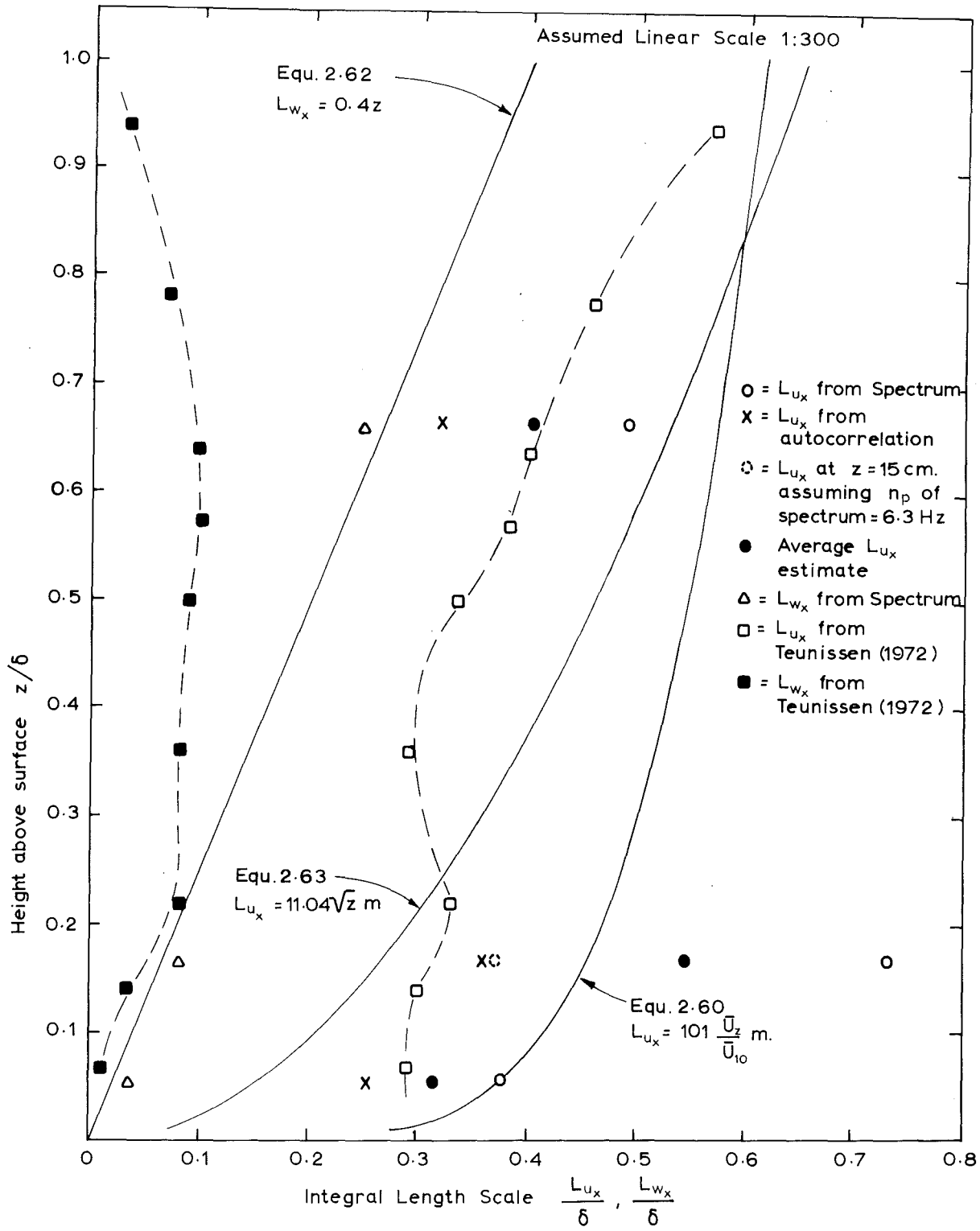

Fig. 6·51 VARIATION IN TURBULENT LENGTH SCALE WITH HEIGHT — LAYOUT 14.

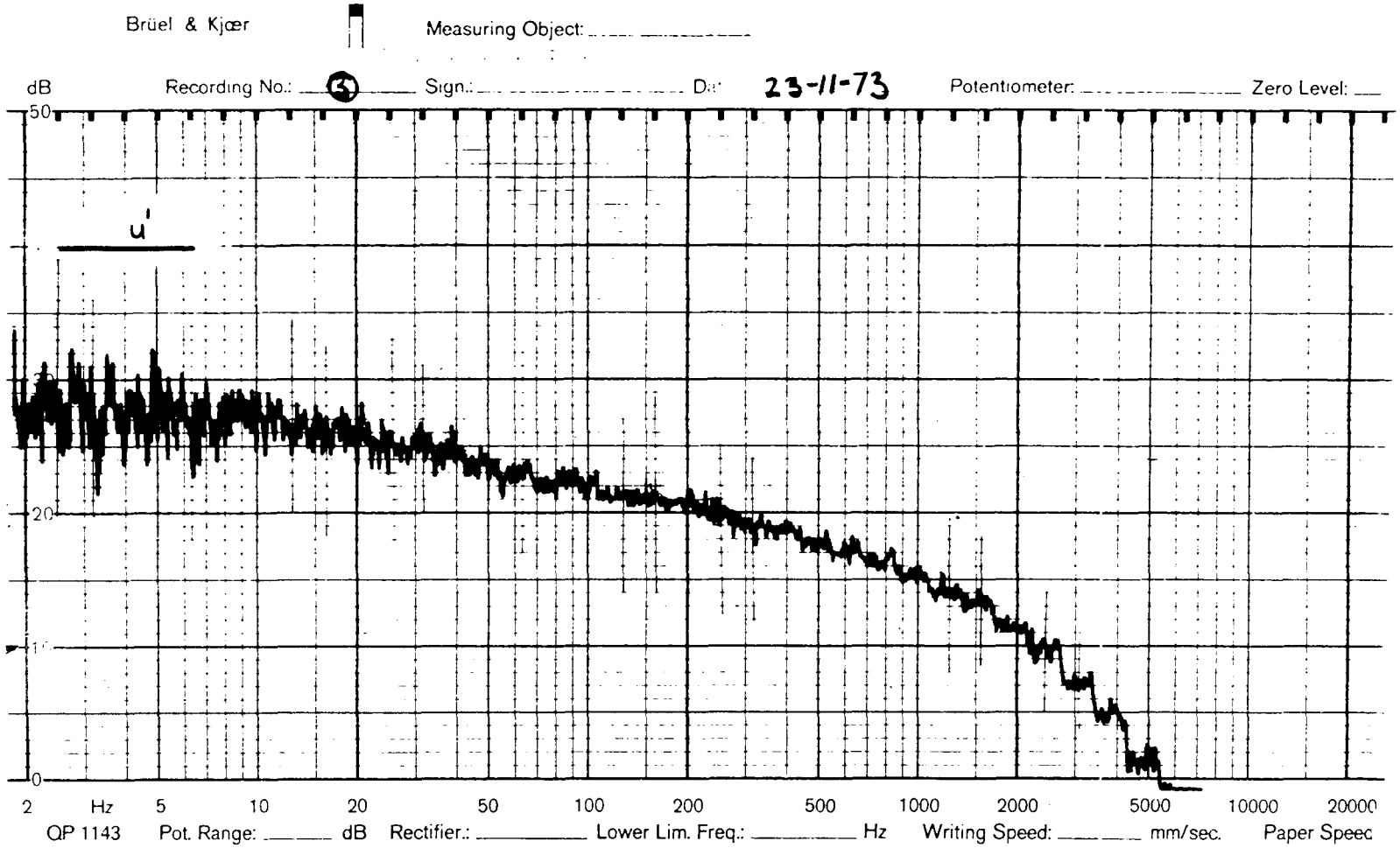

Fig. 6.52 SPECTRUM CHART RECORD – LAYOUT 14, z = 15 cm

Summing up, it was felt that at z = 60 cm, estimates of turbulent length scales were more accurate from the spectral data, where the clearly defined peak of an approximately isotropic spectrum could be used. At z = 5 cm and 15 cm, length scale estimates from the correlation data may be more accurate. If this were so, variation in L_{u_x} with height would be better than at first appears from Fig. 6.51.

As discussed in 3.5 and 3.6, previous simulations almost all show length scales of turbulence decreasing with height above the surface layer, and little attention has usually been paid to obtaining the correct variation in length scale with height. Teunissen (1972) aimed for increasing length scale with height, and obtained this, in his 1:1715 scale simulation although the rate of increase in L_{u_x} with height did not fit Eqn. 2.63. In the present work, the rate of increase in L_{u_x} with height is also incorrect, but Fig. 6.51 and Table 6.9 indicate that L_{u_x} is too high at z = 15 cm rather than too low at z = 60 cm, the high value of L_{u_x} at z = 15 cm relating to the high Reynolds stress levels around this height, and thus to the high shear introduced at the entrance to the working section.

Estimates of linear scaling for the simulation, made using the methods in Appendix 7 are summarised in Table 6.9. Considering first the methods based on comparison of turbulent length scales, it is seen that Eqn. 2.63 (p. 64) (after Teunissen, 1970) again predicts large linear scaling near the floor, of the order of 1:100. Use of Eqn. 2.60 (p. 61) leads to linear scaling estimates, which with the spectral peak estimates of L_{u_x} at least, average about 1:300. Eqn. 2.61 (p. 62) leads to generally lower values for the linear scaling as in earlier layouts. Comparison of boundary layer depth, turbulent intensity profiles and roughness length between wind tunnel and atmosphere, in each case leads to a linear scaling of about 1:300.

Accepting that for a 1:300 scale simulation, L_{u_x} is too large at z = 15 cm and slightly small at z = 60 cm, the 1:300 linear scaling between wind tunnel and atmosphere was considered a reasonable overall assessment of the boundary layer, taking the evidence of Table 6.9 as a whole. The variability among different estimates of linear scaling appears in other simulations. Counihan (1969), for instance, found a linear scale of 1:2000 based on mean velocity and turbulent intensity profiles, but 1:4000 based on comparison of length scales of turbulence between wind tunnel and atmosphere. The common trend, is in fact, for linear scaling estimated from mean velocity and turbulent intensity profiles to be larger than that estimated by compar-

TABLE 6.9 LAYOUT 14.

Location		Linear Scaling $d_m : d_a$ based on-				Turbulent Length Scale L_{u_x} from Spectrum	Linear Scaling $d_m : d_a$ based on-			Turbulent Length Scale L_{u_x} from Autocorrel^n	Linear Scaling $d_m : d_a$ based on-	
X m.	z cm.	$\frac{\delta_m}{\delta_a}$	$\frac{z_{o_m}}{z_{o_a}}$	Turbulent Intensity Profiles	Matching Autocorrel^n Data		Equ.2·60	Equ.2·61	Equ.2·63		Equ.2·60	Equ.2·63
9	5	1:310	-1:250	-1:300	-1:600	34cm.	1:310	1:500	1:50	22·9cm	1:500	1:115
9	15	1:310	-1:250	-1:300	-1:600	66·4	1:180	1:290	1:40	32·5	1:415	1:170
9	60	1:310	-1:250	-1:300	-1:600	44·2	1:380	1:630	1:370	28·7	1:640	1:880

ison of length scales of turbulence or spectral peaks between wind tunnel and atmosphere.

The estimates of L_{w_x} were plotted for comparison with model curves for the atmosphere, and in Fig. 6.51 show good agreement with the curve $L_{w_x} = 0.4z$ (Eqn. 2.62), but values at z = 5 cm and z = 15 cm are rendered very approximate by the anisotropy near the floor. Teunissen's (1972) L_{w_x} values are plotted for comparison.

6.4.7 Flow Self-Preservation at X = 11 m:

In Fig. 6.53 mean velocity profiles downstream of Layout 14, at X = 11m, are shown. Lateral uniformity has improved slightly, but acceleration of the flow in the first 12 cm above the floor is evident. This internal boundary layer growth was largely overcome by later fitting of Torro baseboard between X = 9.15 m and X = 11.6 m (e.g. see Fig. 8.8, p.369). The logarithmic plot of Fig. 6.53 tends to exaggerate the change to the mean velocity profile at X = 11 m because of the distorted vertical scale.

The u component turbulent intensity profiles of Fig. 6.54 show almost no change from those at X = 9 m, except below z = 20 cm, where turbulent intensity decreases towards the floor. The new $u'/\bar{U}_\infty$ intensity, at the surface, of 0.1 (corresponding to the smooth floor) is close to that at X = 9 m in Layout 1 (smooth floor).

The u velocity component spectra of Fig. 6.55 show similar shape to those of Fig. 6.49 with an extensive region of approximately -2/3 slope. The peak wave numbers are predictably lower, however. At z = 15 cm, n_p appeared to have moved to a frequency lower than the lower limiting frequency of the spectral analyser, but was taken as n_p = 2Hz, or $k_p = 0.14\ m^{-1}$. Length scales of turbulence derived from the spectral peaks summarised in Table 6.10, show an increase over those at X = 9 m (Table 6.8). Variation with height in the estimates of linear scaling, is similar to that at X = 9 m. The spectra at X = 11 m show the need for spectral analysis facilities with a lower low frequency limit, e.g. n_{min} = 0.1 Hz.

From the checks made, flow self-preservation at X = 11 m was considered acceptable, particularly after the addition of the extra Torro baseboard panels. In view of the approximate nature of methods used to evaluate the linear scaling of an atmospheric boundary layer simulation, the small increase in linear scaling between X = 9 m and X = 11 m was not considered significant.

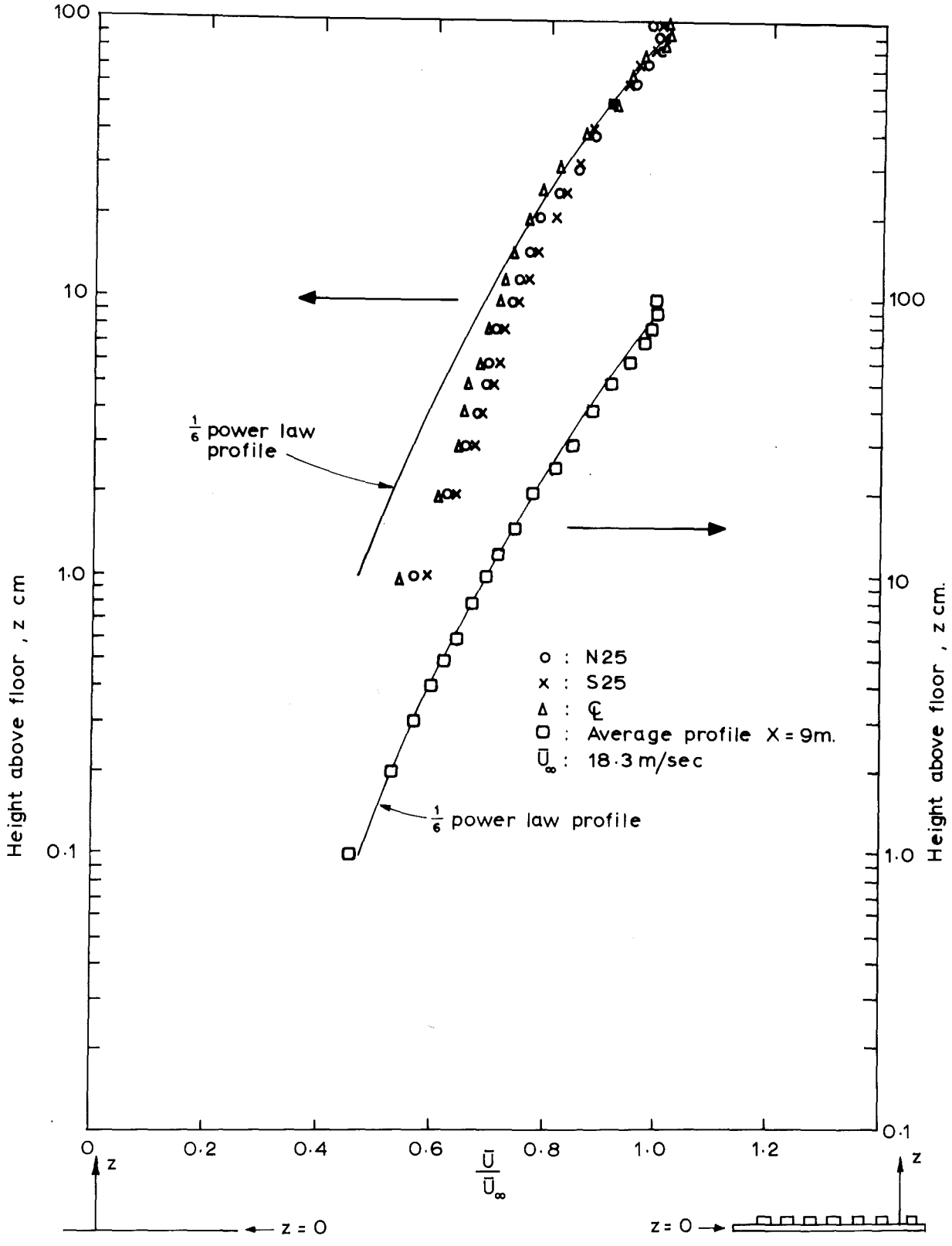

Fig. 6.53 MEAN VELOCITY PROFILES AT X = 11m. - LAYOUT 14.

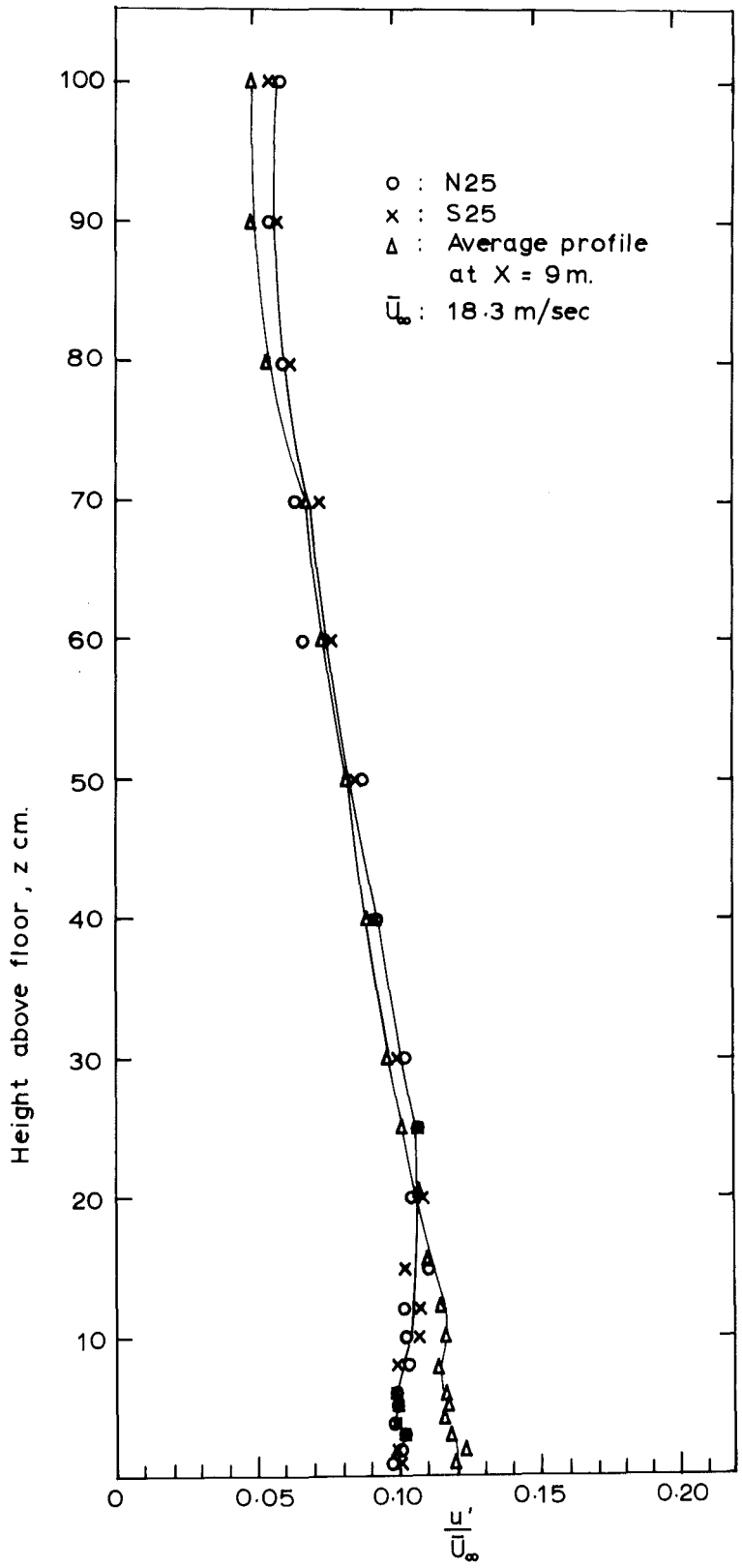

Fig. 6·54 TURBULENT INTENSITY PROFILES AT X = 11m.-LAYOUT 14.

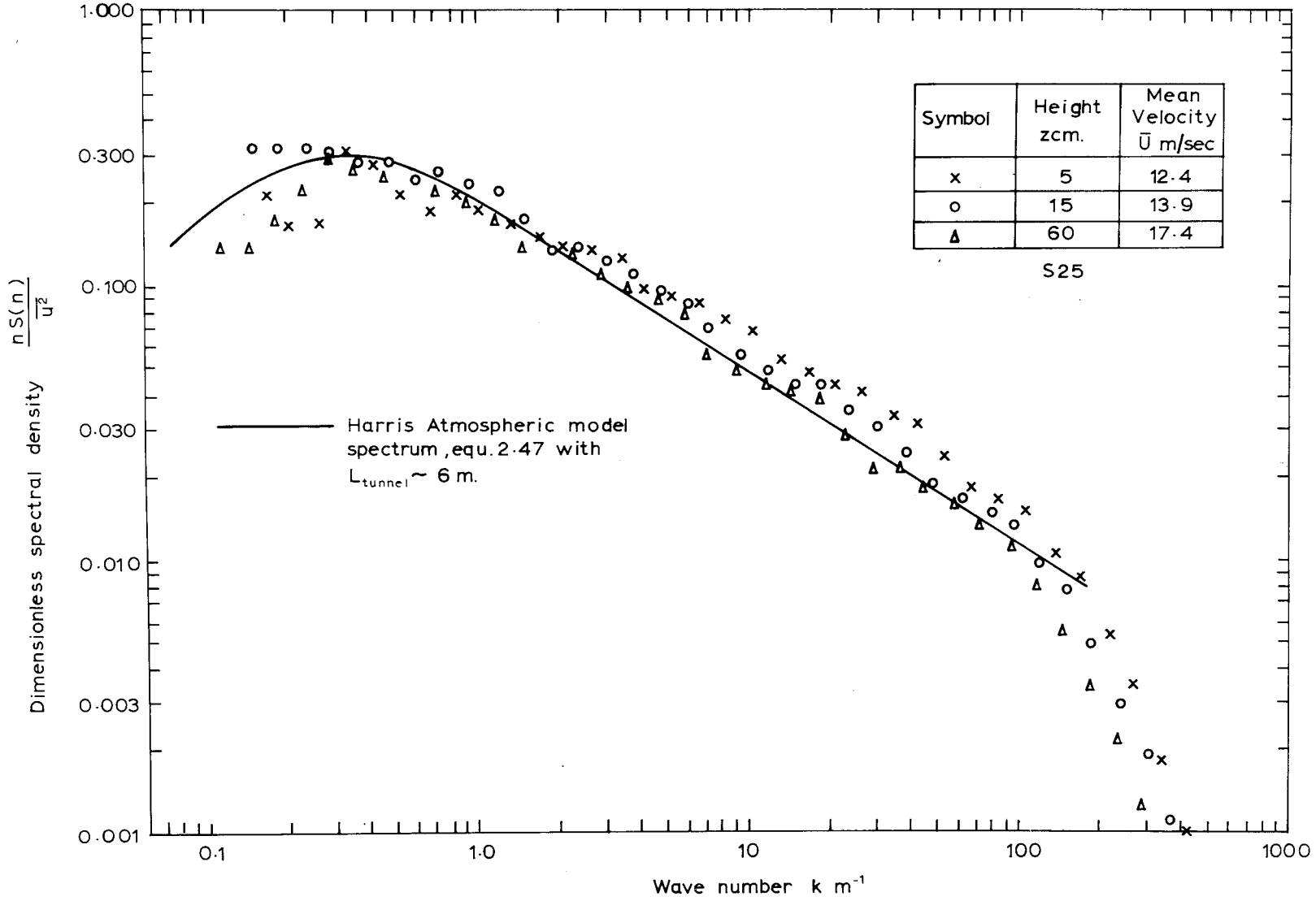

Fig. 6·55 ENERGY SPECTRA FOR u VELOCITY COMPONENT X = 11m. LAYOUT 14.

TABLE 6·10 LAYOUT 14

Location		Spectral Peak Wave No. k_p m^{-1}	Turbulent Length Scale, cm $L_{u_x} = \frac{0.146}{k_p}$	Linear Scaling $d_m : d_a$ based on -			
				$\frac{\delta_m}{\delta_a}$	$L_{u_{xm}} / L_{u_{xa}}$		
X m.	z cm.				Equ.2·60	Equ.2·61	Equ.2·63
11	5	0·33	44·2	1:300	1:230	1:360	1:30
11	15	-0·14*	—	1:300	—	—	—
11	60	0·30	48·7	1:300	1:290	1:450	1:300

* k_p uncertain. L_{u_x} not estimated.

6.4.8 Static Pressure Gradient in Working Section - Layout 14:

With the final boundary layer generating layout, static pressure variation across the working section was negligible at X = 9 m. Along the working section, there was a 1 mm W.G. increase in static pressure between X = 1 m and X = 9 m, i.e. a slightly adverse pressure gradient. This small deviation from the desired constant pressure condition was felt acceptable, and roof divergence was left unchanged, except between X = 9.75 m and X = 12.2 m, where the last 8 ft roof panel was set level to give constant cross-sectional area over most of the test section.

6.5 CONCLUSIONS TO THE WIND MODELLING PROGRAMME

6.5.1 What Has Been Achieved?

In 6.3 and 6.4, the stepwise building up of a neutrally stable, simulated rural atmospheric boundary layer, of approximately 1:300 linear scale, has been described. The method used involved techniques that have been previously used in part, such as an initial trip fence, or coarse grid. In the present work it was, however, attempted to synthesise the final boundary layer generating arrangement by a more rigorous process of incremental addition of the three basic components, grid, surface roughness and trip fences, to the initially bare tunnel working section. The use of successive trip fences to adjust mean velocity profile and turbulence structure along the working section has a parallel in the full scale rural boundary layer, where shelterbelts, small forests and farm buildings spaced across the fields have a similar effect on the flow. This similarity in the flow processes between wind tunnel and atmospheric surface layer was considered desirable at the outset.

Of the rural boundary layer simulations described in the literature, only those of Davenport and Isyumov (1967) and Cermak and Arya (1970) used pure boundary layer growth, and more than twice the boundary layer generation distance was required to achieve a similar linear scaling to that in the present work. Of the others, where 'step change + boundary layer growth' schemes were used, most were of small linear scale, i.e. of order 1:1000 to 1:4000. Armitt and Counihan (1968) achieved 1:250 scale in a rural boundary layer simulation, but with unacceptable lateral non-uniformity. Littlebury (1970) also suggests 1:250 scale for his simulation, but data presented do not enable a good evaluation of the fidelity of the simulation. The present simulation, using a different combination of existing techniques, represents an advance over previous accelerated boundary layer growth schemes

in most respects, in that a relatively large linear scale of 1:300 has been obtained, with the following requirements of the model flow satisfied:

(i) Fully aerodynamically rough flow.
(ii) Absence of pressure gradients.
(iii) Correctness of mean velocity profile.
(iv) Correctness of turbulent intensity profiles (apart from small excess in w' in middle region of boundary layer).
(v) An approximate constant stress surface layer.
(vi) Satisfactory scaling of u and w component energy spectra.
(vii) Integral length scales of turbulence substantially correct.
(viii) Good lateral uniformity.

A possible scale effect in the use of trip fences to promote rapid boundary layer growth appeared in the present simulation, where Reynolds stress levels were uncharacteristically high, for a rural boundary layer, in the surface layer. The high Reynolds stress values appeared to be accompanied by values of w' and L_{u_x} that were larger than required in this region. This problem does not seem to occur in small scale simulations (e.g. 1:2000 scale) where an initial trip fence is used.

Subsequent to the testing of Layout 14, a paper by Cook (1973) was obtained describing the use of coarse grid + trip fence + surface roughness for an urban boundary layer simulation. Cook's technique lends support to the method used in the present work, and the high levels of Reynolds stress recorded by Cook ($-\overline{uw}/\bar{U}_{10}^2 \simeq 0.030$) would be more acceptable for urban boundary layer modelling work. Development of an urban boundary layer simulation should be readily possible from the existing model rural flow by alteration to trip fences in combination with, say, the Torro block surface roughness of Layout 5, and a 3 in bar size in the initial coarse grid. With the maximum working section height of 1.37 m in the atmospheric wind modelling working section, only a partial depth model urban boundary layer will be able to be generated, if a 1:300 scale is used.

While Ludwig and Sundaram (1969) have pointed out that only the atmospheric surface layer can be accurately modelled in a wind tunnel, the usual practice was adopted in the present work, of modelling a full depth atmospheric boundary layer, recognising that increasing inaccuracy above the surface layer occurs owing to the neglect of Coriolis effects. In the simulation it was attempted to produce profiles of mean velocity, turbulent intensity and turbulent length scale, which with the energy spectra, conformed closely to idealised atmospheric models given in Chapter 2. The necessity for this may be questioned. For instance, how important were the

changes made to the flow between Layouts 3 and 14, for which the boundary layers were similar? Turbulent intensity data of Ivanov (1965) in Fig. 6.43 (p. 291) show the variability that exists in the atmosphere at one location, and as pointed out in 2.4.3. ±10% variation in power law mean velocity profile exponent at one location can be expected,depending on approach wind direction, speed and thermal stability. Thus approximate simulation of such parameters as mean velocity profile may be acceptable for engineering purposes. The author considers, in retrospect, that correctness of the turbulence structure is more important to the simulation than rigorous obedience to a design mean velocity profile, particularly in an accelerated growth boundary layer where the mean velocity profile may not characterise the turbulence in the flow.

In progressing from the bar grid simulation of an atmospheric boundary layer, described in 4.2, to the boundary layer finally achieved in Layout 14 using coarse grid, trip fences and surface roughness, a substantial improvement in linear scaling and fidelity to atmospheric turbulence structure was achieved. The addition of trip fences which gave the threefold increase in linear scaling between Layouts 2 and 14 did, however, lead to the high shear stress levels in the surface layer, and this problem may ultimately be avoided only by using lower, more uniform surface roughness, and a longer boundary layer generation distance.

6.5.2 Performance of the Wind Tunnel and Instrumentation:

Within the limitations imposed by design constraints, the wind tunnel was satisfactory for the atmospheric wind modelling exercise. The maximum free stream speed of about 19 m/sec in the wind modelling working section is probably adequate for most purposes. Possible improvements to the wind tunnel have been discussed in 5.3 and 5.4. For the wind modelling work, two desirable improvements will be the removal of the residual mean flow swirl that persists in the working section under part load conditions, and implementation of steadier mean flow speed at full load. Fitting of downstream guide vanes after the fans will allow different fan blade pitch settings, which should enable both these aims to be achieved.

The working section cross-section area and length are just large enough for a 1:300 scale simulation. Larger cross-section and length would be useful in the future, and a more suitable tunnel, which could be constructed if funds became available, would have a working section 3 m wide x 2 m high in cross-section,30 m in length, with a speed range of 0 - 30 m/sec, and with a uniform flow of not more than 0.5% turbulent intensity at the start of the working section.

The flow measuring equipment performed reliably, but certain limitations in the accuracy of operation and reading were present, as discussed in Appendix 6. These problems should be overcome when hot wire anemometer signals are processed directly on the Hewlett Packard 2100-A computer, which will be able to perform more accurately the functions at present handled by the analogue equipment of Fig. 6.1.

6.5.3 Suggestions for Future Work:

(a) Instrumentation:

(i) A calibration rig for the hot wire anemometers should be constructed. For the atmospheric wind modelling work it would need a speed range from 0 - 20 m/sec at least, and an essential would be uniform, swirl-free, constant temperature flow.

(ii) An electronic sensor may be able to be constructed which would indicate loss of hot wire anemometer or lineariser gain due to ambient temperature rise in the flow, and enable readjustment of the gain without traversing the probe back to a reference position in the flow. An alternative would be to purchase some temperature compensated probes.

(iii) On line access to the HP 2100-A computer should be implemented before the next major project involving extensive use of the hot wire anemometers. While mean velocities and RMS velocity fluctuations can be adequately read from the analogue equipment, greater resolution, frequency range and accuracy is needed for spectral analysis and auto-correlation.

(b) Atmospheric Wind Modelling:

(i) Further boundary layer generating schemes should be investigated with the aim of achieving more correct levels of shear and variation in length scale of turbulence with height above the floor. Existing graded blockage or accelerated boundary layer growth schemes, including the present work, tend to produce turbulent length scales which decrease, or increase too slowly above the surface layer. (See Review of 3.5).

Major alterations to the present system could be tried, such as rotating vane gust generators (Lindley and Bowen, 1974)

or an air jet system such as used by Teunissen (1972). The former system has the disadvantages of generating gusts at a discrete frequency and is really suitable only for special applications, such as dynamic excitation of a slender structure. Teunissen's (1972) air jets + trip fence + roughness may hold some hope. The use of individually fed air jets is analogous to a grid where the flow through one mesh orifice is not related to the flow through others. It might therefore be possible to obtain larger length scale with increasing height by use of graded orifice sizes, without losing the ability to produce the desired mean velocity profile. Teunissen's results showed that a trip fence was required to achieve high enough turbulent intensity. Development of the air jet system may remove the need for the additional trip fence.

(ii) Measurements of Reynolds stress, $-\rho\overline{uw}$, are required over various terrains in the atmosphere, to a height of at least 100 m. This would establish more definite criteria for a Reynolds stress model profile in wind tunnel simulations of atmospheric flow.

(iii) Experiments and analysis are required to determine what degree of fidelity to atmospheric mean flow and turbulence structure is required in the simulated boundary layer. While close similarity to the atmospheric flow ensures that effects of the model flow on, say, a model structure will be similar to the full scale situation, certain experiments appear to require incomplete simulation of the wind. For instance, a tall, slender structure, with dominant natural frequency may require simulation of only a limited range of gust frequencies and an approximate mean velocity profile. The relative importance of different parameters describing the flow may have to be determined for each different modelling situation, by a process of varying each one independently (where possible), e.g. variation of turbulent length scale while turbulent intensity and mean velocity profile are held constant.

(iv) Urban boundary layer modelling should be attempted in the University of Canterbury wind tunnel, developing the work of Davenport and Isyumov (1967) and Counihan (1973), and Cook (1973). 60,000 Torro blocks are waiting to become model buildings!